BIOLOGICAL APPLICATIONS OF FLUORESCENT IMAGING

BY

Kristin C. Halfpenny

Dissertation

Submitted to the Faculty of the

Graduate School of Vanderbilt University

in partial fulfillment of the requirements

for the degree of

DOCTOR OF PHILOSOPHY

In

Chemistry

August, 2009

Nashville, Tennessee

Approved:

David W. Wright

Brian O. Bachmann

Richard N. Armstrong

Laurence J. Zwiebel

To my loving parents –Mom, Dad, Angie and James–

Without whom I would not be who I am today.

ACKNOWLEDGEMENTS

The completion of the work within this document could not have been completed without the contribution of many people, all of whom have helped me more than I could have imagined and for whom I will be forever grateful. First and foremost is my advisor, Dr. David Wright. He has been a source of moments of encouragement and mountains of frustration, both to my benefit. He has never failed to challenge me to “figure it out” while simultaneously serving as a guide to point me in the right direction. It is very few who have such an intellectual relationship with their dog as David has with his beloved Gracie. Every time Gracie would enlighten him with academic insight, it inspired me to one day have such a fruitful relationship with my own dogs, Sadie and Daisy (though they are still far from achieving the level of sophistication that comes from Gracie). David has kept me focused at times when I had begun to lose sight of my goal of becoming an independent thinking scientist and for that I can not thank him enough.

I also must thank my committee members who have been witness to some of my largest stepping stones along this journey. Whether in his classes, rotating in his lab, or in just having a casual conversation on the elevator, Dr. Brian Bachmann has served as a model for me. Despite his accomplishments, he has remained approachable and willing to help. He has an unarming demeanor that makes learning from him a pleasure, especially as a young easily intimidated graduate student. Dr. Larry Zwiebel brought a biological touch to a graduate student that was resistant to straying too far from her chemistry comfort zone. I am especially thankful to Dr. Zwiebel for taking an extra moment during my IRP to help me feel comfortable when it became evident, through my rather rapid rate of speech, that my nerves had taken over. It is this sort of relationship with students that makes for a great mentor. Finally, Dr. Richard Armstrong has always challenged me with poignant questions. The epitome of the hidden iceberg, Dr. Armstrong remained largely quiet during my presentations, only speaking when he had a question that truly challenged me to think. These challenges have forced me to develop my ability to think on my feet and learn to draw from my knowledge to reach a reasonable conclusion when the answer is not at the tip of my tongue. This is a rare skill that is only developed with someone to challenge it. Each of my committee members have offered a unique perspective to my work and with this perspective, guidance that has helped me develop as both a student and a scientist.

The Wright lab, and all its members, has become like a small family over the five years I have been here. Like a family, we have laughed and yelled and cried together. Though each member of the lab has offered me immeasurable amounts of academic help that is not what I remember most about any of them. My lab elders welcomed me into a lab that was unlike any other I had seen in the Chemistry department. During our tenure in the lab together, Dr. Scott Miller, Dr. Clare Kenny Carney, and Dr. Elizabeth Benzten helped me learn many lessons that have carried me through graduate school. Despite their wisdom, it is their antics that I look on fondest. Regardless of their accomplishments, I will always think of Scott and Liddy on the day that I came into the lab and an argument over the placement of a George Bush bumper sticker had escalated to throwing things. When I arrived, Liddy was taking things off Scott's desk and throwing them into the floor, while in retribution, Scott was acting in kind at Liddy's desk. Despite their seniority, I was forced to scold both of them into submission before the situation could be resolved. Their passion for politics carried over into all things they did and that is something I admire about them. For admiration for Clare did not entirely manifest itself until I myself sat here writing this document. Always the one to achieve whatever she set for herself, Clare not only wrote her dissertation while pregnant, she defended her thesis only a week after giving birth. After experiencing the work necessary to put together a document like this, I can not imagine the dedication Clare must have had to do it while also carrying a baby. She has my unending respect. Three other members of the Wright lab that served as mentors and friends during my early years are Dr. Aren Gerdon, Goska Broncel and Dr. Sarah Sewell Peirce. Aren has always been one of the most laid back individuals I know and his calm spread to anyone he is around. His presence always brought a peace to the lab that was lacking without him, and always needed in a group like this. Goska is single-handedly responsible for my mastering of the polish language. Between our "word of the day" and my complete mastery of polish curse words, Goska has impacted my vocabulary in a way few others have and she is greatly missed now that she has returned to Poland. Finally, I would not have made it without a friend like Sarah, whose propensity for detail always astounded me. Sarah was a meticulous scientist and still a goofy fun person.

The members of the Wright lab who have considered my peers, who have been here with me for the majority of my tenture, hold a special place in my heart. Alex, Reese, Ryan, Leila, Melissa and Jonas have become the people I think of when I think of the Wright lab. Joining the lab together, Alex, Reese and I had that special bond that you can only have with people of your incoming class. From the day I met her our first day at Vanderbilt, Alex was and continues to be one of the most outgoing and friendly people you can meet. She has served as an unofficial ambassador between the Wright lab and each incoming class, striving to get to know and include them in life in and out of the Chemistry department. I often wonder what a day is like in the world of Reese Harry. He is both a source of constant amusement and, when necessary, a critical voice, willing play the devil's advocate to help you completely work through a problem….or just offer you a beer if when it is the best answer. Though they joined the lab a little later, Ryan, Melissa, Jonas and Leila have each contributed to my life in lab in their own way. When you think of Ryan, you can't help but think of his cutting sarcasm. An avid baseball fan, Ryan never failed to tell me that he hated my hat anytime I wore a cubs or Yankees hat, a joke that spanned years. Never was it more amusing though then the day Ryan thought he had finally made me mad with his constant proclamations of hatred. After the usual comment of "I hate your hat," I had run out of witty comebacks and simply responded "ok" leading Ryan to believe I had finally had enough. Moments later I returned to my computer to find an email from Ryan apologizing if he had finally gone too far, and assuring me that he was only kidding. To this day, I am disappointed on the days that I wear either my cubs or Yankees hat and no one tells me they hate it. It feels like something is missing. Melissa Carter, once my young rotation student (poor melissa) has grown into her own scientist and one of the few beacons of sanity in writing my dissertation. I guess the expression "misery loves company" rings true because without her sharing this experience with me, I don't think I would have made it with any remnants of sanity remaining. I could only hope that each person has their own Melissa to help get them through the challenges in their lives. When I think of Jonas, there is only one thing that comes to mind –bay JK. As my baymate for the past year, Jonas has truly become someone that I turn to for not only advice about gold nanoparticles, but when I need a willing ear. He has patiently supported me through many of the hardest moments of both my personal and professional life and for that, I would give him the baymate of the year award if such a thing existed…perhaps I will invent one just for him. The number of "bay-wide" ordinances we have instated have brought me great joy, whether bay diets or birthday countdowns. I truly hope that wherever I go next, I sit next to somewhere as great as bay JK with someone as great as Jonas. And then there is Leila. Leila has become one of my closest friends in graduate school. As with any friendship, we have had our ups and downs but when I look back on my favorite times in graduate school, many of them include Leila. As my roommate, Leila was instrumental in many ridiculous adventures. None stand out in my mind though, more than the day we realized our heat was broken when it was 30 degrees outside. That was the day Leila learned how to build a fire. Only after an 11pm trip to walmart to buy all the necessary fire-building supplies, including self starting logs, a complete andiron set and several packages of fire wood. When the fire was finally built, around 1am, we huddled around the newly built fire and ate cocoa puffs and took "family photos" with the dogs. I have confidence that should I ever get trapped outdoors on a blistery cold night, the skills I acquired that night will see me through…provided I have a few starter logs handy. There are othe members of the lab who have come later but still made an impact on my daily life. Catherine Prudom will forever be regarded as my benefactor as her many cooking adventures often resulted in lunches for myself and John Stone's daily check in's to see how life is going have made each day a little more pleasant. As I see my own graduate career coming to an end, there are new Wright lab members who are just beginning to flourish in theirs. Anh, Josh, Becca, and Steven continue to amaze me with the zest they have for their work and I hope that it carries them through a productive graduate career mastering the ways of both hemozoin and RSV. I am confident they will carry on the traditions of the Wright lab, such as the quote wall, faithfully.

Throughout my time at Vanderbilt, there have been many people outside the confinements of the Wright lab who have made significant scientific contributions to my work that need to also be acknowledged. Specifically, I would like to thank Sean Shaffer in the Cell Imaging Resource Core for all of his help mastering confocal microscopy and his continual assistance anytime the instrument simply chose not to cooperate with me that day. I would also like to thank Mike Warnament for pointing me in the direction of flow cytometry when I needed a quantitative approach to many of cell-based problems. This has been a tool that I have found to be immeasurably useful over the years and without his guidance, I might not have discovered it. In that same vane, Kevin Weller, Dave Flaherty, and Brittany Matlock in the flow cytometry core have been infinitely patient as I continued to bring them new challenges. Finally, I also owe thanks to Mike Linquist in the Crowe lab for helping me with the 4-D spinning confocal and his patience when I anger the instrument with my 30 gig files.

Though the people I see on a daily basis as I move though my time here at Vanderbilt have made each day more interesting, it is the people in my life who have nothing to do with work that have made it bearable. To those people, I owe a special thank you. Without the unending support of my family, none of this would have been possible. My mom, dad, stepdad and stepmom have been the solid support which I have leaned on for my entire life and these five years have only proven their strength. Always understanding when I was a neglectful daughter and ready to listen when I demanded their attention, they have stood by me through each trial I have faced in graduate school. Even without understanding what any of it meant, my mom has patiently listened to me vent about the in's and out's of a failed experiment for countless hours. I also want to thank my brother and sister, Scott and Bethie, for the support they have given me over the years and more importantly, the fun we have had together. Though they are not mentioned here by name, the support my family has given me is not limited to my parents and siblings and to all of them, I owe a huge show of gratitude. Finally, beyond my family, the love and support (and distractions) of my friends have made graduate school an experience I will never forget. Though all my friends are amazing in their own rite, there are a few in particular who have meant more than I can say. Jordana Taylor Hazel, Steven Shulze and Sarah Hubbard have been my closest friends for years, and despite their distance, three of the most constant things in my life over the past five years. There are few people in the world that I can count on more than them and for that they will forever hold a special place in my heart. Not to mention, Steve, my friend from New Jersey, is one of the most awesome people I know, obviously. Within the world of graduate school, two people stick out as someone that has impacted me both academically and socially. Those people are Tim Panosian and Sarah Musser. Each of them brilliant scientist in their own rite, Tim and Sarah have been there when I needed to talk science, or just needed to talk. It is rare to find someone who can fill both those needs and to find two has been remarkable. I know they will both go on to great things with their lives and I can't wait to see what they are. If Vanderbilt has brought me one great joy, it has been VIBE and all of the people in it. Serving as my escape from science, I don't think this would have been possible without it. I am particularly thankful for VIBE because of the special people it has brought into my life. Sabrina Johnson Turner came into my life here in Nashville at a time would I could not have needed her more. She is a joy and my twin and continues to amaze me as she takes over the legal world. She is the Demi Lovato to my Selena Gomez. VIBE has also brought me Ali

Wilhelm, my “undergrad friend.” When I look back over the last six months of my life, the one thing that has carried me through has been Ali and her unwaving love of froyo. Who knew a frozen treat could be so therapeutic. Last but not least, Jordan Mason who, even in our darkest moments, never stopped supporting me in everything I do. In the past year and a half, Jordan has stepped into the role of my best friend and filled some very large shoes with amazing grace. He has managed to teach me a new found respect for a super charger while still catching all the rambling stories I bombard him with on a daily basis. During the final challenges of graduate school, Jordan has provided me something to look forward to each day when I leave the lab and for that I am eternally grateful. More than a boyfriend, he has been an unbelievable friend without which all of this would have been much less fun.

With the support and friendship of so many amazing people, I feel like I have been truly blessed while in graduate school and have not yet begun to repay these people for what they have done for me over the years. Each of them holds a special place in my heart and I hope that I can one day do for them what they have done for me….Oh yea, and the money…can’t forget the money! I’d like to thank the National Institute of Health for their financial support (Grant # NIH R03AI060827).

TABLE OF CONTENTS

Page

Chapter

Appendix

LIST OF TABLES

Table Page

LIST OF FIGURES

LIST OF SCHEMES

Scheme Page

CHAPTER I

INTRODUCTION

Fluorescent Microscopy

The phenomenon of fluorescence was first observed by Sir John Frederick William Herschel in 1845. Herschel noted that when a solution of quinine was illuminated with sunlight, it exhibited an "extremely vivid and beautiful celestial blue colour."(9) These early descriptions clearly demonstrated the recognition of an unusual phenomenon which, at the time, could not be explained scientifically. Years later, the phenomenon he described, which would come to be known as fluorescence, would become a critical component in the development of a method of microscopy utilized to study interactions that occur on a scale too small to be seen with a light microscope. Today, fluorescent microscopy is applied to a wide range of applications from protein-protein interactions to the effect of small molecules on biological systems.

Fluorescent and Confocal Microscopes

It was an interest in the first discovered fluorophore, quinine, which led to the development of the first spectrofluorometer. During World War II, there was an increased interest in the detection of antimalaria drugs such as quinine by the Department of War. Early drug assays showed that the fluorescence property of the molecule would make an effective detection strategy and lead to a subsequent program at the National Institute of Health to develop the first spectrofluorometer.(9) Today, fluorescent microscopes are a staple in the study of biological systems and have been developed for the use of multiple fluorophores, allowing the researchers to learn about a number of interactions simultaneously.

Fluorescent microscopes resolve fluorescence as a function of spatial coordinates in either 2 or 3 dimensions for objects on the micro-scale. The most commonly used fluorescence microscope is known as an epifluorescent microscope. Epifluorescent microscopes are set up so that both excitation and observation is from above (epi-) the specimen. An epifluorescent microscope has four main components which result in the specific detection of fluorescence.(10; 11) The first of these is the light source which is used for excitation of the specimen and typically is either a xenon arc lamp, mercury-vapor lamp or a wavelength specific laser. The second and third components are an excitation filter and a dichoric mirror (or dichromatic beam splitter) which are both responsible for allowing only light of the wavelength necessary for excitation to reach the specimen. The final component is the emission filter which is located between the the objective

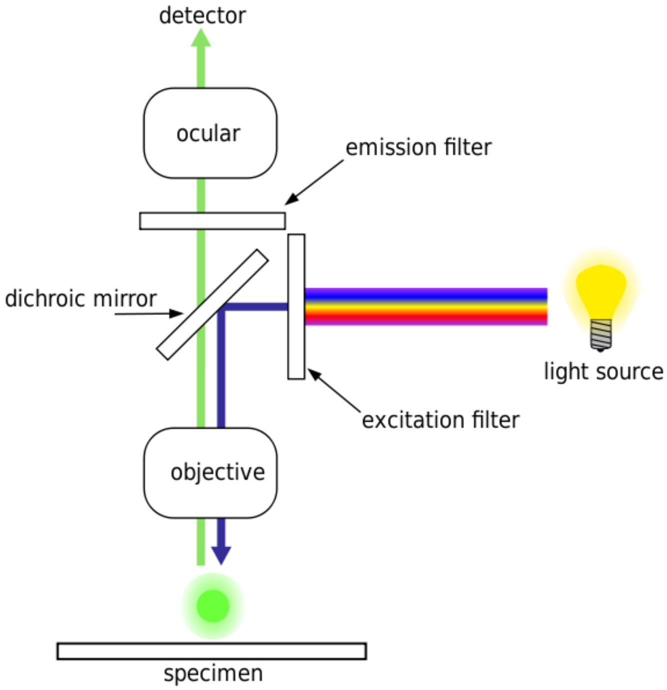

Figure 1. Optical set up of an epifluorescent microscope. In an epifluorescent microscope, both illumination and detection come from above the specimen. Further, the use of a dichoric mirror filters the illumination light so that the specimen is only hit with a particular wavelength of light which will lead to excitation. Only the emitted fluorescent light and reflected excitation light is then directed to the objective, and is filtered further so that only the fluorescent light reaches the detector by the emission filter.(5)

and the detector. The emission filter then seperates the reflected excited light from the emitted light so that only the fluorescence (emitted light) is detected.(10; 11) With these components, a specimen which has been labeled with a specific fluorophore, is illuminated with a corresponding wavelength of light resulting in excitation of the specimen. This causes fluorescence emission which is then separated from the reflected illumination light by the emission filter and the fluorescence is detected (**Figure 1**).(10) In the case of the epifluorescent microscope, because most of the excitation light passes through the specimen unaltered, only reflected excitation light reaches the objective together with the emitted fluorescent light, giving an improved signal to noise ratio.(10) Though a basic epifluorescent microscope is useful for a number of applications, it can not give the resolution necessary to focus on specific planes within a specimen. In the case of biological applications, such as protein trafficking, simply being able to confirm fluorescence within a specimen is not enough, the ability to look at the exact location of the fluorescence is needed. As a result, an improved fluorescent microscope, known as a confocal microscope, was developed.

The development of the confocal microscope revolutionized microscopy the way few things before it had. Its power lies in the unique resolution it offers:

> "With the new microscope, one can slice incredibly clen, thin optical sections out of thick fluorescent specimens; view specimens in planes tilted to, and even running parallel to, the line of sight; penetrate deep into light-scattering tissues; gain impressive three-dimensional (3D) views at very high resolution; obtain differential interference or phase-contrast images in exact register with confocal fluorescence images; and improve the precision of microphotometry."(12)

The concept of the first confocal microscope was devised by a post doc at Harvard University in 1957 named Marvin Minsky.(12) Today the basic idea of the confocal has been developed into a laser-scanning confocal microscope which is used in a broad range of biological applications.

While traditional epifluorescent microscopes give images with depths of 2-3 µm, the confocal microscope is able to yield images with depths less than 1 µm thick, simultaneously rejecting out of focus light.(4) A typical confocal microscope is set up similar to an epifluorescent microscope with the addition of a pinhold apparatus known as the detector apparatus (**Figure 2**).(4; 12; 13) The ability of the confocal microscope to give images of such thin focal planes is the result of this detector apparatus located between the emission filter and the detector. Only the light emitted from a narrow plane of the specimen, known as the focal point, will be traveling in a path which allows them to transverse the pinhole apparatus. Any light originating from other planes will simply strike the walls of the pinhole apparatus.(4; 12; 13) The pinhole apparatus is also responsible for

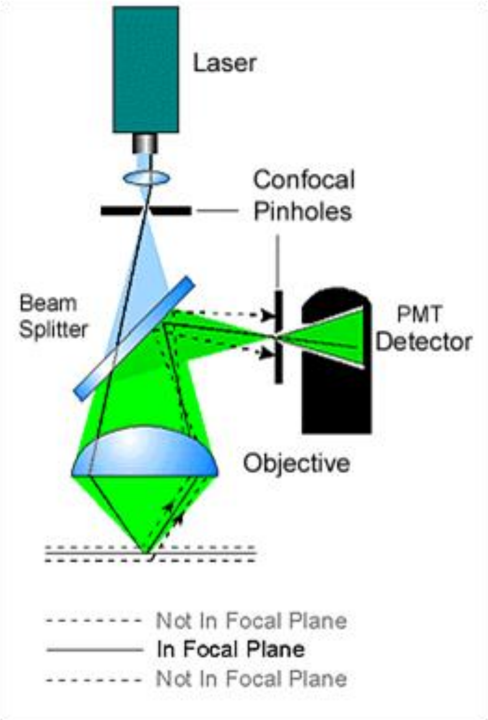

Figure 2. Optical Set up of a Confocal Microscope. The confocal microscope includes a pinhole apparatus which allows only light that originates on a particular plane (focal point) to be detected. All other out of focus light is blocked by the pinhole apparatus.(5)

pinhole and the thickness of the focal point. As the pinhole diameter increases, so does the thickness of the focal point; for larger pinholes, confocality is essentially lost.(4) The use of a pinhole apparatus to discriminate fluorescent signal results in the detection of only one focal point at a time; therefore, in order to create a 2D image of an entire plane, it is necessary to scan the plane one focal point at a time.(4; 11; 13) Two methods are typically employed to do this. The first is the use of a Nipkow disc which is a rotating disc containing pinholes. The second, which is used in laser-scanning confocal microscopy, is the use of a laser beam reflecting off vibrating mirrors.(4; 11; 13) In this method, a cathode ray tube (CRT) is used to recreate the 2D image of the plane after the scan is complete. By collecting scans of each focal plane, the images can in turn be used to create a 3D image of the entire specimen.

The advantages of the confocal microscope over traditional epifluorescent microscope are immediately evident when comparable images of the same specimen are compared (**Figure 3**).(4)

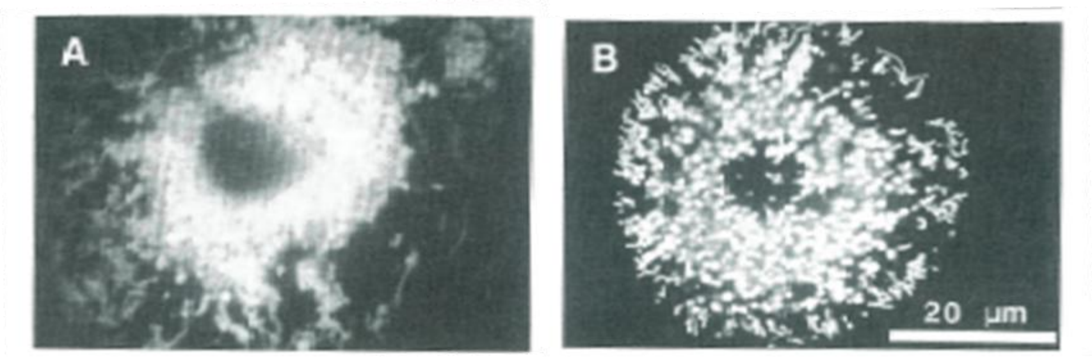

Figure 3. Comparision of the images from an epifluorescent microscope and a confocal microscope. In a normal epifluorescent microscope, emitted light from out of focus planes above or below is also detected in the image, leading to blurring (A). The addition of the pinhole apparatus in the confocal microscope yields images that have more detail and are free of background fluorescence (B).(4)

The most notable advantages are reduced blurring of the image from light scattering, increased effective resolution and an improved signal to noise ratio. Confocal microscopes also offer the ability to make xy scans over large areas of specimen and recreate 3D images of the specimen.(12) Because confocal micrscopy offers such advances in fluorescent microscopy, it has been applied here to the study of a wide range of biological systems. Here we discuss a number of applications wherein we have applied confocal microscopy to solving a scientific question.

Applications of Confocal Microscopy to Biological Systems

Monitoring β-hematin degradation in macrophage cells by confocal microscopy

An acute malaria infection is marked by a host inflammatory response, which produces chills and fevers, and anemia, arising from the destruction of an enormous percentage of red blood cells.(14) However, this not the only pathology associated with the disease- there is also substantial but specific immune system dysfunction in parasite infected patients, brought on, in particular, by the phagocytosis of hemozoin. Hemozoin (Hz) is a heme dimer based biomineral that is formed by the malaria parasite as a detoxification method to remove excess free heme that results from the parasites catabolism of host hemoglobin.(15-18) Native Hz consists of two components – the biomineral Fe-heme core, and a lipid peroxidation product coating that arises from interactions with the red blood cell membrane when it ruptures.(19) The immunomodulatory effects of the phagocytosis of native hemozoin span a range from the inability of phorbol esters or N-formyl-L-methionyl-L-leucyl-L-phenylalanine (FMLP) stimulation to produce oxidative burst, the inability of Hz-laden macrophage to kill ingested bacteria, fungi or tumor cells or even ingest opsonized, damaged erythrocytes.(19; 20) The inhibitory effects of Hz phagocytosis on macrophage function is not global, however. There is evidence that Hz-laden cells are still viable and adherent, as well as able to maintain normal DNA and protein synthesis levels and only slightly abnormal ATP levels.(20) This suggests that Hz associated dysfunction is a specific process and not just global poisoning of macrophage cells. Unfortuntely, the mechanism of this specific inhibition is not well understood. Our project aim them was to individually assess the components of native Hz – the biomineral core and the lipid peroxidation products which coat it- to attempt to elucidate the source of this immunomodulatory activity.

When exploring this project, we found particular interest in the previous literature that showed that native hemozoin was not degraded within macrophage cells, even up to 72 hours after phagocytosis (**Figure 4**).(2)

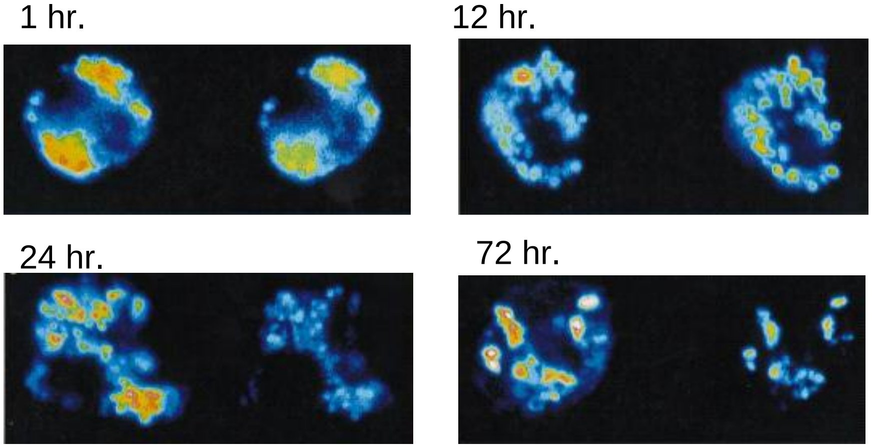

Figure 4. Confocal microscopy of hemozoin. Confocal microscopy shows the presence of hemozoin in phagolysosomes of macrophages for up to 72 hours after phagocytosis. (2)

It was this trait of Hz-induced macrophage dysfunction that opened the door to the use of confocal microscopy to assess the effect of the biomineral core of Hz on the particular ability of macrophage to handle phagocytosed material. To do this, the synthetic form of Hz known as β-hematin (BH) was used. BH is structurally identical to the Fe-heme core of Hz but has not been exposed to the biological component of Hz.(7) By using this synthetic version, we were able to focus entirely on the effect of the biomineral core alone, excluding potential contamination of biological products. Confocal microscopy was used to discover whether the persistence of native Hz within macrophage cells was a result of the resistance of the biomineral core to the reactive oxygen and nitrogen species with which macrophage cells are equipped to handle phagocytosed material or if it was the result of a larger magnitude malfunction.

Corresponding biochemical experiments suggested preliminarily that BH is susceptible to being degraded by the reactive oxygen and nitrogen species found in functional macrophages, but these alone gave no insight into the behavior of BH inside macrophage cells. For this, we turned to confocal microscopy. To determine whether BH was able to persist inside macrophage cells, its intrinsic fluorescent properties were used to directly image the biomineral after phagocytosis. By doing this, it was clear that in macrophage cells which had only been treated with BH, the ability to degrade the biomineral was not affected; rather, the biomineral was readily degraded (**Figure 5**). This suggested preliminarily that the persistence of native Hz in macrophage cells was a product of different component acting upon the cells to cause the observed dysfunction. To identify this component, we turned to the biological component of native Hz – the coating of lipid peroxidation products found associated with the biomineral core in native Hz.

When the lipid peroxidation products found associated with native Hz were analyzed, a variety of primary and secondary oxidation products were identified. In particular, 4-hydroxynonenal (HNE), a highly reactive electrophile, was identified. Through a series of experiments (described in greater detail in Chapter 2), we were able to conclude that HNE inhibited macrophage ability to produce reactive oxygen and nitrogen species as a result of the inhibition of oxidative burst. To investigate how this inhibition affects the macrophage ability to degrade BH, we once again turned to the power of imaging and confocal microscopy. By repeating the BH phagocytosis experiment with the additional step of pretreating the cells with

HNE, it became clear through the image analysis that BH was not being degraded in HNE-treated cells (**Figure 5**). This result, combined with the earlier biochemical experiments, allowed us to conclude that the lipid peroxidation products associated with native Hz were the culprit in the immunomodulation seen associated with the phagocytosis of native Hz. In this project, confocal microscopy proved to be instrumental in allowing us to investigate the fate of the BH in a biologically relevant environment.

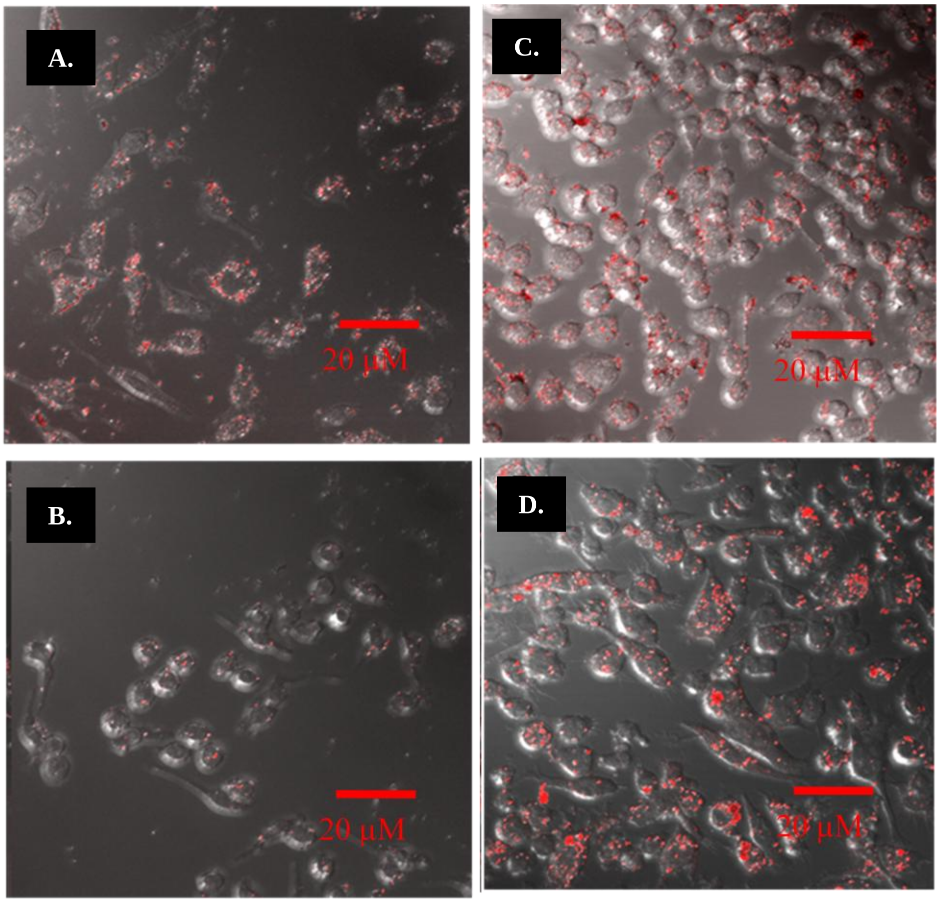

Figure 5. BH degradation in RAW macrophage cells. Confocal of BH in RAW macrophage cells after 0 hours shows a strong fluorescent signal (A) compared to 72 hours where the fluorescent signal from the BH is nearly completely dimished (B). When cells are pretreated with HNE prior to phagocytosis, samples look similar at 0 hours (C) but the fluorescent signal from BH persists after 72 hours (D).

Investigating the functional consequences of HNE adduction to PKC

The intensely reactive nature of HNE has led to its implication in the pathology of a wide range of diseases including cancer, athlescelarosis, arthritis, and is considered a marker of oxidative stress. (21) It has also been shown to inhibit oxidative burst, the mechanism by which macrophage cells produce reactive oxygen and nitrogen species.(20) Proper oxidative burst is essential in the ability of the innate immune system to handle and destroy phagocytosed microbes. As a result, its inhibition by HNE is of special interest. Though the mechanism by which HNE is able to inhibit oxidative burst is not fully understood, preliminary research has shown that it HNE is able to form adducts on Protein Kinase C (PKC).(20) PKC isozymes make up a family of serine/threonine kinases which function in a number of cellular systems. While the function of different PKCs can vary widely, the specific isoform $PKC_{\beta II}$ has been found to be necessary for the assembly of the NADPH complex, without which, a cell is unable to produce reactive oxygen species.(22) Because of this, the interaction of HNE and $PKC_{\beta II}$ was explored.(23)

When $PKC_{\beta II}$ was treated with HNE, western blot analysis showed that HNE was able to form an adduct on the protein. To gain information about the location and number of HNE adducts formed, MS/MS was used.(23) This method allowed the peptide fragments of the protein to be analyzed and those which showed a shift corresponding to the addition of HNE to an amino acid within that peptide. These positive peptides were then further analyzed by looking at the b and y ion fragments to determine the exact location of the HNE adduct. Through this analysis, five sites where HNE had formed an adduct were identified.(23) These five adducts were located on His 479, His597, Cys572 (or Lys573), Cys586 and His30.(23) By knowing the location of the HNE adducts, interesting hypotheses about the effects of these adducts can be proposed. However, they do not give any information about the functional consequences of the addition of these adducts. To explore this, we once again turned to confocal microscopy.

One of the major actions associated with proper PKC activation is it's translocation from the cytosol of the cell, where it remains in its resting state, to being associated with the plasma membrane. (24) This translocation has been shown to be particularly crucial for the proper assembly of the NADPH complex.(25) PKC translocation is the result of activation by a number of receptors, most importantly diacylglycerol (DAG) or its commonly utilized analog phorbol-12-myristate-13-acetate (PMA).(24) As a result, we were interested in using confocal microscopy to study the effect of the HNE adducts on the ability of PMA to induce translocation of PKC$_{\beta II}$. For this study, PKC$_{\beta II}$ was labeled using anti-PKC antibodies in samples either before or after PMA activation and the extent of translocation as analyzed. Further, both samples which had been pretreated with HNE and control samples which had not been exposed to HNE were analyzed. (23) As shown in **Figure 6**, translocation of PKC was seen when macrophage cells were treated with PMA. However, in samples which had been pretreated with HNE, the same fluorescent ring characteristic of the antigen being located near the membrane of the cell, was not seen. Instead, the fluorescence continued to have a morphology akin to that seen in the unactivated samples. This indicated that HNE treatment was inhibiting the ability of PKC to translocate from the cytosol to the membrane upon activation with PMA.

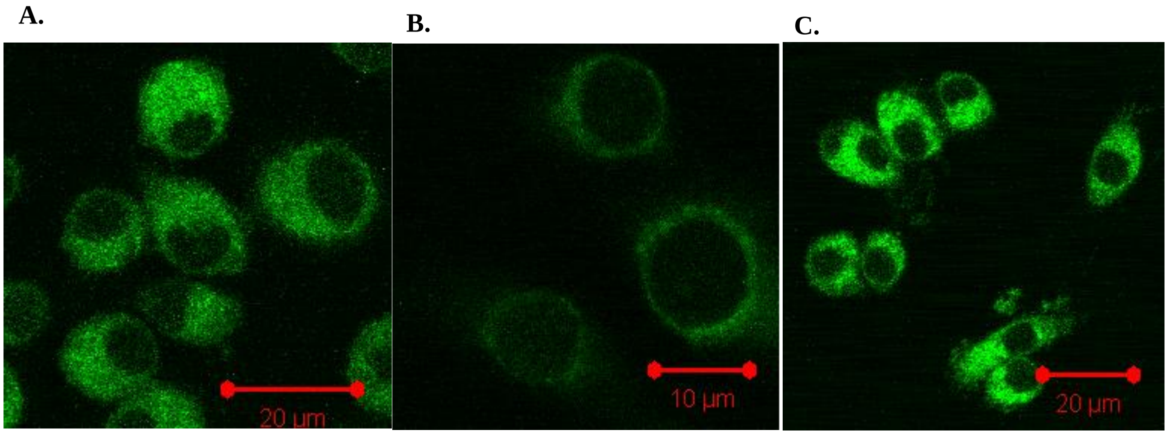

Figure 6. PMA-induced translocation of PKC$_{\beta II}$. A) Untreated RAW cell samples were fixed with paraformadlehyde and labeled with Anti-PKC primary The samples should display a large distribution of PKC throughout the cytosol of the cell. B.) In cells which were activated with PMA it is evident that the PKC has now translocated and is concentrated at the plasma membrane of the cells. C.) However, cells that were treated with 35 μM prior to PMA activation did not demonstrate the same translocation seen in PMA activation alone

Confocal microscopy allowed us to assess the functional effects of HNE adducts on PKC in a number of ways. Not only were we able to explore the impact of HNE adducts on PKC translocation, but it could be applied to other functional aspects of proper PKC activation to draw conclusions about how these adducts affected the protein (see chapter 3 for more detail about other confocal experiments).

The use of confocal microscopy in these experiments served to highlight some of the challenges in using this technique to capture a process such as PKC translocation. PKC translocation is a dynamic process which happens within a matter of minutes of PMA treatment. Because this experiment was being performed in fixed cells, it required a lot of optimization to capture the process; an error of minutes could cause it to be completely missed. This demonstrated one of the challenges of using confocal microscopy to capture processes at the cellular rate. This is not the only challenge of confocal microscopy, however.

Lessons from Respiratory Syncytial Virus

A collaboration with the Wright Lab and the Crowe lab has aimed to both detect and study Respiratory Syncytial Virus (RSV). RSV and other respiratory viruses combine to form the number one reason for medical presentation in the United States. Worldwide, RSV itself causes 6.5 million infections and 1 million deaths annually. Despite the prevelance of this virus, it is still not well understood. As a result, we set out to develop an intracellular RNA probe to study the progression of viral RNA in live cells. To do this, we attempted to apply extracellular labeling techniques to our intracellular efforts. Specifically, we attempted to utilize streptolysin O (SLO) enzyme to reversibly form pores in the cell membrane. SLO is able to create a pore in the cell membrane by attaching to chloresterol and polymerizing, forming a channel about 30 nm in diameter. With the use of SLO, it was our goal to be able to internalize a quantum dot (QD) which would in tern be able to label the viral RNA of RSV. However, this endeavor was met with a fatal snag, QDs proved just too large to allow for entry into the cell. From this it became clear that despite the power of microscopy, it is still limited by the tools available, especially the tools available to study RNA in live cell environments.

The Challenge of Improving Microscopy

Limitations of Microscopy

As the attempts to use QDs for a real-time intracellular probe demonstrated, there are limitations to the applications to which microscopy can effectively be applied. In fact, there are three main limitations: resolution, multiplexing and the ability to capture dynamic cellular processes. The limitations of microscopy are largely an artifact of the tools available to probe different subcellular biological systems.   Though the microscopes themselves may be sensitive to detect low levels of fluorescence and multiple colors almost simultaneously, the probes available to specifically label and detect these components are not of a high enough caliber to maximize the potential of the instrument. As we discovered with the RSV project, this is particularly true with the labeling and imaging of RNA.

Development of a New Probe for RNA imaging

The challenges faced when trying to label RNA in live cells became quite apparent in the failed attempt to incorporate QDs into live cells for the labeling of RSV viral RNA.   At the present there are a number of common methods available for the labeling of RNA, each with their own advantages and limitations. Reverse Transcriptase PCR (RT-PCR) is a highly specific and sensitive tool for detection of specific RNA sequences.(26-28) RT-PCR has been used successfully in the detection of low levels of RNA making it a useful method when sample is limited. Unfortunately, this method is labor intensive and contamination is a constant concern. More importantly, RT-PCR cannot be used to study live cells because the RNA must be extracted rendering it for useless in studying the molecular mechanisms of RNA trafficking. Fluorescently-labeled oligonucleotide probes have also been widely employed to explore and quantify intracellular RNA. Some of these methods include Förster resonance energy transfer (FRET) pairs, molecular beacons, and *in situ* hybridization(29-33). These probes are designed to hybridize with a specific RNA sequence, providing *in vivo* spatial information about that particular strand of RNA. However, probe internalization is a significant challenge with these techniques. Various transfection methods have been developed to shuttle fluorescently labeled oligonucleotides into cells including cationic lipids and polymers, modified viruses, dendrimers, and liposomes. Each of these methods has limitations and ultimately the necessity of chemical transfection reagents limits the utility of these probes. Further, these probes are also susceptible to rapid degradation by cellular nucleases leading to high backgrounds, false positives and poor target detection. Although these obstacles can be circumvented by cell fixation, doing so renders them inapplicable for live cell imaging. Recently, the unique advantages of nanoparticles have been exploited to develop probes that overcome a number of limitations found with the aforementioned methods.(34; 35)

AuNPs functionalized with oligonucleotides have been shown to efficiently enter live cells without the aid of harsh transfection/permeabilization agents and have limited cytotoxic effects. The recent development of “nano-flares” (NF) takes advantage of these qualities to yield a real-time probe capable of detecting specific RNA sequences with minimized background interference.(34) A NF consists of an AuNP conjugated to a long probe sequence of DNA, which is compliment to the RNA of interest. There is also a short hybridzed “reporter” strand of fluorescently- tagged DNA. In this state, the organic fluorophore is quenched as a result of its proximity to the AuNP. Upon hybridization of the probe strand with the target RNA compliment, the reporter strand is released, spatially separating it from the AuNP and resulting in a fluorescent signal that can be correlated to the presence of the RNA sequence of interest.(34) While NFs overcome many of the challenges faced by previous approaches, their design yields a signal that diffuses away from the hybridized RNA/NF construct. Consequently, important spatial information is lost in live cell microscopy applications.

After assessing the benefits and limitations of each of the present methods for RNA imaging, As a result, we set out to improve the technology available by developing a new probe that could be used for the live cell imaging of RNA that would allow not only for detection of RNA but for imaging of it in such a way to gave spatial information about the RNA trafficking. In the development of this probe, a list of critieria was developed that laid out the necessary characteristics in order to develop a probe that would meet the needs of our system. Specifically, our goal of this project was to apply chemical methods to the development of a novel nano-based probe for RNA imaging that meets all the demands of an ideal probe for LIVE CELL APPLICATIONS and overcomes the limitations of previous methods. We also wanted to apply the use of this probe to the RSV viral system to detect and label viral RNA. With this in mind, the list of optimal properties this probe had to possess are listed as follows:

1. Easily Synthesized and Characterized
2. Specific –*in vitro*
3. Favorable *in vivo* properties
    a. Minimal cytotoxic effects
    b. Stabile
    c. Readily Internalized
    d. Specific –*in vivo*
4. Multiplexing Capabilities
5. Gives Spatial Information

With this set of guidelines, we chose to apply the advantages of nanotechnology and in particular, AuNPs in designing the basis of our construct (for more details on these advantages, see chapter 4). As a result, we have developed a new probe for studying RNA trafficking that exploits the advantages of oligonucleotide functionalized AuNPs and overcomes the spatial limitations of previous designs. Nanoblossom (NB) probes consist of an AuNP conjugated to a strand of hairpin DNA, which contains a fluorophore at the 3′ end (**Figure 7**).

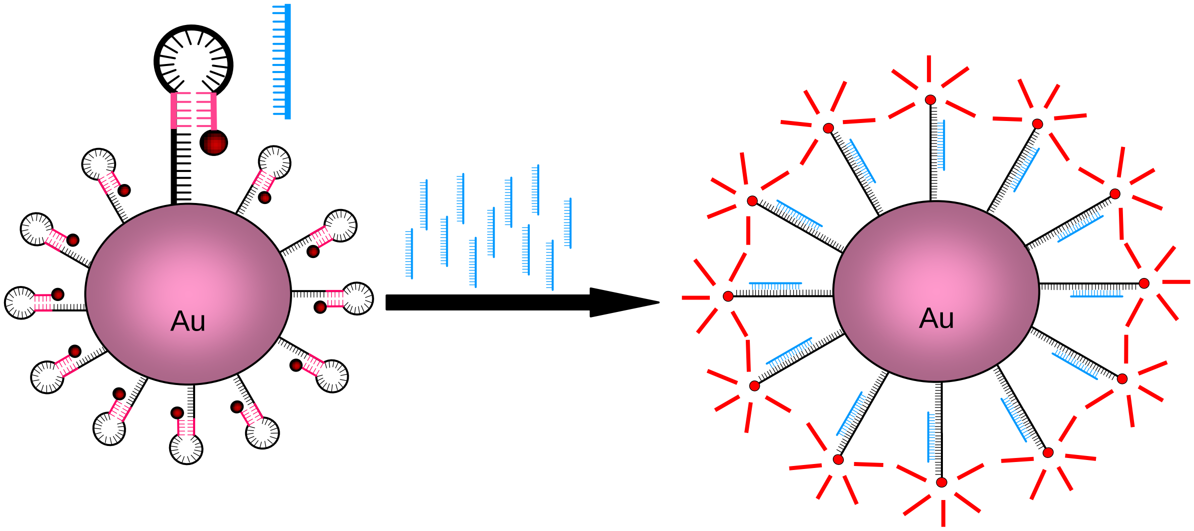

Figure 7. Nanoblossom Construct. Nanoblossoms were synthesized by conjugating a 26 base hairpin DNA with a T-10 linker to a Au nanoparticle through a 5' thiol. In the closed state, the fluorophore is quenched due to its proximity to the gold nanoparticle. However, upon binding with the appropriate compliment, the hairpin opens and the fluorophore is then a sufficient distance from the nanoparticle to overcome the quenching. This allows for the detection of compliment by monitoring fluorescence intensity. Importantly because the fluorophore does not dissociate, the fluorescence intensity can be used to learn about the spatial orientation of the RNA.

A specific sequence of RNA, the compliment to the "loop" region of the DNA hairpin, can be detected through hybridization with the NB. Without compliment DNA or RNA, the hairpin sequence of the NB oligonucleotide remains folded, with the fluorophore quenched due to the proximity of the gold nanoparticle surface. Upon binding the specific RNA target, the hairpin opens and the fluorophore extends a sufficient distance from the nanoparticle to overcome quenching. More importantly, the fluorophore does not dissociate from the NB. This allows not only the detection of the RNA of interest, but also the identification of its spatial location in real time. Once this probe was designed and synthesized for a specific sequence, in our case a sequence compliment to a region of genomic RSV RNA, it was characterized and implemented to our system. We were able to show that it was synthesized in a straightforward Au-thiol conjugation, yielded specific fluorescent signal and had minimal adverse effects when used in an *in vivo* system. More importantly, because of the nature of the construct, it allowed us to label RSV RNA in live cells and confidently gain spatial information about the location of that RNA. This was possible because the NBs can easily be combined with traditional labeling techniques to multiplex label a particular sample and as a result, achieve spatial resolution about the target sequence. In this way, a new tool was developed that can be applied to any system of interest to allow for live cell imaging of a specific sequence of RNA to learn about how that sequence is trafficked within the cellular environment.

Conclusion

Fluorescent microscopy, and in particular, confocal microscopy is a powerful tool that allows the user to move beyond imaging specimen on the whole cell level and begin to probe the events happening on a subcellular level. When applied to a biological question, fluorescent microscopy can provide information about cellular events that would be difficult to answer by another method. Here we have shown two examples of just such problems. The application of confocal microscopy to determine the fate of BH in macrophage cells in the absence and presence of lipid peroxidation products. In doing this, we were able to determine that it was these oxidation products that caused the macrophage dysfunction associated with native Hz phagocytosis. In another example of the power of fluorescent microscopy, the effects of HNE adduct formation on PKC function were assessed. In doing so, it was possible to determine that the formation of HNE adducts inhibited the ability of PKC to translocate upon PMA activation. Not only that, but the HNE treatment inhibited the intracellular calcium flux normally seen with

PMA activation of PKC. Each of these systems relied on microscopy to solve a specific biological question; however, it also began to highlight the challenges of using microscopy to capture dynamic biological processes.

Despite its potential, fluorescent microscopy has its limitations. The most challenging of these is the use of available probes for multiplexed imaging and capturing biological processes at the rate in which they occur. In order to overcome these limitations, we developed a novel probe that would allow for easier live cell imaging of RNA and then applied it to the detection and imaging of RSV viral RNA. NBs have proven to be easily sysnthesized and specifically label a particular sequence of RNA. It can also be combined with traditional labeling techniques to give multicolor images that allow you to draw spatial information about the RNA as it is trafficked within a cell. With the development of this new probe, we have made steps towards overcoming the limitations that are faced by this powerful tool.

CHAPTER II

THE BASIS OF IMMUNOMODULATORY EFFECT OF MALARIA PIGMENT (HEMOZOIN)

Statement of Effort

This project was the collaborative efforts of several people. I personally was responsible for the contribution of experiments pertaining to the exploration of BH degradation. These included *in vitro* degradation by ROS and RNS and the asscociated kinetics experiments. It also included *in vivo* studies of BH degradation within macrophage cells both by confocal microscopy and flow cytometry. While these experiments yielded interesting results, they could not have been conclusive without additional experiments contributed by Dr. Clare Kenny Carney and Dr. Alexandra Rutledge. Dr. Clare Kenny Carney was kind enough to explore the inhibition of oxidative burst by both BH and various lipid peroxidation products. Dr. Alexandra Rutledge helped provide a greater biologically relevant context by performing the ghost inhibition studies. By taking all of these experiments together, we were able to draw reasonable conclusions about the immunomodulatory effects of native Hz by studying its individual components. Other minor contributions were made by Dr. Melissa Carter, Dr. Sarah Sewell Pierce, Reese Harry, Dr. Crystal Miller, Malgorzata Broncel, Ravinder Deol, Jacob Schaff.

Introduction

Malaria is the most lethal tropical parasitic disease facing the world today, responsible for 1.5-2.7 million deaths and 300-500 million acute infections annually.(36) Put into perspective, this year alone, malaria will kill the same number of people that AIDS has killed in the past 15 years combined.(37) Not only does malaria cause a substantial loss of life, but also the economic toll of prevention and treatment in developing countries can be devastating. The direct and indirect costs of malaria are estimated to slow the growth of developing countries by 1.3% per year as compared to countries without malaria.(36) According to the World Health Organization, malaria is considered one of the major public health challenges responsible for inhibiting the development of underdeveloped regions, on the same caliber as HIV/AIDS and tuberculosis. The global impact of this disease has led to the need to better understand the pathology of the parasite, specifically how it modulates the host's immune system.

Though historically malaria was believed to have stemmed from fetid marshes, malarial infections are actually caused by parasites of the *Plasmodium* genus. Though there are four species of Plasmodium which can infect human hosts, *Plasmodium falciparum* is the most common and severe.(38) The vector responsible for transmission of the parasite is the female *Anopheles* mosquito which requires blood meals to produce eggs. As shown in **Figure 8**, sexual reproduction of the parasite takes place in the gut of the mosquito, and sporozoites, the parasitic form responsible for transmission, eventually travel to the salivary glands. During her next feeding, the female *Anopheles* injects the sporozoites into the human host.(38) Once in the vasculature, the sporozoites travel to the liver where they undergo a series of asexual

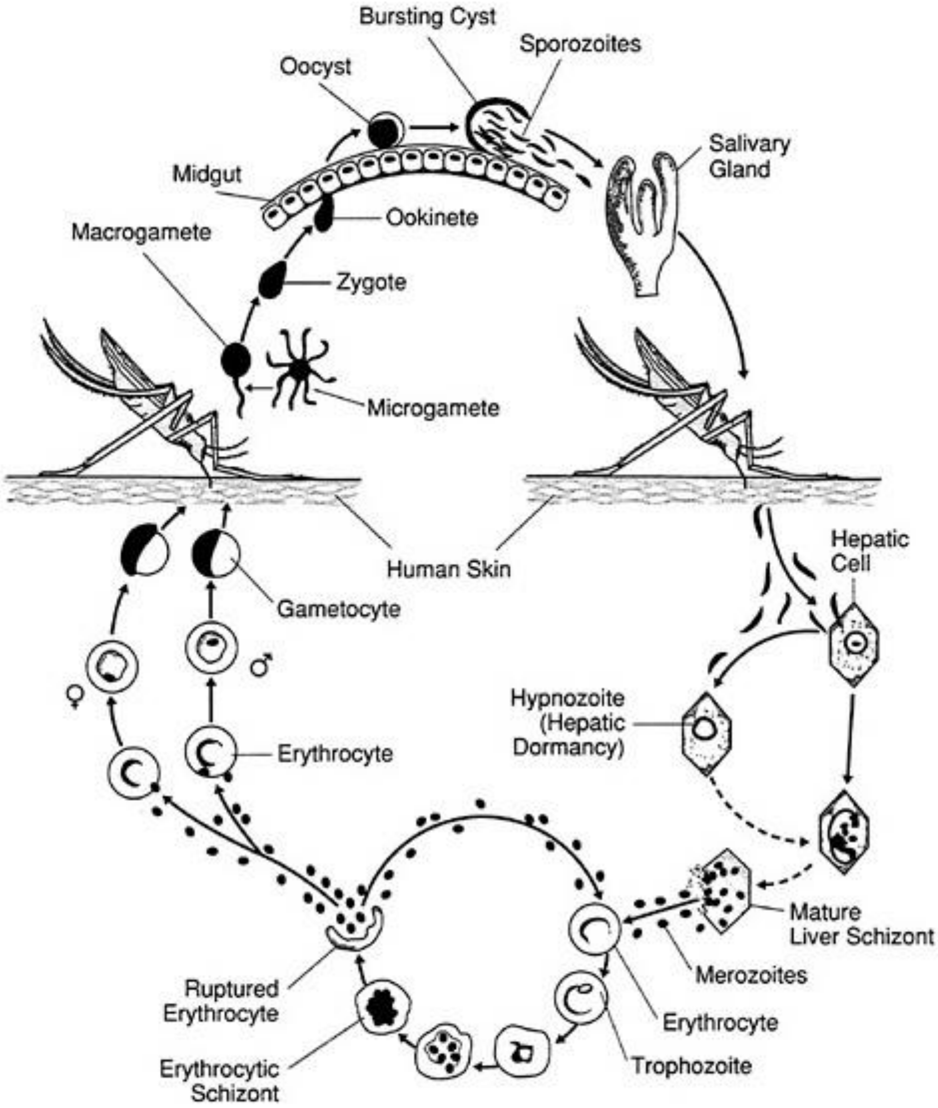

Figure 8. Lifecycle of *Plasmodium falciparum*. *Plasmodium falciparum* goes through developmental stages in both the female Anopheles mosquito and a human host. (151)

reproductions and develop into a feeding trophozoite that resides in the liver. After approximately a week, the trophozoites transform into merozoites and leave the hepatocytes.(38) The parasite then penetrates erythocytes in the blood. It is this intraerythrocytic cycle that is of interest to us. During the intraerythrocytic stage, the parasite again transforms into a feeding trophozoite, digesting up to 80% of the host hemoglobin inside an acidic (pH 4.8-5.0) lysosome called the digestive food vacuole as a source of amino acids needed for growth and development.(15) This enzymatically regulated catabolic process may result in the release of the free heme (ferric protoporphyrin IX, Fe(III)PPIX) at concentrations as high as 400 mM.(16) This accumulation of heme results in the inhibition of digestive vacuole proteases, lipid peroxidation, generation of oxidative free radicals, and eventual lysis of the parasite.(39-42) In order to circumvent this challenge, a detoxification pathway has evolved whereby free heme is aggregated in insoluable biomineral known as hemozoin.(43) As the parasite continues to develop, eventually the erythrocyte cells rupture, releasing the parasite, hemozoin and cell debris into the vasculature. From here, the parasite can either enter another erythrocytic cell or be ingested by another female *Anopheles* mosquito during a blood meal, thus completing the life cycle.(3; 38)

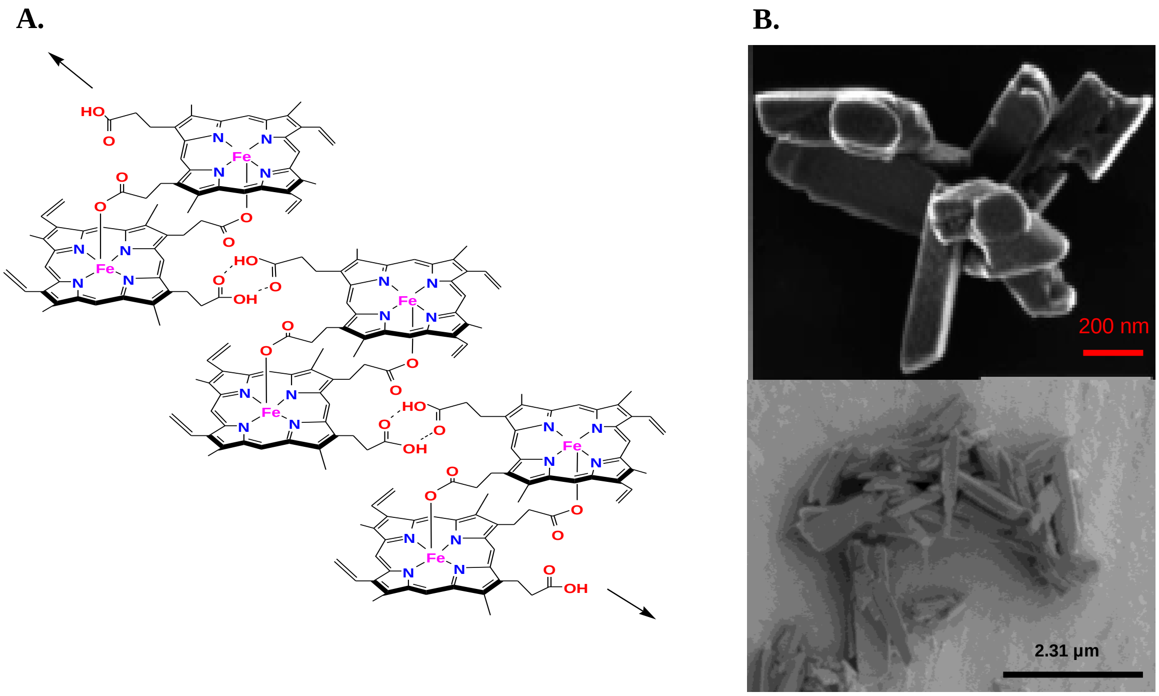

Figure 9. The structure and SEM of hemozoin. A. The structure of the biomineral hemozoin (3) B. An SEM image of hemozoin isolated from *P. falcipurum* (top) and β-hematin (bottom).(8)

Hemozoin (Hz) is comprised of heme dimers that hydrogen bond to form long thin spicules. Though there was much debate over the structure of Hz, the final structure was determined using Rietveld refinement combined with X-ray diffraction.(3) Shown in **Figure 9**, the planar heme dimers have reciprocal Fe-O bonds to one of the propionic side chains of protoprophyrin IX. Hydrogen bonding between the free propionic acid groups allows the diner to form an extended network, which results in biomineral formation.(3) β-hematin is a synthetic form of hemozoin that is synthesized through a dehydrohalogenation reaction between hemin chloride and 2,6-lutidine developed by Bohle.(7) However, structural identity between β-hematin and native hemozoin was proven by IR, ESR, and x-ray absorption spectroscopy.(17)

Synchronized rupture of the red blood cells (RBCs) results in the release of the parasite and hemozoin along with other cellular debris, including the lipid membrane of the erythrocyte, into the vasculature.(38) The innate immune system then responds to this cellular damage by phagocytosis of the hemozoin particulates, among other cellular debris. Under normal conditions, a microbe phagocytosed by a macrophage would be degraded through a number of synergistic mechanisms. The first mechanism by which macrophage cells destroy microbes is through the biogenesis of the phagosome containing the particulate to the mature phagolysosome.(44) During phagocytosis, a unique organelle known as a phagosome is formed around the foreign material as it enters the cell. Originally thought to function through a simple mechanism, this organelle has been shown to participate in a dynamic array of interactions ranging from membrane protein recycling to microtubular formation with other organelles for specific protein exchange.(45) The result of all these exchanges is the development of a biochemically distinct organelle known as a phagolysosome. The internal environment of a mature phagolysosome is loaded with hydrolases and other lysosomal enzymes. It also has a pH of five or below and is rich in reactive oxygen and nitrogen species produced by the macrophage cell. This mature phagolysosome houses the harsh environment responsible for degrading the majority of phagocytosed material.(46-48)

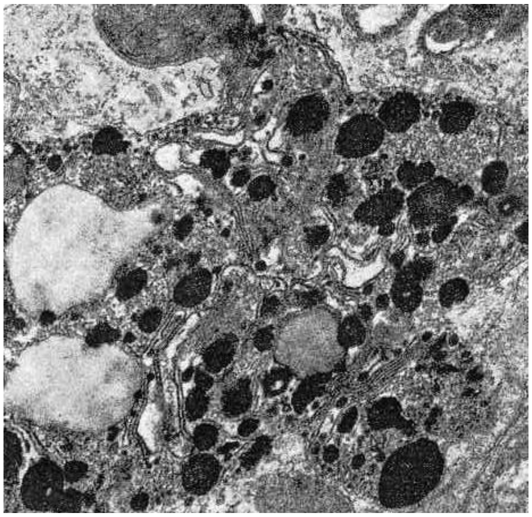

Figure 10. EM of native hemozoin. After erythrocyte rupture, hemozoin is phagocytosed by macrophage cells. (1)

The second mechanism by which macrophage cells can destroy phagocytosed microbes is through a process known as respiratory or oxidative burst.(49) Phagocytosis of a microbe activates the formation of a plasma membrane-associated complex known as NADPH-oxidase. Once activated, NADPH-oxidase transfers electrons from NADPH to molecular oxygen to form reactive oxygen intermediates such as superoxide anion (O_2^-). The superoxide anion quickly reacts to form secondary reactive oxygen species such as hydrogen peroxide, hydroxyl radical and hypochlorous acid, all of which readily destroy phagocytosed microbes.(50) NADPH-oxidase is not the only free radical-generating system, however. Inducible nitric oxide synthase (iNOS) is an enzyme that produces nitric oxide by catalyzing the conversion of arginine to citrulline after lipopolysaccharide (LPS) activation.(49) Nitric oxide can then react with hydrogen peroxide or superoxide to form peroxynitrite, a powerful anti-microbial.(49) These reactive oxygen and nitrogen species (ROS and RNS) create a potent environment capable of destroying phagocytosed microbes.

Despite multiple mechanisms for destroying microbes, hemozoin presents a challenge to macrophage cells. After erythrocyte rupture, native hemozoin released into the vasulature is phagocytosed by macrophages (shown in **Figure 10**) but is not degraded.(2) Moreover, native hemozoin has been shown to impair several other macrophages. Following phagocytosis of hemozoin, the macrophage's capacity to generate oxidative burst is diminished and lipid peroxidation is induced.(19) There is a lot of controversy in the literature over the exact biological activity of macrophage cells in response to the phagocytosis of hemozoin. Various aspects of cell vitality have been reported to be diminished, including phorbol ester-induced oxidative burst, rephagocytosis, killing of ingested bacteria, fungi or tumor cells and response to interferon γ stimulation.(19; 51-54) Additionally, there is an increased production of immunosuppressive molecules such as porstaglandine E_2.(51) In vivo, increased levels of the highly reactive 4-hydroxy-2-nonenal (HNE) and hydroxylated fatty acids have been correlated to hemozoin phagocytosis.(53-55) Despite these deleterious effects, other cellular functions appear to go unaffected including ATP levels, cell adhesion and the lack of apoptosis. Though some cellular processes remain unaffected, it is clear that the hemozoin-induced changes cause the macrophages to be irreversibly incapable of degrading phagocytosed native hemozoin.(2) In fact, native hemozoin has been shown by confocal microscopy to remain present in phagolysosomes of macrophage cells for up to 72 hours (shown in **Figure 11**).(2)

While there is a growing consensus in the literature that native hemozoin maintains immunosuppressive activity, there is considerable controvery over the reactivity of the synthetic form, β-hematin (BH). Studies have generated a contradictory assortment of results. Some resports find that synthetic hemozoin can induce a proinflammatory (increased TNF-α, IL-6, MIP-1α, MIP-1β and chemotactic cytokinds) response in macrophage cells(56-58) while others highlight an anti-inflammatory (decreased TNF-α, IL-6, and chemotactice cytokines) response.{Schwarzer, 1999 #15;Taramelli, 1998 #107;Taramelli, 1995 #106;Taramelli, 1998 #108} Furthermore, there are varying reports about the ability of BH to inhibit oxidative burst and rephagocytosis. Once again, some studies indicate that the synthetic form is able to inhibit the production of ROS and RNS(60), while others claim that it does not.(55) Unfortunately, previous studies of the effect of hemozoin phagocytosis on macrophage function have utilized a variety of different methods of acquiring and purifying the hemozoin. Most of these methods are not thorough and either do not attempt to purge the hemozoin of biological debris or do not completely rid the hemozoin of cellular debris such as membrane lipids. As a consequence, the resulting biological response can not be attributed to a specific source.

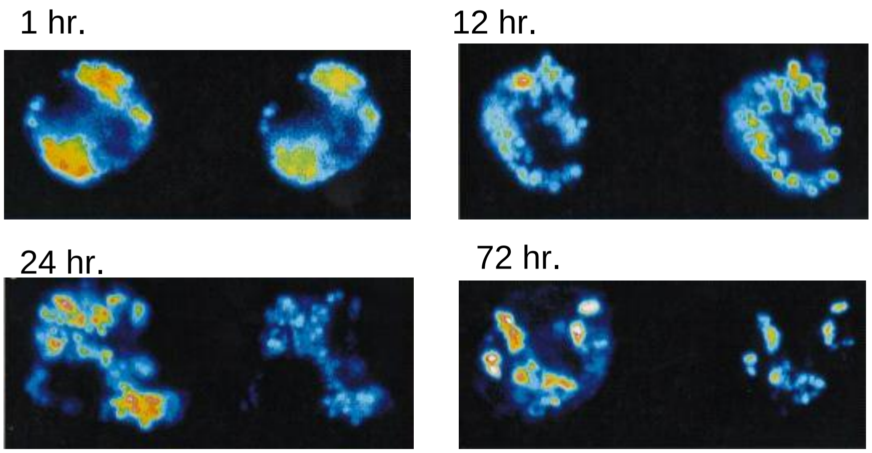

Figure 11. Confocal microscopy of hemozoin. Confocal microscopy shows the presence of hemozoin in phagolysosomes of macrophages for up to 72 hours after phagocytosis. (2)

The state of hemozoin must be carefully defined in order to elucidate which components may be interacting to disrupt the host immune response. Native hemozoin refers to the material isolated from parasitized RBCs and washed gently to remove cellular debris but left with a coat of lipids absorbed onto the hydrophobic plate of porphyrins.(19) Purified hemozoin, however, has also been isolated from *P. falciparum*; however, lipid extractions have been performed in attempts to remove the gradient of oxidized lipid products from the biomineral by detergent or organic solvents.(62; 63) Finally, synthetic hemozoin, BH, is material that has been synthetically prepared and purified.(7; 17) Given the emerging importance of hemozoin in modulating a host immune response to malarial infection, and the literature controversy surrounding the specific role of the biomineral, a careful examination of the effects of the constitutive components of the malaria pigment—both the biomineral core and the lipid peroxidation coat— on macrophage response would significantly clarify the understanding of the process.

Materials and Methods

Materials

All chemicals were used as received unless otherwise noted. *N*-(1-Napthyl)ethylenediamine (NED), sulfanilamide, piperazube-1,4-bis(2-ethanesulfonic acid) (PIPES), Sepharose 2B, lippopolysachharide (LPS), sodium hypochlorite, diethylamine/nitric oxide sodium complex (DeaNO), and hemin chloride were obtained from Sigma-Aldrich (St. Louis, MO, USA). Phorbol-12-myrisate-13-acetate (PMA) and HNE were purchased from Calbiochem (San Diego, CA, USA). 2,6-Lutidene was obtained from Acros Chemicals. Cayman Chemicals (Ann Arbor, MI, USA) supplied the 15-*S*-hydroxyeicosatetraenoic acid (15-HETE). Fetal bovine serum was purchased from Atlanta Biologicals (Atlanta, GA, USA). Penicillin/streptomycin was obtained from Cellgros Mediatech (Herdon, VA, USA). The murine macrophage cell line, RAW 264.7, originally obtained from the American Type Culture Collection (ATCC TIB-71) was a kind gift from the Virginia Shepherd laboratory (Vanderbilt University). Lysotracker Red was obtained from Invitrogen. Packed RBCs were donated from the VUMC Blood Bank. All other chemicals were purchased from Fisher Scientific (Hampton, VA, USA) unless otherwise specified.

All powder diffraction X-ray studies were performed with a Scintag X_1 θ/θ automated powder difractometer with a copper target, a Peltier-cooled solid state detector and a zero-background silica (510) sample support. The step size was 0.02, preset time 25 s. All samples were scanned from 4 to 35 ° 2θ. Fuorier transform IR (FTIR) spectroscopy was carried out in a KBr pellet using an ATI Mattson Genesis Series FTIR spectrophotometer and scanning electron microscopy was performed with a Hitachi S-4200 scanning electron microscope. All UV-vis spectroscropy was carried out either with an Agilent 8453 diode-array spectrophotometer or with a Bio-Tek Synergy HT multidetection microplate reader. The Bio-Tek Synergy HT multidetection microplate reader was also used for fluorescence measurements. All work done in an inert atmosphere was accomplished in a two-port Vacuum Atmospheres 2000-M glove box. All chromatography was performed inside a 4 °C chromatography refrigerator. Confocal images were obtained using a Zeiss LSM 510 Meta inverted confocal microscope equipped with LSM Image Browser software. Quantative analysis of the fluorescence of these images was accomplished using Metamorph software. Cell sorting for BH degradation flow cytometry experiments was done on a Miltenyi Automacs Magnetic Cell Sorter.

BH preparation and characterization

BH was synthesized using a modification of the Bohle dehydrogalogenation method.(7) In an inert atmosphere, 0.3 g of hemin chloride was dissolve in minial amount of 2, 6-lutidine (usually approximately 4 mL) with stirring. Upon completion of dissolution, 40 mL of 1:1 mixture of anhydrous methanol and dimethyl sulfoxide (DMSO) was added and te flask was sealed and covered with foil to protect the mixture from ambient light. After leaving the mixture undisturbed for 3 months, it was removed from the inert atmosphere and the black solid product was collected via vaccum filtration onto a 0.45-μm filter. Relying on the differential solubility of hemin chloride and BH, excess free heme and small aggregates were removed by exhaustive washings in methanol, DMSO, 0.1 M sodium biocarbonate, pH 9.0, and deionized water. Once agan, the solid was isolated using vaccum filtration onto a 0.45-μm filter and was dried overnight at 150 °C. The resulting BH was characterized using IR spectroscopy, scanning electron microscopy and X-ray diffraction, with the results matching previously reported spectra.(3; 17; 64)

Cell Culture

The adherent murine macrophage cell line, RAW 264.7, was maintained in continous culture with RPMI 1640 medium (GIBCO/BRL), supplemented with 10% (v/v) heat-inactivated fetal bovine serum, and 100 μg/mL penicillin/strptomycin (complete medium) in an atmosphere of 5 % CO_2, 5% humidity at 37 °C. Cell viability was determined by Trypan Blue exclusion using a hemocytometer.

Measurement of ROS and RNS production

Measurement of ROS was accomplished using luminal-dependent luminescence. In these experiments, RAW 264.7 cells were plated overnight in complete medium at a density of 4 x 10^6 cells per well in a six-well plate. The following day, the medium was removed, the cells gently washed with phosphate-buffered saline (PBS) and treated. After 3 hrs of incubation at 5 % CO_2, 5% humidity at 37 °C, the supernatant was removed, cells gently washed with PBS and NADPH oxidase was activated by the addition of 1.0 mL of 100 nM PMA in PBS. After 4 min, 950 μL of this supernatant was collected into a luminescence tube followed by the addition of 50 μL of 1.0 mM luminal (in PBS). Luminescence was immediately measured using a Monolight 3,010 luminometer for 10 s. Alternatively, ROS were monitored using dichlorofluorescein diacetate (DCF-DA). In these reactions, cells were plated overnight in complete medium at density of 5 x 10^5 cells per well in a 24-well plate. The next morning, the cells were washed, then treated with HNE or 15-HETE, 100 nM PMA in PBS and 8 µM (final) DCF-DA for 60 min at 37 °C and 5 % CO_2, 5% humidity. The formation of the fluorescent dicholorfluorescien was monitored with the Bio-Tek Synergy HT multidetectionmicroplate reader using a 485/20 excitation filter and a 528/20 emission filter. It is important to recognize that this assay, unlike the luminal assay described earlier, does not involve preincubation of the cells with HNE or 15-HETE. All assays were performed in triplicate and the average value is reported with the standard deviation.

Triplicate measurement of RNS was accomplished using the Griess assay. For these experiments, RAW 264.7 cells were plated overnight in complete medium at a density of 5 x 10^5 cells per well in a 24-well plate. The next day, cells were treated and then stimulated by the addition of 10 µL of 50 µg/mL LPS (1 µg/mL final) followed by incubation in 5% CO_2, 5% humidity at 37 °C. After 24 hrs, 300 µL of the supernatant was removed from the cells and spun down at 13,200 rpm for 15 min. A 100-µL aliquot of the supernatant was then transferred to a 96-well plate and the production of NO was monitored using the Griess assay. For this assay, 100 µL of each sample was reacted with 50 µL of 1 % sulphanilimide in 5% phosphoric acid, followed by 50 µL of 0.1 % NED. After 5 min, the absorbance of the resulting azo complex was measured at 540 nm using a Bio-Tek Synergy HT multidetection microplate reader. To investigate the effect of BH on the production of ROS and RNS, 120 µg/mL (final concentration) BH suspended in complete medium was used in all cases unless otherwise specified.

Reaction of HNE and 15-HETE on stimulated RAW 264.7 cells

The ability of HNE and 15-HETE to inhibit PMA- and LPS-stimulated oxidative burst was analyzed. To examine the effects of HNE and 15-HETE on the activation of NADPH oxidase, 5 x 10^5 cells per well were plated in 24-well plates. The following day, the cells were treated in triplicate with HNE (0-100 µM) or 15-HETE (0-12 µM) and incubated in 5% CO_2, 5% humidity at 37 °C. After 60 min, the cells were examined for NADPH oxidase activity using DCF-DA, a dye that is converted to the fluorescent dichlorofluorescein in the presence of oxidizing species (described earlier). To investigate LPS inhibition, 5 x 10^5 cells per well were plated in 24-well plates overnight. Subsequently, the cells were washed once with PBS, followed by treatment with HNE (0-20.5 µM) or 15-HETE (0-20 µM), followed by stimulation of iNOS with LPS (1 µg/mL final per well). These samples were allowed to incubate for 24 hrs before analysis of the supernatant via the Greiss assay (described earlier).

Ghost cell preparation

To obtain erythrycyte membranes (ghosts),(65; 66) 3.0 mL of packed RBCs was suspended in 12.0 mL of 5 mM NaH_2PO_4 supplemented with 150 mM NaCl, pH 8.0 and centrifuged at 1,000 *g* for 10 min. The supernatant was removed and the pellet was resuspended in the same buffer system. After repeating the wash cycle four times to removed packaging contaminants, the pellet was resuspended in 5 mM NaH_2PO_4, pH 8.0 at 10% hematocrit. The suspension was rigiously shaken and placed in an ice bath for 15 min prior to loading 15.0 mL (6% of the bed volume) onto a Sepharose 2B column (2.5 cm x 50 cm) located in a 4 °C chromatography refrigerator and equilibrated in 15 mM Pipes buffer with 0.1 mM EDTA, pH 6.0. The sample was eluted with 20 mM *N*-(2-hydroxyethyl)piperazine-*N*'-ethanaesulfonic acid (HEPES) buffere supplemented with 146 mM sodium chloride (pH 7.4) at flow rate of 15 mL/hr and 700 µL fractions were collected. Elution of ghosts was monitored by absorbance of aromatic residues in proteins at 280 nm and they were typically found to be eluted in the dead volume. Relavent fractions were pooled and ghosts were collected by centrifugation (10,700*g*, 15 min, 4 °C). The supernatant was removed and the white pellet was resuspended in 20 mM HEPES buffer supplemented with 146 mM sodium chloride, pH 7.4. In order to disrupt the membranes, samples were alternately vortexed with glass beads for 2 min followed by placement in an ice bath for 2 min for a total of five cycles. It should be noted that collection of reactive RBC ghosts is nontrivial and extremely sensitive to minor changes.

Reactions between RBC ghosts and BH were prepared in test tubes with a total volume of 2 mL. RBC ghosts, normalized to an absorbance of 0.7 at 280 nm, were added first, followed by 500 µL of 3 mg/mL BH (0.75 mg/mL final) and the samples were taken up to 2-mL volume with RPMI 1640 complete medium. After stirring for 24 hr at RT, the reaction mixtures were centrifuged for 15 min at 5,500 rpm to pellet ghost membranes and BH, RAW 264.7 murine macrophage cells were then treated in triplicate with varying amounts of the supernatant (from 0 to 100%). Luminol-dependent luminescence (see earlier) was used to measure the effect of the supernatant of the ghost-BH reaction on the production of ROS and the Griess assay (see earlier) was used to monitor the effects on the production of RNS.

Degradation of β-hematin by ROS

To study the ability of ROS to degrade BH in vitro, reactions between BH and standardized 0-100 mM hydrogen peroxide (67)and 0-10 mM sodium hypochlorite (68) were prepared in triplicate. Breifly, to a 1.5-mL microcentrifuge tube, 100 µL of a 2.0 mg/mL suspension of BH in 100 mM sodium acetate buffer pH 4.8 was added to 300 µL of sodium acetate buffer, follwed by the addition of 100 µL of the appropriate concentration of hydrogen peroxide or sodium hypochlorite. Prior to incubation in a 37 °C water bath for 20 h, the solutions were capped, covered with Parafilm and vortexed. After incubation, the samples were centrifuged at 13,200 rpm for 30 min to pellet the remaining BH. The clear supernatant was removed and the pellet washed once with deionized water and recentrifuged. Finally, the BH was dissociated into free heme by dissolving the pellet in 1.0mL of 1.0 M NaOH and the absorbance of free heme was monitored at 400 nm using a Bio-Tek Synergy HT multidetection microplate reader to quantitate the remaining heme.

Degradation of β-hematin by RNS

To study the ability of RNS to degrade BH in vitro, reactions between BH and 0-100 mM DeaNO, a nitric oxide (NO) releasing agen, were prepared in triplicate. Briefly, to a 1.5-mL microcentrifuge tube, 100 μL of a 2.0 mg/mL suspension of BH in 100 mM sodium phosphate buffer pH 7.4 was added to 390 μL of sodium phosphate buffer, followed by the addition of 10 μL of the appropriate conentration of DeaNO. Prior to incubation in a 37 °C water bath for 20 h, the solutions were capped, covered with Parafilm and vortexed. After incubation, the samples were centrifuged at 13,200 rpm for 30 min to pellet the remaining BH. The brown supernatant was removed and the pellet washed once with deionized water and recentrifuged. Finally, the BH was dissociated into free heme by dissolving the pellet in 1.0 mL of 1.0 M NaOH and the absorbance of free heme was monitored at 400 nm using a Bio-Tek Synergy HY multidetection microplate reader. At concentration of DeaNO of 25 mM or greater, it was necessary to add 10 μL of 5.0 M NaOH and allow the tube to rotate overnight to obtain complete dissociation of the BH pellet. Finally, the absorbance of free heme was monitored at 400 nm using a Bio-Tek Synergy HT multidetection microplate reader in order to quantitate the remaining BH. Additionally, IR spectroscopy was used to analyze the formation of an Fe-NO complex at the 50 mM DeaNO concetration. The amount of NO released by DeaNO in this experiment was verified by running a series of control reactions. Here, the samples were prepared and treated exactly as those described earlier except the 100 μL of BH was replaced with 100 μL of sodium phosphate buffer. To analyze the amount of NO produced, the Griess assay (69) was employed. It should be noted that Fe(III)PPIX solutions may absorb onto plasticware and can exist in different aggregation states, resulting in minor changes in absorbance.

Kinetics of Degradation of β-hematin by ROS and RNS

To study the rate of ROS and RNS degradation of BH in vitro, reactions between BH and standardized 0-100 mM hydrogen peroxide (67), 0-10 mM sodium hypochlorite (68), and 0-100 mM DeaNO were prepared in triplicate. Here the samples were prepared and treated exactly as those described earlier exacept the incubation time was varied from 0-24 h in three hour incriments yeilding nine time points for each kinetic experiment.

Confocal microscopy

The localization of BH inside acidic phagolysosome was demonstrated using lysotracker, a pH-sensitive dye. Here, 5 x 10^4 cells were plated overnight, followed by a gentle PBS wash. Next, the cells were treated with 100 μL of 0.12 mg/mL BH suspended in complete medium and allowed to phagocytose in an atmosphere of 5 % CO_2, 5 % humidity at 37 °C. After 90 min, the cells were washed two times with PBS, and were treated with 2 mL of 100 nM PMA diluted in complete medium. After 10 min of 5% CO_2, 5 % humidity at 37 °C, the PMA was removed, the sample washed with PBS and covered with 2 mL of fresh PBS. Approximately 5 min prior to imaging, 4 μL of 20 μM lysotracker diluted in PBS was added to the dish. Fluorescence imaging of BH was accomplished by excitation at 514 nm followed by collection using a band-pass filter from 533.2 to 542.9 nm. Lysotracker fluorescence was obtained by excitation at 543 nm followed by the use of long-pass 585-nm filter for emission. The images were stacked into a composite figure in order to determine colocalization. Confocal microscopy was also utilized to determine the fate of BH that has been phagocytosed by RAW 264.7 macrophage cells. Cells were plated at 5 x 10^4 cells per dish onto Mat-Tek dishes. The following day, the cells were gently washed with PBS, followed by treatment with 100 μL of 0.12 mg/mL BH suspended in completely medium. After 90 min at 5 % CO_2, 5 % humidity and 37 °C, the samples were gently washed twice with PBS to remove any unphagocytosed BH. Fresh complete medium was added to the top, followed by incubation for 0, 48, and 72 h in an atmosphere of 5 % CO_2, 5 % humidity at 37 °C. At each time point, the samples were gently washed once with PBS, convered with 2 mL of fresh PBS and immediately imaged on the Zeiss LSM 510 Meta inverted confocal microscope. Fluorescence imaging of BH was accomplished by excitation at 514 nm, followed by collection using a band-pass filter from 533.2 to 542.9 nm. In order to quantiate the fluorescence emission from the samples, projections were made of the z-stacks from 300 to 400 cells per samples and Metamorph software was used to quantiate the amount of fluorescence above the background threshold. The effect of HNE treatment on BH degradation in RAW 264.7 macrophage cells was studied by confocal microscopy in the manner described above. However, directly after treatment with BH (as previously described), the samples were treated with 35 μM HNE and incubated in an atmosphere of 5 % CO_2, 5 % humidity at 37 °C for 3-4 h. The samples were then gently washed with PBS to remove any excess HNE. Fresh complete medium was added to the top, followed by incubation for 0, 24, and 48 h in an atmosphere of 5 % CO_2, 5 % humidity at 37 °C. Finally, samples were imaged as described above.

Flow Cytometry

To determine the ability to distinguish β-hematin-laden cells from control cells by flow cytometry, a preliminary experiment compared the emission of these two populations. The samples were prepared by plating 1 x 10^6 cells in a 10 cm dish and incubating for 24 hours in an atmosphere of 5 % CO_2, 5 % humidity at 37 °C. The half samples were then treated with 5 mL of 0.12 mg/mL suspension of β-hematin in RMPI 1640 medium. The samples were incubated in an atmosphere of 5 % CO_2, 5 % humidity at 37 °C for 90 min. All samples were then washed three times wth PBS to remove any excess β-hematin, or RPMI 1640. Five milliliters of 0.05% EDTA/trypsin solution was added to each plate and incubated in 5 % CO_2, 5 % humidity at 37 °C for 1 hour. After incubation, the samples were scraped and 15 mL of RPMI 1640 was added to quench the trypsin. The samples were then centrifuged at 1500 rpm for 5 min. The pellet was resuspended in 200 µL of PBS and centrifuged again for 5 min at 1500 rpm. The pellet was resuspended in the working solution of 250 µL 0.5% BSA in PBS. All samples were then run on Custom Becton Dickinson five-laser LSRII analytical cytometer. The samples were excited at 630 nm and emission was detected at 680 nm. Approximately 10,000 cells were analyzed from each sample. To assess the degradation of BH in RAW 264.7 cells by flow cytometry, 1 x 10^6 cells were plated into T-25 flasks and allowed to grow to 80% confluency in an atmosphere of 5 % CO_2, 5 % humidity at 37 °C. The samples were then treated with BH as described above. After BH treatment, the cells were disassociated from the T-25 culture flask by aspirating the media and adding 5 mL of Cell Stripper solution to the sample for 30 min. The samples were then prepared for analysis and sorting by flow cytometry as described above. All samples were then run on a Custom Becton Dickinson five-laser LSRII analytical cytometer, with excitation at 630 nm and emission detection at 680 nm. The remaining sample was then sorted based on positive fluorescent signal using a Miltenyi Autosort Magnetic Cell Sorter and re-plated into three new T25 culture flasks. These sample was then incubated for either 24, 48 or 72 hours in an atmosphere of 5 % CO_2, 5 % humidity at 37 °C. Analysis was repeated at the appropriate time interval for each sample to determine the overall BH degradation original RAW 264.7 cell population. The effect of HNE treatment on the degradation of BH in RAW 264.7 macrophage cells was explored in a similar fashion. Samples were plated, treated and analyzed as described above. However, directly following BH treatment, samples were treated with 35 µM HNE for 3-4 hrs. In all flow cytometry experiments, the viabily of the samples was determined by the addition of 1 ng/mL of propidium iodide (PI) buffer to each sample. The fluorescence for each sample determined the number of dead cells within the sample population.

Results and Discussion

BH synthesis and characterization

The Bohle method of synthesis was used to synthesize BH for studies of the heme dimer core of BH (**Scheme 1**).(7) This dehydrohalogentation method requires three months for BH formation, ultimately leading to BH that has the long rod morphology seen with native maralia hemozoin.(7) Once synthesized, the BH is cleaned taking advantage of the differential solubility of the BH crystal and any aggregated heme monomers and dimers with repeated washes in water and sodium bicarbonate. The high pH of the sodium bicarbonate successfully dissolves any heme monomers and dimers which would remain aggregated within the BH crystals without dissolving the BH itself, which is resistant to dissolution at pH 9 (**Figure 12**).(6)

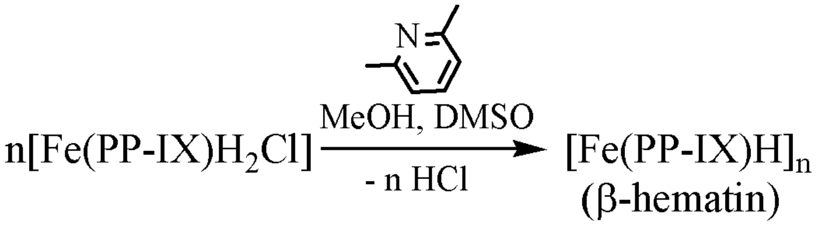

$$n[Fe(PP\text{-}IX)H_2Cl] \xrightarrow[-\ n\ HCl]{MeOH,\ DMSO} [Fe(PP\text{-}IX)H]_n$$

(β-hematin)

Scheme 1. Bohle method of BH synthesis. β-hematin is a synthetic form of hemozoin that is synthesized through a dehydrohalogenation reaction between hemin chloride and 2,6-lutidine developed by Bohle.(7)

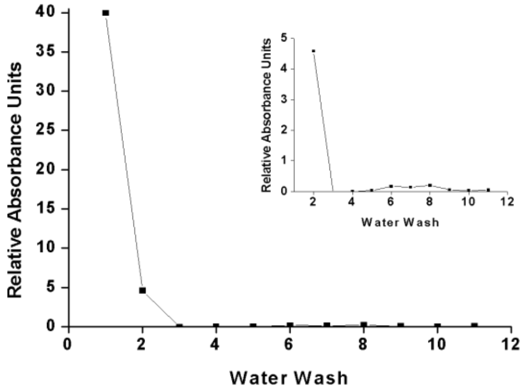

Figure 12. Differential Solubility of BH. Plot of β-hematin purification showing the decrease in non-crystallized hemin chloride during differential solubility washes as monitored by Soret band absorption. Insert shows details at low absorbance.(6)

Once cleaned, the BH was characterized to show that it was structurally identical to native hemozoin. To do this, both IR and XRD were utilized. The XRD of BH shows characteristic peaks at 7, 21 and 24 2θ. It is evident that the BH has been cleaned of any contimaint starting material by the lack of a peak at 23 2θ which is representative of the presence of hemin chloride (**Figure 13**). Additional analysis of the synthesized BH by IR revealed two characteristic hemozoin peaks: 1211 cm^{-1} and 1664 cm^{-1} (**Figure 14**). The peak at 1211 cm^{-1} corresponds to C-O stretch of the propionic side chain; the 1664 cm^{-1} peak corresponds to C=O stretch.(8) These characterization processes were used to ensure that the BH used in experiments studying the effects of the dimeric heme core were performed with a synthetic version of hemozoin that was structurally and spectroscopically indistinguishable from native hemozoin.

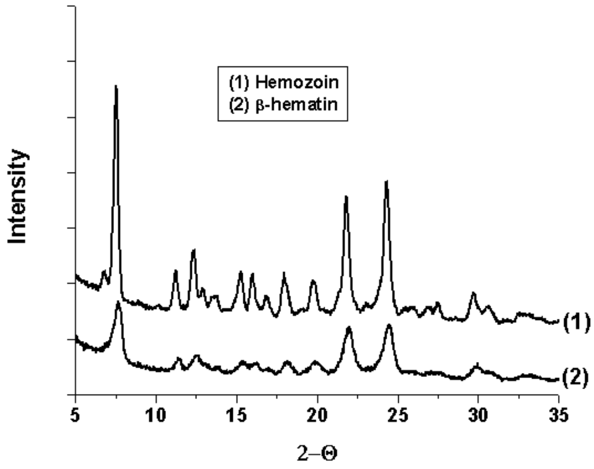

Figure 13. XRD of BH. The XRD of BH synthesized by the Bohle method shows the distinct peaks at 7, 21 and 24 2θ that represent the characteristic peaks of the hemozoin biomineral.

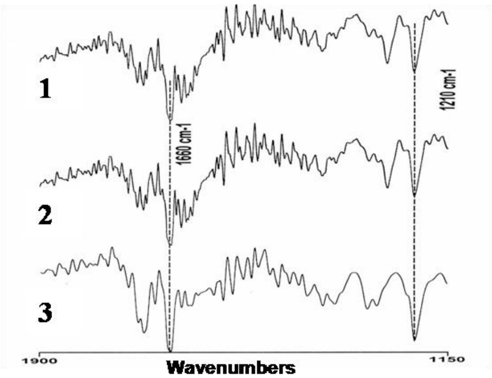

Figure 14. IR of BH. IR of (1) β-hematin from Ziegler et al. *J. Am. Chem. Soc.* **1999,** 121, 2395, (2) β-hematin prepared via the dehydrohalogenation rection, and (3) *P. falciparum* hemozoin.

Effect of BH on ROS and RNS production

Biologically, the production of ROS and RNS in phaocytic cells is predominantly mediated by the action of two enzymes: NADPH oxidase and iNOS. The production of ROS during oxidative burst is a result of the activation of NADPH oxidase. Activation of this constitutively expressed enzyme results in the reduction of molecular oxygen to the superoxide anion which is rapidly converted to secondary species such as hypochlorous acid (HOCl), the hydroxyl radical ($OH^{\cdot}$) and hydrogen peroxide (H_2O_2).(66; 70-72) RNS are initiated by the induction of nitric oxide synthase. Once translated, iNOS produces nitric oxide, which in turn can react with molecular oxygen to form a variety of derivatives, including NO_2, N_2O_3, NO_2^-, and NO_3^-. (69) Together, these species act to degrade foreign pathogens. Considering the innate toxicity of these reactive microbicidal agents, their modulation is an important component in establishing a successful parasitic infection.

BH's ability to modulate the activity of NADPH oxidase was exhamined.(6) As seen in Figure 20, BH does not inhibit the production of ROS in PMA-stimulated RAW mouse macrophage cells. Preincubation with up to 0.4 mg/mL BH showed no inhibitory effect on superoxide anion production as mueasured by luminolenchance luminescence. (6) Resports have similarly indicated no inhibition of ROS in mouse macrophage-like B10R, BV2 microglial and peritoneal macrophage cells lines.(63; 73) In contrast, phagocytosis of native hemozoin by human monocyte-derived macrophages resulted in inhibition of PMA-stimulated NADPH oxidase in a dose-dependant fashion.(19; 53)

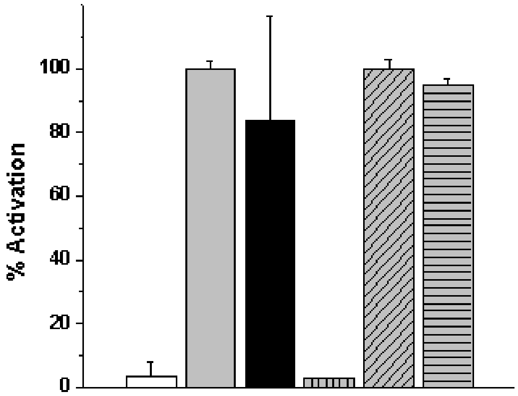

Figure 15. BH effect on RNS and ROS production. Effect of β-hematin on ROS and RNS production. ROS production was assessed by DCF-DA (first 3 columns) where the *white column* correlates to the percent activity of unstimulated cells, *grey* is the activity of cells stimulated with PMA and *black* are cells treated with β-hematin and stimulated with PMA. The Griess assay was used to assess RNS production (last 3 columns) where the *vertical grey* column corresponds to unstimulated cells, *diagonal grey* is the activity of cells stimulated with LPS and *horizontal grey* is the activity of cells treated with β-hematin and stimulated with LPS.(6)

Challenge of LPS-stimulated iNOS in RAW mouse macrophage cells with BH does not inhibit the production of RNS either (**Figure 15**).(6) In control reactions with unstimulated cells, levels of detected NO increased as levels of BH were increased, owing to the particular activation (**Figure 16**), indicating healthy, functioning macrophage cells.(6) Additionally, 24 hr preincubation of RAW macrophage cells with BH does not inhibit restimulation with LPS (**Figure 17**).(6)

The results shown in Figure 16 are consistent with studies in mouse macrophage-like B10R and N11 microglial cells which show no BH-dependant inhibition of NO(62) but are

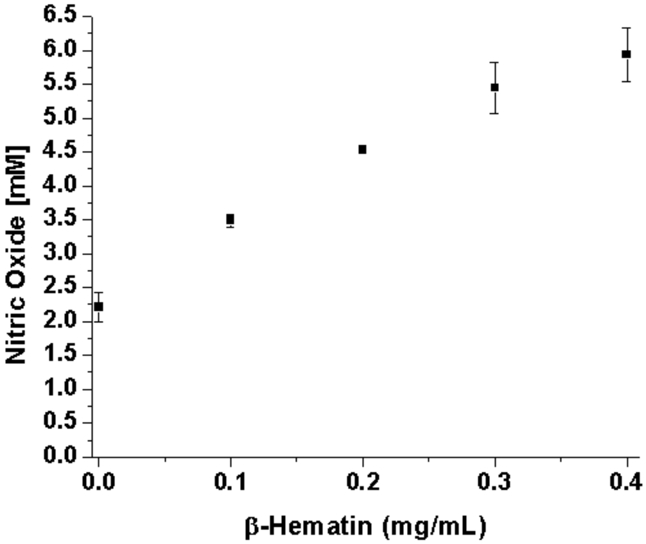

Figure 16. BH impact on NO production. Effect of increasing levels of β-hematin on NO production in Raw 264.7 cells as measured by the Griess assay.(6)

contradictory to a report with murine peritoneal macrophages that appears to indicate BH inhibition of NO.(60) Further, hemozoin directly isolated and exhaustively purified to remove all absorbed proteins, lipids and carbohydrates consistently has been shown to not inhibit NO production in human peripheral blood mononuclear cells and mouse macrophage B10R microglial cells.(62; 74) Consequently, the results presented herein and in the preponderance of published data suggest that NO production is not inhibited with BH treatment. In contrast, native hemozoin has been shown to decrease NO production in murine peritoneal macrophages.(75) The stark contrast concerning the immunoreactivity of BH versus native hemozoin with regards to modulating ROS and RNS production implies that there exists a biochemical distinction between the two.

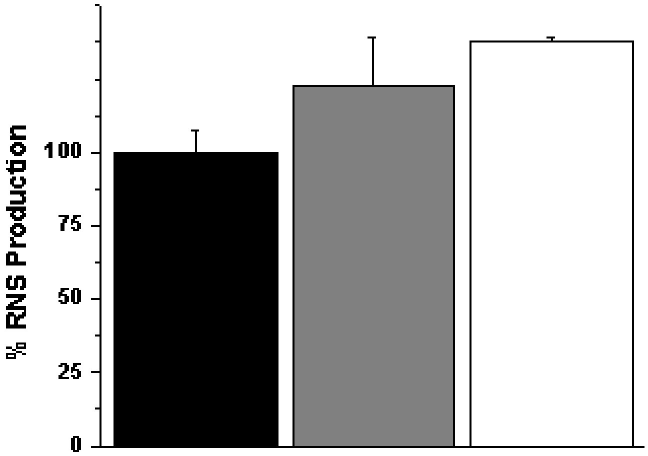

Figure 17. Effect of BH treatment on restimulation with LPS. Effect of preincubation of RAW cells with β-hematin on RNS production as assessed by the Griess assay. The *black* column corresponds to RNS production of cells stimulated with LPS, the *dark grey* column is cells treated simultaneously with β-hematin and LPS, and the *white* column represents cells first treated for 24 hours with β-hematin followed by restimulation with LPS for another 24 hours.(6)

Degradation of BH by ROS and RNS in vitro

If BH does not effectively inhibit the intracellular production of ROS and RNS, then these molecules should be available to react with the phagocytosed heme aggregate; however, experiments suggest that hemozoin can persist for up to 72 hrs within the phagolysosome.(2) The differential inhibition capability between β-hematin and native hemozoin suggests that the immunosuppressive activity of native hemozoin is a result of more than just the biomineral structure. Consequently, the effects of these microbicidal agents on BH stability may provide some degree of insight into the apparent biochemical differences between BH and hemozoin. In a series of *in vitro* experiments, the susceptibility of BH to degradation by hydrogen peroxide, sodium hypochlorite and nitric oxide was carried out.(6) For these experiments, both the concentration dependency and the kinetics of degradation were investigated.

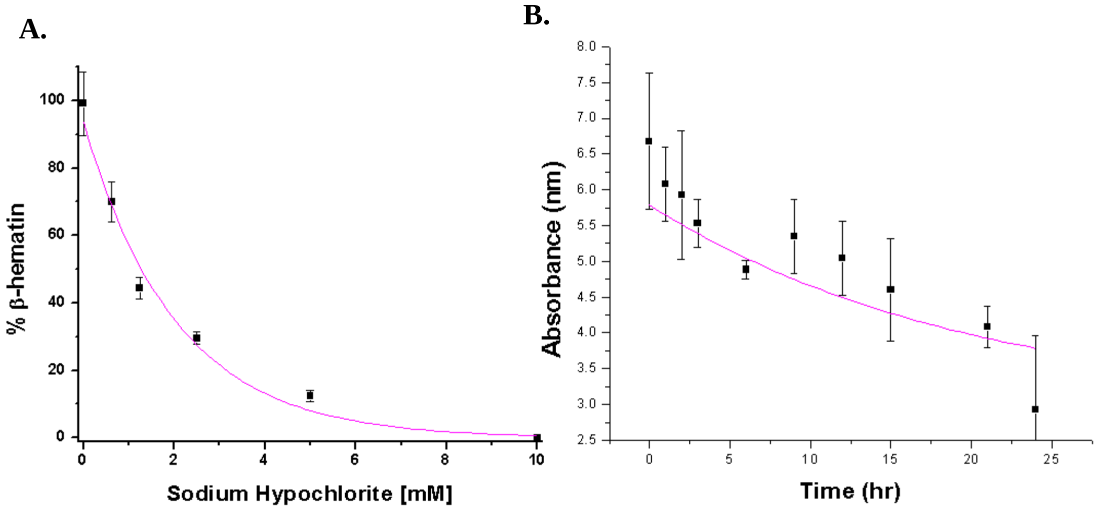

Figure 18. BH degradation by HOCl. A. β-hematin degradation by sodium hypochloite (EC_{50} = 5.5 mM). B. β-hematin degradation by sodium hypochlorite kinetics (IC_{50} = 19 h).(6)

BH showed a mark sensitivity to HOCl at pH 4.8, the pH of the phagolysosome, with an EC_{50} value of 5.5 ± 0.1 mM (**Figure 18A)**.(6) At a hypochlorite concentration of 10 mM, the kinetic data revealed an IC_{50} of 19 h for the β-hematin degradation (**Figure 18B)**. The degradation of BH in the presence of HOCl results in the loss of aggregate integrity and the formation of an insoluble orange product. The HOCl-mediated oxidation of the protoprophyrin IX methylene bridge likely results in the opening of the ring and release of iron. The consequence of such a reaction would be the dissolution of the aggregate and formation of a product similar to bilirubin, the tetrapyrole end product of biological heme degradation by heme oxygenase.(76)

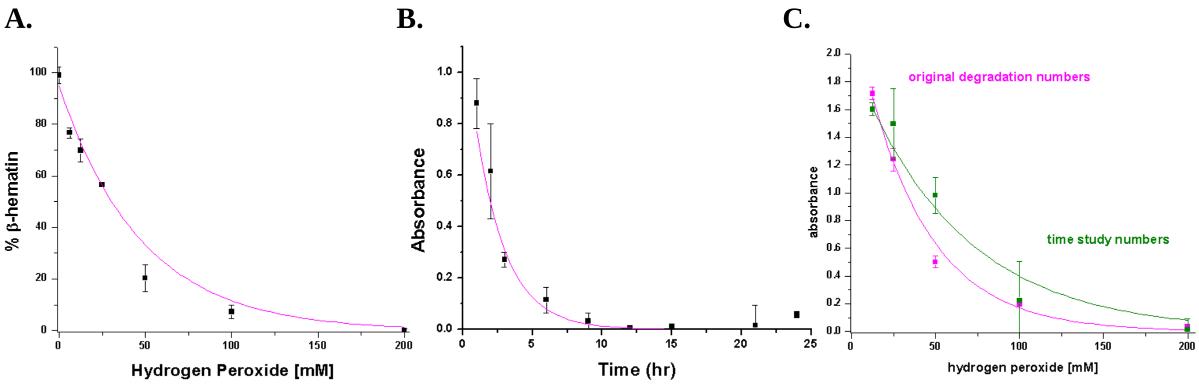

Figure 19. BH Degradation by H2O2. A. β-hematin degradation by hydrogen peroxide (EC_{50} = 38.8 mM). B. β-hematin degradation by hydrogen peroxide kinetics (IC_{50} = 2.2 h). C. Comparison of β-hematin degradation at 21 hours for concentration dependant study and kinetics data.

As can be seen in **Figure 19A**, β-hematin was readily degraded by hydrogen peroxide exhibiting an EC_{50} value of 38.8 mMThough this experiment was allowed to incubate at 37 °C for 20 hours, studies into the kinetics showed that the IC_{50} of the degradation was 2.2 h with a H_2O_2 concentration of 200 mM (**Figure 19B**). The kinetics experiment was repeated for concentrations ranging from 200 mM to 12.5 mM. Comparing the values obtained at the 21-hour mark for each concentration with those obtained in the concentration-dependant study verified the accuracy of the concentration-dependant study data (**Figure 19C**). This value is consistent with hydrogen peroxide degradation of BH reported by Chen et al., who examined pigment stability in the contect of hemoglobin catabolism within the digestive vacuole.(8) In this process, Hb, which also contains a five coordinate heme-Fe group, is degraded by hydrogen peroxide to release free iron. Reactions between Fe(III)PPIX and hydrogen peroxide have been reported to result in formation of four dipyrrolic propentdyopents, hematinic acid and methylvinylmalemide.(77) Heme-Fe(III) can react with hydrogen peroxide to generate a formal perferryl species [$^{+}$heme-

Fe(IV)=O or heme-Fe(V)=O]which can then react with the olefinic porphyrin bridge to form a glycol and regenerate the ferric heme (**Scheme 2**).(78)

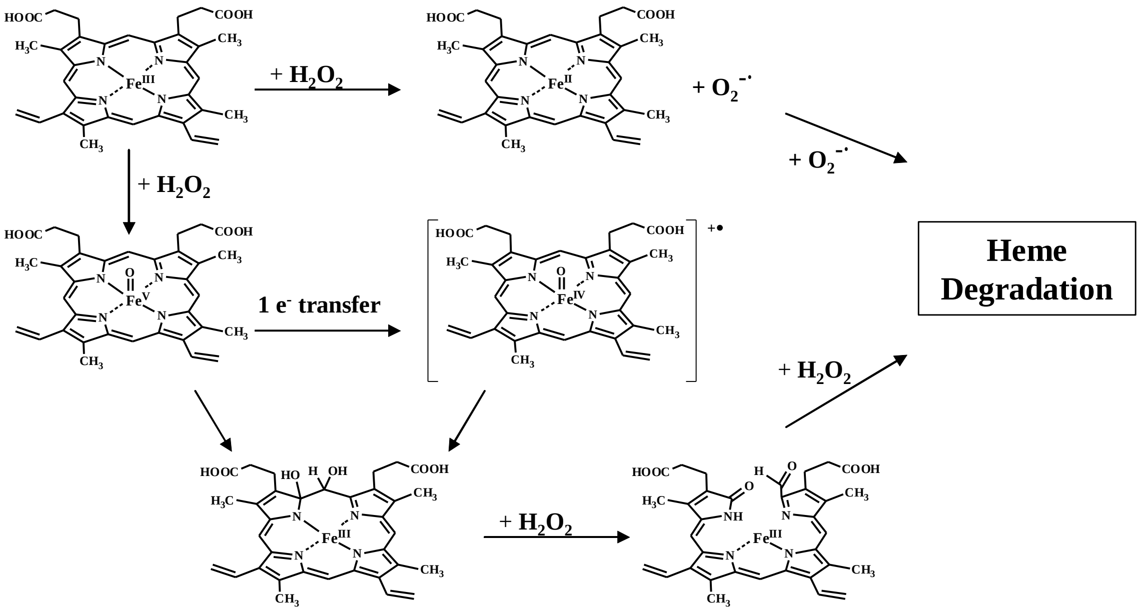

Scheme 2. Purported pathway of BH degradation by H_2O_2 .

The ferric heme reacts with another molecule of hydrogen peroxide to cleave the glycol and form an amide and an α-formly pyrrolic species. Repeating this reation in other methane bridges results in the breakdown of the prophyrin to dipyrroles and monoryrroles.(77; 78) Further enhancement of the degradation process is obtained when the reaction of heme-Fe(III) and hydrogen peroxide results in the formation of heme-Fe(II) and superoxide anion. The superoxide anion is able to oxidize the tetrapyrole rings of heme, leading to the degradation of heme and the release of iron.(79) With hemozoin being a dimer consisting of Fe(III)PPIX units, it is plausible that its degradation process in the prescence of hydrogen peroxide is similar to those described for other metal containing prophyrin systems.

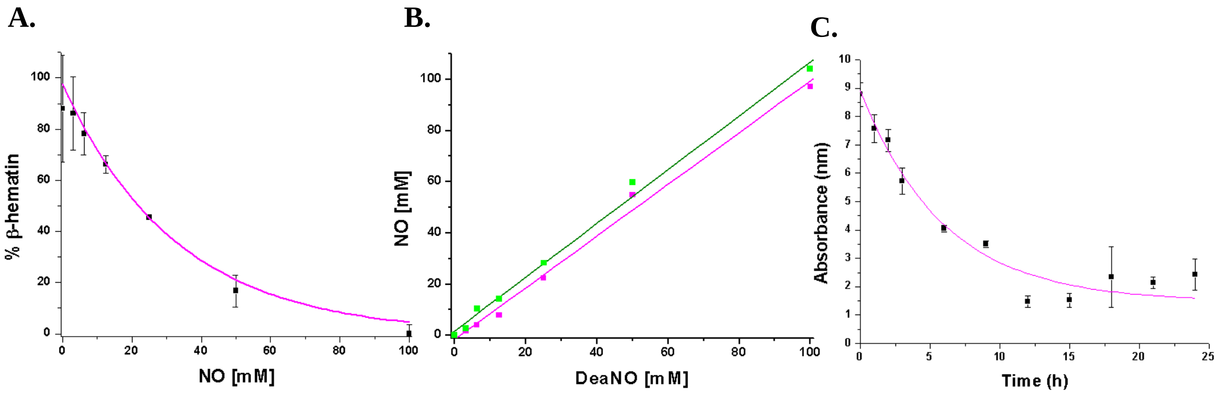

Figure 20. BH degradation by NO. A. β-hematin degradation by NO (IC_{50} = 39 mM). B. Quantitation of NO released by DeaNO. Control containing no β-hematin shown in green. Supernatant from NO degradation shown in pink. There is a consistent decrease in the amount of NO found in the supernatant of the degradation as compared to the control at all concentrations. C. Kinetics of β-hematin degradation by NO.

These studies also focused on nitric oxide's ability to degrade β-hematin. DeaNO, a NO releasing agent, was used as a surrogate for nitric oxide. Exposure to NO was successful in degrading β-hematin, with an EC_{50} value of 33 ± 6.7 mM (**Figure 20A**). To monitor the release of NO from the DeaNO, the Griess assay was performed on both the supernatant of the degradation experiment and on control experiments containing no β-hematin. As shown in **Figure 20B**, there was a consistent decrease in the amount of NO present in the supernatant of the degradation experiment as compared to control experiments. Notably, the control showed complete recovery of NO released by DeaNO when quantitated by the Griess assay. This resurgence implies that the decrease of NO in the degradation experiment was a result of NO being utilized during the degradation process. The kinetics of this degradation showed that for a NO concentration of 100 mM, the IC_{50} was 5.7 hours, well below the 20 hours allowed in the concentration dependent study (**Figure 20C)**.

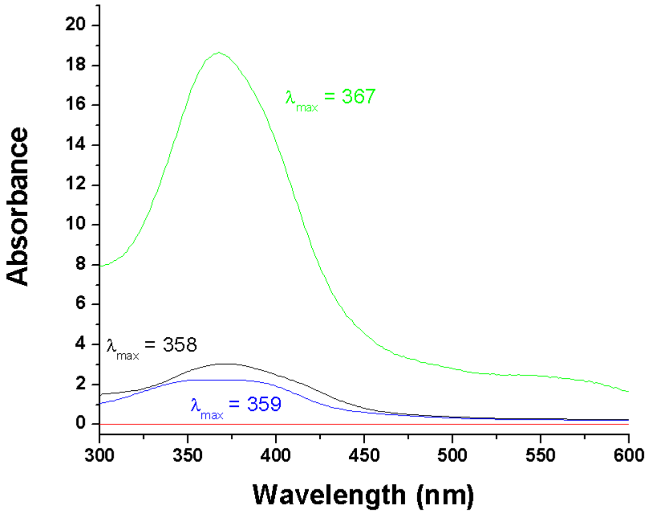

Figure 21. UV of NO-heme compounds formed during BH degradation by NO. The absorbance of hematin in sodium phosphate buffer is shown in blue. The absorbance of the remaining BH from 100 mM NO degradation is shown in black. The absorbance for BH in sodium phosphate is shown in red and hematin which has been reacted with NO is shown in green. There are two peaks for hematin with the predominant absorbance at 385 nm. The predominant peak for the BH from the NO degradation has shifted to 357 nm.

Interestingly, it was observed that the supernatant of this experiment was a brown color that deepened as the DeaNO concentration was increased. In contrast, the H_2O_2 and NaOCl degradation had clear supernatants suggesting a different mechanism of degradation. Also, when the remaining β-hematin was dissolved for quantitation, it required a much more concentrated amount of NaOH to be completely dissolved. This suggested that something on the surface of the β-hematin had changed. To further investigate the surface change of the β-hematin, the UV spectra was taken of the dissolved β-hematin remaining from the degradation studies. This spectrum was compared to the spectrum of hematin, shown in **Figure 21**. There is a λ_{max} shift from a predominant peak at 385 nm for hematin to 357 nm for the β-hematin that remained from the NO degradation experiment. This suggested that the surface of the β-hematin was being altered during the degradation process. The combination of this data suggests that NO readily binds to the iron of β-hematin during the degradation process. NO binding to ferric heme and formation of a ferric nitrosyl complex likely results in the spontaneous autorediction of the iron to the ferrous state.(80) In terms of stability, reduction of the iron will result in an increased radius, weakening the iron-nitrogen bonds of the porphyrin. Further, NO acts as an extremely strong ligand and its binding to the iron of heme groups has been shown to exert a large repulsive force on the ligand *trans* to the NO, potentially disrupting the reciprocating propionate linkages within the crystal lattice of hemozoin.(81) IR analysis isolated reaction products prior to complete degradation revealed a vibration at 1636 cm^{-1} consistent with NO coordination in an Fe(II) porphyrin complex (**Figure 22**).(80)

Regardless of the potential mechanisms of degradation, the insoluble BH biomineral is sensitive to the ROS and RNS that are generated upon phagocytosis. Further, it is recognized that the crystals of BH are large enough to allow awater into the lattice.(82) Therefore, it is feasible that small molecules such as HOCl, H_2O_2, and NO work their way into the crystal lattice, disrupting the structural integrity of hemozoin from within as well as on the surface. The lower EC_{50} value (5.5 mM) of HOCl compared with that of H_2O_2 (38.0 mM) is consistent with it being a much more reactive microbicidal agent.(74) Additionally, the ability of H_2O_2 to degrade heme is known to decrease in acidic environments, whereas HOCl degradation is inversely affected by the acidity.(83) NO is not a particularly strong microbicidal agent either, so it is not that surprising that its EC_{50} value is also higher that than of HOCl.(84) Finally, it is important to note that the concentration regimes of HOCl, H_2O_2 and NO examined here are relativent to biologically reported concentrations produced within professional phagocytic cells.(20; 84) To investigate the facts of BH inside RAW cells, BH was phagocytosed and its *in vivo* stability examined.

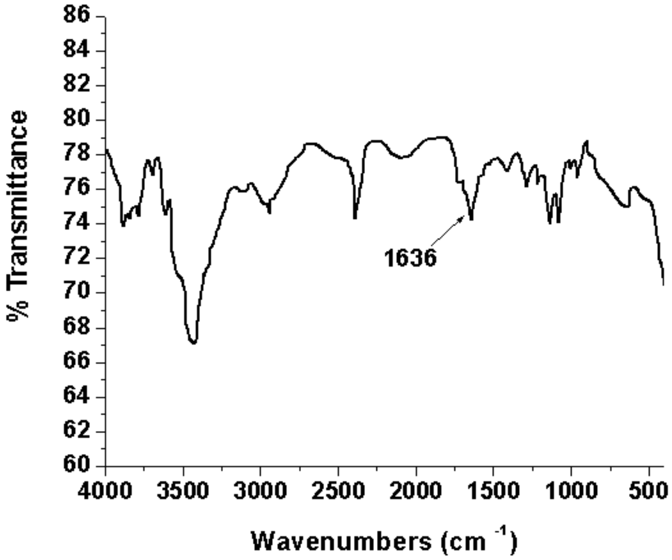

Figure 22. IR of product formed from BH degradation by NO. IR of the BH-NO complex obtained by reacting β-hematin with 50 mM DeaNO and isolated prior to complete degradation.

Degradation of BH by RAW 264.7 murine macrophage cells

Confocal microscopy offers an advantage over traditional microscopic techniques because the user can view only one particular plane of interest within a thick sample without interference from other planes. When applied to cell imaging, this feature gives the user the ability to determine where a fluorophore is located within the cell both within the x-y plane as well as the z-plane. By utilizing the natural fluorescence of β-hematin, it is not necessary to add any fluorophores in order to monitor the extent of β-hematin degradation. In order to accurately quantitate the amount of β-hematin remaining in the cells, the experiment must focus solely on the β-hematin located *within* the cells. This required the exclusion of any residual fluorescence from β-hematin located above or below the actual cells. Confocal microscopy, therefore, was the most appropriate method for performing this experiment.

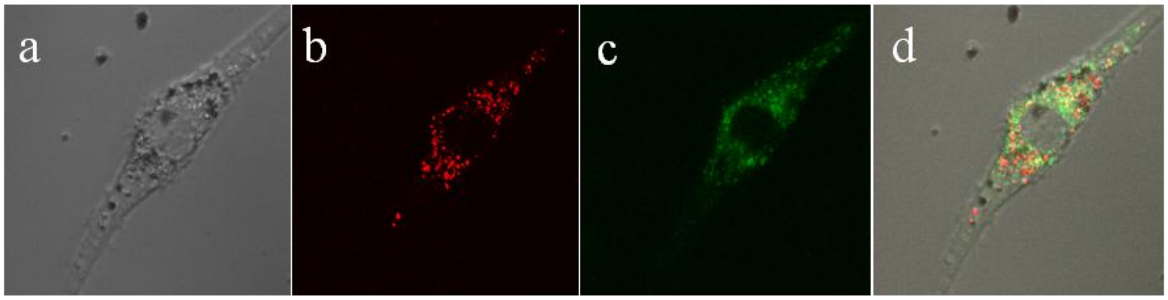

Figure 23. Localization of BH to the phagolysosome. Colocalization of β-hematin inside the acidic vacuoles as examined by Confocal microscopy. A. The differential interference contrast (DIC) image of the cell. B. Excitation at 514 nm followed by emision using a band pass filter from 533.2-542.9 allowed for the imaging of β-hematin fluorescence. C. Excitation at 543 nm followed by the use of a long pass 585 nm filter for emission allows for visualization of the lysotracker fluorescence. D. Composite figure of a-c demonstrating the colocalization of β-hematin inside the acidic vacuoles.

Before monitoring the degradation of β-hematin within macrophage cells, it was first necessary to show the successful phagocytosis β-hematin. The colocalization of BH inside the acidic vacuoles was shown using the inante fluorescence of BH and Lysotracker Red, a dye specific to acidic compartments such as the phagolysosome. The use of this dye presented a number of problems that required optimization. Early attempts to obtain a colocalization image resulted in a high background on certain focal planes which masked the actual fluorescence of both the lysotracker and the β-hematin. It was determined that the media was the cause of this background. A number of controls eventually determined that the use of PBS instead of media during cell imaging resolved this issue. A second problem occurred in the attempts to find two channels that were mutually exclusive through which to view both the lysotracker and β-hematin. β-hematin has a very narrow emission spectra and the use of pre-made excitation/emission programs resulted in the inability to collect adequate β-hematin fluorescene. Therefore, the use of a customized excitation/emission program was used which excited the β-hematin channel with a 514 nm laser and detected emission with a 533.2-542.9 nm bandpass filter. The lysotracker channel was excited with a 543 nm laser detected emission with a 585 longpass filter. This very specific combination gave good fluorescence in both channels without bleed-through. Here, the images of BH fluorescence and the fluorescence of the lysotracker dye clearly show BH colocalizing to acidic vacuoles of the macrophage cells (**Figure 23**). The orthogonal slices (*XY* and *XZ)* of the confocal image also revealed segregation of BH exclusively within the cells, confirming that it had indeed being phagocytosed.(2)

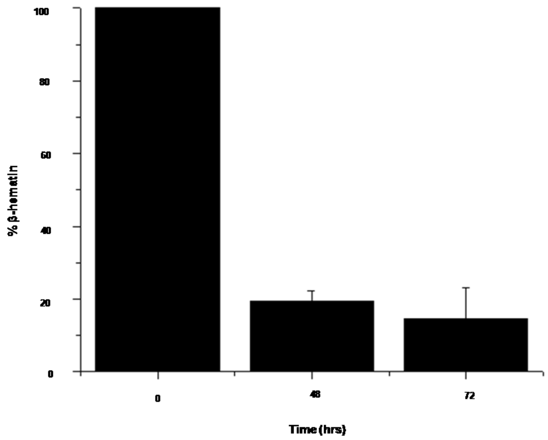

Figure 24. Quantitated fluorescence of Degradation of BH in RAW macrophage cells. There is a 78% decrease in fluorescence associated with BH 72 hours after phagocytosis by RAW macrophage cells.

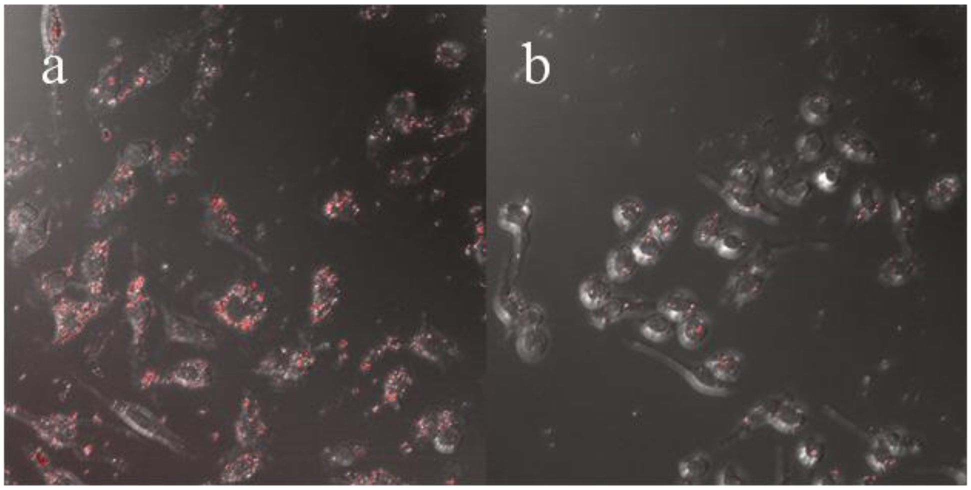

Figure 25. Confocal Image of Degradation of BH in RAW cells. Confocal images β-hematin degradation inside RAW cells at time zero (A) and after 72 hours (B). Fluorescence images were obtained by excitation at 514 nm followed by collection of the emission spectra using a band pass filter from 533.2-542.9 nm.

The quantitative analysis of BH stability as a function of time was probed at 0, 48, 72 hrs. The macrophage cells were treated with β-hematin to elict phagocytosis. After a period of 90 minutes, excess β-hematin was washed away and the samples were allowed to incubate for the appropriate amount of time. The cells were imaged using the above mentioned excitation/emission configuration. For each of cell sample, 300-400 cells were quantitated to obtain an average fluorescence for that sample, and each time point was done in triplicate to ensure reproducibility. Normalizing the fluorescence at the time zero, it was determined that in both unactivated and PMA activated cells, BH had been degraded by 67.2 ± 6.5% after 48 hrs and that by 72 hrs it had been degraded by 76.8 ± 2.7% (**Figure 24**). Visually, the results clearly show dismishing fluorescence, noted by a marked decrease in the amount of red fluorescence ofver the time course of the experiment (**Figure 25**). Controls in the absence of cells shows that BH fluorescence itself did not decrease with time, indicating the degradation observed was not due to photobleaching of BH. Because of the small sample size used to assess degradation of BH by confocal microscopy, this was confirmed by the use of flow cytometry. Flow cytometry allows for the analysis of samples in the tens of thousands of cells as compared to hundreds assessed by confocal microscopy. Preliminary experiments were performed to determine whether the presence of BH within RAW cells was detectable by flow cytometry (**Figure 26A**). These experiments showed a significant shift in both front and side scatter of cells indicating that they have increased in both size and internal complexity. Further, when excited with a 630 nm laser, the fluorescent signal emitted at 680 nm was significantly increased after treatment with BH. This emission corresponds to the fluorescence emitted as a result of exciting the heme complex. The large shift in fluorescence indicates that it is possible to distinguish a BH positive sample population from a control population (**Figure 26B**). The use of flow cytometry to assess the

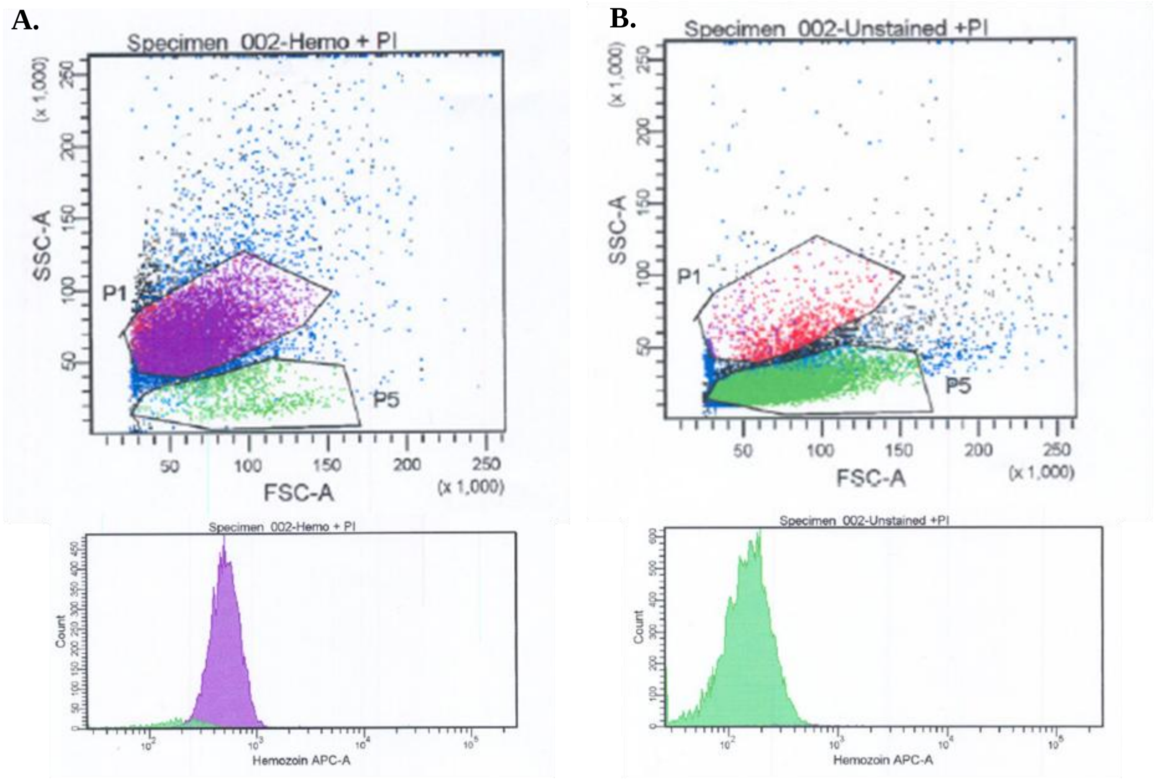

Figure 26. Detection of BH in RAW by flow cytometry. Flow cytometry was used to distinguish BH positive RAW cell populations (A) from control populations (B). Upon phagocytosis of BH, an increase of front and side scatter are seen, as well as an increase in fluorescence associated with the BH

amount of BH present in a cell population directly after phagocytosis and 48 hours after phagocytosis indicated a marked decrease in the percent of the population which yielded a BH positive fluorescent signal (**Figure 27**).

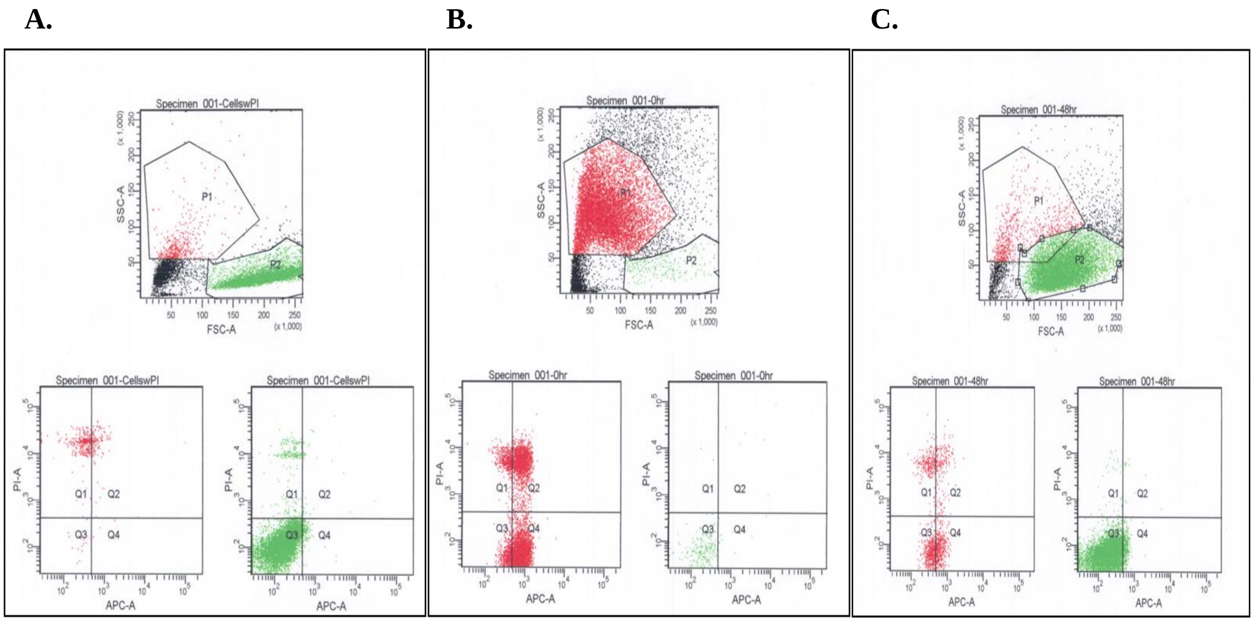

Figure 27. BH degradation in RAW cells by flow cytometry. A. Control untreated RAW populations showed low scatter and fluorescence. B. After phagocytosis with BH, there is an increase in internal complexity and fluorescence (indicated in red). C. After 72 hours, the same samples from B were analyzed and the signal as a result of the BH has decreased substantially indicated BH degradation over 72 hours.

This substantial degradation of β-hematin by macrophage cells is a marked contrast to the apparent stability of native hemozoin within human peripheral blood monocytes.(2; 54) These results, together with the observation that the ROS and RNS production was not inhibited by BH, and that the model reactions highlight BH sensitivity to microbicidal agents, indicate that the fate of BH is vastly different from that of native hemozoin despite the structural identity of the heme dimer core. This discrepancy suggests the biomineral alone is not responsible for the inhibitory effects of hemozoin phagocytosis on macrophage cells. To determine the source of hemozoin immunosuppression, it was necessary to look at the difference between hemozoin and β-hematin: the biological environment.

Inhibition of oxidative burst by HNE and 15-HETE

When parasite-infected RBC's rupture, they release the parasite, hemozoin and cellular debris into the vasculature.(49) Analysis of native hemozoin has shown that the biomineral is coated with a gradient of oxidized membrane lipids, including HETE's and HODE's, which lead to secondary oxidation products, such as HNE.(55) Recently, it has been determined that hemozin is able to nonenzmatically generate significant quantities of hydrozyated fatty acids(41; 55) and to mediate the oxidation of fatty acides such as arachidonic and linoleic acid to produce secondary oxidation products like HNE.(85) Levels of HNE and 15-HETE within hemozoin-laden macrophages have been found up to 230 nmol per 10^{10} cells and 33-39 µM, respectively.(53; 54) HNE is an α,β-unsaturated aldehyde produced from lipid peroxidation.(86) It reacts primarily with the sulfhydryl group of cysteine, the side chain amino group of lysine and the imidazole of histidine.(87) This reactivity makes it a potent biological agent capable of forming protein adducts affecting a range of cellular functions. At relatively low concentration, HNE disrupts cytoskeletal integrity, impairs mitochondrial respiration, inhibits DNA, RNA and protein synthesis, stimulates neutrophil chemotaxis, and modulates platelet aggregation and changes in response to second messenger pathways.(88) Similarly, 15-HETE has been shown to generate pathophysiological effects such as altered permeability of endothelial cells, edema, increased adherence of RBCs and induced chemotaxis and chemokinesis.(41; 55) Consequently, macrophage function may be impaired by the presence of these immunoreactive molecules.

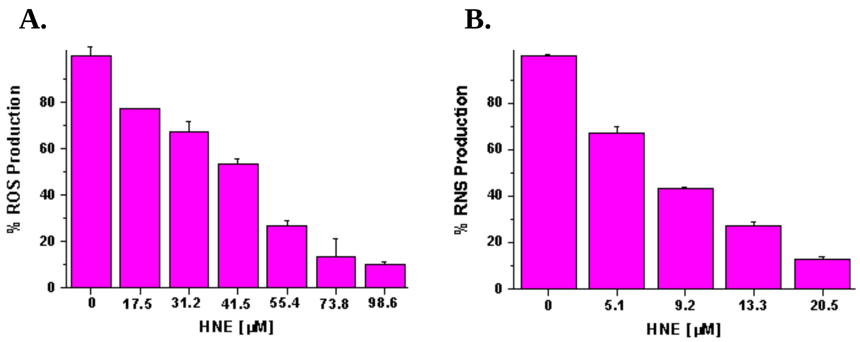

Figure 28. HNE inhibition of oxidative burst in RAW macrophage cells. Concentration dependent effect of HNE treatment on oxidative burst. Inhibition of ROS production (A) with increasing concentrations of HNE in RAW 264.7 cells as assessed by DCF-DA. Inhibition of RNS production (B) with increasing concentrations of HNE as assessed by the Griess assay.

RAW cells treated with HNE followed by stimulation with PMA demonstrated a concentration-dependent inhibition of oxidative burst (**Figure 28A**). As the concentration of HNE increased up to 100 µM, stimulation of NADPH oxidase was inhibited, with an EC_{50} value of 45.9 µM. Studies of HNE inhibition of superoxide in human neutrophils have shown a similar response, with an EC_{50} value of 27 µM, consistent with the results reported here for mouse macrophage cells.(89) LPS-activated iNOS was similarly inhibited by HNE in a concentration-dependent manner, with EC_{50} values of 9.2 µM (**Figure 28B**). Generated from the most abundant class of polyunsaturated fatty acids, HNE contains three functional groups, is lipophilic and easily diffusible, and highly reactive with cellular components, all characteristics that make HNE an efficient means of disrupting the host immune system in malaria.(21) Previous reports have demonstrated that at concentrations over 10 µM, HNE is capable of inhibiting the activity of protein kinase C (PKC), a key signaling protein in NADPH oxidase activation.(54) HNE is highly reactive with proteins, disrupting function by protein adduct formation.(21) In fact, there has been a suggestion of the possible formation of HNE adducts on PKC.(90) This is just one potential target that HNE may interact with once inside the macrophage that may lead to inhibition of oxidative burst.

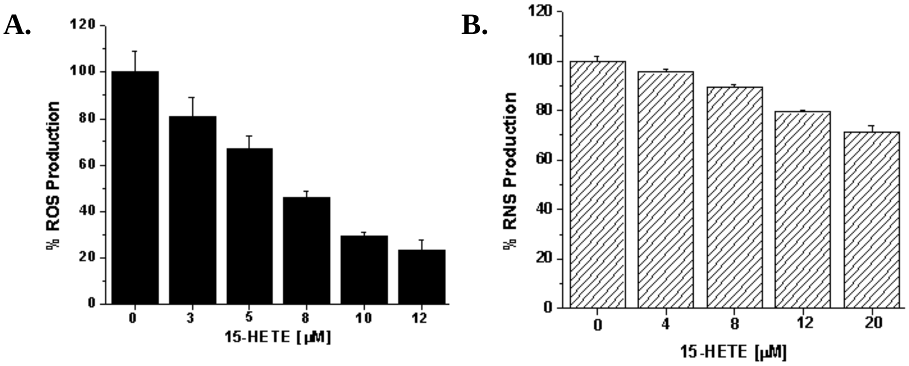

Figure 29. 15-HETE inhibition of oxidative burst in RAW macrophage cells. Concentration dependent effect of 15-HETE treatment on oxidative burst. Inhibition of ROS production (A) with increasing concentrations of 15-HETE in RAW 264.7 cells as assessed by DCF-DA. Inhibition of RNS production (B) with increasing concentrations of 15-HETE as assessed by the Griess assay.

Similarly, incubation with 15-HETE resulted in a concentration-dependent inhibition of PMA-stimulated burst, with an EC_{50} value of 8.0 µM (**Figure 29A**). Human monocytes threated with 15-HETE have displayed a similar trend, with 100% inhibition of ROS production at 15 µM 15-HETE.(54; 55) LPS-activated iNOS was also inhibited up to 28.5% in the presence of 15-HETE (**Figure 29B**). While treatment of phagocytic cells with 15-HETE clearly results in the loss of ROS and RNS production, the mechanism of inhibition is not immediately obvious other than subsequent degradation of 15-HETE to HNE. The inhibition of oxidative burst with these highly reactive agents points towards the importance of hemozoin not as a toxic substance itself, but rather as a mediator of the oxidation of fatty acids to form highly reactive and toxic molecules such as HNE and 15-HETE. Additionally, the particulate nature of the detoxification biomineral ensures that it will be targeted by the innate immune system.

Reaction of BH with erythrocyte ghosts

The aforementioned results suggest that the inhibitory effects of hemozoin are due to its ability to react with membrane lipids and form highly reactive, immunosuppressive molecules. To examine the effects of the constitutive components of the malaria pigment on macrophage response in an appropriate model system, BH was reacted with membrane lipids from erythrocyte ghosts. During the purification, the elution of the ghosts was monitored by the absorbance of aromatic residues in proteins at 280 nm (**Figure 30**).

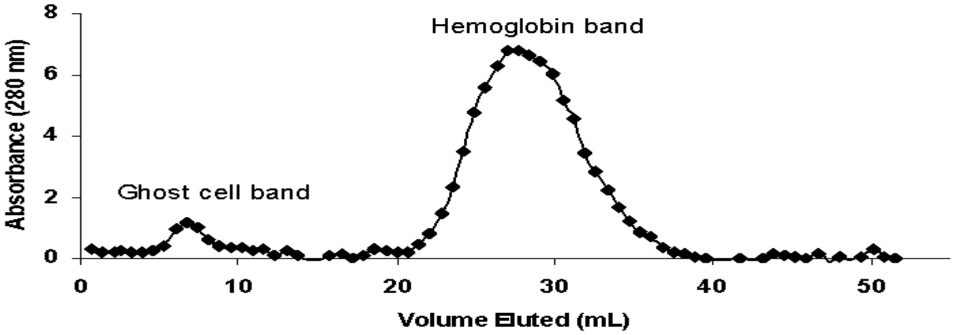

Figure 30. Elution profile of purified RBC ghosts from Sepharose 2B column. The RBC ghosts were purified from other cellular debris by monitoring the UV absorption at 260 nm.

After purification of ghosts and following the overnight reaction with BH, RAW macrophage cells were treated with the reaction supernatant. NADPH oxidase in PMA-activated RAW cells was inhibited in a concentration-dependent manner (**Figure 31A**), as was the activation of iNOS in LPS-activated cells (**Figure 31B**). There was no detectble inhibition of ROS or RNS production upon treatment of BH or ghost supernatants alone, indicating that it is the products from the reaction between the two that cause the inhibition (**Figure 32**).

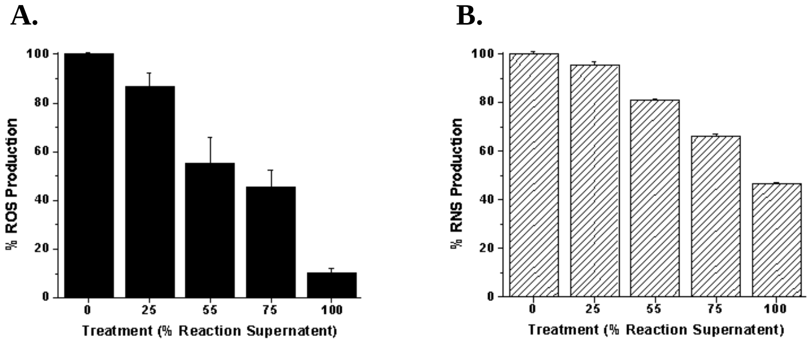

Figure 31. Inhibition of oxidative burst by RBC ghosts which have been incubated with BH. Inhibitory effect of the products of ghost and β-hematin interactions on oxidative burst. Inhibition of ROS production (A) was obtained using luminol-enhanced chemiluminescence and inhibition of RNS (B) was obtained using the Griess assay.

hemozoin into a milieu of cellular debris, providing a substrate for the nonenzymatic, heme-catalyzed peroxidation that results in a toxic gradient of primary and secondary fatty acid oxidation products. Although the precise mechanism and cellular targets remain unelucidated, it is these products, not the aggregate of dimeric heme units, which effectively inhibit RAW NADPH oxidase and iNOS activity within macrophage cells.

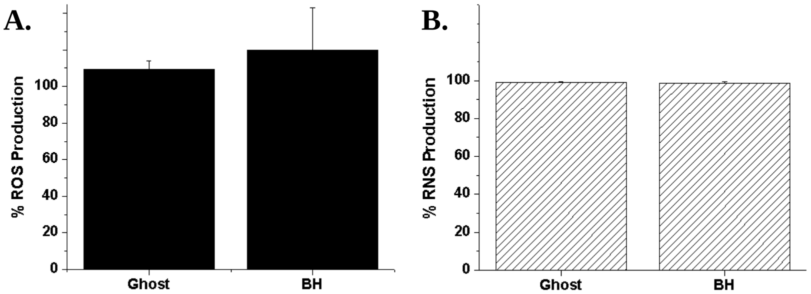

Figure 32. Inhibition of oxidative burst by RBC ghosts only. Effect of ghosts and β-hematin alone on the production of (A) reactive oxygen species as measured by luminol-enhanced chemiluminescence and (B) reactive nitrogen species as monitored by the Griess assay.

BH Degradation by HNE

After demonstrating that the oxidized lipid products were essential to disrupting ROS/RNS production, the individual roles of some these oxidation products were probed to understand the complex mechanism of macrophage dysfunction under conditions of oxidative stress on the cells. Specifically, a series of experiments were designed to determine the effect of HNE on macrophage ability to degrade β-hematin.

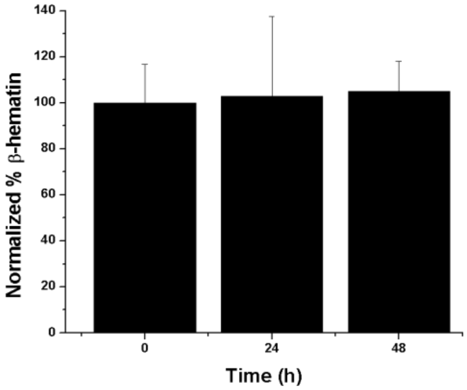

Figure 33. Quantitated fluorescence of degradation of BH in RAW macrophage cells treated with HNE. When treated with HNE, no significant degradation of BH in RAW macrophage cell s is seen after 48 hours.

Both confocal microscopy and flow cytometry show that functional macrophage cells are capable of degrading β-hematin. However, when the same confocal experiment was repeated after samples were treated with HNE for a period of 3-4 hours prior to incubation, the outcome was in stark contrast. Because there was no significant degradation seen after 48 hours in the untreated degradation samples, this experiment was slightly altered to use only 0, 24 and 48 hour time points, each in triplicate. Compared to the untreated experiment, the cells treated with HNE (both activated with PMA and non-activated) had no significant degradation over the 48

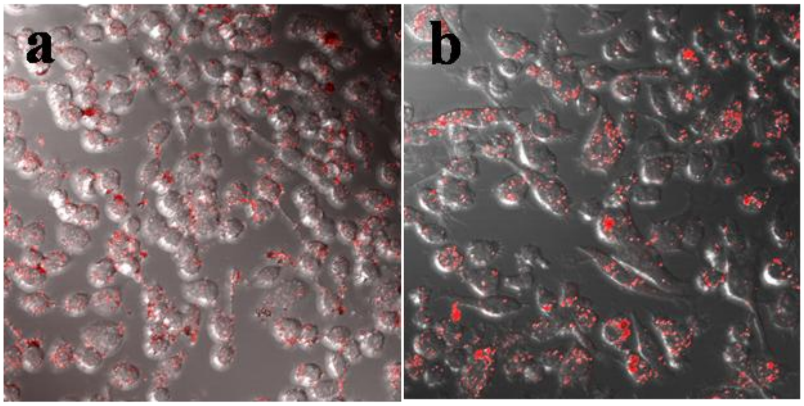

Figure 34. Confocal Image of Degradation of BH in RAW cells after HNE treatment. Confocal images β-hematin degradation inside HNE treated RAW cells at time zero (A) and after 48 hours (B). Fluorescence images were obtained by excitation at 514 nm followed by collection of the emission spectra using a band pass filter from 533.2-542.9 nm.

hour time period. As shown in **Figure 33**, the projection images visually suggested no degradation, which was confirmed by the quantitation of the average fluorescence (**Figure 34**). Analysis of BH degradation in HNE treated RAW cells by flow cytometry yielded similar results. There was substantially less degradation seen in the HNE treated populations after 48 hours as seen in the populations not treated with HNE. However, within the context of the larger sample population analyzed by flow cytometry, it becomes clear that all degradation is not halted by the treatment with HNE. The degradation of BH is nonetheless largely impaired by the treatment of HNE (**Figure 35**).

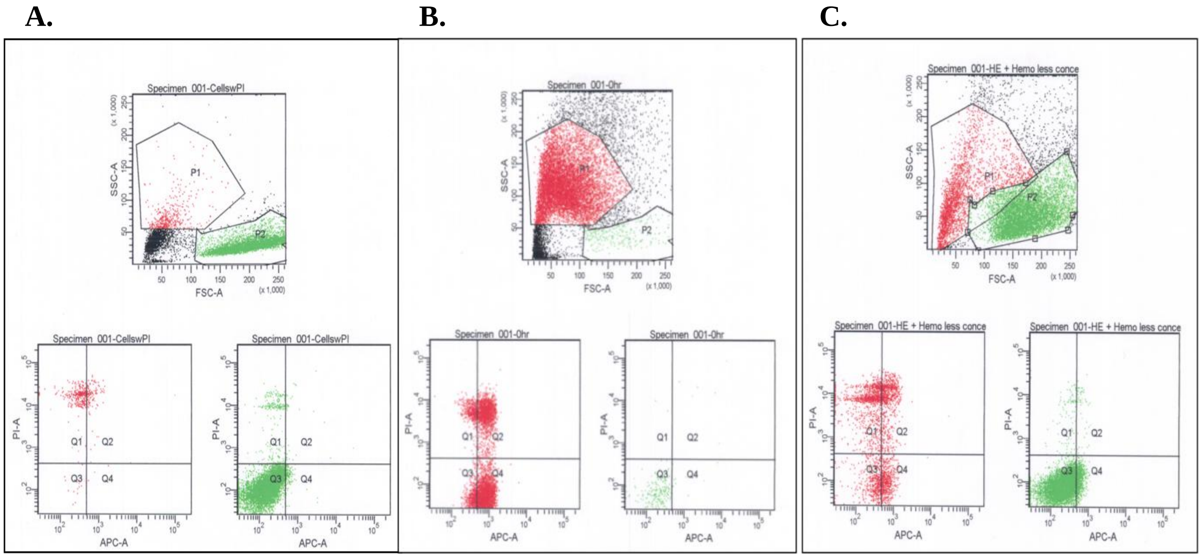

Figure 35. BH degradation in RAW cells treated with HNE by flow cytometry. A. Control untreated RAW populations showed low scatter and fluorescence. B. After phagocytosis with BH, there is an increase in internal complexity and fluorescence (indicated in red). C. After 48 hours, the same samples from B were analyzed and the signal as a result of the BH has decreased a marginal amount but a significant percent of the population still yields higher fluorescence and side scatter indicating HNE inhibited BH degradation.

Conclusion

The composition of native hemozoin released uon RBC rupture has been reported to be 65.1% proteins, 15.5% Fe(III)PPIX, 5.9% carbohydrates and less than 1% lipids and nucleic acids.(20; 91) Both hemozoin and Bh are able to interact with membrane lipids to generate high levels of reactive secondary metabolites such as HNE and 15-HETE. Inside hemozoin-laden macrophages, levels of these agents reach between 20 and 40 µM.(55; 92) These molecules act as immunosuppressive agents that are capable of disrupting oxidative burst (both NADPH oxidase and iNOS-activated) and represent the key to understanding reactivity differences between structurally identical native hemozoin and BH. Clearly, native hemozoin inhibits the activation of oxidative burst and is stable inside macrophages for long periods of time.(2; 53) In contrast, BH is sensitive to themicrobicidal agents of oxidative burst, and macrophages are capable of degrading this material. Significantly, native hemozoin which has been thoroughly washed to remove debris from RBC rupture (including lipids) reacts in a fashion identical to BH, where it does not inhibit oxidative burst.

Native hemozoin is complex material with a similarly complex reactivity. By systematically examining each of the malaria pigment's components, we have been able to dissect their impact on the immune reactivity of a macrophage cell line. Further, via the reaction between synthetic BH and RBC ghosts, we were able to effectively reconstruct the observed immunomodulating reactivity of native hemozoin. In this fashion, we propose that hemozoin functions to construct a toxic minefield which disrupts the immune response to the parasitic infection. The presence of particulate hemozoin and RBC debris invites the professional phagocytic cells to the site, trapping the cells into a veritable sea of reactive and toxic species which freely diffuse across the cell membrane and/or are brought inside as hemozoin is phagocytosed. Once there, the highly reactive molecules, generated from the hemozoin-mediated oxidation of membrane lipids, disrupt macrophage function.

The hemozoin-mediated immunomodulation presented here represents but one aspect of how this biomineral helps regulate the host/parasite interaction. Recent results also suggest a role for immunomodulation activity originating from the dimer heme moiety in Toll-like receptor 9 activation and cytokine production perturbation.(56; 93) Hemozoin has also been shown to suppress the adaptive immune system by modulating dendritic cell function and maturation, thus allowing further evasion of the immune system. T cells which are subsequently activated by these modulated dendritic cells are characterized by decreased proliferation and effector functions. This modulation of adaptive immune system activation may contribute to infection seen in malaria-endemic areas.(94) Thus, parasitic survival strategy involves native hemozoin modulation of the host immune system on multiple fronts, innate and adaptive, ensuring parasitic success throughout the centuries despite host adaptations. Continued efforts to elucidate the exact mechanism behind these immunomodulations are critical for the development of new approaches to fighting this disease.

Future Work

Though the degradation of BH was inhibited by the pretreatment with HNE, this is not the only lipid peroxidation product found associated with native Hz. It is not even the only lipid peroxidation product shown to inhibit oxidative burst. As a result, it would interesting to continue the degradation assays by flow cytometry to assess the effect of a range of these lipid peroxidation products on the stability of BH inside macrophage cells. Even more interesting would be the pre-treatment of the macrophage cells with the BH/ghost incubation supernatant that contains the entire range of lipid production products that BH is capable of producing. By using this supernatant, which would most closely resemble the make up of lipid peroxidation products seen associated with native Hz, this would allow the fate of BH to be investigated in the most biologically relevant context.

CHAPTER III

PROTEIN KINASE C ADDUCTION AND MODULATION BY 4-HYDROXY-2-NONENAL

Statement of Effort

This project was the collaborative effort of Dr. Clare Kenny Carney and me. The undertaking to study the HNE adducts formation on PKC and the resulting functional consequences had two distinct halves – the identification of HNE adducts and the exploration of PKC functions as a result. My goal was to determine how the formation of HNE adducts on PKC including the immediate and downstream effects of PMA activation such as translocation of PKC from the cytosol to the plasma membrane and a flux in intracellular calcium levels. I also aimed to study the location of the HNE adducts in relation to the proteins tertiary structure by building and analyzing a PKC homology model. The complimentary effort of identifying the location of the HNE adducts by mass spec was performed by my colleague Dr. Clare Kenny Carney.

Introduction

The protein kinase C (PKC) family is a group of 12 distinct isoforms of ser/thr kinases found throughout a wide range of cell types. Each isoform is categorized into three classes based on structural homology and cofactor dependence; however, there is growing evidence that individual isoforms display specificity in regulating distinct cellular events.(95) Although the three PKC classes have structural differences, they all contain and a regulatory N-terminal domain, where structural differences are found, and a conserved catalytic C-terminal domain. (22) The regulatory domain of classical PKCs (PKCα, β_I, β_{II}, and γ) contain a C1 and C2 subdomain which bind phorbol ester/diacylglycerol (DAG) and Ca^{2+} respectively.(22) The regulatory domain of the novel PKCs (PKCδ, ε, η, and θ) is similar but is Ca^{2+} independent as it does not contain a Ca^{2+} binding site. In contrast, the regulatory domain of atypical PKCs (PKCζ,ι, and μ) have a structurally different C1 subdomain and lack a C2 subdomain altogether rendering them independent of phorbol ester, diacylgylercol and Ca^{2+}.(22) Despite the structural diversity of each class, most PKCs utlize two zinc-fingers within the C1 domain (except ζ which only contains one.)[11] Each of these zinc-fingers lies within one of the conserved Cys domains, which together makes up a 50 amino acid highly homologous stretch of the regulatory domain.(96) Within this domain, there are 6 conserved cysteine residues and 2 conserved histidine residues which tetrahedrally coordinate two Zn^{2+} ions.(96) The unique structural characteristics of PKC are integral in its activation and translocation.

Activation of classic PKCs is a multistep process that begins when PKC is activated by Ca^{2+} and phospholipid resulting in the translocation of the enzyme to the inner cell membrane.(97) The membrane-bound protein is then further activated by the secondary messenger, diacylglycerol or tumor promoting phorbol esters.(98) Previous studies have focused on the importance of the zinc-finger motifs in the activation of PKC by diacylglycerol or phorbol esters.(96) In particular, Korichneva et al. have shown that during the activation of PKC, there is a conformational change that results in the release of the chelated Zn^{2+} ions from the zinc fingers.(96) The conformational change that occurs upon ligation of DAG or phorbol ester promotes insertion of a portion of PKC to be inserted into the lipid bilayer ultimately removeing the pseudosubstrate domain from the active site of the enzyme.(97; 98) The removal of the pseudosubstrate exposes the active site and allows subsequent phorsphorylation of substrate Ser or Thr residues.(97)

PKCs have been shown to regulate various cellular processes that range from mitogenesis, cell adhesion, apoptosis, angiogenesis, invasion, to metastatis. (95) The variable regulation of each isoform has been associated with cardiomyopathy, heart failure, diabetic cardiovascular complications, cancer as well as a variety of immune dysfunctions.(99). Specifically, $PKC_{\beta II}$ contributes to superoxide formation through the activation of NADPH oxidase, resulting in respiratory burst in macrophage cells.(22; 99). Similarly, PKC_{ε} has been associated with macrophage signaling events as a result of LPS or GM-CSF, phagocytosis, and NO production.(22; 96; 100; 101) The wide range of functions specific to different PKC isoforms has been associated largely with the subcellular localization of enzyme, rather than substrate specificity.

The diversity of PKC function has made it a central component in a wide range of pathologies, making it an intriguing target for drug development. Though there are a variety of inhibitors such as strausporin that inhibit through ATP binding site competition, these are not very specific for PKCs with respect to other kinases. In the development of PKC specific inhibitors, a large number of compounds which showed this desired specificity worked through a mechanism that involved the formation of PKC adducts. These type of inhibitors usually function through a modification of protein cysteine residues and fall into two categories: those that target the catalytic domain, and those that target the regulatory domain. Inhibitors that target the catalytic domain have been shown to inhibit kinase activity through a variety of mechanisms including S-cysteinylation, S-thiolation, S-cysteaminylation, and alkylation of cysteine residues in either the active site or at a critical Cys452 switch.(100; 102-104) The distinctive structure of PKC, with its regulatory domain that is unique among other kinases, has shifted the focus of inhibitor development from the catalytic domain to this uncommon regulatory domain. These inhibitors typically result in the loss of phorbol ester binding. One class of compounds inhibits in the regulatory domain by a "cage type" mechanism. These compounds, which includes calphostin C and hypericin, bind to a Ca^{2+}-induced hydrophobic site, then a light reaction results in the production of reactive oxygen species which selectively modify oxidation susceptible amino acides in the vicinity.(97; 105) Interestingly, selenocompounds have been shown to inhibit PKC through both the catalytic domain (at low concentrations), as well as through further modification in the regulatory domain (at higher concentrations).(96; 101; 106) The mechanism of inhibition in the regulatory domain is believed to involve the collapse of the critical zinc fingers found in the cys-domains as a result of modification of the zinc-coordinating cysteine residues.(96; 101; 106) Though inhibiting PKC through adduct formation has been a focus for to combat the pathology associated with inappropriate PKC activitivation, in proper PKC adduct formation *in vivo* has been implicated in many of the pathologies associated with oxidative stress.

4-hydroxynonenal, a major product of lipid peroxidation, has also been connected to a number of oxidative-stress linked cellular activities, including growth inhibition and apoptosis.(107) HNE has also been implicated in the pathology of conditions such as cancer, arthritis, arthrosclerosis, cardiac disease, malaria, and neurological diseases such as Alzheimer's disease.(90; 108-110) HNE, a highly reactive aldehyde, forms shift base adducts to protein thiol and amino groups, often modulating their activity (**Figure 36**).(111) High levels of HNE in macrophage cells have been associated with the inhibition of oxidative burst, the mechanism of reactive oxygen species (ROS) production crucial to the destruction of phagocytosed material. *Schwarzer et al*. have shown exposure of monocytes to HNE at concentration of 10-100 μM resulted in the formation of a PKC-HNE complex and a corresponding loss of PKC activity. (109)

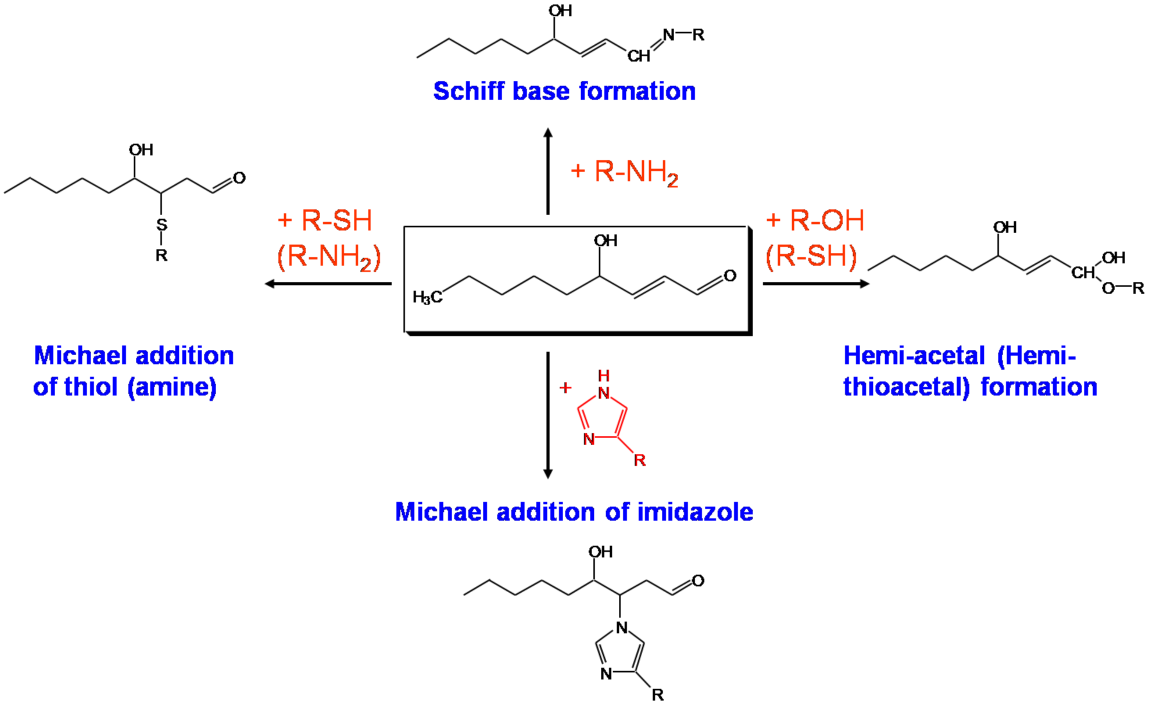

Figure 36. HNE reactivity with Amino Acid Sidechains. HNE is a reactive electrophile that can readily form adducts on cysteines, lysines and histadines.

While there are potentially several proteins whose function may be affected by HNE adduction, the connection between increased levels of HNE and decreased PKC activity provides an intriguing initial target. Given that there is little information available about the structure of PKC, elucidating the specific amino acids targeted by HNE using mass spectrometry in conjunction with biochemical experiments exploring the functional consequences of these adducts will yield important clues about the structure and function of this enzyme and its mechanism of inactivation.

Materials and Methods

Materials

Protein kinase C βII, human recombinant (PKC βII), 4-hydroxy-2-nonenal (HNE), phorbol-12-myristate-13-acetate (PMA), and polyclonal anti-PKC antibodies were purchased from Calbiochem. Novex 10% Tris-glycine gels were purchased from Invitrogen. Luminol (3-aminophthalhydrazide) and dithiolthreitol (DTT) were obtained from Sigma-Aldrich. Monoclonal anti-HNE antibodies were purchased from Oxis Research. Sequencing grade modified bovine trypsin was obtained from Promega. Iodoacetamide (IAA) was obtained from Acros Chemicals. Fetal bovine serum was purchased from Atlanta Biologicals. Penicillin/streptomycin was purchased from Cellgro mediatech. Oregeon Green Calcium-indicating dye was obtained from Invitrogen. The mouse macrophage cell line, RAW 264.7, originally obtained from the American Type Culture Collection (ATCC TIB-71) was a kind gift from the Virginia Shepherd lab (Vanderbilt University). All Uv-vis spectroscopy was caried out on a Bio-tek Synergy HT Multidetection Microplate Reader. Luminescent measurements were performed on a Moonlight 3010 Luminometer. An Invitrogen Xcell Surelock™ complete mini-vertical electrophoresis system was used for all gel electrophoresis and western blotting studies. Confocal studies were performed on a Zeiss LSM 510 Meta inverted confocal microscope. Liquid chromatography mass spectrometry (LC-MS-MS) was performed on a Thermofinigan LTQ LC-MS-MS system equipped with Xcalibur 1.3 and Bioworks 3.1 software.

Cell Culture

The adherent mouse macrophage cell line, RAW 264.7, was maintained in continuous culture with RPMI 1640 medium (GIBCO/BRL), supplemented with 10 % (v/v) heat-inactivated fetal bovine serum, and 100 μg/mL penicillin/streptomycin (complete medium) in an atmosphere of 95% humidity and 5% CO2 at 37^{o}C. Cell viability was determined by Trypan Blue exclusion using a haemocytometer.

Measurement of Reactive oxygen species.

RAW 264.7 cells were plated overnight in complete RPMI 1640 medium at 4E6 cells/well in a 6 well plate. The following day, the media was removed and the cells were washed one time with PBS followed by treatment with HNE (0-50 µM) prepared in cold medium. After 3 hours in 95% humidity and 5% CO2 at 37^o C, the supernatant was aspirated and oxidative burst was stimulated by the addition of 100 nM PMA prepared in PBS. After four minutes of stimulation, 950 µL of the supernatant was pipeted to a luminometer tube followed by the addition of 50 µL of 1.0 mM luminol (50 µM final). Luminescence was measured for ten seconds using a Moonlight 3010 Luminometer.

Cell treatment with HNE for western blot analysis.

RAW 264.7 mouse macrophage cells were plated overnight at a density of 4E6 cells per 100 mm dish. The following day, the cells were treated with 10 mL of 35 µM HNE prepared in media and incubated at 37 oC, 95% humidity and 5% CO_2. Once the allotted time (0, 0.5, 1.0, 1.5, 2.0, 2.5, and 3.0 hours) had passed, the samples were removed from the incubator, washed with 3 times with cold PBS, and treated with 400 µL of cold lysis buffer (25 mM Tris-HCl, pH 7.4, 0.25 mM sucrose, 2.5 mM EDTA, 2.5 mM DTT). After five minutes of rapid agitation, the samples were scrapped, pipetted to microcentrofuge tubes, and gently sonicated with a probe sonicator. Next, the samples were centrifuged for 45 minutes at 13,200 RPM. The supernatant was collected and protein content was analyzed using the Biorad DC assay kit.

Western blot analysis.

All samples examined by gel electrophoresis/western blotting, were prepared at a 2 μg/μL concentration and run on Novex 10 % Tris-glycine gels (Invitrogen) followed by transfer to polyvinylidene difluoride (PVDF) membranes (Invitrogen). After complete transfer, the membranes were blocked for 1 hour or overnight with 5 % nonfat dry milk dissolved in Tris-Tween buffer (TBST) composed of 25 mM Tris-HCl, pH 7.4, with 137 mM NaCl, 2.7 mM KCl, and 0.01 % Tween 20, TBST. PKC obtained from the cells was detected by incubation with rabbit polyclonal anti-protein kinase C(α/β) (371-388) antibodies (diluted 1: 230 in 5% nonfat dry milk) for 2 hours at room temperature. Standard PKC βII was detected by incubation with rabbit polyclonal anti-PKC βII primary antibody (diluted 1:100 in 5 % nonfat dry milk) for 2 hours at room temperature. For both, incubation with the primary was followed by TBST washing and incubation with a horseradish peroxidase-conjugated goat anti-rabbit secondary antibody (diluted 1:2000 in 5 % nonfat dry milk) for 1 hour at room temperature. HNE adducted proteins were detected by incubation with mouse monoclonal anti-HNE primary antibody (diluted 1:500 in 5 % nonfat dry milk) for 2 hours at room temperature, followed by incubation with a horseradish peroxidase-conjugated goat anti-mouse secondary antibody (diluted 1:2000 in 5 % nonfat dry milk) for 1 hour at room temperature. An ECL Western blotting analysis detection system (Amersham Biosciencees) was used to visualize the bands in all cases.

Cell treatment with HNE for confocal microscopy.

For all samples, RAW 264.7 mouse macrophage cells were plated overnight at a density of 5E4 cells per Mat-tek dish. The following day, the cells were treated with either 100 μL of 35 μM HNE prepared in media or left untreated and incubated at 37°C, 95% humidity and 5% CO_2. After 3 hours, the cells were washed 3 times with PBS and activated by the addition of 100 μL of 100 nM PMA. After 30 seconds, the samples were quickly washed 3 times with PBS. Next, the cells were fixed in 3.7% paraformaldehyde at 37°C, 95% humidity and 5% CO_2. After 10 minutes, the samples were rinsed twice with PBS and permiabilized by treatment with 0.2% Triton X-100 for ten minutes at room temperature. After 3 washes with PBS, the samples were blocked with 2% BSA 1 hour at 4°C. Next, The cells were labeled with anti-PKC primary antibodies (1:500 dilution), followed by 10 nM 525 nm quantum dot conjugated goat anti-mouse secondary antibodies. After labeling, samples were washed twice with PBS, covered with 2 mL of fresh PBS and immediately imaged on the Zeiss LSM 510 Meta inverted confocal microscope. Fluorescence imaging of PKC was accomplished by excitation at 488 nm, followed by collection using a long-pass filter 505 nm.

Reaction of PKC with HNE.

For these experiments the βII isozyme was chosen as it is most closely linked with oxidative burst. PKC βII (20 µg, 0.37 mg/mL shipped in 20 mM HEPES, pH 7.5, 2 mM EDTA, 2 mM EGTA, 5 mM DTT, 100 mM NaCl, 0.05 % TRITON® X-100, 50 % glycerol) was diluted to 400 µL with 20 mM Tris- HCl buffer, pH 7.4 and transferred to a Millipore Ultra free spin filter (MWCO 10 kDa). The samples were centrifuged at 3500 g for 12 minutes followed by removal of the eluent and addition of 200 µL of Tris-HCl buffer and recentrifugation. This cycle was repeated 4 times to remove glycerol and exchange buffer systems. The sample was then concentrated to a volume of 30 µL and treated with either 1 µL ethanol or 1 µL of 7.4 mM HNE prepared in ethanol (30:1 HNE:protein). After 3 hours at 37 oC, the samples were washed with 10% ethanol to remove unreacted HNE. Subsequently, samples for gel analysis were washed 3 times with 200 µL of Tris buffer. Samples to be digested were reduced by the addition of 100 mM sodium borohydride for 10 minutes followed by 3 washes with 200 µL of AMBIC buffer (50 mM ammonium bicarbonate, pH 8.0) to obtain the correct pH for tryptic digestion. Formation of the HNE adduct on recombinant PKC βII was confirmed using western blotting techniques (**Figure 37**).

Reaction of PKC with PMA followed by HNE.

The buffer exchanged PKC βII was diluted up to 400 µL in Tris-HCl, pH 7.4, containing 10 µM CaCl2, and 50 nM PMA and incubated for 5 minutes at 37 oC. The sample was then concentrated to 30 µL and a 30 fold excess of HNE was added. The reaction was incubated at 37 oC for 3 hours and prepared for tryptic digestion as described above. Formation of the HNE adduct on recombinant PKC βII was confirmed using western blotting techniques (**Figure 37**).

Protein Digestion.

PKC βII, PKC βII reacted with HNE, and PKC βII reacted with PMA followed by HNE were concentrated to a volume of 30 uL containing approximately 10 µg of protein. To these samples, 45 mM dithiothreitol (1/10 v/v) was added followed by a 20 minute incubation at 60 oC. Next, 100 mM iodoacetamide (IAA) was added (1/10 v/v) and the samples were incubated in the dark for 10 minutes followed by the addition of sequencing grade modified bovine trypsin at a ratio of 1:50 protease:protein (w/w). The reactions were incubated overnight at 37 oC and stopped by the addition of 1 µL formic acid.

Mass Spectrometry.

Liquid chromotrography-mass-spectrometry (LC-MS) and LC tandem MS (LC-MS-MS) were used to analyze digested PKC βII, PKC βII reacted with HNE and PKC βII reacted with PMA followed by HNE. LC-MS with data dependent scanning and LC-MS-MS analyses were performed on a Thermofinnigan LTQ ion trap mass spectrometer equipped with the NanoSpray source and using positive ESI and flow injection in acetonitrile/water (50:50 v/v) with 0.1% formic acid at a flow rate of 700 nL/min. The column is a packed tip, 100 µm X 11 cm, packed with Monitor C18 (Column Engineering), 5µm, 100 angstrom. The PKC βII, PKC βII reacted with HNE, and PKC βII reacted with PMA followed by HNE adducts were subsequently detected and confirmed using the protein database search software SEQUEST (112) and the P-Mod (113) algorithm for ion series-based identification of MS-MS spectra corresponding to modified PKC βII sequences.

PKC Homology Model

Homology model of murine $PKC_{\beta I}$ catalytic domain (residues 402 to 665) was generated using the PHYRE server using the sequence of $PKC_{\beta I}$ as a starting model (accession number MP_032881.1). Electrostatic values were assigned using PQR server with the AMBER calculations.

Imaging of Ca^{2+} Flux by Confocal Microscopy

For all samples, RAW 264.7 mouse macrophage cells were plated overnight at a density of 5E4 cells per Mat-tek dish. The following day, the cells were treated with either 100 µL of 35 µM HNE prepared in media or left untreated and incubated at 37°C, 95% humidity and 5% CO_2. After 3 hours, the cells were washed 3 times with PBS and treated with 1 nM Oregon Green Ca^{2+} sensitive dye diluted in complete RPMI media and incubated at 37°C, 95% humidity and 5% CO_2 for 1 hr. The samples were then quickly washed 3 times with PBS. The samples were then imaged pre-activated on the Zeiss LSM 510 Meta inverted confocal microscope, exciting with a 488 argon laser and collecting emissions using a 505 long pass filter. The samples were then activated by the addition of 100 nM PMA. Fifteen minutes after activation, the samples were imaged again using the same settings, keeping the detector gain consistent between samples. .

Results

Effect of HNE on reactive oxygen species production and formation of HNE adducts

The ability of HNE to modulate the activity of NADPH oxidase was examined. RAW cells incubated with HNE for 3 hours followed by stimulation with PMA demonstrated a concentration dependent inhibition of oxidative burst (**Figure 38A**) with an EC_{50} value of 18.4 ± 1.2 µM. Further, RAW mouse macrophage cells were treated with 35 µM HNE and analyzed from 0-3 hours (**Figure 38B**). Studies of HNE inhibition of superoxide in human neutrophils have

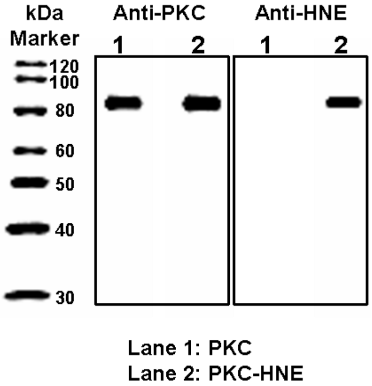

Figure 37. Western blot analysis of HNE modified PKC from cell lysates. Western blot analysis was used to visualize PKC bands with monoclonal anti-protein kinase c antibodies (A). Additionally, HNE adduct formation on PKC was visualized with monoclonal anti-HNE antibodies (B).

shown a similar response with an EC_{50} value of 27 µM (114). These results suggest that HNE is able to inhibit stimulation of oxidative burst in a concentration dependent manner but do not highlight the loci of the molecular mechanism behind such inhibition. Previous reports have demonstrated that at concentrations over 10 µM, HNE is capable of inhibiting the activity of PKC (80kDa (115).

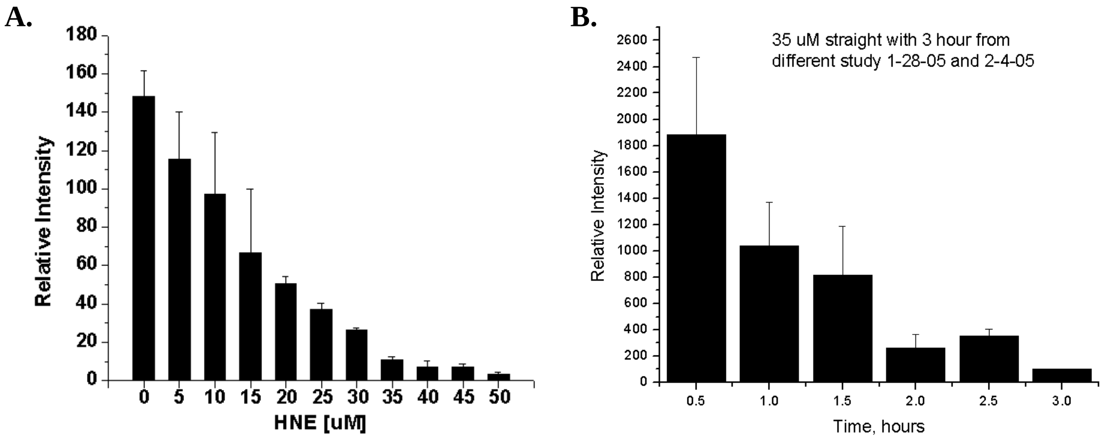

35 uM straight with 3 hour from different study 1-28-05 and 2-4-05

Figure 38. Effect of HNE treatment on oxidative burst in RAW cells. A. Inhibition of ROS production with increasing concentrations of HNE as assessed by luminol enhanced chemiluminescence. B. Inhibition of ROS production with 35 µM HNE over time as assessed by luminol enhanced chemiluminescence.

To examine the possibility of HNE forming adducts on PKC, cell lysates from samples treated with 35 µM HNE were examined by western blot analysis. The amount of cytosolic PKC obtained from the cell lysates remains fairly consistent from 0 to 3 hours (**Figure 39**). However, the HNE bands, absent at 0 hour, slowly begin to increase in concentration with time, suggesting increased adduct formation with time. This time dependent formation has been seen before with HNE adduction on myoglobin (116). While western blot analysis detected the adduction of HNE to PKC, it is unable to elucidate the affect of this adduct on PKC function.

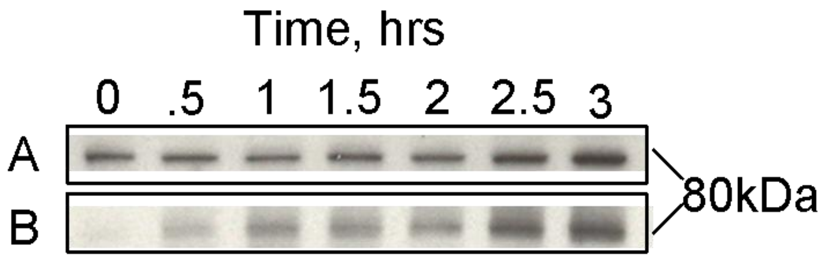

Figure 39. Effect of HNE treatment on PKC translocation. PKC bands visualized with monoclonal anti-protein kinase c antibodies (A). HNE adduct formation on PKC visualized with monoclonal anti-HNE antibodies (B). The translocation of PKC from the cytosol to the membrane was monitored simultaneously with the appearance of HNE adducts on the protein. It was found that the amount of cytosolic PKC remainded consistent (A) as the HNE adducts formed.(B).

Mapping the loci of HNE adduction

The classic PKC isoforms (α, -βI/βII and γ) are the most closely correlated with macrophage oxidative burst. Protein kinase $C_{\beta II}$, in particular, is closely linked to oxidative burst. For this reason, it was selected as the isoform. To avoid the potential contamination of the protein with other cellular component, standard recombinant $PKC_{\beta II}$ protein was used. Mass spectrometry was utilized to determine the specific amino acid site(s) of HNE adduction. PKC βII (control), PKC βII reacted with HNE, and PKC βII reacted with PMA and

Peptide	Modification	Percursor Observed	Precursor Calculated	Amino Acid Modified
LDNVMLDSEGHIK	unmodified	735.9	735.9	His 479
469-481	HNE	814.9	814.9	
EHAFFR	unmodified	403.6	403.7	His 597
596-601	HNE	482.8	482.8	
EAVAICK	unmodified	733.5*	733.4*	Cys 572 or
567-573	HNE	891.5*	891.5*	Lys 573
RLGCGPEGER	unmodified	NO	537.3	Cys 586
583-592	HNE	616.3	616.3	
NVHEVK	unmodified	725.4*	725.4*	His 30
30-35	HNE	883.5*	883.5*	

* indicates [M+1H] instead of [M +2H], NO: Not Observed

Table 1. Unmodified and HNE-modified PKC peptides observed by LC/MS/MS after tryptic digestion.

then HNE were tryptically digested for LC-MS-MS. These peptides were analyzed using LC-MS data dependent scanning and LC-MS-MS on a Thermofinnigan LTQ system. Adducts were subsequently detected and confirmed using the database search software Sequest (112) and the P-Mod algorithm (113) for ion series-based identification of MS-MS spectra corresponding to modified PKC sequences . While analysis of the mass spectral data with Sequest confirmed protein digested fragments and some HNE adduction sites, P-Mod allowed for a more in depth analysis of protein modifications and revealed 5 potential sites of adduction for the HNE treated unstimulated PKC (**Table 1**). Adducts to His32, His479, His597, Cys572, and Cys586 were all found to have mass additions consistent with HNE adduction via Michael addition. Activation of the enzyme with PMA (in the presence of Ca2+) before HNE treatment resulted in the formation of the same adduct pattern with the exception of His 479 where no adduction was found. Sodium borohydride reduction of the protein prior to trypsin treatment was performed in an attempt to stabilize potential lysine/HNE Schiff base adducts for subsequent detection, but no lysine modifications were observed in these samples (**Table 1**).

Tandem mass spectrometry of the HNE modified peptides gave conclusive data concerning the specific amino acids to which HNE had adducted (**Figures 46-50**). Mass addition of 158 m/z has been shown to represent the presence of a Michael addition of reduced HNE to a peptide. In the tandem MS/MS spectra, a series of b and y ions that correspond to cleavages along the peptide backbone are observed. The b series results from N-terminal backbone cleavages and the y series ions reflect the C-terminal peptide backbone cleavages. After identification of peptides that may be targeted by HNE adduction, a targeted ion scan of the adducted precursor peptide was generated. Trapping these ions followed by tandem MS/MS fragmentation allowed for multiple scans of the same peptide and therefore averaged b and y ion spectra. Figures 46-50 illustrate the b and y ion traces of the HNE modified peptides, while figures 51-54 illustrate the b and y traces of the native peptides. Finally, figures 55-58 illustrate the b and y traces of sample stimulated with PMA prior to HNE treatment. Figures 46-58 can be found at the end of this chapter. The formation of modified secondary ions (a ions), b ions with loss of H_2O or NH_3 further supports the evidence of peptide modification. Tables 2-6 which contain all observed secondary ion can be found in at the end of this chapter.

Figure 46 shows the LC-MS/MS spectra for the tryptic peptide NVHEVK (residues 30-35) the HNE modified protein (spectra for unmodified **Figure 51**). A conclusive b and y ion fragmentation pattern exists for a Michael adduct on His 32 of this peptide. Compared to the control peptide, most notable is the 158 increase in both the b 3 and the y 4 ion in the HNE modified peptide. Daughter b and y ions upstream from the addition site show consistent 158 increases in mass (including b4 and b5). Based upon the characteristic 158 increase in relevant fragmentation ions, it was concluded the HNE reacted with the imidazole group of His32 to form a Michael adduct. Similar examination of the LC-MS/MS spectra of the HNE modified RLGCGPEGER peptide (residues 583-592) revealed the presence of an HNE Michael addition at Cys 586 (**Figure 47,** PMA activated **Figure 55**). Here, increases of m/z 158 beginning at y7 (b ion at the site not seen) are clear in the aldehyde-modified peptide. Ions upstream of the adduction site show 158 mass unit increases as well, including b5-b9, y8 and y9 indicating Michael addition of HNE to the thiol group of Cys586 forming a Michael adduct. For the modified peptide EHAFFR (residues 596-601), LC-MS/MS reveals a fragmentation pattern consistent with a Michael adduct on His597 **(Figure 48**, spectra for unmodified **Figure 52**, PMA activated **Figure 56)**. Compared with the control peptide, both b2 and y5 ions in the HNE modified peptide show mass increases of 158 with daughter b ions (b3-b5) upstream from the addition site also showing 158 increases in mass. Together these results indicate HNE reacting with the imidazole group of the H597 to form a Michael adduct. The LC-MS/MS spectra (**Figure 49**, spectra for unmodified **Figure 53**, PMA activated **Figure 57**) of the HNE modified LDNVMLDSEGHIK peptide (residues 469-481) contains a mass addition of m/z 158 beginning at the b11 and y3 ions and continuing with upstream ions b12 and y4-y11 indicative of a Michael addition at His479. The LC-MS/MS spectra (**Figure 50**, spectra for unmodified **Figure 54**, PMA activated **Figure 58**) of the modified peptide EAVAICK (residues 567-573) reveals a fragmentation pattern consistent with either a Michael addition on C572 or K573. Increase of m/z 158 beginning at b6 and y2 are seen in the HNE modified peptide as compared to the control. However, the mass of the b6 ion also corresponds to modified y6 with loss of NH_3, making it difficult to determine whether or not the adduct is on the cysteine or the lysine specifically. Ions upstream of the adduction site show 158 mass unit increases as well, including y2-6. Again, without the presence of y1 (modified or unmodified), a conclusive identification of adduction site can not be determined. However, the presence of modified b6 with loss of water (727.41) does indicate that the adduct is most likely resides on the cysteine residue, although no conclusion can be at this time.

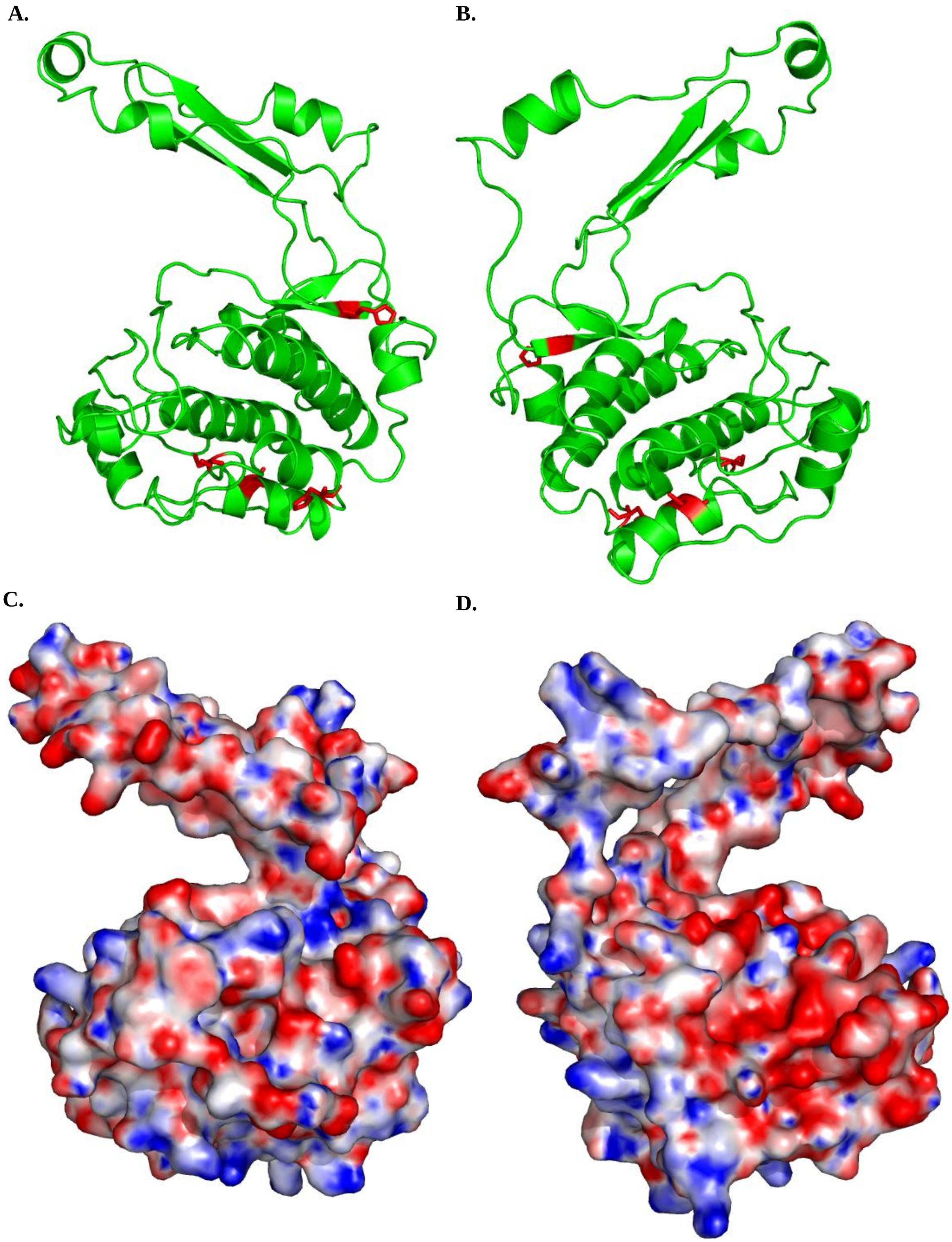

Figure 40. Homology model of HNE adduction sites on PKCβI with hydrostatic surface. Ribbon views of PKC$_{\beta I}$ homology models with the HNE adduction sites (red) show that they are largely congregated on the lower side of the catalytic domain with the exception of H479 (A and B). Further analysis of the hydrostatic surface reveals that the adducts are in a region of low charge density.

PKC Homology Mapping of HNE adducts

Though the crystal structure of PKC$_{\beta II}$ has not been determined, the crystal structures of several members of the protein kinase C family have been constructed. The high levels of homology, 90% between the classical type of PKC members makes the crystal structure of PKC$_{\beta I}$ a valid structure for comparison to study the location of the HNE adducts on tertiary structure of PKC$_{\beta II}$.(117) Not surprisingly, the homology structures showed that the majority of the adducted residues were located near the surface of protein (**Figure 40**). It also showed that the four sites of adductions were located along the same region of the protein. This region of the protein is largely solvent assessable and has an overall low charge density. His597 and C572 are found to be located in two helix structures.

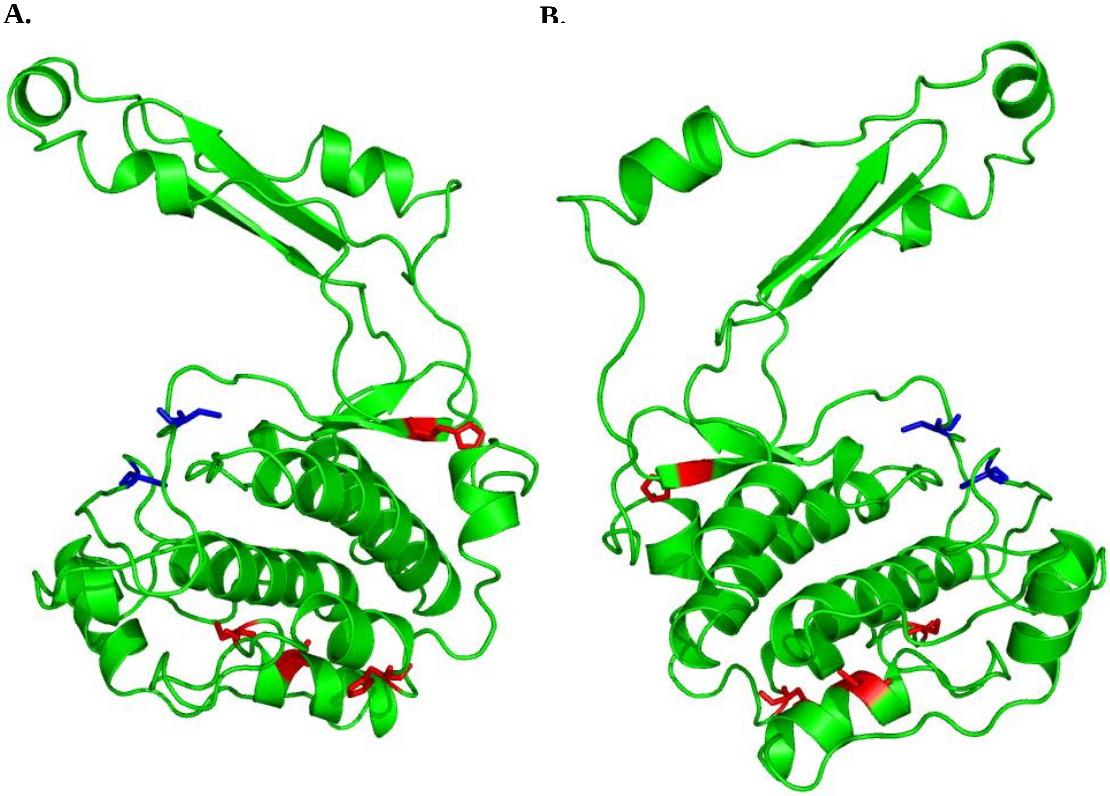

Figure 41. Homology model of HNE adduction sites and adduction sites of other PKC inhibitors on PKC$_{\beta I}$. The addition of C502 and C488 (blue) to the homology model shows that these residues, which are the adduction sites of active-site targeting inhibitors, is located in a different domain than the HNE adduction sites (red).

The addition of the HNE adduct could feasibly lead to the disruption of hydrogen bonding within these helices. By contrast, two residues, C502 and C488, not adducted by HNE but often seen adducted by other inhibitors, specifically active site targeting inhibitors, are located on at a different point on the surface of the catalytic domain (**Figure 41**). This region of the domain surface has a higher negative charge density than the location of our HNE adducts. Further , when the active site residues of the catalytic domain were also ploted on the homology model, C502 and C488 are found to be near the catalytic active site (**Figure 42**). By contrast, the HNE adduction sites are located on the other side of the catalytic domain from the active site.

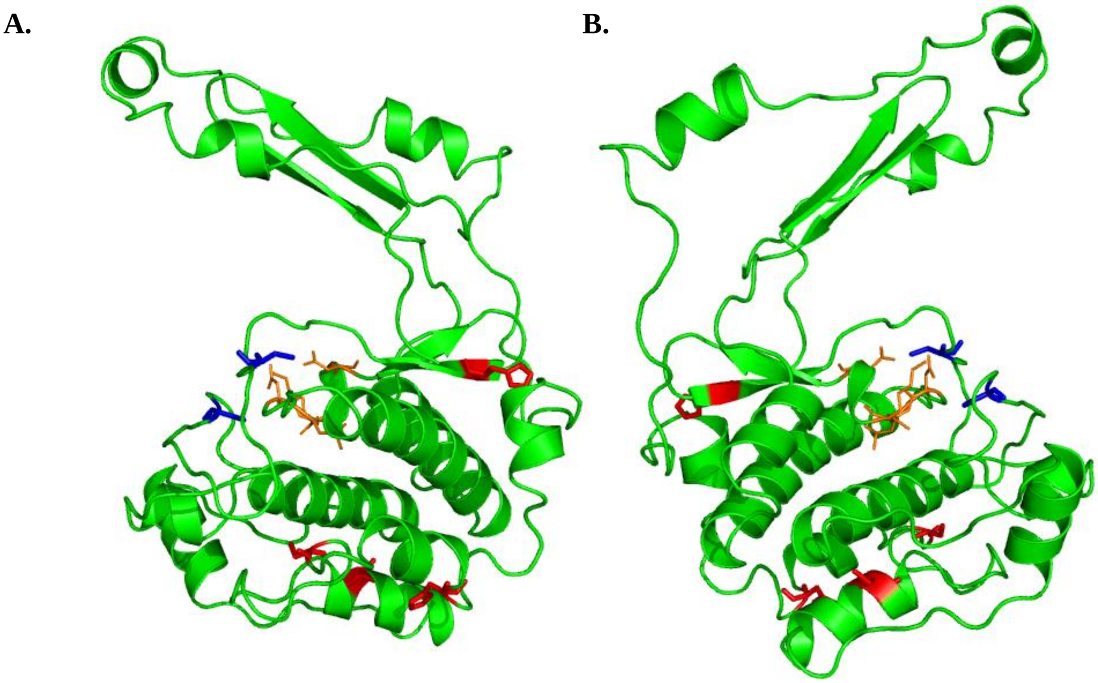

Figure 42. Homology model of HNE adduction, Active site targeting inhibitor adduction, and active site residues on PKC$_{\beta I}$. When the active site residues are highlight (orange), it is evident that residues C502 and C488 (blue) are near the active site, as expected for the adduction sites of active-site targeting inhibitors. The HNE adduction sites (red), however, are not located near the active site suggesting their mode of inhibition is not related to inhibition of the active site.

Effect of HNE adduction on PKC function

To investigate the effect of HNE adduction on PKC function, two aspects of the activation of PKC were investigated: protein translocation and Ca^{2+} influx. A critical step in proper PKC activation is the translocation of the cytosolic form of the protein to the membrane.(117) The effect of HNE on PKC translocation was examined by confocal microscopy. Anti-PKC antibodies were used to image the subcellular location of the protein prior to and following PMA activation. Before PMA activation, PKC is seen principally in the cytosol for all samples (**Figure 43**).

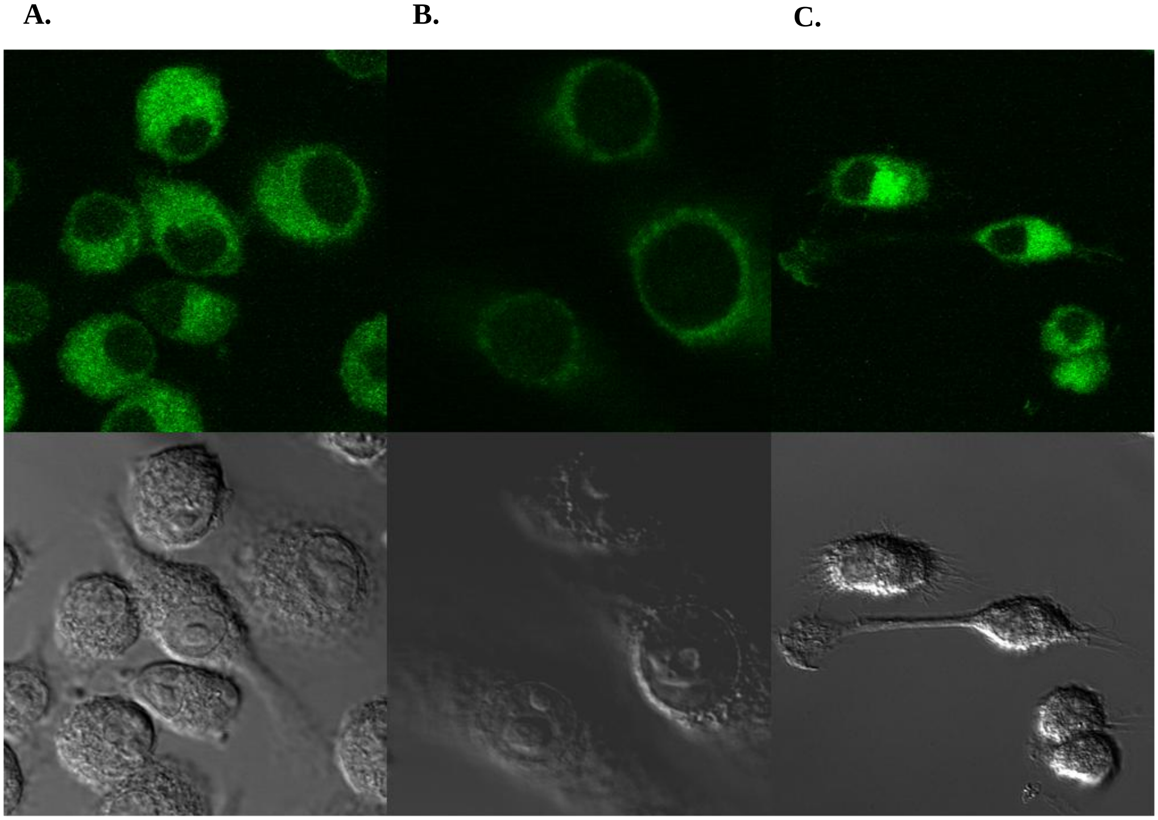

Figure 43. Confocal analysis of PKC translocation. A) Untreated RAW cell samples were fixed with paraformadlehyde and labeled with Anti-PKC primary antibodies, followed by 525 quantum dot conjugate secondary antibodies. The samples should display a large distribution of PKC throughout the cytosol of the cell. B.) Cells which were activated with PMA were fixed and labeled similar to the untreated samples. However, in these samples, it is evident that the PKC has now translocated and is concentrated at the plasma membrane of the cells. C.) However, cells that were treated with 35 μM prior to PMA activation did not demonstrate the same translocation seen in PMA activation alone. Instead, the PKC remained distributed throughout the cytosol as seen in the untreated samples. This indicated HNE treatment resulted in a dysfunction of PKC which inhibited its translocation upon phorbol activation.

Following PMA activation, cells that were not treated with HNE demonstrated rapid translocation of PKC from the cytosol to the plasma membrane in a manner consistent with previous reports. In contrast, cells treated with HNE prior to PMA activation did not show translocation, but rather remain diffused throughout the cytosol (**Figure 43**). These images provide evidence that the adduction of HNE to PKC has serious deleterious consequences on the protein function. In order to begin to elucidate potential mechanisms through which HNE exerts these effects, the region(s) of the protein being modified must first be determined. Though the above experiments were able to successfully demonstrate both the presence of HNE adducts and potential ramifications, , the data does not yield the specific location nor the number of adducts present on PKC.

Further downstream affects of HNE adduction were also investigated to assess the extent of PKC activation, specifically an increase in intracellular calcium levels within in the cell. When PKC is properly activated by PMA, the PMA receptors are stimulated leading to the activation of PKC coupled with phospolipase C.(117) This activation leads to the formation of 1,2-diacylglycerol (DAG) and increased intracellular Ca^{2+} levels due to its release from inositol 1,4,5-triphosphate-sensitive Ca^{2+} stores. Confocal microscopy was used to study the effect of treatment with HNE on the extent of intracellular Ca^{2+} flux after activation with PMA. To do this, samples were treated with a calcium specific dye, Oregon Green, and the extent of fluorescence was correlated to the amount of calcium present in a particular cell (**Figure 44**). In control cells which had been activated with PMA, there is a distinct increase in fluorescent signal from the Oregan Green Calcium sensitive dye, corresponding to an increase in intracellular calcium. However, when previously treated with 35 µM HNE for three hours, treatment with PMA does not elicit similar increases in fluorescence. This indicates that the treatment with HNE in disrupting the ability of PMA to activate the RAW cells in a way which results in the inhibition of Ca^{2+} influx. This inhibition is likely the result of HNE adduction to PKC resulting in the inability

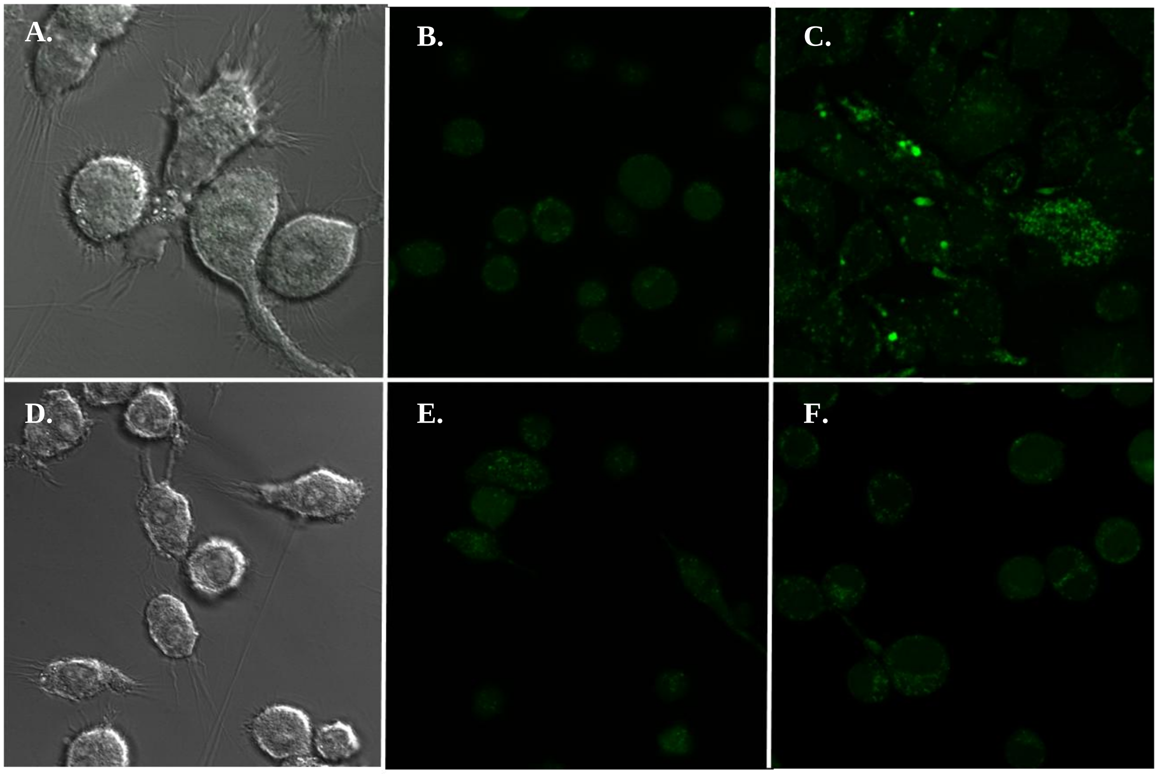

Figure 44. Confocal images of Ca2+ flux in RAW cells. Untreated control (A) and HNE treated (D) RAW cells gave no fluorescent signal as a result of auto fluorescence. When the control (B) and HNE treated samples (E) are treated with the calcium sensitive dye, Oregon Green, low levels of fluorescence are seen. When the control, Oregon green treated samples are activated with PMA, an increase in fluorescence is seen corresponding to an increase in intracellular calcium (C). When HNE, Oregon green treated cells are stimulated with similar levels of PMA, no increase in fluorescence is seen (F).

of the protein to be activated by PMA, which therefore fails to trigger the release of Ca^{2+}.

Discussion

Due to the variety of key roles PKC plays in cellular signaling, inhibition of this enzyme results in disturbed cellular functioning. HNE is a known mediator of oxidative stress, and its presence is capable of reducing enzymatic activity. Confocal studies showed that the presence of

HNE results in the reduction of PMA-induced PKC translocation, a key step in proper PKC activation. Mass spectrometry revealed that the majority of HNE adducts were found in the catalytic domain (H479, H597, C572, C586) and one was found in the regulatory domain (H32). The important relationship between PKC function and structure underlies the detrimental impact of HNE adduction. The impact of these specific adduct sites can not be determined from mass spec along, however, clues to their interations can be found by examining the available information on PKC activity and its inhibition.

There have been many studies looking at inhibition of the catalytic domain. For example, studies using a peptide substrate analogue (*N*-biotinyl-Arg-Arg-Arg-Cys-Leu-Arg-Arg-Leu) have shown that adduction at critical catalytic domain cysteines can have devastating functional consequences.(118) This potent peptide inhibitor is thought to work by the formation of a disulfide linkage between Cys502 (all residue numbers are based on the numbering for the βII isoform) of PKC and the cysteine residue of the analogue, an adduction which results in enzymatic inactivation. Another example of PKC inhibitors which work by forming disulfide linkages with catalytic cysteine residues are the Selenocompounds.(119; 120) Selenite and selenocystine inactivate PKC through redox reactions with catalytic site cysteine residues; it is thought specifically C386, C488, C502 and C572. Of note, C572 is also the location of one the adduction sites seen as a result of HNE treatment. While the exact role of C572 in PKC activation has not been elucidated, it is clearly a site sensitive to adduction and worthy of further investigation.

The idea of a small molecule inactivating PKC is not novel. There are several other small molecules which have been shown to shown to inactivate PKC through the formation of covalent adducts to catalytic domain cysteines. For instance, 4-hydroxytamoxifen (OH-Tam), an oxymetabolite of the chemopreventive agent tamoxifen, has been shown to irreversibly inactivate PKC *in vitro*.(121) OH-TAM works by generating a phenoxyl radical from the phenolic compound which can react with vicinal thiols, resulting in PKC inactivation. N-ethylmaleimide has been shown to inactive PKC-ε through S-cysteaminylation of Cys 386.(122) Similarly, chelerythrine, a specific PKC inhibitor, alkylates cysteine residues within the catalytic domain resulting in enzyme inactivation. This benzophenanthridine alkaloid reacts with cysteines through an electrophilic iminium carbon with the requirement of a basic residue in close proximity to fulfill the need for a lower pK_a.Cys572, one of the sites of HNE adduction, is one of only two cysteines in the catatlytic domain flanked by a basic residue. Perhaps this site is sensitive also to chelerythrine. Either way, Cys572 is a residue of interest for future studies aimed at examining which sites of HNE adduction are most important for PKC inactivation. While many inhibitors have focused on the catalytic domain, the regulatory domain is also sensitive to adduction and infactivation of PKC.

The N-terminal regulatory domain of PKC is responsible for a number of roles critical in the proper activation and regulation of the enzyme including autoinhibition by the pseudosubstrate, and translocation and activation of the enzyme by phorbol ester binding. H32, a site sensitive to HNE modification, directly flanks the pseudosubstrate region and it has been determined that any change to the pseudosubstrate sequence can render it less sensitve to phorbol activation.(122) This suggests the addition of the H32 HNE adduct could affect the binding affinity of the substrate for the catalytic active site, reducing the enzyme response to phorbol ester activation.Conversely, the additional bulk caused by the H32 adduct could limit the ability of the pseudosubstrate to be removed from the catalytic active site during conformational change resulting from activation.

Another mechanism through which modification of H32 could be detrimental to activation is interruption of PMA binding. Though H32 has not been shown to directly bind PMA, it lies near the PMA-binding site and is involved in hydrogen bond stabilization of PMA binding. However, even without inhibiting PMA binding, the H32 HNE adduct could hinder proper PMA activation through the regulatory domain. The binding of PMA has been associated with formation of a hydrophobic patch of the protein which then drives translocation of the enzyme from the cytosol to the membrane. However, studies using PMA derivatives have shown that by modulating the hydrophobicity translocation to the membrane upon PMA binding can be interrupted. It is reasonable then to postulate that the addition of an HNE adduct, which contains a carbonyl and hydroxyl group, within close proximity to the cys-rich regions responsible for PMA binding could alter the hydrophobicity of the surface. The result then would be an impaired ability to evoke protein translocation. Intriguingly this would allow a mechanism by which HNE could cripple PKC function without direct interaction with the catalytic site.

The construction of a PKC homology model of the $PKC_{\beta I}$ catalytic domain to explore the location of the several of the HNE adducts with respect to the tertiary structure of the domain. Despite the lack of a cystral structure for $PKC_{\beta II,}$, the high level of homology between the classic PKC isoforms makes it possible to explore the local environment of the residues which are adducted by HNE within the context of the protein structure. In the catalytic domain, there were four residues which were found to have HNE adducts, H479, H597, C572, and C586. Of these residues, two of them in particular, C572 and H579, are found to be located within a series of helices (**Figure 45**). The close proximity of these four helices would imply that an extensive amount of hydrogen bonding, both inter and intra-helix. It could be easily hypothesized that the bulky HNE adducts could disrupt the hydrogen bonding, destabilizing the network of helices. Because the catalytic domain is made up of little more than a small number of helices and loops, the destablilization of two of these helices could lead to a decrease in the overall stability of the entire domain. To explore this hypothesis, a simple circular dichorism experiment could be performed PKC to determine is there is a decrease in helical structures after treatment with HNE.

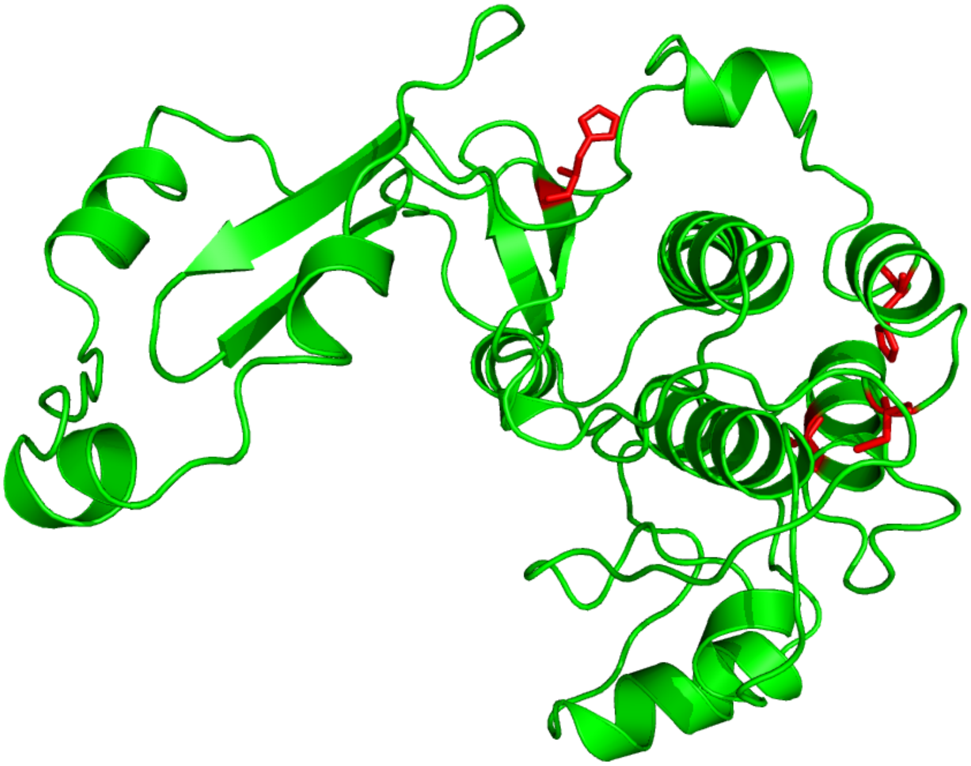

Figure 45. Homology model of HNE adduction sites demonstrate interaction of residues with helical structures. Two of the sites of HNE adduction, C572 and H597, are located in helical secondary structure of the catalytic domain. The adduction of these residues could lead to hydrogen bonding disruption and consequently, the destabilization of the domain.

Two of the most common sites of adduction by other types of PKC inhibitors, C502 and C488 are not found to be sites of HNE adducts. When these two residues are mapped on the homology model, they are found to be located in an entirely different region of the catalytic domain. This region has a much higher negative charge density than the location of the HNE adducted residues. Further, these residues are located in much closer proximity to the catalytic active site of the domain. Because the type of inhibitors that form adducts at C502 and C488 are typically active site selective, it is reasonable to hypothesize that the active site targeting of these inhibitors allow them to access residues that are largely hidden in the inactive state of the domain. By targeting the active site, these inhibitors allow the protein to undergo the necessary changes to become active. During the activation of the protein, a number of events, including the binding of a number of activators, phosphoralyation and the removal of the psuedosubstrate, all induce changes which lead to an active state protein. This active state is then inhibited by the active site targeting inhibitors. Because of all the changes undergone by the protein during activation, it is reasonable to deduce that residues which were previously inaccessible, including C502 and C488, could become accessible to these inhibitors. However, because treatment with HNE does not induce the active state of the protein, these residues would remain inaccessible to HNE and therefore resistant to adduction.

It is imperative to determine which sites of adduction are the most sensitive to HNE using a time study of the formation of HNE adducts. Along the same lines, future work examining which of the adducts plays the most important role in the inhibition of PKC activation will help illucidate more information about the structure/function relationship of PKC. Cys572 is of interest as it a site that has been shown to be sensitive to adduction previously and has been thought to be involved in the inactivation of PKC with various inhibitors such as selenocompounds and chelerythrine. While it is not expected that every adduct site found in this study is crucial for PKC inactivation, there is literature precedence suggesting Cys572 is a potentially a key target of HNE modification.

Conclusion

As the major aldhydic byproduct of membrane peroxidation, HNE has been the focus of much concentrated study from cellular apoptosis to stimulation of fibrogenesis and inflammation to protein adduction (116; 123-126). HNE is believed to play a role in a several diseases from malaria (115) to Alzheimer’s, indicating the global importance of this molecule (123). Due to its highly reactive nature, the increased levels of HNE found monocytes that have phagocytized the malaria pigment hemozoin (127) indicate the immunomodulatory role this molecule may play in malarial disease. HNE is a well-known cytotoxic agent due to its ability to modify the amino acid side chains. The inhibition of oxidative burst mediated by HNE may be due to the highly reactive HNE forming Michael and Schiff base adducts on residues of key proteins within the macrophage. Once formed, these adducts may inhibit the activity of the protein through multiple pathways. For example, adducts may form on or adjacent to active site residues, blocking substrate binding, or perhaps adduction results in a conformation change in the protein that prevents the active conformation of the protein. Clearly, the inhibitory nature of HNE on PKC is due to the formation of covalent adducts on key amino acid residues. These results suggest that the highly reactive nature of HNE may lead to the loss of key cellular functions by disrupting protein function. It has been shown here that the presence of the HNE adducts not only inhibits PKC translocation upon activation with PMA, it also inhibits the increase in intracellular Ca^{2+} typically seen with PMA activation of PKC. The location of these HNE adduction sites points to residues on the protein that may be of interest for continuing the work to understand how protein kinase c functions.

Future Work

While we have begun to investigate the functional consequences of HNE adduct formation on PKC activation, sweeping questions still remain. The present data clearly demonstrates that the formation of all five HNE adducts limits the translocation of PKC, it does not give information as to the exact adduct (or adducts) which have the debilitating effects on the enzyme. Combined with kinetics experiments to evaluate the order of HNE adduct formations, it would be interesting to see which had the greatest effect on PKC function. It would be also be useful to take a closer look at the inhibition of intracellular calcium flux. The preliminary studies suggest that the intracellular calcium flux typically seen with PMA activation is inhibited by pre-treatment with HNE. By taking a more quantitative approach, it would be possible to determine the extent to which the calcium flux is being inhibited and determine if there is partial activation of PKC even with HNE treatment or if it is completely inhibited. Beyond the expansion on these functional studies, other studies might give insight into the mechanism of PKC inhibition. PKC contains two critical zinc fingers which are essential to proper PKC function. The formation of HNE adducts might destablilize these zinc fingers ultimately destabilizing the entire enzyme. By investigating the dissociation constant of the zinc ions, you would investigate any possible effects on zinc finger stability associated with HNE adduct formation.

b and y ion traces for HNE Modified PKC peptides

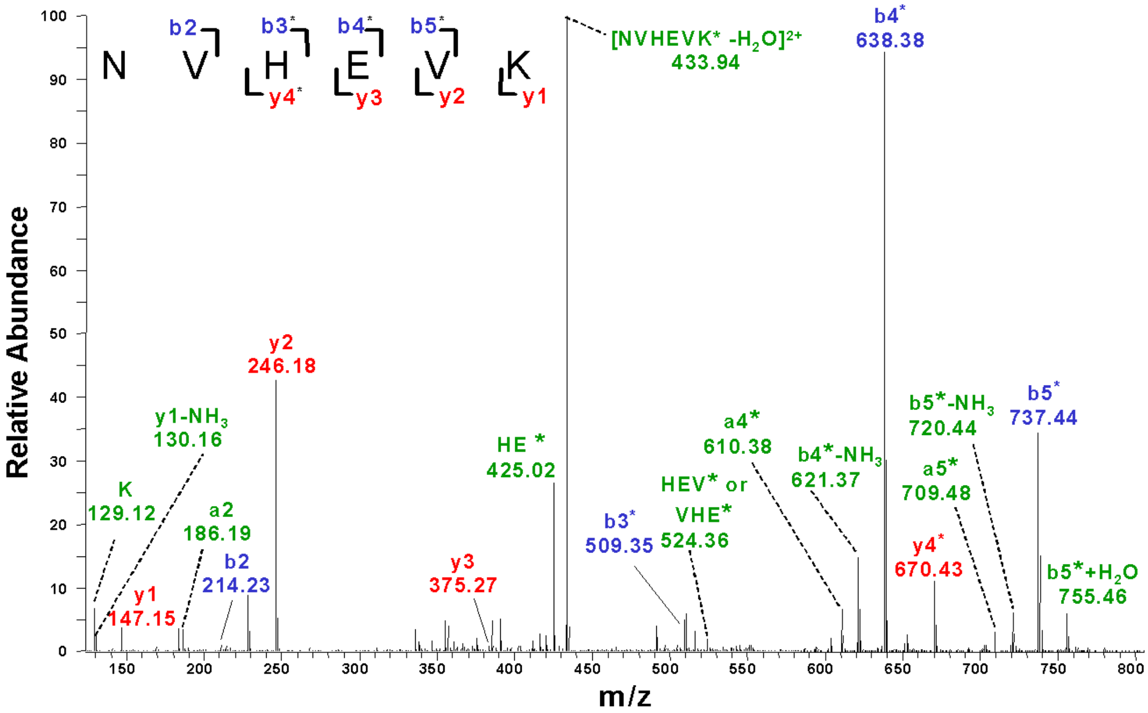

Figure 46. MS/MS of HNE modified NVHEVK peptide. Deconvoluted MS/MS spectra obtained from the LC/MS/MS analysis of the tryptic peptide NVHEVK of HNE-modified PKC. $[M+2H]^{+2}$ 442.3 is shown.

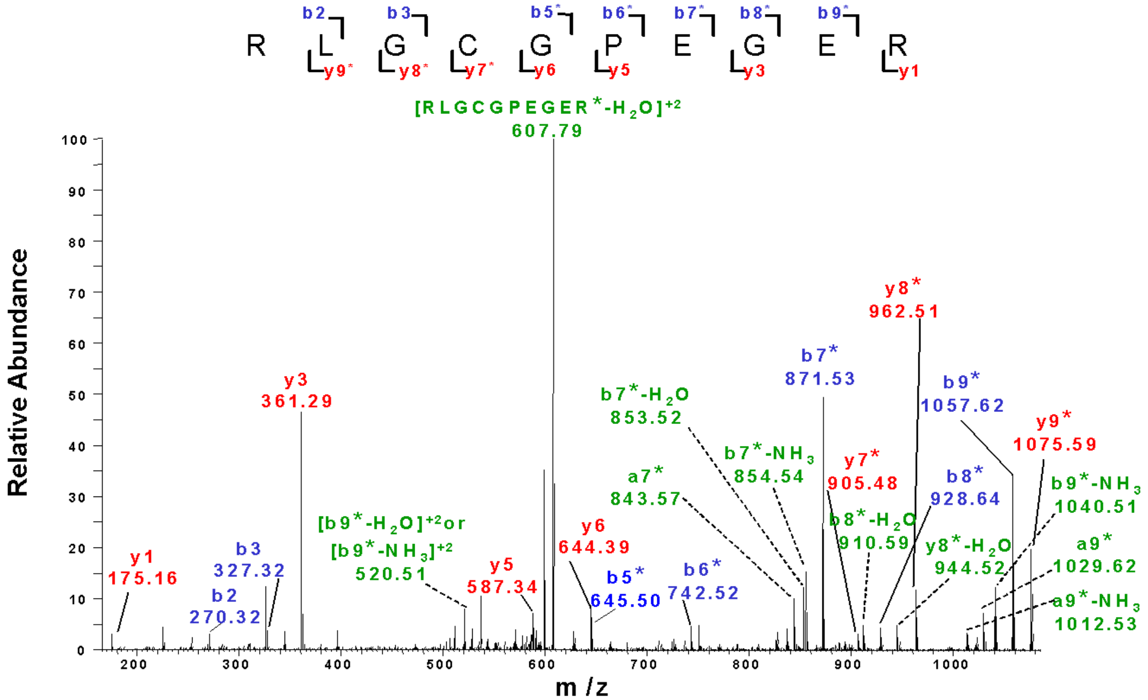

Figure 47. MS/MS of HNE modified FLGCGPEGER peptide. Deconvoluted MS/MS spectra obtained from the LC/MS/MS analysis of the tryptic peptide RLGCGPEGER of HNE-modified PKC. $[M+2H]^{+2}$ 616.3 is shown.

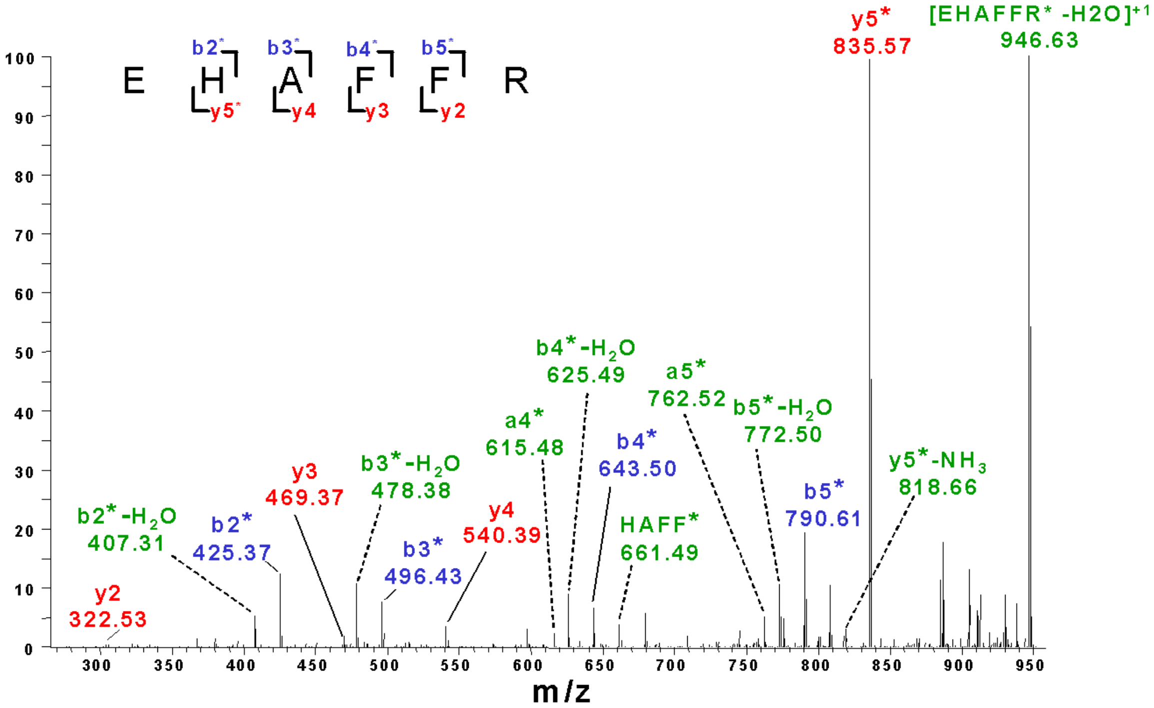

Figure 48. MS/MS of HNE modified EHAFFR peptide. Deconvoluted MS/MS spectra obtained from the LC/MS/MS analysis of the tryptic peptide EHAFFR of HNE-modified PKC. $[M+H]^+$ 964.5 is shown.

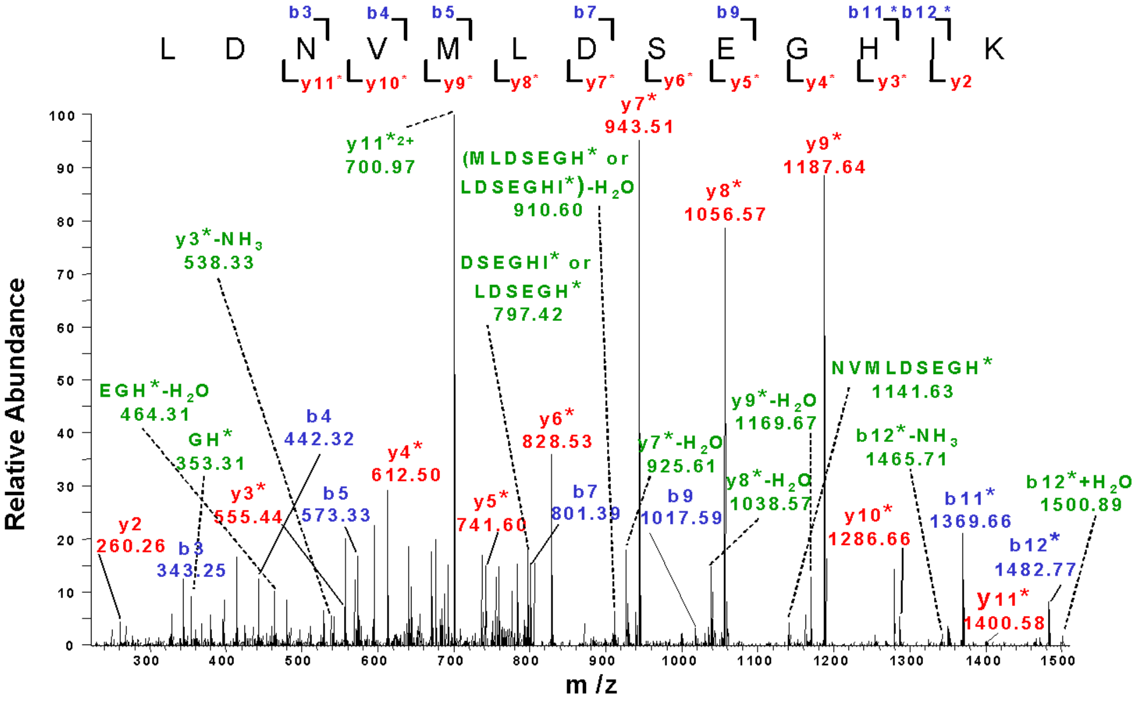

Figure 49. MS/MS of HNE modified LDNVMLDSEGKIK peptide. Deconvoluted MS/MS spectra obtained from the LC/MS/MS analysis of the tryptic peptide LDNVMLDSEGKIK of HNE-modified PKC. $[M+2H]^{+2}$ 814.9 is shown.

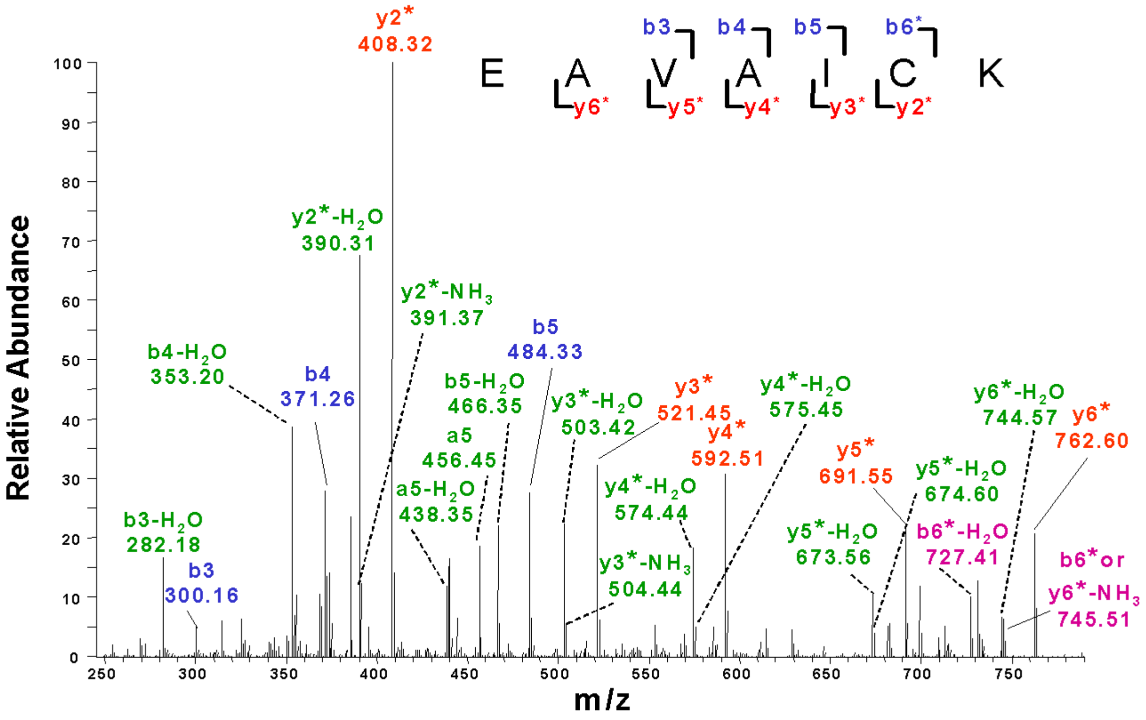

Figure 50. MS/MS of HNE modified EAVAICK peptide. Deconvoluted MS/MS spectra obtained from the LC/MS/MS analysis of the tryptic peptide EAVAICK of HNE-modified PKC. $[M+H]^+$ 891.5 is shown..Purple indicates ions that are evidence of modification of the cysteine residue.

<u>B and y ions for unmodified PKC peptides</u>

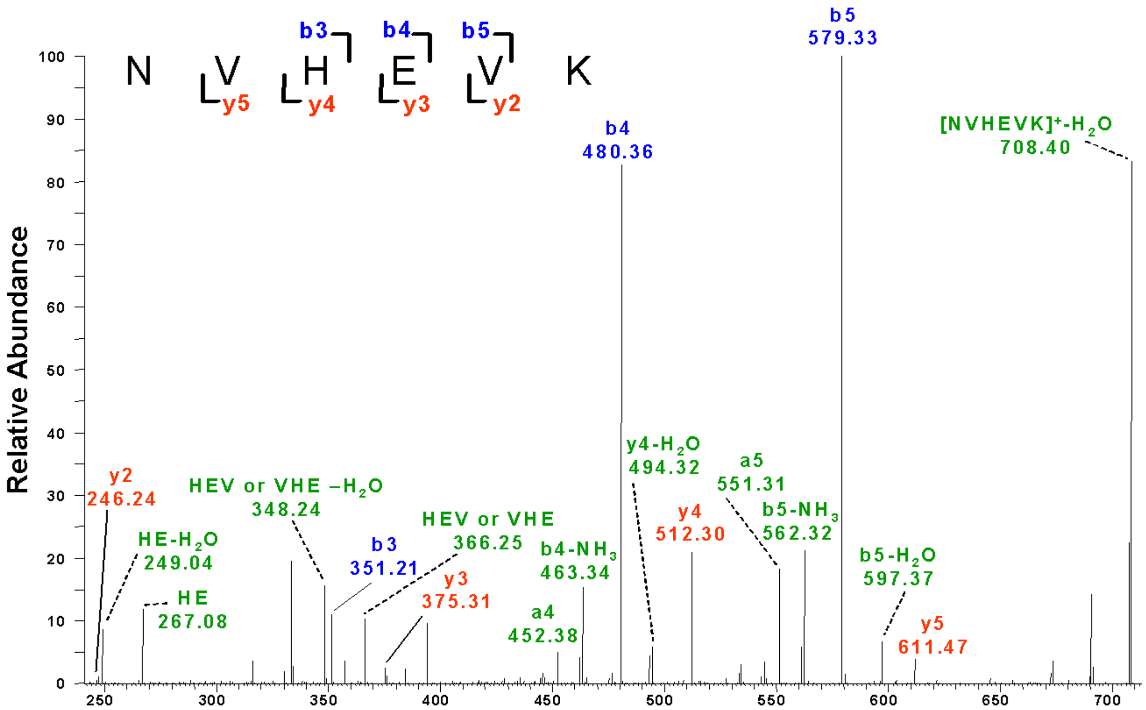

Figure 51. MS/MS of unmodified NVHEVK peptide. Deconvoluted MS/MS spectra obtained from the LC/MS/MS analysis of the tryptic peptide NVHEVK of native PKC. $[M+H]^+$ 725.5 is shown.

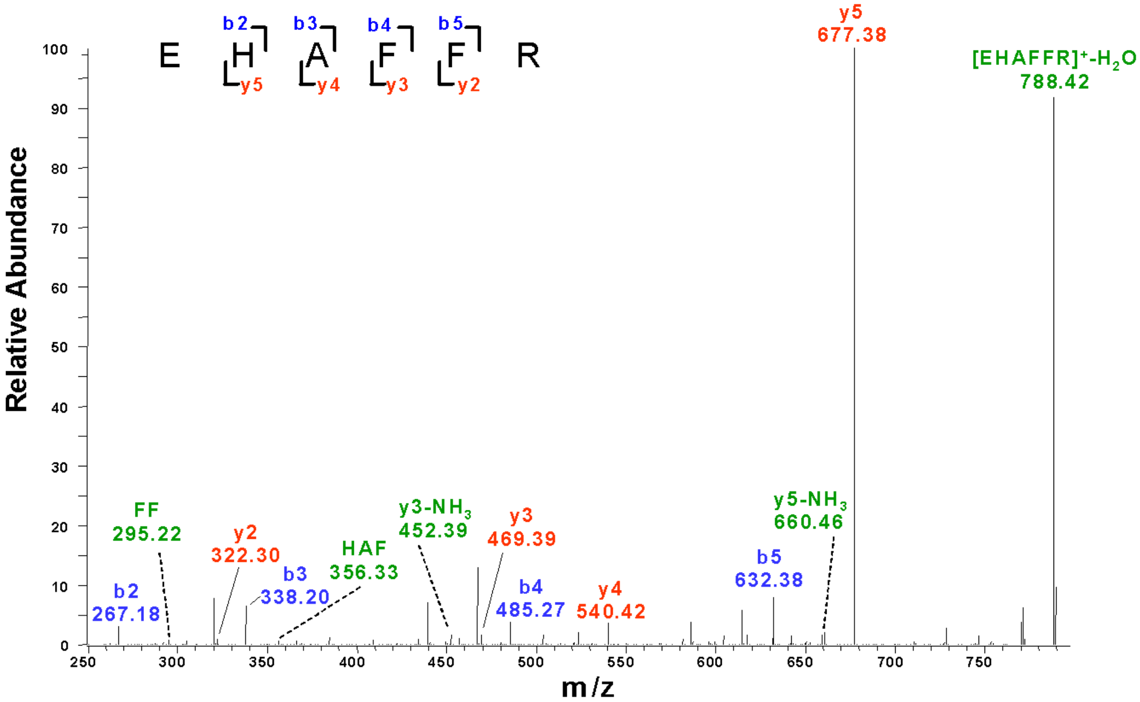

Figure 52. MS/MS of unmodified EHAFFR peptide. Deconvoluted MS/MS spectra obtained from the LC/MS/MS analysis of the tryptic peptide EHAFFR of native PKC. $[M+H]^+$ 806.5 is shown.

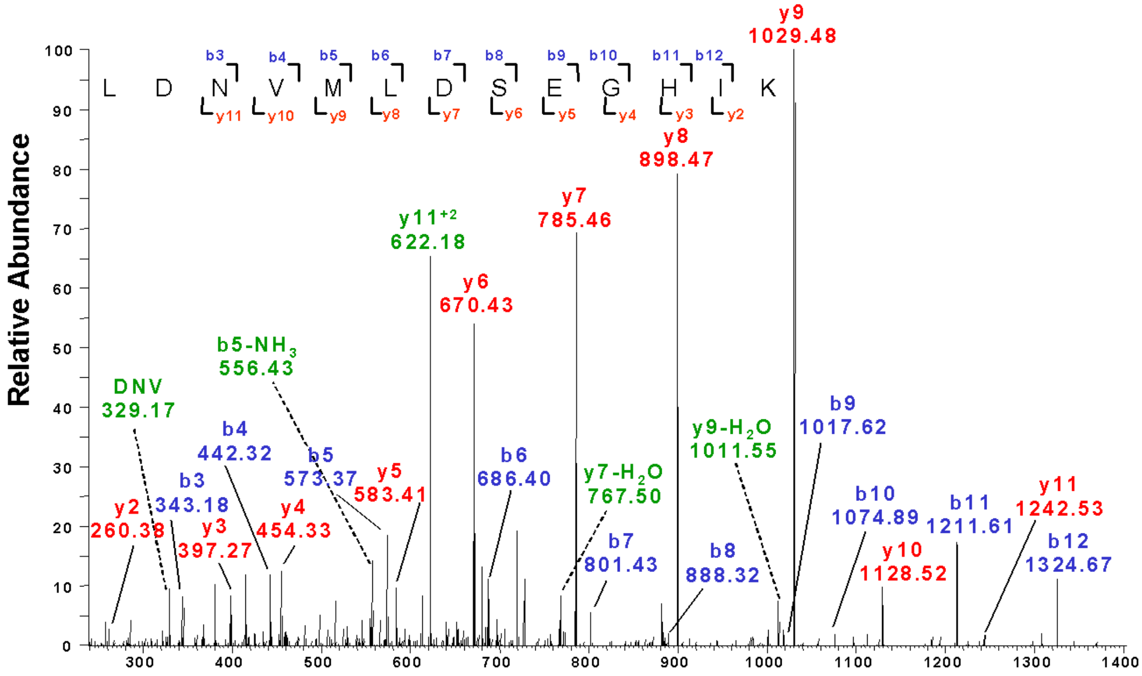

Figure 53. MS/MS of unmodified LDNVMLDSEGKIK peptide. Deconvoluted MS/MS spectra obtained from the LC/MS/MS analysis of the tryptic peptide LDNVMLDSEGKIK of native PKC. $[M+2H]^{+2}$ 735.9 is shown.

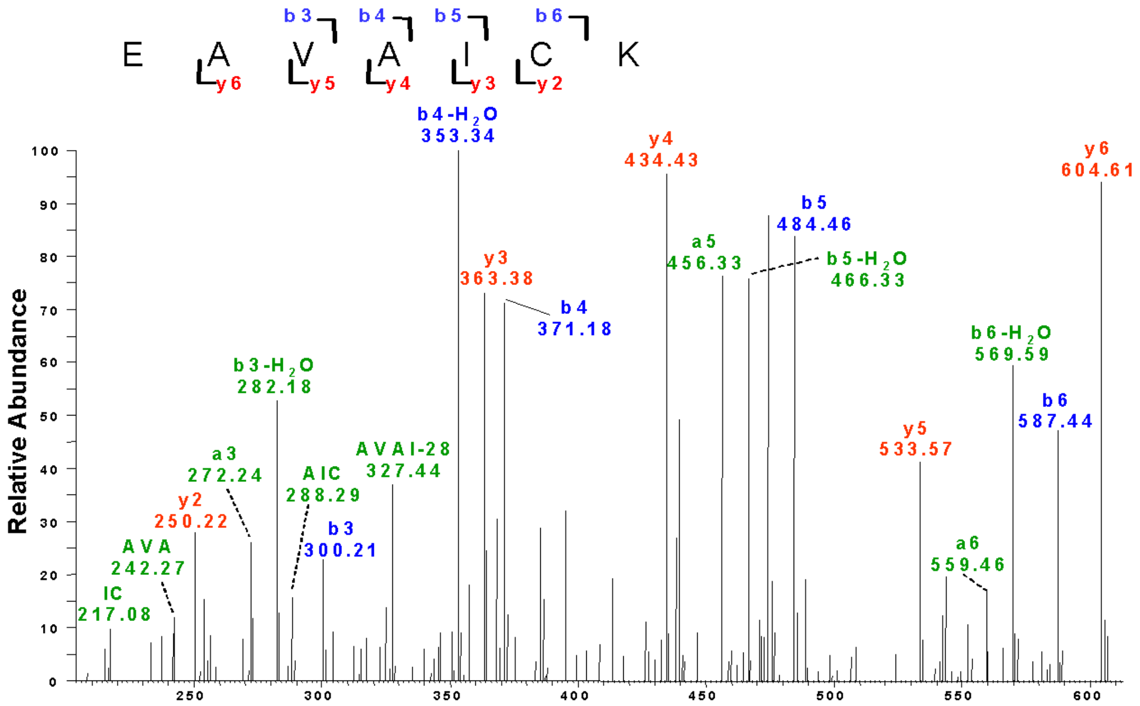

Figure 54. MS/MS of unmodified EAVAICK peptide. Deconvoluted MS/MS spectra obtained from the LC/MS/MS analysis of the tryptic peptide EAVAICK of native PKC. $[M+H]^+$ 733.6 is shown

B and y ion traces for PMA activated HNE modified PKC peptides

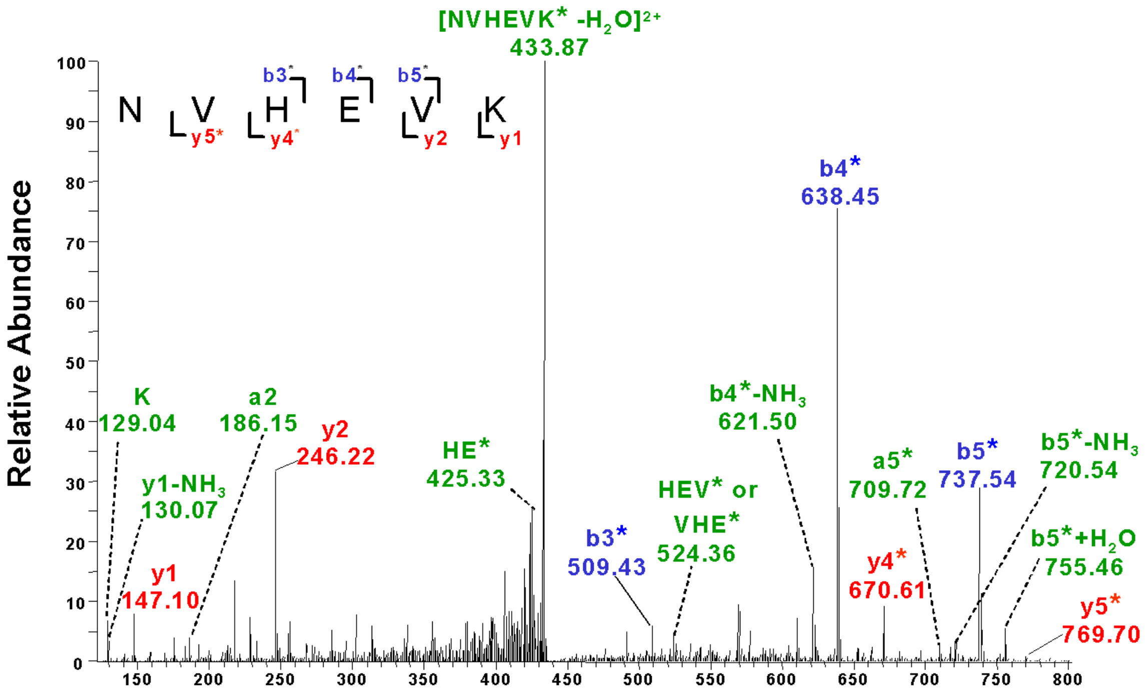

Figure 55. MS/MS of PMA activated HNE modified NVHEVK peptide. Deconvoluted MS/MS spectra obtained from the LC/MS/MS analysis of the tryptic peptide NVHEVK of HNE-modified PMA-treated PKC. $[M+2H]^{+2}$ 442.3 is shown.

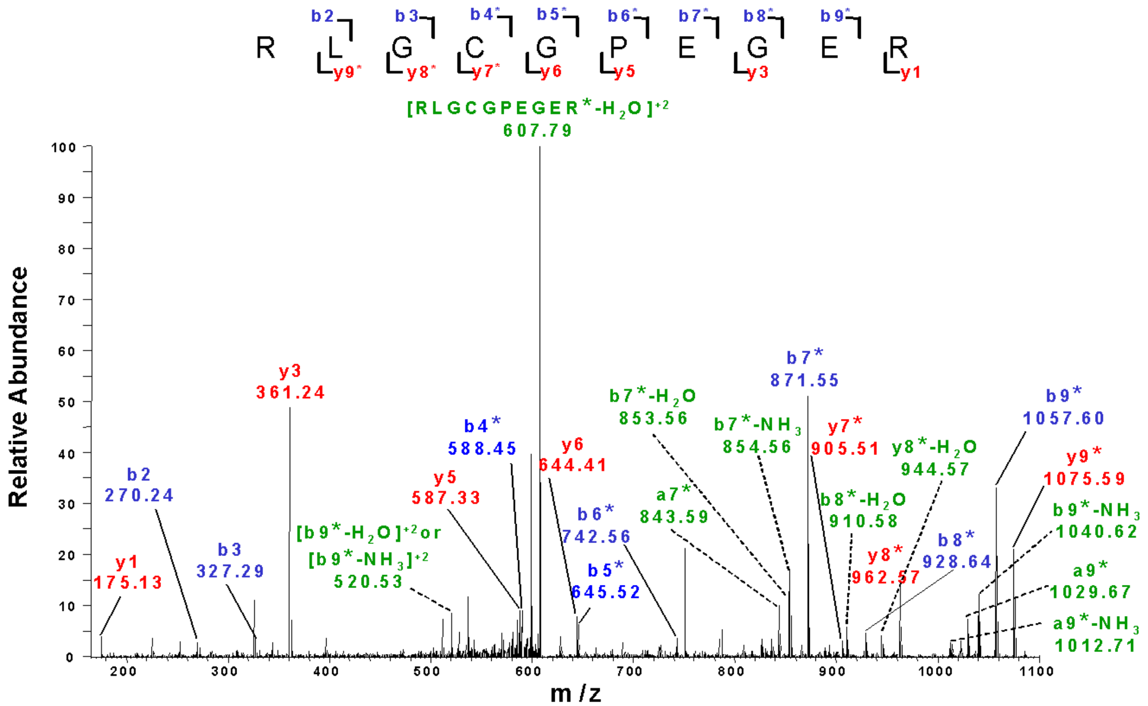

Figure 56. MS/MS of PMA activated HNE modified RLGCGPEGER peptide. Deconvoluted MS/MS spectra obtained from the LC/MS/MS analysis of the tryptic peptide RLGCGPEGER of HNE-modified PMA-treated PKC. [M+2H]$^{+2}$ 616.3 is shown.

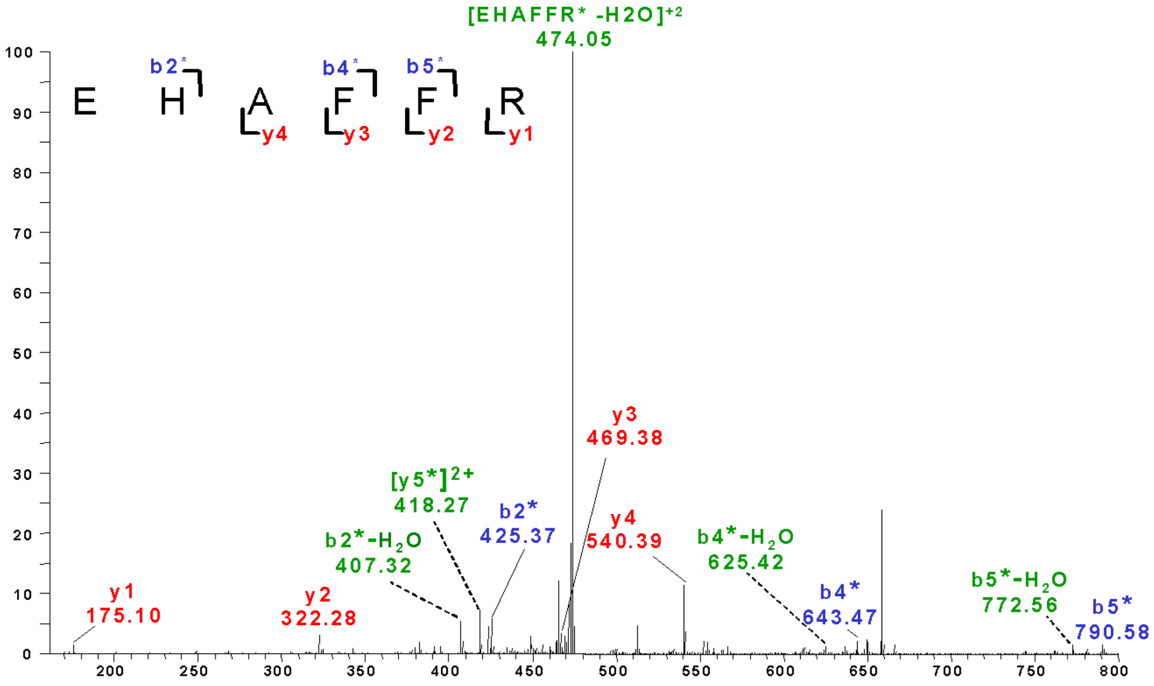

Figure 57. MS/MS of PMA activated HNE modified EHAFFR peptide. Deconvoluted MS/MS spectra obtained from the LC/MS/MS analysis of the tryptic peptide EHAFFR of HNE-modified PMA-treated PKC. [M+2H]$^{+2}$ 482.8 is shown.

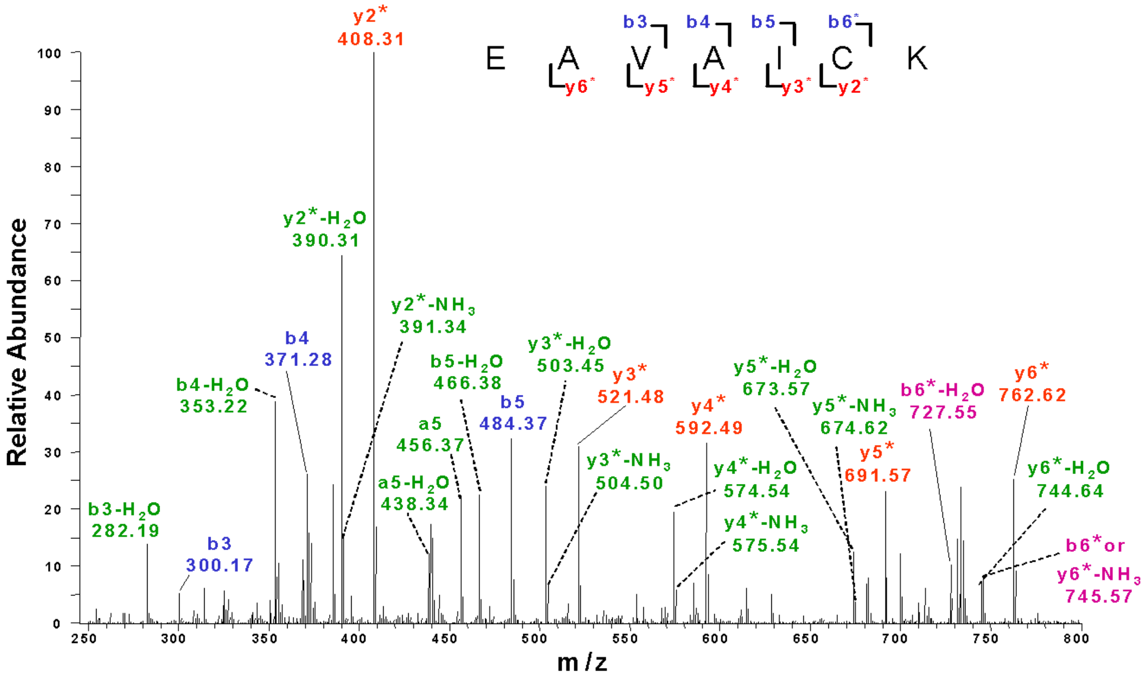

Figure 58. MS/MS of PMA activated HNE modified EAVAICK peptide. Deconvoluted MS/MS spectra obtained from the LC/MS/MS analysis of the tryptic peptide EAVAICK of HNE-modified PMA-treated PKC. $[M+H]^+$ 891.5 is shown. Purple indicates ions that are evidence of modification of the cysteine residue.

Table of Secondary Ions

Fragment	Treatment	Obs.	Calc.	Fragment	Treatment	Obs.	Calc.
K	Control	129.1	129.1	HEV or VEH	Control	366.2	366.2
	HNE	129.0	129.1		HNE	524.4	524.3
	PMA HNE				PMA HNE	524.4	524.3
y1-NH_3	Control			a4	Control	452.4	452.2
	HNE	130.2	130.1		HNE	610.4	610.4
	PMA HNE	130.1	130.1		PMA HNE		
a2	Control			b4-NH_3	Control	463.3	463.3
	HNE	186.2	186.1		HNE	621.5	621.5
	PMA HNE	186.2	186.1		PMA HNE	621.4	621.4
HE-H_2O	Control	249.0	249.1	y4-H_2O	Control	494.3	494.3
	HNE				HNE		
	PMA HNE				PMA HNE		
HE	Control	267.1	267.1	a5	Control	551.3	551.3
	HNE	425	425.2		HNE	709.5	709.4
	PMA HNE	425.3	425.2		PMA HNE	709.7	709.4
[NVHEVK-H_2O]$^{2+}$	Control			b5-NH_3	Control	562.3	562.3
	HNE	433.9	433.8		HNE	720.4	720.4
	PMA HNE	433.9	433.8		PMA HNE	720.5	720.5
b5-H_2O	Control	597.4	597.3	b5+H_2O	Control		
	HNE				HNE	755.5	755.4
	PMA HNE				PMA HNE	755.5	755.4
HEV or VEH-H_2O	Control	348.2	348.2				
	HNE						
	PMA HNE						

Table 2. Secondary ions from fragmentation of NVHEVK

Fragment	Treatment	Obs.	Calc.	Fragment	Treatment	Obs.	Calc.
a2-NH$_3$	Control	225.2	225.2	b7-H$_2$O	Control	853.5	853.5
	HNE	225.2	225.2		HNE	853.6	853.5
	PMA HNE				PMA HNE		
b2-NH$_3$	Control			b7-NH$_3$	Control		
	HNE	253.3	253.3		HNE	854.5	854.4
	PMA HNE	253.2	253.2		PMA HNE	854.6	854.4
y3-NH$_3$	Control			b8-H$_2$O	Control		
	HNE	344.3	344.2		HNE	910.6	910.6
	PMA HNE	344.2	344.2		PMA HNE	910.6	910.6
y4-H$_2$O or	Control			y8-H$_2$O	Control		
[Y8-H$_2$O]$^{2+}$	HNE	472.4	472.2, 474.7		HNE	944.5	944.5
	PMA HNE				PMA HNE	944.6	944.5
[b9-H$_2$O]$^{2+}$ or	Control			a9-NH$_3$	Control		
[b9-NH$_3$]$^{2+}$	HNE	520.5	520.3,520.8		HNE	1012.5	1013
	PMA HNE	520.5	520.3,520.8		PMA HNE	1012.7	1013
[RLGCGPE	Control			a9	Control		
GER-H2O]$^{2+}$	HNE	607.8	607.8		HNE	1029.7	1030
	PMA HNE	607.8	607.8		PMA HNE	1029.7	1030
y6-NH$_3$	Control			b9-NH$_3$	Control		
	HNE	627.5	627.5		HNE	1040.6	1041
	PMA HNE	627.5	627.5		PMA HNE	1040.6	1041
a7	Control						
	HNE	843.6	843.5				
	PMA HNE	843.6	843.5				

Table 3. Secondary ions from fragmentation of RLGCGPEGER

Fragment	Treatment	Obs.	Calc.	Fragment	Treatment	Obs.	Calc.
FF	Control	295.2	295.1	a4	Control	615.5	615.5
	HNE				HNE		
	PMA HNE				PMA HNE		
HAF	Control	356.3	356.2	b4-H_2O	Control		
	HNE				HNE	625.5	625.3
	PMA HNE				PMA HNE	625.4	625.3
b2-H_2O	Control			y5-NH_3	Control	660.5	660.3
	HNE	407.3	407.3		HNE	818.7	818.5
	PMA HNE	407.3	407.3		PMA HNE		
$[y5]^{2+}$	Control			HAFF	Control		
	HNE	418.4	418.4		HNE	661.5	661.4
	PMA HNE				PMA HNE		
$[EHAFFR\text{-}H_2O]^{2+}$	Control			a5	Control		
	HNE	474.1	474.3		HNE	762.5	762.4
	PMA HNE				PMA HNE		
y3-NH_3	Control	452.4	452.2	b5-H_2O	Control		
	HNE				HNE	772.5	772.4
	PMA HNE				PMA HNE	772.6	772.4
b3-H_2O	Control			$[EHAFFR\text{-}H_2O]^{+1}$	Control	660.5	660.3
	HNE	478.4	478.3		HNE	946.6	946.5
	PMA HNE				PMA HNE		

Table 4. Secondary ions from fragmentation of EHAFFR

Fragment	Treatment	Obs.	Calc.	Fragment	Treatment	Obs.	Calc.
DNV or a6^{+2}	Control	392.2	392.2, 392.7	DNVMLDS-NH_3	Control	758.7	758.3
	HNE	392.2	392.2, 392.7		HNE		
	PMA HNE				PMA HNE		
GH	Control			y7-H_2O	Control	767.5	767.4
	HNE	353.3	353.2		HNE	925.6	925.5
	PMA HNE				PMA HNE		
MLD	Control			DNVMLDS	Control		
	HNE	360.3	360.2		HNE	775.7	775.3
	PMA HNE				PMA HNE		
a4-NH_3	Control			b7-NH_3	Control		
	HNE	397.2	397.2		HNE	784.1	784.4
	PMA HNE				PMA HNE		
a4	Control			DSEGHI or	Control		
	HNE	414.3	414.2	LESEGH	HNE	797.4	797.4
	PMA HNE				PMA HNE		
[EGH-H_2O]	Control			b8-NH_3	Control		
	HNE	464.3	464.3		HNE	871.5	871.4
	PMA HNE				PMA HNE		
a5-NH_3 or	Control			MLDSEGH or	Control		
VMLDS-H_2O	HNE	528.4	528.3	LDSEGH-H_2O	HNE	910.6	910.4, 910.5
	PMA HNE				PMA HNE		
y3-HN_3	Control			y8-H_{2O}	Control		
	HNE	538.3	538.4		HNE	1039	1039
	PMA HNE				PMA HNE		
b5-NH_3 or	Control	556.4	556.2	y9-H_2O	Control	1012	1012
NVMLD-NH_3 or	HNE	556.3	556.2		HNE	1170	1170
DNVML-NH_3	PMA HNE				PMA HNE		
				NVMLDSEGH	Control		
y11^{+2}	Control	621.8	622.2		HNE	1142	1142
	HNE	701.0	701.0		PMA HNE		
	PMA HNE			b12-NH_3	Control		
b6-NH_3	Control				HNE	1466	1466
	HNE	669.4	669.3		PMA HNE		
	PMA HNE			b12+NH_3	Control		
VMLDSE	Control				HNE	1501	1501
	HNE	675.6	675.3		PMA HNE		
	PMA HNE						

Table 5. Secondary ions from fragmentation of LDNVMLDSEGHIK

Fragment	Treatment	Obs.	Calc.	Fragment	Treatment	Obs.	Calc.
IC	Control	217.1	217.1	y3-H_2O	Control	503.4	503.3
	HNE				HNE	503.5	503.3
	PMA HNE				PMA HNE		
AVA	Control	242.3	242.2	y3-NH_3	Control		
	HNE				HNE	504.4	504.3
	PMA HNE				PMA HNE	504.4	504.3
a3	Control	272.2	272.2	a6	Control	559.5	559.4
	HNE				HNE		
	PMA HNE				PMA HNE		
b3-H_2O	Control	282.2	282.2	b6-H_2O	Control	569.6	569.3
	HNE	282.2	282.2		HNE	745.5	745.4
	PMA HNE	282.2	282.2		PMA HNE		
AIC	Control	288.3	288.1	y4-H_2O	Control		
	HNE				HNE	574.4	574.4
	PMA HNE				PMA HNE	574.5	574.4
AVAI-CO	Control	327.4	327.2	y4-NH_3	Control		
	HNE	327.4	327.2		HNE	575.5	575.4
	PMA HNE				PMA HNE	575.5	575.4
b4-H_2O	Control	353.4	353.2	y5-H_2O	Control		
	HNE	353.2	353.2		HNE	673.6	673.4
	PMA HNE	353.2	353.2		PMA HNE	673.6	673.4
a4	Control			y5-NH_3	Control		
	HNE	343.3	343.2		HNE	674.6	674.4
	PMA HNE				PMA HNE	674.6	674.4
y2-H_2O	Control			b6-H_2O	Control		
	HNE	390.3	390.3		HNE	727.5	727.4
	PMA HNE	390.3	390.3		PMA HNE	725.6	725.4
y2-NH_3	Control			y6-H_2O	Control		
	HNE	391.4	391.4		HNE	744.6	744.6
	PMA HNE	391.3	391.3		PMA HNE	744.6	744.6
a5-H_2O	Control			y6-NH_3	Control		
	HNE	438.5	438.5	or b6	HNE	745.5	745.5, 745.4
	PMA HNE	438.3	438.3		PMA HNE	745.6	745.5, 745.4
a5	Control	456.3	456.3	[EAVAICK-H_2O]$^{+2}$	Control		
	HNE	456.5	456.3		HNE	873.6	873.5
	PMA HNE	456.4	456.3		PMA HNE	873.6	873.5
b5-H_2O	Control	466.3	466.3				
	HNE	466.4	466.3				
	PMA HNE	466.4	466.3				

Table 6. Secondary ions from fragmentation of EAVAICK

CHAPTER IV

NANOBLOSSOMS: A LIVE CELL PROBE FOR THE DETECTION OF RESPIRATORY SYNCYTIAL VIRUS

Statement of Effort

. In the design, development and application of the nanoblossom probes, I was assisted by Dr. Ash Jayagopal and Jonas Perez. In the design and synthesis of the nanoblossoms, I performed all synthesis and characterization assays including both the *in vitro* characterization of the probes themselves as well as characterizing their *in vivo* properties. The *in vivo* assays included exploring the cytotoxcity, stability, specificity in the cellular environment and the rate of transfection. Because my largest interest I this project was aimed at developing a tool for effective live cell RNA imaging, I also performed a wide range of *in vivo* labeling and imaging using confocal microscopy including initial RNA labeling experiments as well as multiplexed spatial resolution experiments. While this project was my pet project from its inception, it would not have been possible without the experimental contribution of Dr. Ash Jayagopal and academic insight provide by Jonas Perez. Dr. Ash Jayagopal was kind enough to lend us his expertice by performing the gold colloidal experiments as well as the mechanism of internalization experiments including the endocytosis inhibitors. Jonas Perez was provided indispensible guidance in the early stages of this project without which this project would have been far more difficult to get off the ground.

Introduction

Proper RNA processing and trafficking is essential to nearly all cellular functions. It plays an underlying role in cellular replication, homeostasis, and response to external stimuli.(128; 129) Currently, there are a number of methods available to study RNA, and to some extent, its trafficking. Reverse Transcriptase PCR (RT-PCR) is a highly specific and sensitive tool for detection of specific RNA sequences.(26-28) RT-PCR has been used successfully in the detection of low levels of RNA making it a useful method when sample is limited. Unfortunately, this method is labor intensive and contamination is a constant concern. More importantly, RT-PCR cannot be used to study live cells because the RNA must be extracted rendering it useless in studying the molecular mechanisms of RNA trafficking. Fluorescently-labeled oligonucleotide probes have also been widely employed to explore and quantify intracellular RNA. Some of these methods include Förster resonance energy transfer (FRET) pairs, molecular beacons, and *in situ* hybridization(29-33). These probes are designed to hybridize with a specific RNA sequence, providing *in vivo* spatial information about that particular strand of RNA. However, probe internalization is a significant challenge with these techniques. Various transfection methods have been developed to shuttle fluorescently labeled oligonucleotides into cells including cationic lipids and polymers, modified viruses, dendrimers, and liposomes. Each of these methods has limitations and ultimately the necessity of chemical transfection reagents limits the utility of these probes. Further, these probes are also susceptible to rapid degradation by cellular nucleases leading to high backgrounds, false positives and poor target detection. Although these obstacles can be circumvented by cell fixation, doing so renders them inapplicable for live cell imaging. Recently, the unique advantages of nanoparticles have been exploited to develop probes that overcome a number of limitations found with the aforementioned methods.(34; 35)

The field of nanotechnology capitalizes on the unique properties of nanoscale materials, ranging in size from 1- 100 nm.(130) The underlying basis for the nanoscale properties is closely related to the length associated with it. The fundamental physics and chemistry of a material will change when the dimensions of a solid become comparable to one or more of these characteristic lengths, many of which exist at the nanometer length scale. At this scale, objects such as nanoparticles take on properties and functions that differ from those seen on the bulk scale.(130) A common approach to take advantage of the characteristics of nanoscale materials is to tune their chemical and spectral properties by changing their size and/or shape. This ability to tune the properties of nanoscale material has long been ultilized in electronic and chemical applications such as electrocatalysis, electrochemical sensor devices and redox recognition.(130; 131) Recently the focus has expanded to encompass a new range of biological applications. Nanoparticles, of various compositions, can be effective vehicles for drug delivery. Nanoparticles have also been used to probe the internal cellular structure and dynamics of various biological systems including the vescular secretion of neurotransmitters and distinguishing healthy colon cells from adenocarcinoma cells.(132) The use of magnetic nanoparticles as MRI contrast agents have also led to their use in identifying atherosclerotic lesions in cardiovascular tissue.(133) The development of nanoparticles to study these and other biological systems has demonstrated their versatility and functionality.

Metal nanoparticles have become a critical componet in the development of nanotechnology-based detection methods for respiratory viruses. Gold and silver nanoparticles have garnered much of the attention in this field because of their unique physical and chemical properties. The surface of gold nanoparticles (AuNPs) acts as a soft metal ion that easily binds to soft ligands such as thiols. This reactivity provides an efficient strategy to readily functionalize particles with relevant biological molecules.(134) The deep-red color seen in solutions of AuNPs is the result of the surface plasmon band (SPB), a broard absorption band in the visible region between 510 and 580 nm.(135) The SPB experiences wavelength shifts based on AuNP size, shape, temperature and the nature of functionalized ligands, which has made it the subject of extensive study of the optical spectroscopic properties of AuNPs. The ligand shell of AuNPs alters the refractive index causing either a red or blue shift, allowing SPB shifts to be used to assess the extent of ligand functionalization.(135) AuNPs possess the advantageous ability to act as fluorescence quencher molecules as a result of nonradiative energy transfer from the dye to the metal surface.(136; 137) In the case of chromophore-AuNP composites, the quenching efficiency of AuNPs outperforms that of most organic acceptors. The dominating design factor affecting the efficiency of quenching by the AuNP is the distance between surface of the AuNP and the chromophore.(137) In cases where the chromophore is separated from the AuNP by a bulky spacer, such as antibiodies or carbon-based linker molecules, there is a decrease in quenching seen that corresponds to the increasing distance between the AuNP surface and the chromophore.(137) Each of these properties makes AuNPs interesting platforms for the development of respiratory infection diagnostics.

AuNPs functionalized with oligonucleotides have been shown to efficiently enter live cells without the aid of harsh transfection/permeabilization agents and have limited cytotoxic effects. The recent development of “nano-flares” (NF) takes advantage of these qualities to yield a real-time probe capable of detecting specific RNA sequences with minimized background interference.(34) A NF consists of an AuNP conjugated to a long probe sequence of DNA, which is compliment to the RNA of interest. There is also a short hybridzed “reporter” strand of fluorescently- tagged DNA. In this state, the organic fluorophore is quenched as a result of its proximity to the AuNP. Upon hybridization of the probe strand with the target RNA compliment, the reporter strand is released, spatially separating it from the AuNP and resulting in a fluorescent signal that can be correlated to the presence of the RNA sequence of interest.(34)

While NFs overcome many of the challenges faced by previous approaches, their design yields a signal that diffuses away from the hybridized RNA/NF construct. Consequently, important spatial information is lost in live cell microscopy applications. Here, we have developed a new probe for studying RNA trafficking that exploits the advantages of oligonucleotide functionalized AuNPs and overcomes the spatial limitations of previous designs. Nanoblossom (NB) probes consist of an AuNP conjugated to a strand of hairpin DNA, which contains a fluorophore at the 3´ end (**Figure 59**).

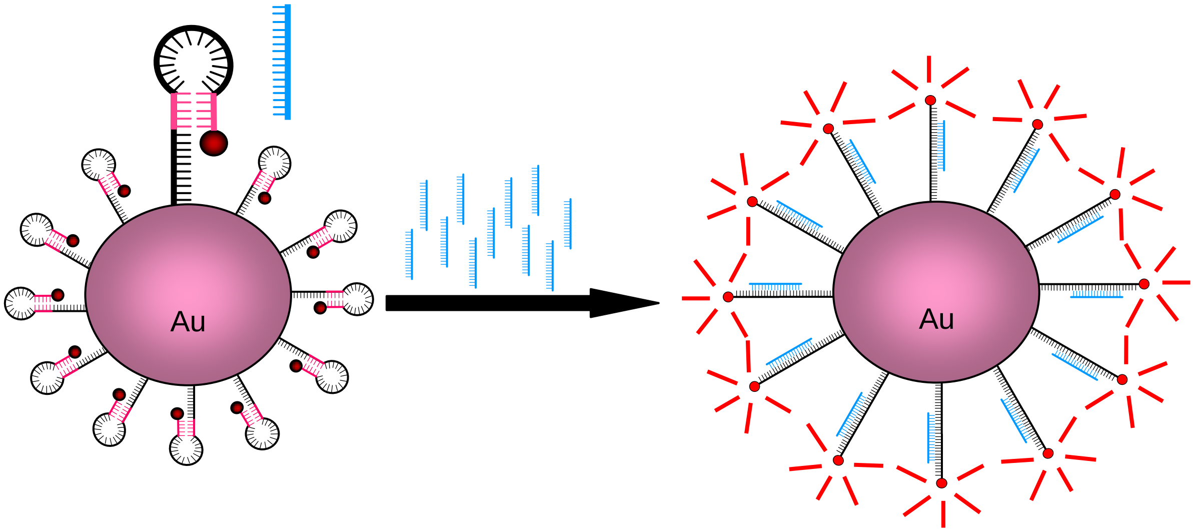

Figure 59. Nanoblossom Construct. Nanoblossoms were synthesized by conjugating a 26 base hairpin DNA with a T-10 linker to a Au nanoparticle through a 5' thiol. In the closed state, the fluorophore is quenched due to its proximity to the gold nanoparticle. However, upon binding with the appropriate compliment, the hairpin opens and the fluorophore is then a sufficient distance from the nanoparticle to overcome the quenching. This allows for the detection of compliment by monitoring fluorescence intensity. Importantly because the fluorophore does not dissociate, the fluorescence intensity can be used to learn about the spatial orientation of the RNA.

A specific sequence of RNA, the compliment to the "loop" region of the DNA hairpin, can be detected through hybridization with the NB. Without compliment DNA or RNA, the hairpin sequence of the NB oligonucleotide remains folded, with the fluorophore quenched due to the proximity of the gold nanoparticle surface. Upon binding the specific RNA target, the hairpin opens and the fluorophore extends a sufficient distance from the nanoparticle to overcome quenching. More importantly, the fluorophore does not dissociate from the NB. This allows not only the detection of the RNA of interest, but also the identification of its spatial location in real time.

RNA viruses, whose replication is dependant on proper RNA translation and trafficking, are an ideal test system to develop NB probes. In particular, we have focused on probes to examine respiratory syncytial virus (RSV) genomic RNA during infection. RSV is the leading cause of lower respiratory tract infections in children under the age of five in the United States, resulting in an estimated 90,000 hospitalizations per year.(138) RSV is an enveloped negative-sense, single stranded RNA paramyxovirus. The attachment (G) and fusion (F) proteins are necessary for proper virion attachment, membrane fusion, and nucleocapsid release into the host cell. The nucleocapsid is composed of genomic viral RNA, nucleoproteins (N), phosphoproteins (P) and polymerase proteins (L) which aid the virus in commandeering host cellular machinery to propagate infection. During viral infection, the full length genomic viral RNA is replicated and packaged with newly synthesized viral proteins which then bud from the cell as a virion, free to infect other cells.(138) Little is known about viral RNA trafficking within host cells during the course of the infection. This is due, in part, to the lack of adequate tools to probe live cells and monitor the progression of infection in real time. When applied to the study of RSV, sequence specific NBs would provide a powerful tool for the detection of viral infection and real-time study of RSV pathogenesis.

Material and Methods

Materials

All chemicals were used as received unless otherwise noted. Fetal bovine serum was purchased from Atlanta Biologicals (Atlanta, GA, USA). Penicillin/streptomycin, trypan blue and Mg^{2+}/Ca^{2+} free PBS were obtained from Cellgros Mediatech (Herdon, VA, USA). The human cell line, HEp-2, was obtained from the American Type Culture Collection (ATCC). Oligonucleotide sequences were purchased from Biosearch Technologies. Gold nanoparticle solutions were purchased from Ted Pella, Inc. RSV type A2 virus and RSV anti F-protein antibodies were a kind gift from the Jim Crowe laboratory (Vanderbilt University). Quantum dots, propidium iodide, calcein-AM, and Alexa Fluor 647 conjugates of transferrin, 70 kDa anionic dextran, cholera toxin B and biotinylated goat anti-mouse antibodies were purchased from Invitrogen Corp. Lab-Tek II chambered coverglass was from Nunc. The Goldenhance autometallographic gold colloid enhancement kit was from Nanoprobes, Inc. Cytochalasin D and Dynasore were purchased from Tocris Bioscience. Brefeldin A was from Epicentre Biotechnologies. Genistein was from Ascent Scientific. All buffers used for endocytosis assays, trypan blue, Nuclear Fast Red, and Chloroquine, Chlorpromazine, nocodazole, nystatin, progesterone, porcine heparin, 2-deoxy-D-glucose, sodium azide, and amiloride were from Sigma Chemical at the highest available purity. All solutions were sterile-filtered through a 0.2 µm Pall Supor membrane syringe filter prior to use in cell cultures. All cell culture materials were obtained from Gibco unless otherwise noted. All other chemicals were purchased from Fisher Scientific (Hampton, VA, USA) unless otherwise specified.

Cell Culture and RSV infection

HEp-2 cells were grown in Opti-MEM growth media supplemented with 2% (v/v) fetal bovine serum (complete Opti-MEM), 2% amphoericin B, 2% glutamine and 0.1 % gentamycin and incubated in an environment of 37 °C with 5% carbon dioxide and 5% humidity. For reproducible sample infection with RSV type A2 at different multiplicity of infections (MOI), the following protocol was used. HEp-2 cells were plated and allowed to grow to 80% confluency in an environment of 37 °C with 5% carbon dioxide and 5% humidity. Once the samples reach 80 % confluency, the cells were counted using Trypan Blue exclusion and a hemocytometer, and the cell count averaged. The determined cell count was multiplied by the desired MOI to determine the correct number of plaque forming units (pfu) needed to treat the samples. This was divided by the virus titer to determine the volume of virus stock to be used in sample infection. Samples were treated with RSV diluted in complete Opti-MEM growth media to the appropriate concentration then incubated for 1 hour. After incubation, complete Opti-MEM growth media containing 0.75% w/v autoclaved methylcellulose was added to each sample and incubated for the appropriate period of infection.

Synthesis and Characterization of Nanoblossoms

To synthesize the nanoblossoms, the genomic RSV compliment DNA strand was used for RSV-NB. The sequence of the strand is CGA CG**A AAA ATG GGG CAA ATA** CGT CG from 5’ to 3’. At the 5’ end, there is a thiol attached to a ten T linker. A Quasar 670 or CAL fluor Red590 fluorophore is conjugated at the 3’ end (RSV-NB-Cy5 or RSV-NB-Red590, respectively). For the GAPDH-NB, the exon 6 compliment strand was used with the sequence CGA CG**G AGT CCT TCC ACG ATA CCA** CGT CG. A CAL fluor Red590 fluorphore is conjugated at the 3’ end. Before attachment to the gold nanoparticle, the hairpin DNA strand was activated to reduce any disulfide bonds formed between strands. To do this, the lyophilized DNA was resuspended in 1:1 solution of 100 mM DTT and 0.2 mM phosphate buffer, pH 8.3, and incubated at room temperature, protected from light. After one hour, the samples were filtered and washed with RNase free water using a Millipore Microcon YM-3 spin filter. After the final wash, the filtered DNA was resuspended and aliquots were stored at -80 °C. The final concentration of this DNA solution was determined by measuring the UV absorption at 254 nm. Once the DNA was activated, it was conjugated to 15 nm gold nanoparticles to form the complete nanoblossom. For this, 450 nM DNA was added to the 2.325 nM Au nanoparticle solution and incubated at RT for 4 hours, protected from light. After 4 hours, phosphate buffer (final concentration = 10mM), Tween 20 (0.1% final concentration) and sodium chloride (0.1mM) were added to the solution, mixing thoroughly between each addition. The solution was incubated at RT for an additional four hours, protected from light. After 4 hours, sodium chloride was added to the solution to give a total sodium chloride concentration of 0.2 mM and incubated for 4 hrs at RT protected from light. This step was repeated. After the final incubation, the solution was centrifuged at 13, 200 rpms for 30 min and the supernatant was removed and kept for later analysis. The Au pellet was resuspended in Mg^{2+}/Ca^{2+} free phosphate buffered saline solution (PBS), using sonication to disrupt the pellet if necessary and washed 3 times in PBS. After the final wash, the Au pellet was resuspended in 1 mL of PBS and the nanoblossom concentration was determined by measuring absorbance at 260 nm and 520. The concentration was calculated using the extinction coefficient for Au nanoparticles ($\varepsilon_{520} = 3.64E8\ M^{-1}cm^{-1}$). The absorbance of the supernatant was also measured at 260 nm to determine the concentration of unconjugated DNA. The ratio of unconjugated DNA to nanoblossom concentration was used to calculate the average number of DNA strands per gold nanoparticle. To do this, the absorbance at 260 of a solution that contained no AuNPs was compared to the supernatant from the NB conjugation experiment to determine the extent bound to the AuNP during conjugation. The emission spectrum of the nanoblossoms was obtained for a 1 µM RSV-NB-Cy5 or GAPDH-NB solution. This solution was incubated with 2 µM RSV compliment or GAPDH compliment, respectively, at

70 ºC for 1 hr and then cooled to RT for 12 hours, protected from light. The emission was collected from 580 to 800 nm on a Cary Eclipse Fluorescence Spectrophotometer, at 1 nm increments. Dynamic light scattering (DLS) data was collected for a 0.25 nM solution of AuNPs only, RSV-NBs only and GAPDH-NBs only. The RSV-NBs and GAPDH-NBs were centrifuged and resuspended in RNase free water prior to DLS measurements. DLS measurements were taken with seven measurements per run, with five runs per samples using a Malvern Zetasizer nanoZS. The runs were then averaged to obtain the size distrubution for particles present in each solution. Resistence to degradation by DNase I was assayed by diluting RSV-NB-Cy5 or GAPDH-NB to 1.6 nM in Mg^{2+}/Ca^{2+} free PBS containing 50 mg/mL of BSA and 0.25 nM $MgCl_2{\cdot}6H_2O$. 0.38 mg/L DNase I was added to the diluted RSV-NB or GAPDH-NB in a black 96 well plate and fluorescence monitored in 1 min increments for 120 min.

Efficiency of NB transfection

Flow cytometry was used to determine the extent of nanoblossom internalization and efficiency of transfection. For this, HEp-2 cells were plated in 6 well plates, and infected as described above, with a MOI of 1. To optimize RSV-NB incubation times, samples were treated with 0.5 nM RSV-NB-Cy5s diluted in culture media and incbuated for either 6, 4, 2, 1, or 0.5 hrs. The samples were washed 3 times with Mg^{2+}/Ca^{2+} free PBS and fresh culture media was then added and samples were allowed to hybridize under these conditions for an additional 12 hours. After 12 hours, the samples were lifted from the plate using a 10 % EDTA solution, centrifuged and resupended in a solution of 1 nM propidium iodide diluted in PBS. The samples were analyzed on a Custom Becton Dickinson five-laser LSRII analytical cytometer using APC excitation and filter settings to measure PI fluorescence signal. The fluorescence signal from the nanoblossoms was simultaneously monitored using a Cy5 excitation/filter set. Gating allowed the PI signal from cells that are positive for nanoblossom fluorescence to be specifically monitored.

In vitro nanoblossom specificity assays

In vitro experiments were performed to demonstrate the specificity of the synthesized nanoblossoms. For each concentration, the NB solution was added to a solution of either the compliment sequence (RSVcomp or GAPDHcomp) or a random sequence, femA. The sequence for RSVcomp from 3' to 5' is TTT TTT TAC CCC GTT TAT TTT TT. The sequence for GAPDHcomp from 3' to 5' is TTT TTT GGT ATC GTG GAA GGA CTC TTT TT. The sequence for the femA control sequence is A GTA TTG GAA GTC GTT CGA AAT TGA TCA CTC GCA from 3' to 5'. The control femA sequence contained approximately the same C and G composition as the RSV compliment. RSV-NB-Red590 specificity was investigated for RSV-NB-Red590 concentrations from 2.885 nM to 1.4 nM, diluted with PBS. For both RSVcomp and femA, concentrations ranging from 1.005 μM to 7.85 nM were investigated. Appropriate concentrations of RSV-NB-Red590 and either RSVcomp or femA were combined in a 96 well plate. The sample was covered, heated to 70 °C for one hour and allowed to cool to room temperature for 12 hours, protected from light. After 12 hours, the fluorescence was measured using a Bio-Tek Synergy HY multidetection microplate reader. The samples were excited using a 530/25 and the emissions will be collected using a 590/30 filter. GAPDH-NB specificity was verified with the same method.

RSV genomic RNA labeling in HEp-2 cells

Confocal microscopy was used to demonstrate the ability of the nanoblossoms to label RSV specific RNA in the human epithelial cell line, HEp-2. HEp-2 cells were plated and infected as described above with an MOI of either 3 or 0.1. Seventeen hours after infection, the samples were treated with 0.5 nM RSV-NB-Cy5 and incubated for 6 hrs. The samples were then gently washed with Mg^{2+}/Ca^{2+} free PBS 3 times, fresh complete Opti-MEM growth media was added to each sample and allowed to incubate for an additional 12 hrs. Immediately prior to imaging, samples were gently washed with Mg^{2+}/Ca^{2+} free PBS 3times and PBS was added to each sample for imaging. Uninfected controls were treated with RSV-NB-Cy5 similarly. Untreated RSV infected controls were treated in a similar manner using complete Opti-MEM media only. Finally, uninfected, untreated controls were also treated in a similar manner using complete Opti-MEM media only. All samples were imaged on a Zeiss LSM 510 Meta inverted confocal microscope equipped with LSM Image Browser software with 40x magnification. The samples were exciting using a 630 laser and emissions were detected using a 650 long pass filter, keeping the detector gain consistent during imaging of all samples.

Microscopic detection of Nanoblossoms in HEp-2 cells

HEp-2 cells were plated on Lab-Tek II chambered coverglass at a density of 50 X 10^4 cells per chamber (1.7 cm^2) in DMEM with 10% FBS, and was maintained at 5% CO_2, 37°C overnight. The following day, HEp-2 cells were infected with RSV at an MOI of 0.25 (12,500 PFU/mL) or left uninfected and cultured for an additional 48 hrs. Following this incubation period HEp-2 cells were rinsed three times in Hank's Balanced Salt Solution (HBSS), and the media was replaced with DMEM containing either 0.5 mM GADPH-NB or 0.2 mM RSV-NB for 4 hours at 37°C. In a parallel experiment, cells exposed to the same NB doses for the same duration were incubated with trypan blue to ensure that cell viability was > 95% to identify spurious uptake results. Following this period, cells were rinsed three times in HBSS, fixed in 4% paraformaldehyde in PBS for 15 min. at room temperature, then rinsed three times in PBS containing 50 mM glycine. HEp-2 cells were then stained for detection of gold colloids using

Goldenhance according to the manufacturer's instructions. Fast Red was used as a nuclear counterstain. The samples were mounted using Cytoseal 60 (Richard Allan Scientific). Cells were then viewed on a Nikon TE2000U microscope at 40X-100X magnification and photographed using a Hamammatsu C7780 cooled CCD color digital camera controlled by Image Pro Plus 5.1 (Media Cybernetics).

Analysis of mechanism of Nanoblossom internalization

HEp-2 cells were plated in 96-well microplates at a density of 5 X 10^4 cells per well and incubated at 37°C and 5% CO_2 in DMEM with 10% FBS overnight. A subset of these wells were selected for RSV infection at MOI = 0.25 the following day, and cells were incubated for an additional 48 hrs. The following day, cells were rinsed three times in serum-free DMEM, and were either untreated or pretreated with 100 µL volumes of DMEM containing nystatin/progesterone, sodium azide/2-deoxy-D-glucose, chlorpromazine, chloroquine, brefeldin A, dynasore, serum, nocodazole, heparin, amiloride, genistein, cytochalasin D, or no additives at specified concentrations for 1 hour. The range of working concentrations of reagents was determined using values reported in the literature, or, when possible, empirically using known tracers of endocytosis: transferrin (clathrin-dependent), cholera toxin B (lipid-raft-dependent), or dextran (caveolar-depedent). An acceptable working concentration for nanoblossom internalization assays was determined when the reagent inhibited internalization of the tracer by > 15% in HEp-2 cells as measured by microplate spectrophotometry. This concentration was used as the middle concentration in a range of 3 concentrations, to evaluate dose-dependent effects. Media was then aspirated and replaced with DMEM containing the same additives as well as RSV-NBs or GADPH-NBs, and incubated for 4 hrs. Following this period, cells were rinsed three times in HBSS, fixed for 15 min. at room temperature with 4% paraformaldehyde in PBS, and analyzed for nanoblossom fluorescence using a Molecular Devices Spectramax M5 microplate reader (Cy5, 647 nm excitation, 665 emission, FAM, 570 nm excitation, 591 nm emission, with auto-cutoff monochromator setting). As several solutions used to dissolve endocytosis study reagents were made in DMSO, cells were incubated with NBs suspended in DMEM with the highest concentration of DMSO used (0.5%) to monitor any solvent-induced effects. Cells were incubated in parallel with endocytosis study reagents, DMEM, and 1 µM calcein-AM as a viability indicator to ensure reagents did not induce significant (> 5%) cell death in any case as determined by fluorescence microscopy and automated image analysis using Image Pro Plus 5.1. Experiments were performed in triplicate.

Cytotoxicity of Nanoblossoms

HEp-2 cells were plated in 6 well plates, and infected as described above, with a MOI that ranges from 0.1 to 3. After 7 hours of incubation at 37 °C, the samples were treated with 0.5 nM RSV-NB and incubated for 6 hrs. After 6 hrs, the samples washed gently with PBS three times, fresh complete Opti-MEM growth media was added and the samples were incubated for an additional 12 hrs. Untreated control samples were treated in a similar manner using complete Opti-MEM media only. After 12 hours, the samples were lifted from the plate using a 10 % EDTA solution, centrifuged and resupended in a solution of 1 nM PI. The samples were analyzed on a Custom Becton Dickinson five-laser LSRII analytical cytometer using APC excitation and filter settings to measure PI fluorescence signal. Gating enabled the PI signal from cells that are positive for RSV-NB fluorescence (monitored using a Cy5 excitation/filter set) to be specifically monitored. The PI signal from untreated infected control samples was compared to that of RSV infected samples treated with RSV-NBs to determine the cytotoxicity.

Multicolor Labeling of HEp-2 cells

HEp-2 cells were plated and infected as described above with an MOI of either 0.1 or 3. Seventeen hours after infection, the samples were treated simultaneously with 0.5 nM RSV-NB-Cy5 and incubated for 6 hrs. The samples were then gently washed with Mg^{2+}/Ca^{2+} free PBS 3 times, fresh complete Opti-MEM growth media was added to each sample and allowed to incubate for an additional 12 hrs. After 12 hours, either the F-protein or cellular markers were labeled. For the F-protein labeled samples, the samples were incubated with anti F-protein primary antibodies for 30 minutes, then goat anti-mouse biotinylated secondary antibodies for one hour. Finally, the samples were incubated with 10 nm 525 strepavidin conjugated quantum dots for 30 minutes. The samples were washed with Mg^{2+}/Ca^{2+} PBS three times between each step. For the samples labeled with cellular markers, samples were treated with 50 nM SYTO-13 nuclear dye and 25 nM Mitotracker dye, diluted in complete OPTI-MEM media and incubated for 30 minutes at 37 ºC. All samples were then prepared for imaging. Immediately prior to imaging, samples were gently washed with Mg^{2+}/Ca^{2+} free PBS 3 times and PBS was added to each sample for imaging. Uninfected controls were treated with RSV-NB-Cy5 similarily. Untreated RSV infected controls were treated in a similar manner using complete Opti-MEM media only. Finally, uninfected, untreated controls were also treated in a similar manner using complete Opti-MEM media only. All samples were imaged on a Zeiss LSM 510 Meta inverted confocal microscope equipped with LSM Image Browser software with 40x magnification. For F-protein labeled samples, the samples were exciting using a 488 laser (525 qdots) and 630 laser (RSV-NB-Cy5) with emissions detected using a 550-620 band pass filter (525 qdots) and 650 long pass filter (RSV-NB-Cy5), keeping the detector gain consistent during imaging of all samples. For samples labeled with ceullar markers, samples were exciting using a 488 laser (SYTO-13), 543 laser (Mitotracker) and 630 laser (RSV-NB-Cy5) with emissions detected using a 500-530 band pass filter (SYTO-13), 550-620 band pass filter (Mitotracker) and 650 long pass filter (RSV-NB-Cy5), keeping the detector gain consistent during imaging of all samples.

Correlation of RSV-NB signal with initial RSV infection

HEp-2 cells were plated, infected and prepared for flow cytometry as described in the cytotoxicity section. The samples were analyzed on a Custom Becton Dickinson five-laser LSRII analytical cytometer using APC excitation and filter settings to measure PI fluorescence signal. The fluorescence signal from RSV-NB-Cy5s was simultaneously be monitored using a Cy5 excitation/filter set. The monitoring of RSV-NB-Cy5 signal highlighted the relationship between the extent of sample infection and nanoblossom fluorescence. The signal was plotted against the MOI for each sample to show the linear range of detection as well as signal saturation. Gating out PI positive cells allowed only viable cells to be monitored.

Virus Titer

To assess the effect of NB treatment on the ability of RSV infection to progress, plaque assays were used to titer viral infectivity for cells which had been treated previously with RSV-NBs. HEp-2 cells were plated in 24 well plates and allowed to grow for 24 hours or to 80% confluency. The samples were then treated with 1 nM RSV-NBs and allowed to incubate for 6 hrs in an atmosphere of 5 % humidity, 5% CO_2 at 37 °C. The RSV-NBs were then removed and replaced with fresh complete Opti-MEM media. Samples were then allowed to incubate for an additional 12 hours in an atmosphere of 5 % humidity, 5% CO_2 at 37 °C. Following incubation, samples were infected with RSV A2. Serial dilutions were used so that individual plaques could be counted after 4 days of infection. To do this, 4 wells were left uninfected, 4 wells were infected with stock, 4 with 10x dilution, 4 with 100x dilution, 4 with 1000x dilution and 4 with 10,000x dilution. The samples were then covered in methylcellulose containing Opti-MEM and allowed to incubate for 4 days in an atmosphere of 5 % humidity, 5% CO_2 at 37 °C. After 4 days, the samples were fixed using cold methanol and the RSV F-protein was labeled. To label the F-protein, the samples were incubated with anti F-protein primary antibodies (1:1000 dilution) for 1 hr at RT, followed by incubation with an HRP conjugated goat anti-mouse secondary antibodies(1:1000 dilution) for one hour. Finally, the samples were treated with HRP substrate for 20 minutes and the plaques were visually counted.

Results

Synthesis and Characterization

To synthesize sequence specific NBs, DNA hairpins were conjugated to an AuNP through a 5′ thiol. Using modifications of molecular beacons developed by *Santangelo et al*, the NB DNA hairpin consists of a 5′ 10 polythymine linker, followed by a 5 base "stem" region found on each side of a "loop" region, which is complimentary to the target sequence.(31) In the closed state, the 5 base stem forms hydrogen bonds with its compliment located on the 3′ side of the "loop" region resulting in a folded conformation. Located on the 3′ terminus is a fluorescent dye (**Figure 59**). This construct is very similar to that of the molecular beacon which typically consists of a strand of hairpin DNA flanked by a fluorophore and a quencher molecule. However, with the NB construct, a single AuNP acts as the quencher for multiple strands of DNA. Typical nanoblossom synthesis results in approximately 40 hairpins per AuNP, as determined by UV-Vis spectroscopy.

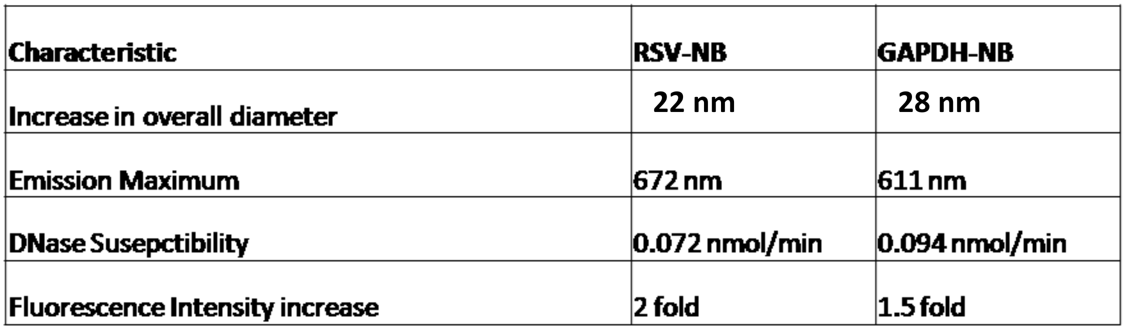

Characteristic	RSV-NB	GAPDH-NB
Increase in overall diameter	22 nm	28 nm
Emission Maximum	672 nm	611 nm
DNase Susepctibility	0.072 nmol/min	0.094 nmol/min
Fluorescence Intensity increase	2 fold	1.5 fold

Table 7. Characterization of RSV- and GAPDH-NBs in the presence of their respective compliments. RSV- and GAPDH-NBs were characterized after synthesis in the presence of the appropriate compliment sequence. The two types of NBs were found to have similar characteristics making GAPDH-NBs a good control sequence for RSV-NBs. The use of differing fluorescent dyes allowed the two NBs to be used simultaneously.

In the design of sequence specific NBs, two different NB were developed – a RSV specific NB and a glyceraldehyde-3-phosphate dehydrogenase (GAPDH) specific NB to serve as a control probe. For the RSV specific NB (RSV-NB), the loop region of the probe targeted a gene end-intergenic start sequence which has three exact repeats and six almost-exact repeats with various numbers of nucleotide mismatches throughout the genome.(139; 140) Similar intergenic repeats are common in other RNA viruses(141), suggesting that the approach may be generalized to the study of other viruses. Successfully used in antisense and small interfering RNA experiments(140-142), this site was considered the most accessible and therefore a prime site for oligonucleotide binding and probe targeting. A NB was also designed that was complimentary to the housekeeping gene GAPDH. This NB probe was used to control for the compromised cell state as a result of infection with RSV. GAPDH is a human glycoprotein involved in a diverse range of activities in mammalian cells. This protein has been implicated in nuclear RNA export, membrane transport and fusion, protein phosphotransferase reactions, and a number of other important cellular functions. The sequence used to design the GAPDH specific NB (GAPDH-NB) is complimentary to a sequence found in the Exon 6 region of the GAPDH gene. Previous studies have shown that this region is not involved in RNA-binding protein interactions or the formation of double stranded RNA, making it a good target.

RSV-NB and GAPDH-NBs characterization is summarized in **Table 7**. Dynamic light scattering showed that the conjugation of closed RSV hairpins on AuNP resulted in an expected increase in overall diameter of 11nm. Similarly a 14 nm increase was seen with the conjugation of GAPDH specific hairpins to AuNP. In order to achieve NB specificity, optimization of the length of the thyamine linker was required. Early efforts to develop a sequence specific RSV-NB utilized a T3 linker. However, this short linker resulted in non-specific fluorescent signal. As a result, the linker was lengthened to T10. In the presence of a DNA strand matching the target sequence (RSVcomp or GAPDHcomp), the hairpin opens, resulting in an emissions peak at 672 nm for the RSV-NB, which contains a Quasar 670 fluorphore, a cyanine 5 (Cy5) equivalent. A

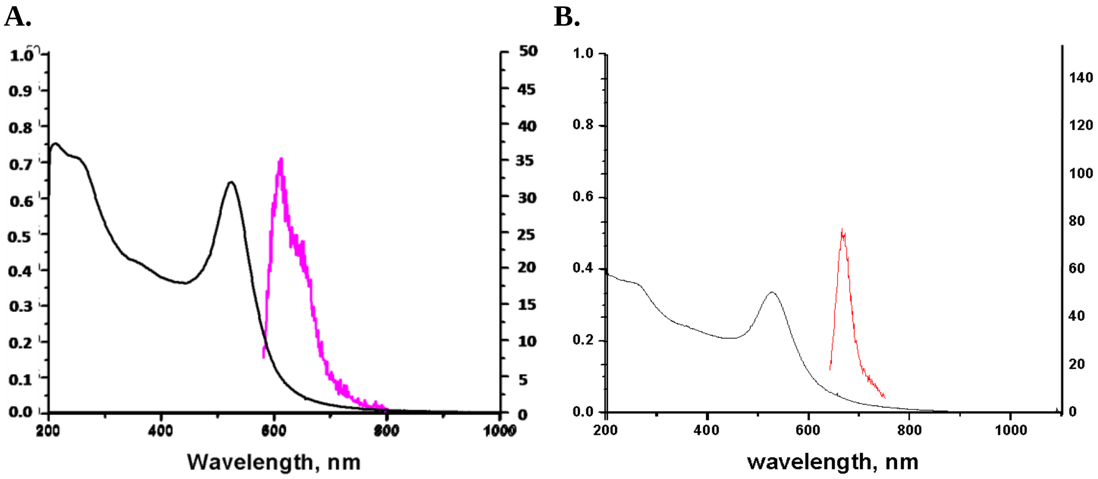

Figure 60. Absorbance and Emission Specta for RSV- and GAPDH-NBs. The RSV-NB have an absorbance spectrum with the characteristic peaks at 254 nm and 520 nm. The open RSV-NB emission spectrum has a λ_{max} at 670 nm (A). The GAPDH-NBs have an similar absorbance spectra and the open GAPDH-NB emission spectrum has a λ_{max} at 611 nm (B).

similar emission peak was seen at 611 nm for the GAPDH-NB which has a CAL fluor Red590 fluorophore at the 3' end (**Figure 60**). This peak is not observed in the closed state for either NB species. To verify signal specificity, RSV-NBs were incubated with either RSVcomp or a nonspecific sequence, femA. RSVcomp hybridized with the NB opening the hairpin, resulting in a 2-fold increase in fluorescent signal compared to femA (**Figure 61**). A titration of RSV-NB with excess compliment shows the expected saturation behavior. Above RSVcomp concentrations of 50 nM, all of the accessible "petals" of the RSV-NB have opened. Similar experiments were performed with GAPDH-NB, which showed a 1.5-fold increase in fluorescence in comparison to femA (**Figure 61**). To determine the susepctibility of the probes to degradation by cellular DNases, RSV-NBs and GAPDH-NBs were exposed to DNase I. In the presence of DNase I, RSV-NBs and GAPDH-NBs were degraded at a rate of 0.072 nmol min^{-1} and 0.094 nmol min^{-1}, respectively (**Figure 62**).

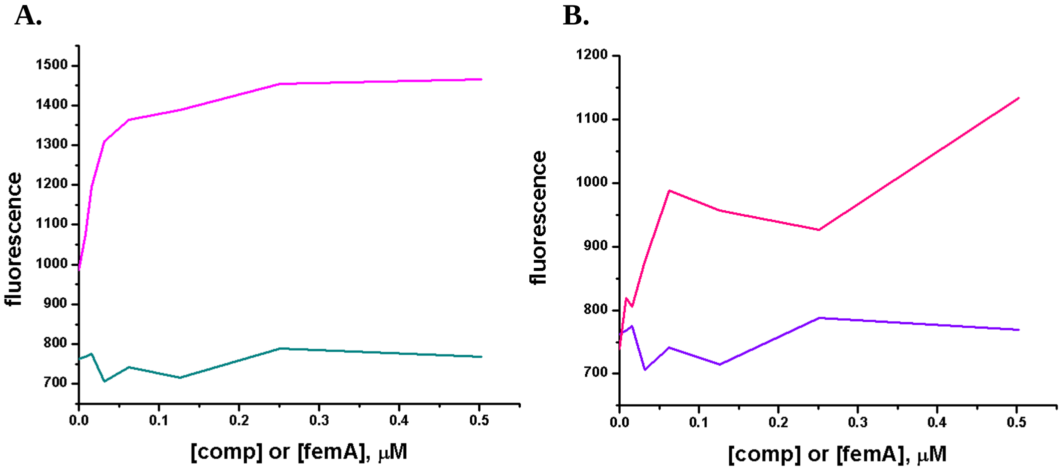

Figure 62. ***In vitro*** **Specificity of RSV- and GAPDH-NBs.** In solution, the RSV-NB specifically hybridizes with the compliment RSV DNA. Hybridization opens the hairpin, allowing the fluorophore to emit a fluorescent signal (A, pink). Similarly, GAPDH-NB specifically hybridized with the compliment GAPDH DNA, emitting a fluorescent signal (B, pink). However, in each case, no fluorescence signal was detected using a noncomplimentary sequence, femA (A and B, blue).

Transfection

RSV-NB *in vivo* specificity was explored in HEp-2 cells. The HEp-2 cell line is commonly used as a model to study RSV infection and is ideal for investigating the intracellular properties of the RSV-NBs. The multiplicity of infection (MOI) of a sample corresponds to the percent of the cell population likely infected during initial infection period. Infected with RSV at a MOI of 3, nearly all cells are infected at the time of imaging.

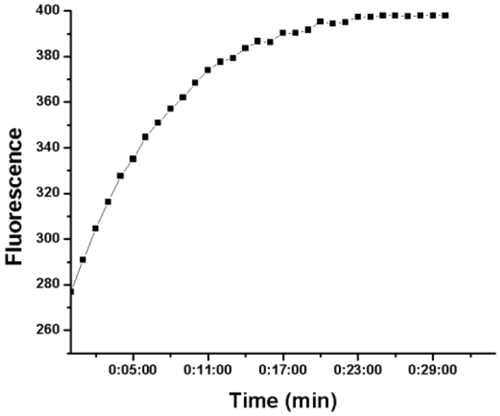

Figure 62. Degradation of RSV-NBs by DNase I. When reacted with Dnase I, the RSV-NBs had a rate of Degradation by Dnase I of 0.072 nmol/min as determined from the linear region of the fluorescence emission spectrum.

Flow cytometry was used to determine if uninfected populations can easily be distinguished from RSV-infected HEp-2 cell populations (MOI = 1, approximately 90% of the cells infected) which have been treated with equal concentrations of RSV-NBs (**Figure 63A**). For these assays, the viability dye PI was used to eliminate signal as a result of dead cells, thereby, insuring all intensity increases were a result of virus detection within viable cells.

Analysis of the RSV-NB signal demonstrates a three fold difference between the fluorescence of uninfected- and RSV-infected cell populations. To further explore the concentration-signal relationship, HEp-2 cells were infected with initial RSV MOIs ranging from 0 to 1 ensuring different levels of infection for each sample at time of analysis (**Figure 63B**). When treated with equal concentrations of RSV-NB, a viral concentration dependant increase in the mean intensity of RSV-NB fluorescence was observed from 0 MOI to 0.5 MOI. For this range of MOIs, this infected percentage would range

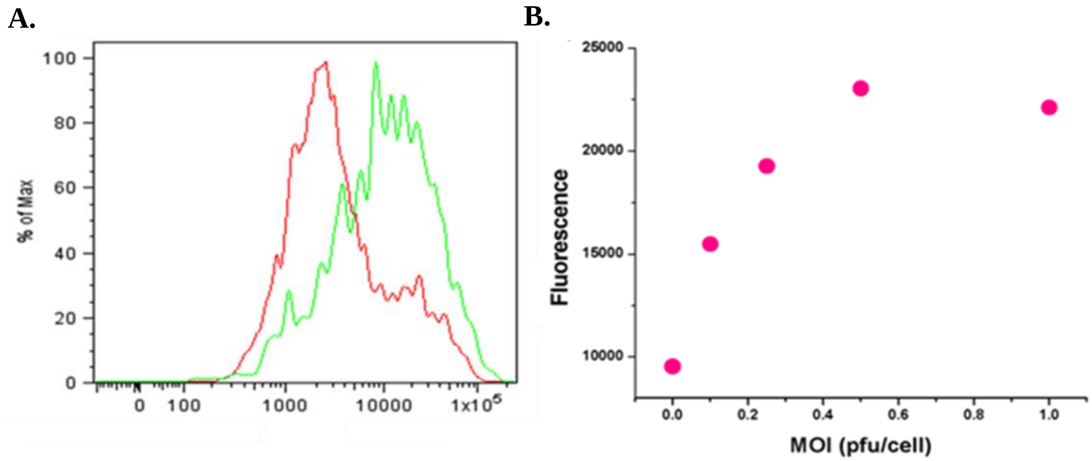

Figure 63. Flow cytometric analysis of RSV-NB signal in RSV-infected cells. A. RSV-infected cell populations can easily be distinguished from uninfected populations when treated with 0.5 nM RSV-NB by monitoring the fluorescence using flow cytometry. The histograms demonstrate that there is a three fold difference between the fluorescence of uninfected cells and RSV-infected cells. B. Flow cytometry was also used to demonstrate the relationship between fluorescent signal and initial RSV infection concentration. When treated with equal concentrations of RSV-NB, the mean intensity of fluorescence increases as a function of initial RSV infection. For this assay, all samples were infected for 35 hours before the signal was detected. This corresponds to the first spike in RNA concentration

from 0 (0 MOI) to 50 % (0.5 MOI) of the cell population. Above 0.5 MOI blossom saturation occurs. Further analysis of the flow cytometry data showed an efficiency of transfection of >95% (**Figure 64**).

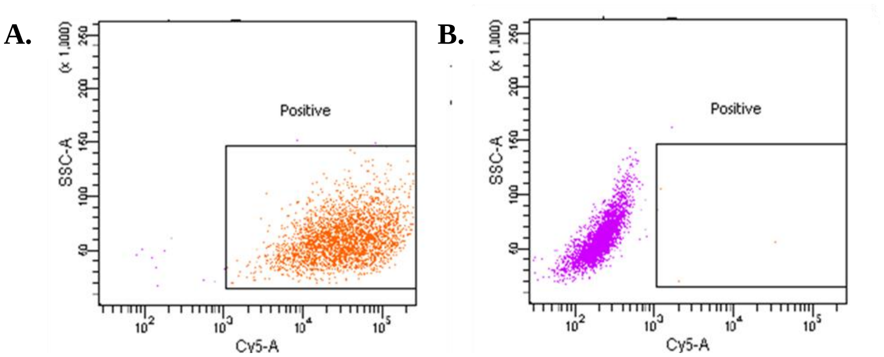

Figure 64. Efficiency of transfection of NBs. In RSV-infected cells which had been treated with RSV-NB , 95.3 % of the population had a positive fluorescent signal, indicating a >95.3 % efficieny of transfection. **B.** In contrast, RSV-infected cells which had not been treated with RSV-NB did not show a positive fluorescent signal.

Further experiments were conducted to verify NB internalization. Gold colloid staining revealed diffuse and perinuclear distribution of NB in the cytoplasm of HEp-2 cells. RSV-NB were visible in RSV-infected cells to the same extent as uninfected cells (**Figure 65**). Using this method, observations indicated that both RSV-NB as well as GAPDH-NB are efficiently internalized in HEp-2 cells, and that internalization is independent of the specific target sequence.

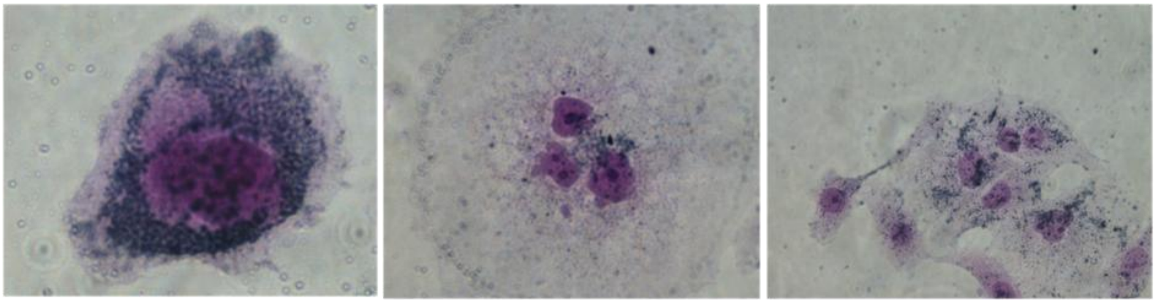

Figure 65. Light micrograph of RSV-NB within HEp-2 cells. Light micrographs of nanoblossoms (black dots) in HEp-2 cells incubated with NBs. Nanoblossoms appear as black punctate spots against the white background due to treatment with the Goldenhance gold colloid amplification kit (Nanoprobes, Inc.). Distribution of the NB is diffuse and perinuclear, qualitatively suggesting a non-endosomal mode of translocation. Cells did not take up trypan blue, the exclusion of which indicates cell viability of labeled cells. (A) HEp-2 incubated with 0.5 nM GADPH-NB. (B) RSV-induced cell syncytium showing intracellular RSV-NB. (C) Uninfected HEp-2 still internalize NB directed against RSV RNA.

To elucidate the mechanism of NB uptake in HEp-2 cells, biochemical and pharmacologic-based endocytosis inhibition assays were performed. These assays evaluated the effects of impairing single modes of classical endocytosis on NB translocation across the cell membrane (**Table 8**). Preliminary studies support the hypothesis that NBs are capable of efficient transport into mammalian cells due to an intimate interaction with lipid domains on cell membranes, rather than energy-dependent endocytosis. Fluorescence-based pharmacologic screening assays revealed that the compounds or conditions that influence cell membrane fluidity

Inhibitor	Mechanism of Action	Effect on NB fluorescence
Chlorpromazine	inhibits clathrin pit formation	none
Chloroquine	inhibits endosomal acidification	<-10 %
Serum	numerous, uncharacterized	-30%
Heparin	competitively inhibits heparin sulfate proteoglycan-mediated endocytosis	none
4C pretreatment	reduces membrane fluidity, inhibits energy-dependent endocytosis	-20%
Azide/2-deoxyglucose	depletes cellular energy	<-10%
Nystatin/Progesterone	depletes membrane cholesterol, inhibits lipid raft/caveolin-mediated endocytosis	30%
Cytochalasin D	inhibits actin-based intracellular transport	<-10%
Nocodazole	inhibits microtubule-based intracellular transport	<-10%
Brefeldin A	inhibits late endosomal trafficking (Golgi-ER sorting)	<-10%
Dynasore	inhibits dynamin-mediated endocytosis (including clathrin, caveolin)	<-10%
Amiloride	inhibits fluid-phase macropinocytosis	none
Genistein	inhibits tyrosine kinases	none

Table 8. Effect of Classic Endocytosis Inhibitor on cellular entry by NB. The observed decrease or increase in relative fluorescence signal in microplate spectrophotometry assays is compared to control. Results are shown for GADPH-NB signal in uninfected HEp-2 cells, although results are representative of those observed for RSV-NB in infected cells.

had profound influences on NB fluorescence (**Figure 66**). Nystatin and progesterone, which induces cholesterol sequestration and disturbs membrane fluidity and continuity, enhanced NB fluorescence by up to 70%. Alternately, preincubation at 4°C, which decreases membrane fluidity, reduced NB fluorescence by over 15%. The presence of fetal bovine serum in the media reduced NB signal by over 20%.

In contrast, inhibitors of classical clathrin-mediated endocytosis (chlorpromazine),(143) dynamin-dependent endocytosis (Dynasore),(144) and macropinocytosis (amiloride),(145) did not exhibit dose-dependent effects on NB signal, nor did downstream trafficking inhibitors such as brefeldin A (Golgi-ER trafficking)(146) and nocodazole (microtubule-assisted trafficking).(147) Even global endocytosis inhibitors such as cellular energy depletion (sodium azide, 2-deoxy-D-glucose)(148) did not reduce NB signal below a 15% margin, suggesting that energy-dependent translocation mechanisms play a minimal role in cytosolic delivery of NBs (**Figure 66**).

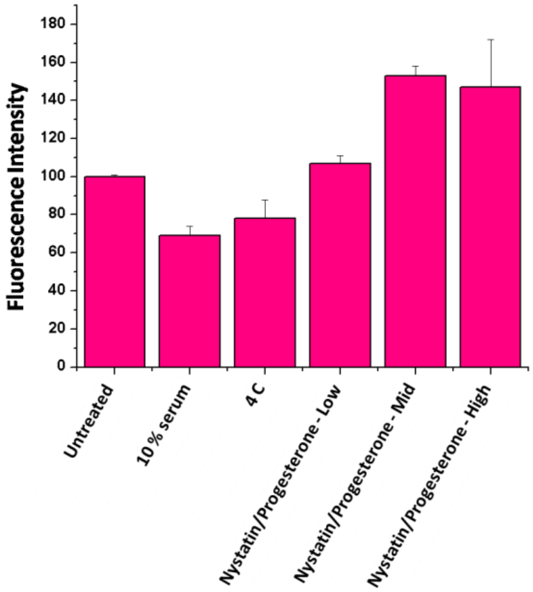

Figure 66. Effect of Global Endocytosis Inhibitors on cell entry by NBs. Summary of major inhibitors and enhancers of NB transport. Results are expressed as mean ± SD, n = 3, for HEp-2 cells incubated with GADPH-NB, although trends were similar for RSV-NB.

The cytotoxic effects of RSV-NB probes were examined by flow cytometry over a wide range of initial infection concentrations. After 35 hours of infection, the samples were treated with PI and analyzed by flow cytometry. At each MOI, samples treated with RSV-NB showed no decrease in cell viability when compared to untreated controls (**Figure 67**). The cell death that was observed resulted from natural virally induced lysis. This result demonstrates that RSV-NB treatment does not have a significant cytotoxic effect at concentrations relevant to signal detection. To determine the effect of NB treatment on the progression of infection, a plaque assay was used. These assays showed that while RSV infection was somewhat hindered by RSV-NB treatment, four days post infection, cells were still heavily infected. Treatment with RSV-NB did not completely halt the progression of the viral infection.

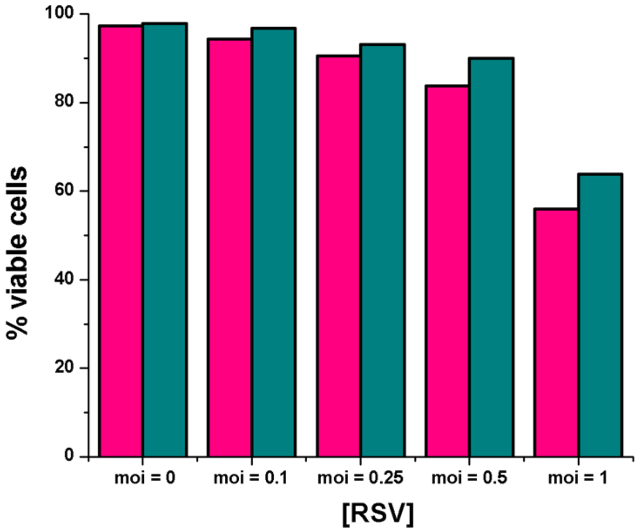

Figure 67. Cytotoxicity of RSV-NBs. Flow cytometry was used to show RSV-NB treated samples (blue) did not show greater cell death than untreated samples (pink). Samples were infected with a specified MOI and the extent of cell death determined after 35 hours infection. The similar percent of viable cells for RSV-NB treated sample and untreated samples indicates that RSV-NBs are not cytotoxic at relavent concentrations.

Labeling

Confocal microscope images showed that RSV-infected samples treated with RSV-NBs displayed a distinct fluorescent signal. The uninfected control samples remained dark at analogous detector gains and were indistinguishable from the untreated control samples (**Figure 68**). Thus, while uptake of NB is nonspecific, fluorescence of NB is RNA-specific. Signal analysis of the orthogonal slices xy and xz reveal that the RSV-NB signal was clearly in the cytosolic region of the cell. Further, the RSV-NBs were likely not localized to an endosome. If they had been sequestered in endosomes, a fluorescent signal would not have been observed as the virus' RNA is found exclusively in the cytosol.

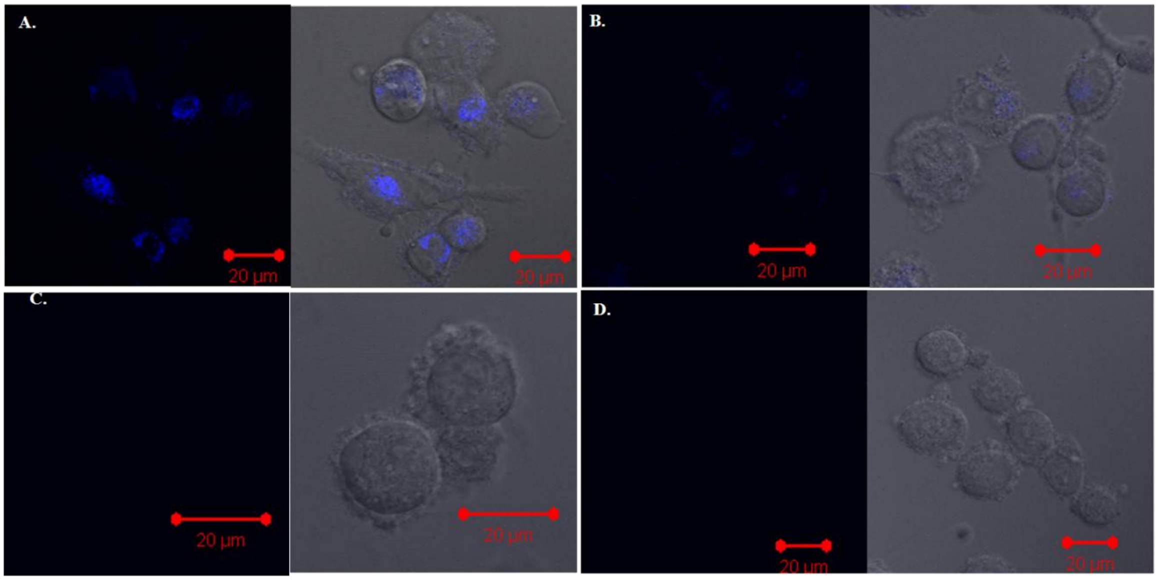

Figure 68. ***In vivo* specificity of RSV-NBs.** RSV-infected HEp-2 cells which have been treated with 0.5 nM RSV-NBs show a distinct fluorescence signal as seen by confocal microscopy (A). By comparison, uninfected HEp-2 cells treated with equal concentrations of RSV-NBs showed no signal at comparable detector gains (B). RSV-infected (C) and uninfected control samples which have not been treated with RSV-NBs also displayed no fluorescent signal.

To confirm the ability of NBs to enter and label viable non-infected cells, GAPDH-NBs were used to label HEp-2 cells (**Figure 69**). These samples clearly demonstrated fluorescent signal when treated with GAPDH-NB that was not present in untreated samples. RSV-infected cells simultaneously labeled with both RSV-NB and GAPDH-NBs showed differential labeling of the GAPDH sequence and viral RSV RNA. These experiments demonstrated the ability to use different sequences on NBs to simultaneously label more than one target RNA sequence. Some colocalization of RSV-NBs and GAPDH-NBs was seen (**Figure 70**). Importantly, while fluorescent signal confirmed the presence of multiple NB species RSV-infected cells, only the GAPDH-NB fluorescence was observed in healthy uninfected cells.

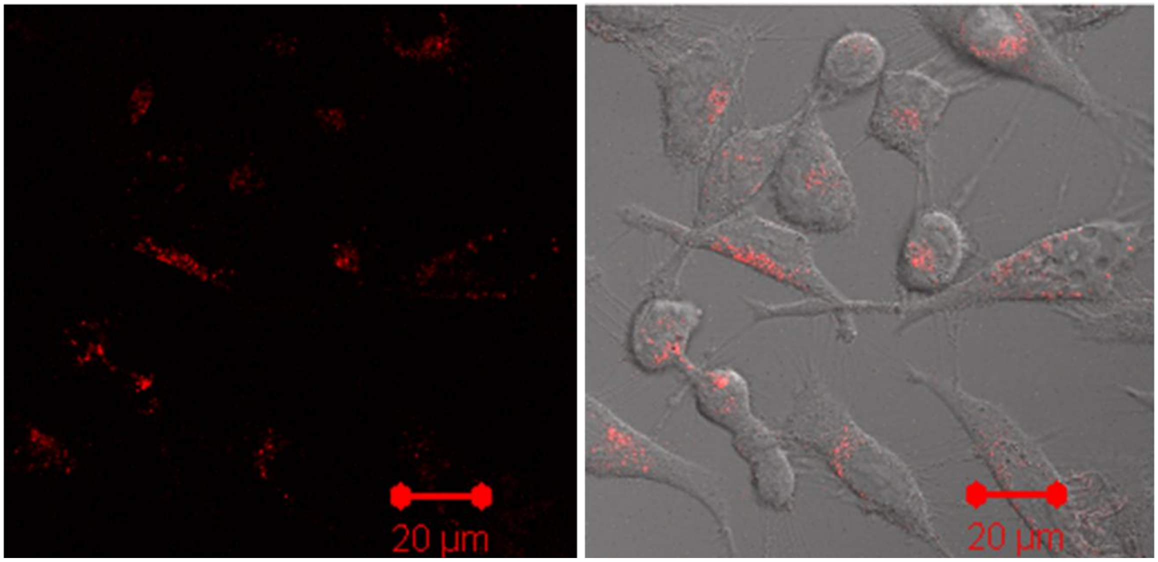

Figure 69. ***In vivo*** **labeling of housekeeping gene using GAPDH-NB.** HEp-2 cells which have been treated with 0.5 nM GAPDH-NBs show a distinct fluorescence signal as seen by confocal microscopy demonstrating the ability of of NBs to enter healthy HEp-2 cells.

Two experiments were performed to explore the multicolor labeling potential of NB and traditional labeling techniques. Multiplexed spatial imaging was used to simultaneously label

RSV viral RNA as well as two cellular organelles, the nucleus and mitochondria (**Figure 71**). Though the nucleus and mitochondria are clearly visible in all samples, fluorescent RSV-NB signal was only visible the in RSV-infected cells. These experiments also clearly show that the RSV-NB signal is not located in the nucleus and rather appears to be in the cytosolic region of the cell, as previously discussed.

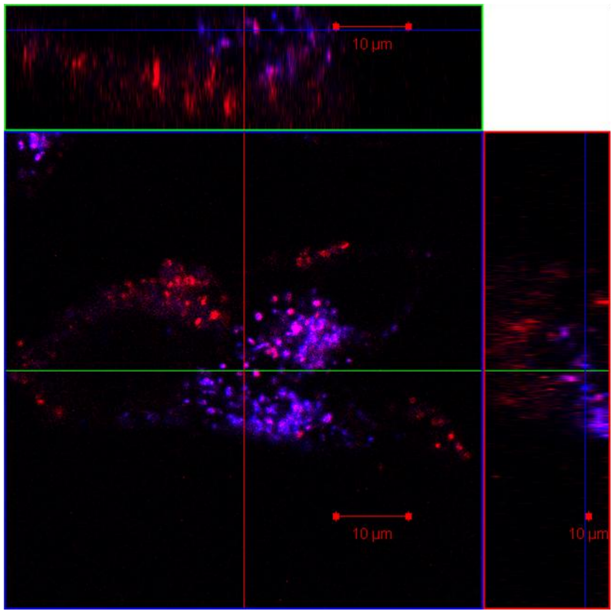

Figure 70. Dual labeling of RSV-infected HEp-2 cells with RSV- and GAPDH-NBs. RSV-infected HEp-2 cells have been treated with both 0.5 nM RSV-NB and 0.5 nM GAPDH-NB show. GAPDH-NB signal (red) can be distinguished from the RSV-NB signal (blue). In these dual labeled samples, areas of colocalization of the GAPDH-NB and RSV-NB signal can be identified. However, the majority of the RSV-NB signal is located in a different cellular region than the GAPDH-NB signal.

The RSV F-protein and viral genomic RNA were colabeled in HEp-2 cells. The F-protein was labeled using anti-F protein primary antibodies and 525 nm quantum dots as previously described in *Bentzen, et al*, then treated with RSV-NBs(149). RSV-infected cells showed the F-protein quantum dots and RSV-NBs found in the same cells with the F-protein signal localized to the surface of the cells and the genomic RNA localized to the cytoplasmic region. In contrast, uninfected samples did not show signal from either the F-protein or RSV-NBs (**Figure 72**).

Discussion

Synthesis and Characterization

An ideal probe to detect and study RNA in live cells would be easily synthesized, suitable for entering live cells, resisting cellular degradation and be able to specifically identify a RNA strand of interest. The characterization of NBs has shown this tool to possess many of these ideal properties. Dynamic light scattering showed a diameter increase expected as a result of the addition of the hairpin DNA to the AuNP; however, it did not show any peaks corresponding to larger diameters which would indicate aggregation of AuNPs. NBs serve as a source of localized high concentration of the probe (40 probe strands per AuNP), and is therefore able to detect low concentrations of compliment. *In vitro* specificity assays showed that NBs could distinguish between its target sequence and a random sequence containing a similar GATC make up. The increased fluorescent signal is on the same order of magnitude as previously seen with other oligonucleotide functionalized AuNP. Moreover, because the use of different dyes gave distinct emissions spectra, NBs for different strands of target RNA can be used simultaneously. In case of both the RSV-NB and the GAPDH-NB, the conjugation of the fluorescently labeled oligonucleotide to the AuNP did not cause a significant shift in the emissions peak.

Previous fluorescently labeled oligionucleotide based tools were susceptible to probe degradation, often resulting in high background. DNase I cleavage would emancipate the oligonucleotide from the surface of the AuNP, relieving the gold-induced quenching. Analogous molecular beacon probes, which are not conjugated to AuNPs, are degraded at a rate of 1.25 nmol

min^{-1}, 17x quicker than RSV-NBs and 13x quicker than GAPDH-NB. Previous reports have shown that NFs are degraded at a rate of 0.275 nmol min^{-1},(34) which is almost 4 times faster than the hairpin configuration of RSV-NBs and GAPDH-NBs. This decreased susceptibility to degradation by DNase I suggests the NB construct may be more stable in cellular environments. This stability allows for a lower background signal from NBs, making them a more reliable probe for both detection and spatial resolution of RNA trafficking.

Transfection

The ability to distinguish RSV-infected HEp2 cell populations from uninfected makes them an interesting candidate for the detection of RSV infections. Similar fluorescent oligonucleotide-based approaches have been applied to the identification of RSV infected cells. Molecular beacons which target end-intergenic regions of bovine RSV have been utilized for the identification of infected cell populations. However, effective delivery requires a reversible permeabilization method such as sterptolysin O (SLO). While this method is considered less damaging than conventional transfection methods, its delivery efficiency is cell-type dependant. In contrast, the NB have been shown to efficiently enter live cells without the aid of any transfection agent. NBs instead show transfection efficiencies of <95% which is consistent with previous literature showing that oligonucleotide functionalized AuNPs can readily pass through the cell membrane into cells. NF's were shown by flow cytometry to have an transfection efficiency of <99%. In addition, cells treated with NF have showed a 2.5 increase in fluorescent intensity as compared to a non-complimentry control. This is similar to the 3 fold signal difference seen by flow cytometry between RSV-infected and uninfected cell populations. This indicates that the NBs are just as efficient of a probe in cell as NFs. However, the use of NB can be expanded beyond simple detection to monitoring viral trafficking because of the unique characteristic that offers spatial resolution. Because the fluorescent signal was specific to RSV-infected cells, additional gold colloid staining examine the presence of NBs in both RSV-infected and uninfected cells. These studies verified the conclusion that the increase in fluorescent intensity seen in RSV-infected cells was the result of NB opening, not more efficient transfection into infected cells.

Though the ability of NBs to readily cross the plasma membrane into cells had been confirmed, these experiments offered little to explain the mechanism of NB uptake. Therefore, the biochemical and pharmacologic-based endocytosis inhibition assays were used to provide insight into potential mechanisms. The increased NB uptake found with nystatin and progestorne may be a result of the depletion of cholesterol by nystatin and progesterone *via* enhanced fluidity of lipid domains. However, these results could be a side effect of the pore forming capabilities of nystatin compounds, although membrane permeabilization has been mainly observed in fungi, not mammalian cells.(150) The observation that 4°C preincubation, impaired NB signal by more than 15%, which is not seen with any specific endocytosis inhibitors, supports the hypothesis that NB uptake is primarily due to lipid membrane-NB interactions. Additionally, the decrease in NB uptake seen in the presence of fetal bovine serum could be either due to serum protein adsorption on NB surfaces, thereby conferring steric hindrance or bulkiness upon the construct, or due to competitive inhibition of the attachment protein(s) or lipid domains on the cell membrane by serum components.(151) The general mechanism accepted for many AuNPs in the size range of 14-100 nm and other functionalized nanoparticles such as DNA wrapped single-walled carbon nanotubes arises from the adhesion of media proteins to the surfaces of nanoparticles during a typical cell culture incubation experiment. This results in receptor-mediated endocytosis. Interestingly however, in the case of NBs, endocytosis inhibitors were found to have minimal effect on the transfection of NBs and energy dependant translocation mechanisms appear to have a minimal influence. With low cellular toxicity, NBs proved to be a promising tool to expand upon to probe their labeling capabilities in live cells experiments.

Labeling

The labeling of viral RNA in RSV-infected HEp-2 cells made it possible to not only identifies infected cell samples, but also where it is localized within the cell. The use of other onligonucledutide functionalized AuNP, such as NFs, could only provide information about presence of RNA, void of spatial information. Previously, RSV has been labeled using molecular beacon probes in live cells. The use of NBs gave image information of equal caliber to the molecular beacons, without many of the drawbacks associated with the use of these probes. At analogous infection times, the NBs are able to detect RSV infection as efficiently as the molecular beacon probes. However, the NBs are more resistant than molecular beacons alone to DNase degradation and therefore are a more reliable tool. The NB signal is also clearly localized inside the cytosolic region of the cell, where viral RNA is expected to be located. In contrast, other nanotechnology based probes such as quantum dots are often sequestered in vesicles or become non-homogenously distributed in the cytoplasm, limiting their use to fixed cells. The nanoblossom approach alleviates these problems and allows for specific RNA monitoring in living systems.

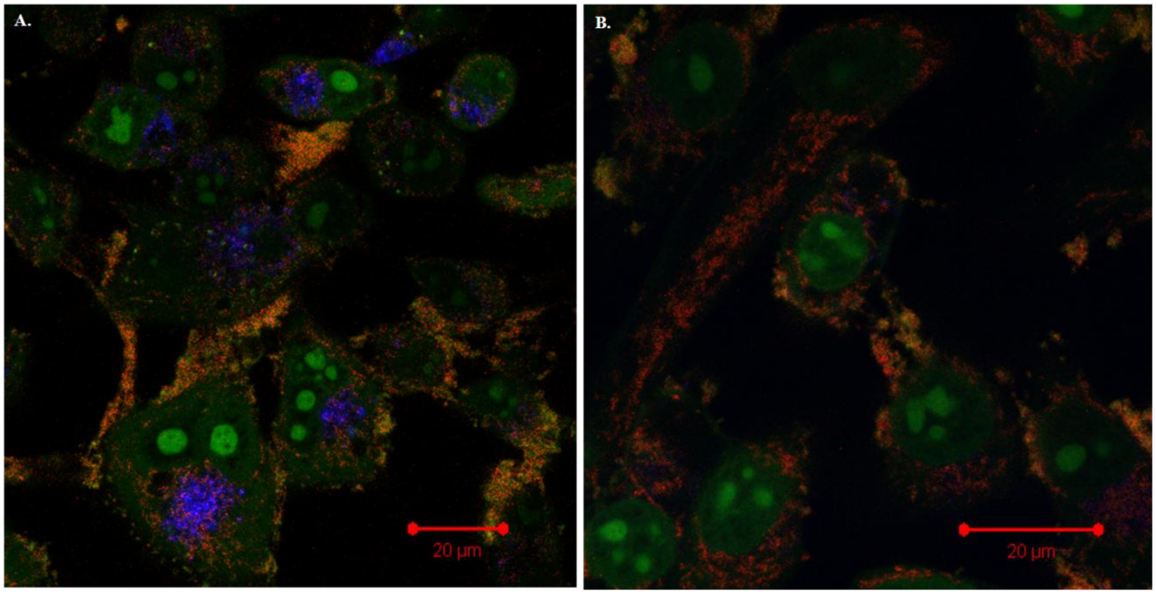

Figure 71. Colabeling of RSV RNA and cellular markers. RSV-infected (A) and uninfected (B) Hep-2 cells were treated with RSV-NB (blue), mitotracker dye (red) and SYTO-13 nucleic acid stain (green). The RSV-infected samples showed a RSV-NB signal located in the cytosolic region of the cells that was not present in the uninfected control samples.

Because RSV-infected cells already represent a compromised host system, it was important to establish that NBs could effectively enter and label healthy cells. For this, a control sequence compliment to the housekeeping gene GAPDH was used to label healthy cells. HEp-2 cells labeled with GAPDH-NB showed fluorescent signal diffused in the cytosolic region of the cell similar to previously published GAPDH-GFP confocal experiments which show localization of GAPDH to the cytosol. The ability of label more than one specific strand of RNA through the use of multiple NBs was explored by labeling HEp2 cells with both RSV- and GAPDH-NBs. Both strands of RNA could be found in the cytosolic region of the cell though they were clearly distinguishable from each other.

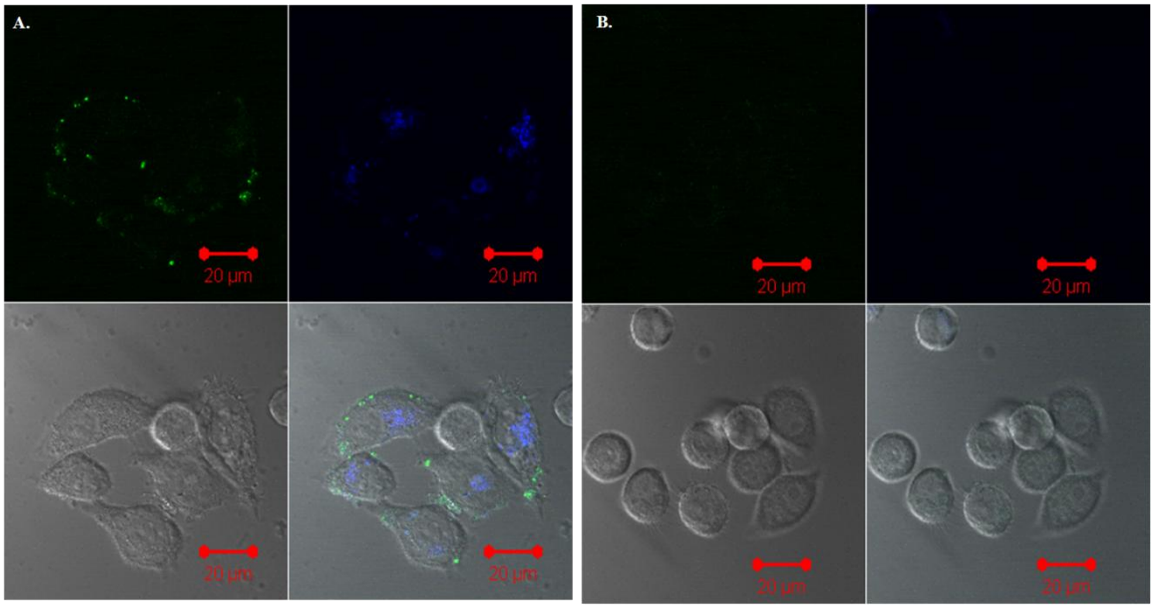

Figure 72. Colabeling of RSV RNA and RSV F-protein. Confocal microscopy was used to demonstrate the multiplexing potential of RSV-NBs as well as illustrate the spatial information avilable by the use of RSV-NBs. For these assays, the viral surface protein, F-protein, was labeled using 525 Qdots and the viral RNA labeled using RSV-NBs. In the RSV-infected samples, the F-protein (green) is visible on the surface of the cell while the viral RNA (blue) is localized to the interior cytosolic region of the cells (A). By comparison, the uninfected control samples did not show a fluroescent signal for either the F-protein or viral RNA (B).

Bs are a specific, stable and nontoxic tool for RNA detection in live cells. The greatest potential of NBs is their ability to obtain spatial information, in particular, the relationship between RNA localization and other aspects of cellular geography in live cells. NBs could be combined with other labeling techniques to acquire enriched spatial information, enabling one to explore the relationship between viral RNA and other cellular components such as organelles or the encoded viral protein. The co-labeling of viral RNA using RSV-NBs and the nucleus and mitochondira using organelle specific dyes demonstrates this ability (**Figure 72**). The cellular markers add a frame of reference for gaining further insight into the cellular location of the viral RNA.

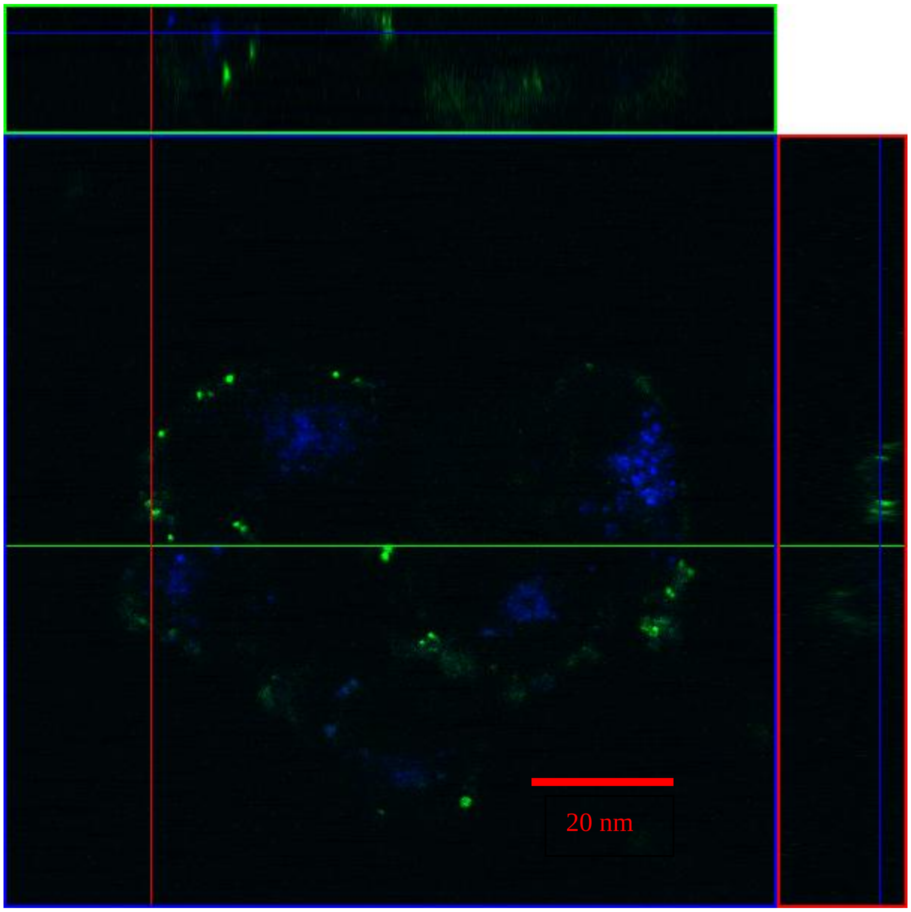

Figure 73. Orthogonial View of Colabeling of RSV RNA and RSV F-protein. The orthogonial view of the RSV-NB/QD dual labeled RSV-infected cells. In these dual labeled samples, as expected, the F-protein is found largely at the surface of the cell whereas the RSV-NBs are localized to the interior of the cell.

Final labeling experiments served to highlight the potential of NBs for live cell labeling and imaging of RNA within the context of a paromyxovirus infection (**Figure 73**). In Figure 78, RSV-NBs were combined with anti-body labeling techniques used in conjuction with quantum dots to simultaneously label both the viral RNA and a viral surface protein, the F-protein. Similar labeling of the F-protein with quantum dots has previously shown that at 35 hours, a small amount of F-protein is already visible on the membrane of an infected cell. However, little was known about the location of the genomic RNA. Our findings were consistent with the expected localization of the F-protein but were able to provide new insight into the location of the genomic viral RNA. It is clear that the viral RNA is still largely localized in the inner region of the cell at this point. However, by tuning the NB probe sequence to regions of RNA specific to certain genes, one would be able to determine exactly how that RNA is trafficked in relation to the protein it encodes for.

Conclusion

There is a need for new probes to label and image RNA in live cells that are able to overcome the limitations of those currently available. To design a better probe, it would require a specific list of optimal characteristics including the ability to be easily synthesized and characterized, specific signal with low non specific signal, favorable *in vivo* properties (low cytotoxicity, stable, and easily internalized) as well as possess the ability to be combined with other traditional labeling techniques to achieve multiplexing and ultimately use this to gain spatial resolution. Nanoblossoms are a novel probe which aim to fulfill these requirements to improve our ability to label and monitor RNA in live cells.

To demonstrate their utility, NBs have been developed within the context of Respiratory Syncytial Virus. As such, NBs are able to provide a new tool to aid in the examination of viral lifecycle. In addition to the detection of RSV, RSV-NBs were used in live cells to relay spatial information about cellular trafficking of RNA. This was demonstrated by the multicolor labeling of cytosolic viral RNA, with RSV-NB, and the viral surface F-protein, with Qdots. By expanding these techniques through the alteration of the hairpin loop sequence and the choice of 3’ terminal dye, NBs can be readily tuned to study multiple specific sequences of RNA simultaneously.

Future Work

The experiments described here demonstrate the most preliminary steps in the development of a probe with great potential. However, the next stages of development would focus on both better characterizing the properties of the nanoblossoms themselves as well as investigating their range of applicability. Specific characterization experiments would include investigating what effect altering the loading of hairpins onto AuNPs would have on amount of fluorescent signal seen in the presence of compliment. It would be interesting to see if the number of hairpins per AuNP would result in an increase of fluorescence associated with more hairpin opening or if the increased number of hairpins would cause a decrease in fluorescent signal as a result of steric interactions inhibiting hairpin opening. Other examples of optimizing and characterizing the NBs would include optimizing the hairpin including the length of the compliment stem and the length of loop sequences. The GATC make up of both the stem sequence and the loop sequence could have potential effects on the specificity of the NB. In the case of the stem, altering the GATC make up could increasing or decreasing the strength of the stem binding. In contrast, the GATC make up of the loop region would effect how strongly the compliment binds to the NB and could effect any potential of the compliment "coming off" of the NB once it had initially bound.

Though characterization and optimization of NBs is important for the development of the probe, it is also important to investigate the range of applicability. To do this, NBs would be applied to the detection and labeling of a variety of RNA sequences and even more interestingly, to a wide range of cell types. In order for NBs to become a widely utilized probe, it is essential to demonstrate that they can be effective tools in systems beyond the narrow one in which we have developed it. Finally, it would be interesting to do more studies into the mechanism of NB internalization. By developing a better understanding of how NBs are able to enter cells, it would give more insight into the potential limitations of the probe because the probe would be limited by its mechanism of internalization to cells which would allow for internalization.

APPENDIX A

LABELING OF CELLULAR ORGANELLES IN MDCK CELLS

Subcellular localization is an important aspect of many biological processes. In the development of tools to study cellular trafficking, the ability to label cellular markers such as organelles is a valuable skill. Here, several organelles have been labeled in the polarized MDCK cells and nonpolar HEp-2 cells including mitochondria, endoplasmic reticulum, nucleus, tight junctions (MDCK only) and actin.

Materials and Methods

Materials

DMEM culture media, OptiMEM culture media, gentimyacin, and phosphate buffered saline were obtained from Gibco. L-glutamine, amphoterician B, non-essential amino acids, and anti-calnexin antibodies were obtained from Sigma. Formaldhyde and bovine serum albumin were obtained from Fisher Scientific. Triton-X was obtained from MP Biomedicals. The human cell line, HEp-2, was obtained from the American Type Culture Collection (ATCC). All other chemicals were obtained from Invitrogen. All chemicals were used as they were received unless otherwise noted.

Cell Culture

The adherent canine kidney epithelial cell line, MDCK, was maintained in continous culture with DMEM (GIBCO/BRL), supplemented with 10% fetal bovine serum, 1% non-essential amino acids, 1% L-glutamine, 1% amphoterician B, and 0.1% gentimyacin in an atmosphere of 5 % CO_2, 5% humidity at 37 °C. The human epithelial cell line, HEp-2, was maintained in OptiMEM culture media, supplemented with 2% fetal bovine serum, 1% L-glutamine, 1% amphoterician B, and 0.1% gentimyacin in an atmosphere of 5 % CO_2, 5% humidity at 37 °C. Cell viability was determined by Trypan Blue exclusion using a hemocytometer.

Cell Labeling and Confocal Microscopy

MDCK cells were plated at 5 x 10^4 cells per dish onto Mat-Tek dishes and allowed to grow to 80% confluency in an atmosphere of 5 % CO_2, 5 % humidity at 37 °C. After 24 hours, the media was aspirated from the samples, which were then gently washed with phosphate buffered saline solution (PBS) 3X to remove any remaining media. The samples were then fixed by incubating with 3.7 % formaldehyde for 10 minutes at 37 °C. Following fixation, the samples were washed 3x with PBS and were subsequently permeablized by incubating 0.2 % Triton X-100 for 7 minutes at 4 °C. After two additional PBS washes, the samples were incubated with 2 % BSA blocking buffer for 1 h at 4 °C, then prepared with the appropriate fluorophore. For tight junction labeling, the samples were incubated for 1 h at 4 °C with an anti-ZO-1 antibody conjugated to a 525 nm quantum dot diluted in PBS (2 % BSA) to a final antibody concentration of 5 mg/mL. The nucleus was labeled by incubating the samples with 2.5 μM TO-PRO-3 iodide nuclear stain (Invitrogen) diluted in PBS with 2 % BSA for 30 min at 4 °C. To label F-actin, samples were treated with 10 μM rhodamine phalloidin (Invitrogen), diluted in PBS (w/ 2 % BSA) and incubated for 30 min at 4 °C. To label the ER, anti-calnexin antibodies were used as primary antibodies and labeled with 525 quantum dots. Samples doubled labeled for actin and the nucleus were first labeled with rhodamine phalloidin (as described above) then washed three times with PBS. This was followed by treating the samples with TO-PRO-3 (as described above). All double labeled samples were treated similarly. For actin/tight junction labeling, the tight junctions were labeled first, followed by F-actin. Nucleus/tight junction double labeling was achieved by first labeling the tight junctions then the nucleus. Finally, the triple labeled samples were labelled initially for tight junctions, washed three times with PBS, labeled with the F-actin dye, washed again 3X with PBS and finally labeled with the nuclear dye. After labeling, all samples were washed three times with PBS, covered with 2 mL of fresh PBS and immediately imaged on the Zeiss LSM 510 Meta inverted confocal microscope. Fluorescence imaging of tight junctions was accomplished by excitation by 488 nm Argon laser, followed by collection using a long pass 515 nm filter. Fluorescence imaging of the nucleus was accomplished by excitation at 633 nm with a He-Ne laser, followed by collection using a long pass 650 nm filter. Finally, fluorescence imaging of F-actin was accomplished by excitation at 543 nm He-Ne laser, followed by collection using a long pass 560 nm filter. The λ_{max} for excitation and emission for each fluorescent label is summarized in **Table 9.** The labeling of HEp-2 cells was done similarly for nucleus and F-actin dyes.

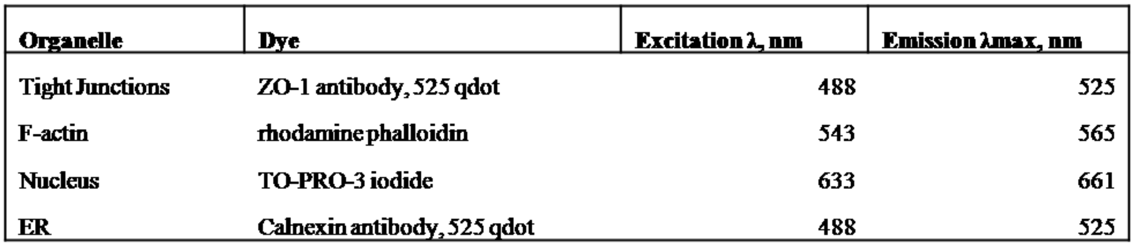

Organelle	Dye	Excitation λ, nm	Emission λmax, nm
Tight Junctions	ZO-1 antibody, 525 qdot	488	525
F-actin	rhodamine phalloidin	543	565
Nucleus	TO-PRO-3 iodide	633	661
ER	Calnexin antibody, 525 qdot	488	525

Table 9. Excitation and Emission wavelengths of Organelle markers.

Results

Samples were either single labeled, double labeled or triple labeled, combing complimentary dyes to label up to three organelles simultaneously. The resulting combinations listed are shown below for MDCK (**Figure 74-80**) and HEp-2 cells (**Figure 81-83**).

MDCK cells

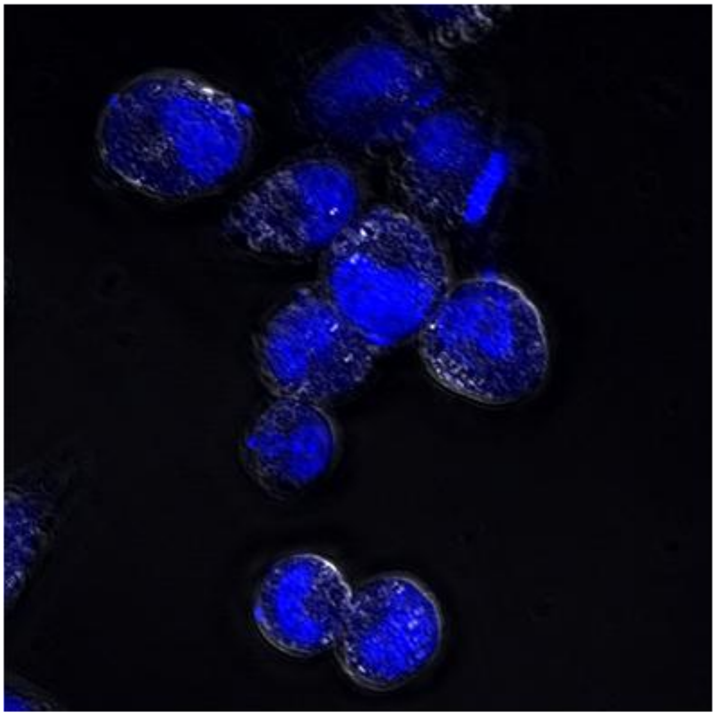

Figure 74. Nucleus labeled MDCK cells.

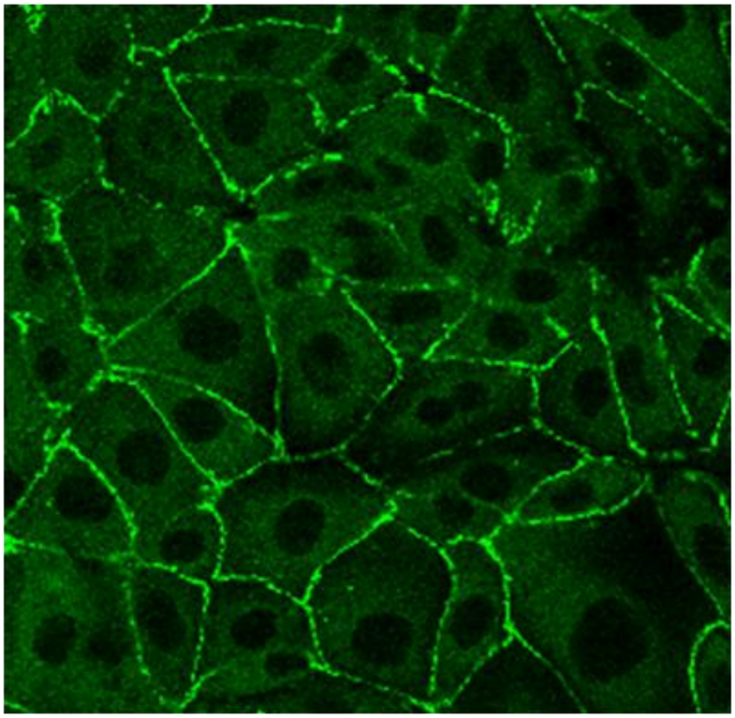

Figure 75. Tight junctions labeled MDCK cells.

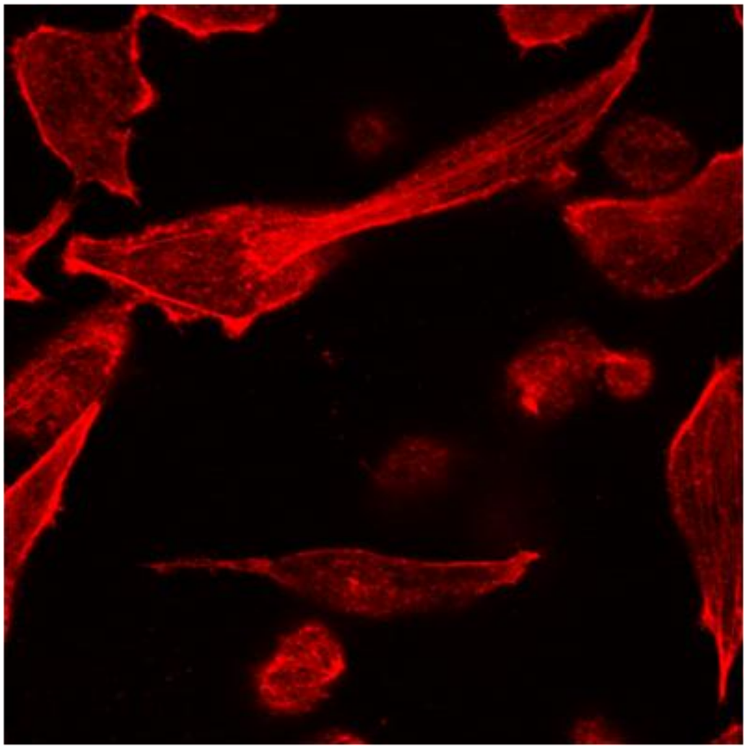

Figure 76. F-actin labeled MDCK cells.

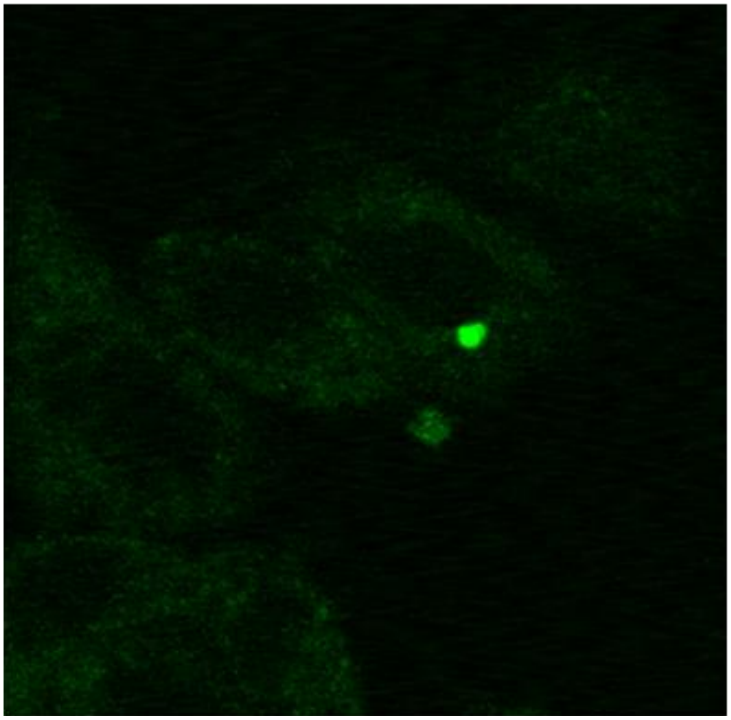

Figure 77. ER labeled MDCK cells.

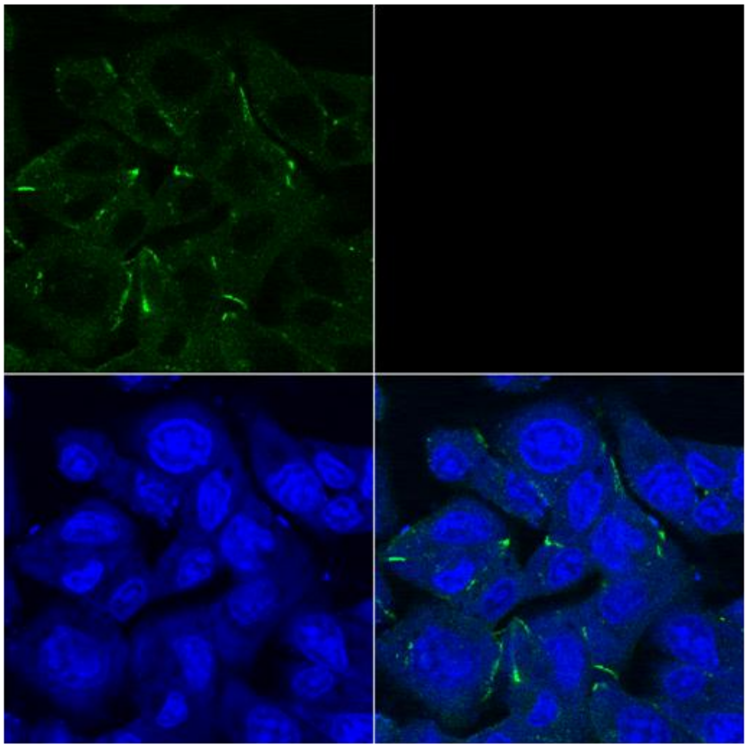

Figure 78. Nucleus and Tight Junction labeled MDCK cells.

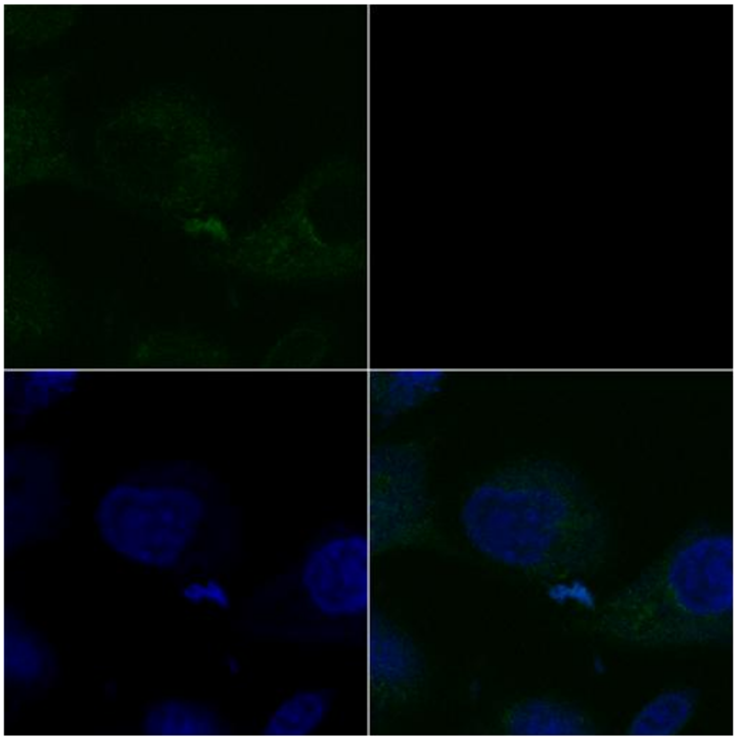

Figure 79. Nucleus and ER labeled MDCK cells.

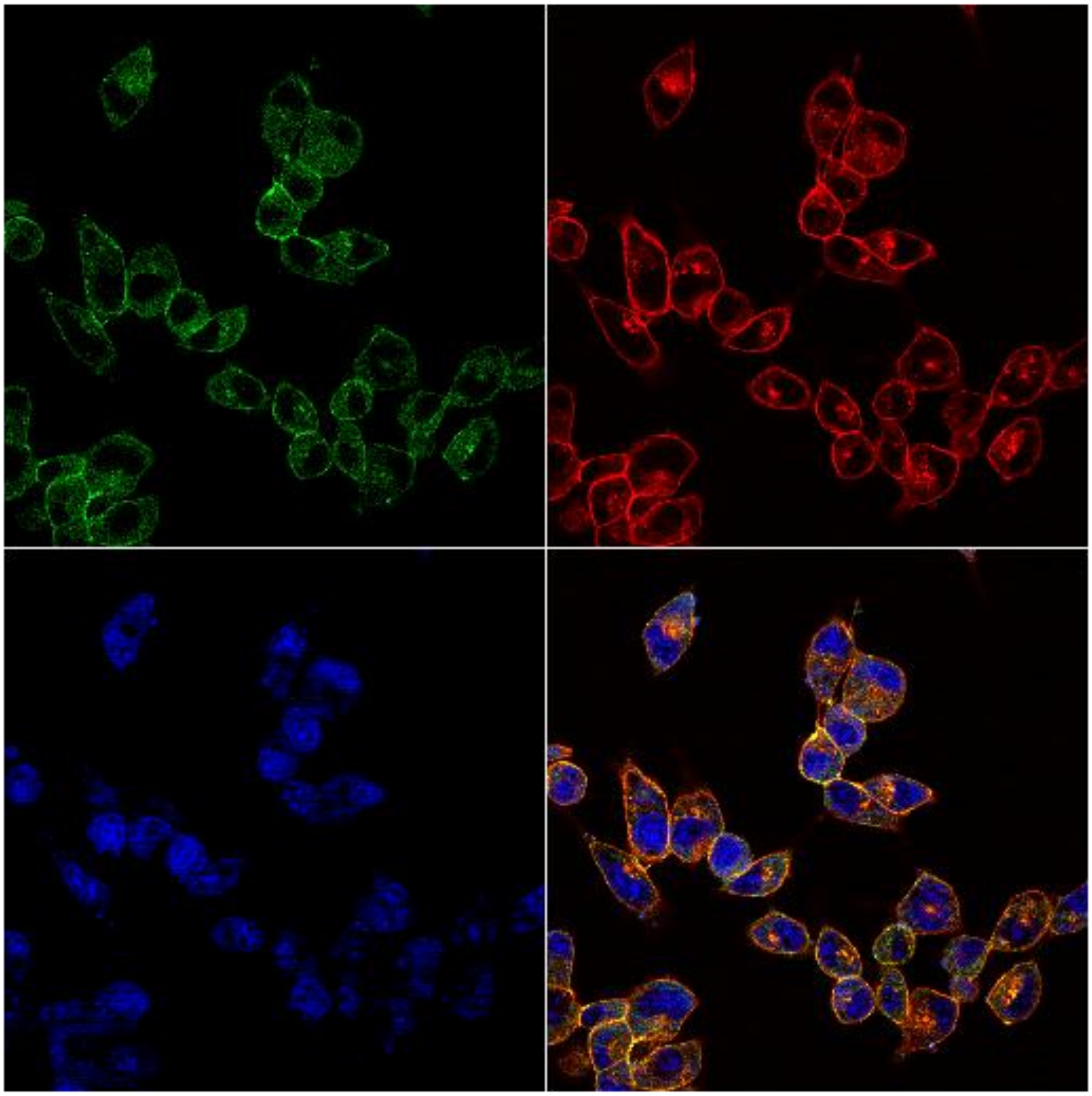

Figure 80. Triple labeled MDCK cells. Nucleus (blue), tight junction (green), and F-actin (red) labeled MDCK cells. Colocalization is shown on bottom right.

HEp-2 cells

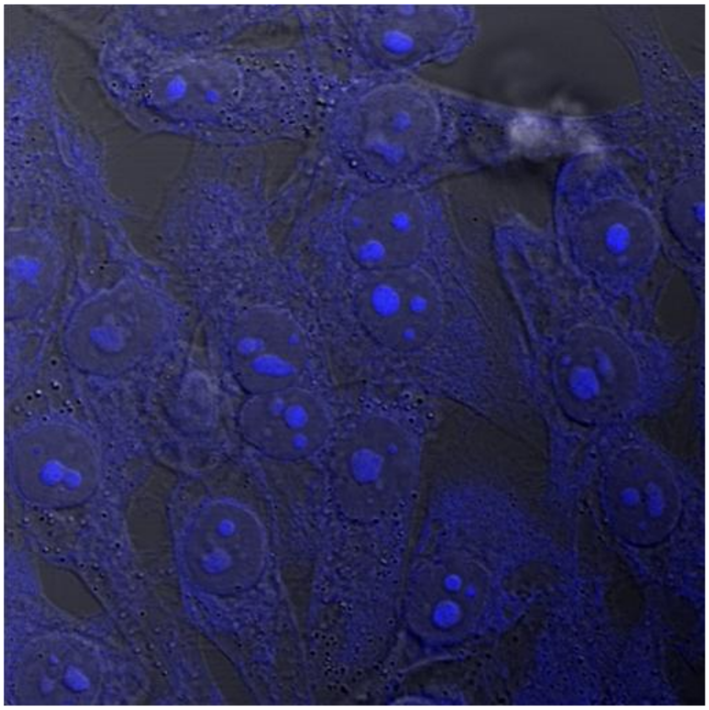

Figure 81. Nucleus labeled in HEp-2 cells.

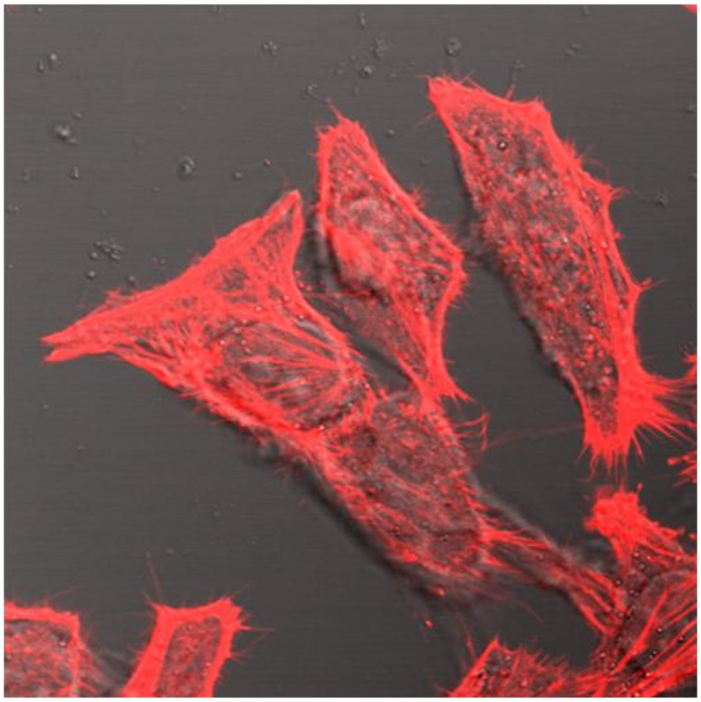

Figure 82. F-actin labeled in HEp-2 cells.

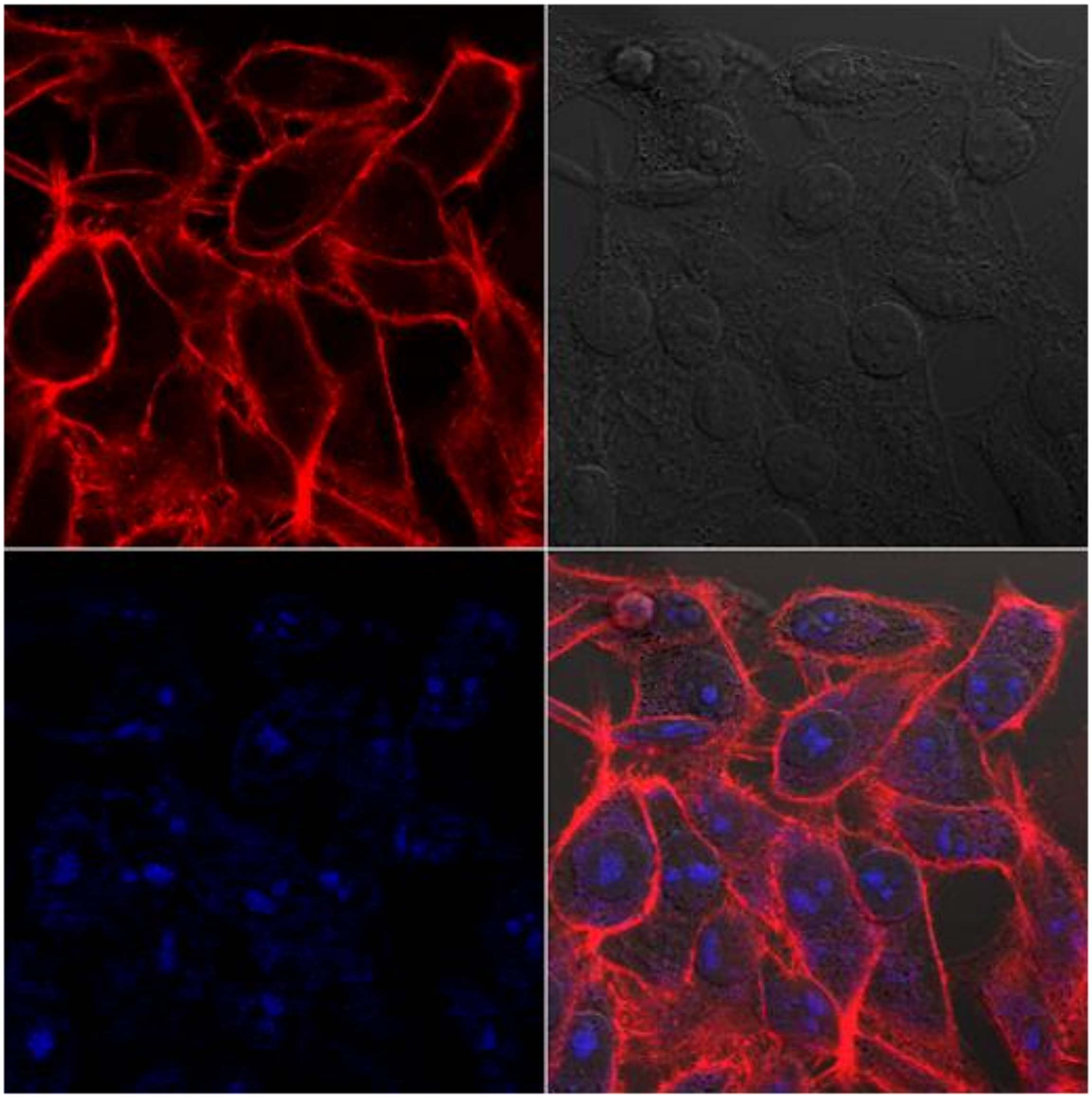

Figure 83. Nucleus and F-actin labeled HEp-2 cells.

APPENDIX B

RSV F-PROTEIN LABELING WITH QUANTUM DOTS IN HEp-2 CELLS AND FISH OPTIMIZATION

The F-protein is a RSV surface protein necessary for proper virion fusion to a host cell as well as the fusion seen in cell to cell infection. Because it is located at the surface of infected cells early in infection, it is a convenient marker for RSV infection. Here a F-protein specific antibody and quantum dots were used to label the F-protein of RSV infected cells in a time dependent manner. The development of fluorescence *in situ* hybridization (FISH) assays has become an interesting diagnostic tool in the development of virus detection systems. FISH is typically performed on cells which have been fixed in a number of ways, depending on the particular cell line of interest. The most critical factors in chosing a proper fixation and permiblization method are the propensity to produce autofluorescence and the interaction of the method with the target sequence. I this appendix, fixation and permiblization protocols for HEp-2 cells have been analyzed for their autofluorescent properties as well as their effect on target nucleic acid sequences to be used in the further development of a RSV-specific FISH protocol.

Materials and Methods

Materials

DMEM culture media, OptiMEM culture media, gentimyacin, and phosphate buffered saline were obtained from Gibco. L-glutamine, amphoterician B, non-essential amino acids, and anti-calnexin antibodies were obtained from Sigma. Formaldhyde and bovine serum albumin were obtained from Fisher Scientific. Triton-X was obtained from MP Biomedicals. All other chemicals were obtained from Invitrogen. All chemicals were used as they were received unless otherwise noted. RSV type A2 virus and RSV anti F-protein antibodies were a kind gift from the Jim Crowe laboratory (Vanderbilt University). The human cell line, HEp-2, was obtained from the American Type Culture Collection (ATCC).

Cell Culture and RSV infection

HEp-2 cells were grown in Opti-MEM growth media supplemented with 2% (v/v) fetal bovine serum (complete Opti-MEM), 2% amphoericin B, 2% glutamine and 0.1 % gentamycin and incubated in an environment of 37 °C with 5% carbon dioxide and 5% humidity. For reproducible sample infection with RSV type A2 at different multiplicity of infections (MOI), the following protocol was used. HEp-2 cells were plated and allowed to grow to 80% confluency in an environment of 37 °C with 5% carbon dioxide and 5% humidity. Once the samples reach 80 % confluency, the cells were counted using Trypan Blue exclusion and a hemocytometer, and the cell count averaged. The determined cell count was multiplied by the desired MOI to determine the correct number of plaque forming units (pfu) needed to treat the samples. This was divided by the virus titer to determine the volume of virus stock to be used in sample infection. Samples were treated with RSV diluted in complete Opti-MEM growth media to the appropriate concentration then incubated for 1 hour. After incubation, complete Opti-MEM growth media containing 0.75% w/v autoclaved methylcellulose was added to each sample and incubated for the appropriate period of infection.

Labeling and Imaging F-protein in HEp-2 cells

HEp-2 cells were plated at 5 x 10^4 cells per dish onto Mat-Tek dishes and allowed to grow to 80% confluency in an atmosphere of 5 % CO_2, 5 % humidity at 37 °C. After 24 hours, the media was aspirated from the samples, which were then gently washed with phosphate buffered saline solution (PBS) 3X to remove any remaining media media and samples were infected as described above. After the appropriate time post infection, the samples were then fixed by incubating with 3.7 % formaldehyde for 10 minutes at 37 °C. Following fixation, the samples were washed 3x with PBS and were subsequently permeablized by incubating 0.2 % Triton X-100 for 7 minutes at 4 °C. After two additional PBS washes, the samples were incubated with 2 % BSA blocking buffer for 1 h at RT. The samples were then incubated with anti F-protein primary antibodies for 30 minutes, then goat anti-mouse biotinylated secondary antibodies for one hour. Finally, the samples were incubated with 10 nm 525 strepavidin conjugated quantum dots for 30 minutes. All samples were imaged on a Zeiss LSM 510 Meta inverted confocal microscope equipped with LSM Image Browser software with 40x magnification. Samples were exciting using a 543 laser with emissions detected using a 560 band pass filter, keeping the detector gain consistent during imaging of all samples.

FISH Fixation and Permiablization Optimization

HEp-2 cells were plated at 5 x 10^4 cells per dish onto Mat-Tek dishes and allowed to grow to 80% confluency in an atmosphere of 5 % CO_2, 5 % humidity at 37 °C. After 24 hours, the media was aspirated from the samples, which were then gently washed with phosphate buffered saline solution (PBS) 3X to remove any remaining media and samples were infected as described above. Seventy two hours post infection, the samples were then fixed with one of the fixation/permiablization method combinations. These combinations are summarized in **Table 10**. To evaluate the effect of each fixation and permiablization combination on the target sequence, the samples were treated with a molecular beacon probe specific for a RSV gene end-intergenic start sequence. This sequence has three exact repeats and six almost-exact repeats with various numbers of nucleotide mismatches throughout the genome. Similar intergenic repeats are common in other RNA viruses, suggesting that the approach may be generalized to the study of other viruses. Successfully used in antisense and small interfering RNA experiments, this site was considered the most accessible and therefore a prime site for oligonucleotide binding and probe targeting. The sequence of the molecular beacon was 5'-Cal Fluor Red-**CGA CG***A AAA ATG GGG CAA ATA* **CGT CG**-BHQ-2-3' where the bold bases form the molecular beacon stem. Control samples were not treated with the molecular beacon. After treatment with the molecular beacon for 1 hr, samples were gently rinsed with PBS three times and prepared for imaging. The samples were imaged on a Zeiss LS LSM 510 Meta inverted confocal microscope equipped with LSM Image Browser software with 40x magnification. To determine the extent of autofluorescence in the region of the molecular beacon excitation and emission, samples were exciting using a 543 laser with emissions detected using a 560 band pass filter, keeping the detector gain consistent during imaging of all samples.

Results

Labeling and Imaging of RSV F-protein

The F-protein was successfully labeled in RSV-infected HEp-2 cells. Fluorescent signal corresponding to the presence of the F-protein could be detected as early as one hour. Each time point post infection saw an increase in fluorescent signal corresponding to an increase in the quantity of F-protein present (**Figure 84A-E**). By contrast, uninfected control samples showed no fluorescence at all time points (**Figure 84F-J**).

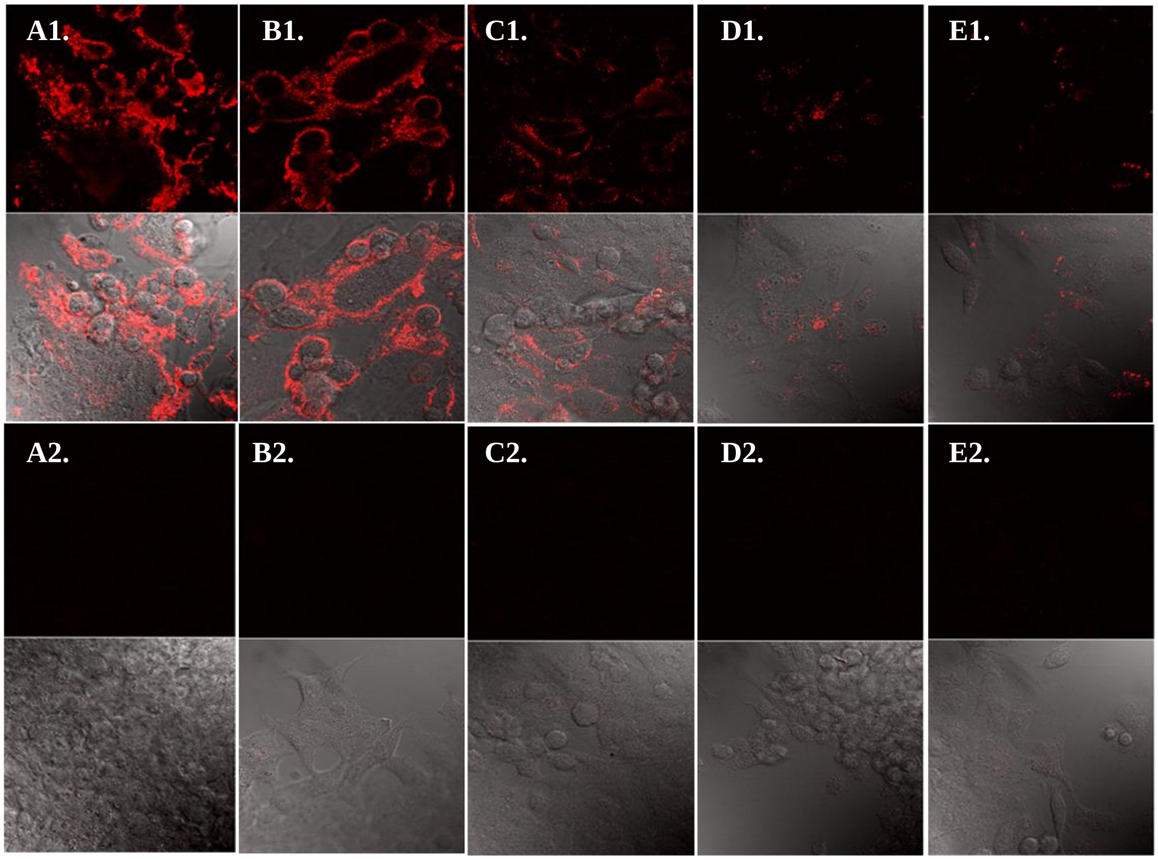

Figure 84. F-protein labeled HEp-2 cells. Infected samples showed an increase in fluorescent signal corresponding to an increase in F-protein present from 1 hr (E-1) to 96 hours (A-1). Uninfected control samples showed no fluorescence at the corresponding time point (A-2 – E-2).

FISH Fixation and Permiablization Optimization

The optimization of fixation and permiablization protocols (fix/perm) was completed by analyzing the effect of thirteen fix/perm combination on autofluorescence and target sequence interactions (**Table 10**). Of these, seven fix/perm combinations included additives aimed at reducing autofluorescence. Most fix/perm combinations showed little autofluorescence but also largely inhibited the binding of the molecular beacon to its target (**Figure 85**). A few fix/perm combinations, GT and GTS in particular, did not interfere with the binding of the molecular beacon with its target sequence. These fix/perm combinations did have higher autofluorescence than others but there was a substantial increase in fluorescence seen with the treatment of the molecular beacons suggesting these are the most promising conditions. Because there is a substantial increase in signal associated with molecular beacon treatment, the autofluorescence can be accounted for by lowering the detector gain for all samples to remove background signal, allowing only fluorescence as a result of molecular beacon binding to be detected.

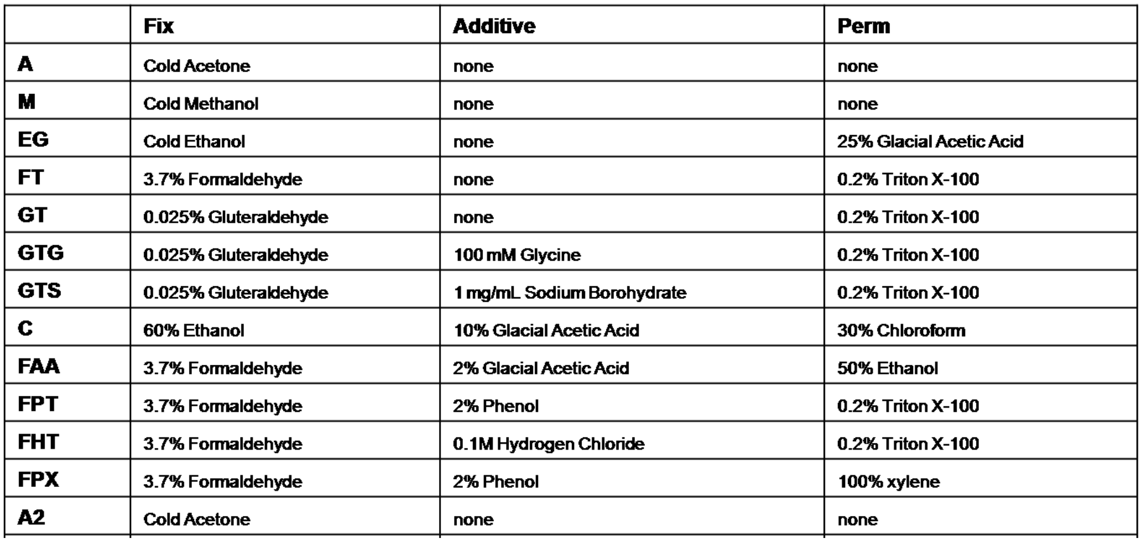

	Fix	**Additive**	**Perm**
A	Cold Acetone	none	none
M	Cold Methanol	none	none
EG	Cold Ethanol	none	25% Glacial Acetic Acid
FT	3.7% Formaldehyde	none	0.2% Triton X-100
GT	0.025% Gluteraldehyde	none	0.2% Triton X-100
GTG	0.025% Gluteraldehyde	100 mM Glycine	0.2% Triton X-100
GTS	0.025% Gluteraldehyde	1 mg/mL Sodium Borohydrate	0.2% Triton X-100
C	60% Ethanol	10% Glacial Acetic Acid	30% Chloroform
FAA	3.7% Formaldehyde	2% Glacial Acetic Acid	50% Ethanol
FPT	3.7% Formaldehyde	2% Phenol	0.2% Triton X-100
FHT	3.7% Formaldehyde	0.1M Hydrogen Chloride	0.2% Triton X-100
FPX	3.7% Formaldehyde	2% Phenol	100% xylene
A2	Cold Acetone	none	none

Table 10. Fixation and Permiablization Methods. The abbreviation representing each protocol is listed on the far left. IN the case of some protocols, additives were used in attempts to decrease autofluorescence. Those are listed in the middle column.

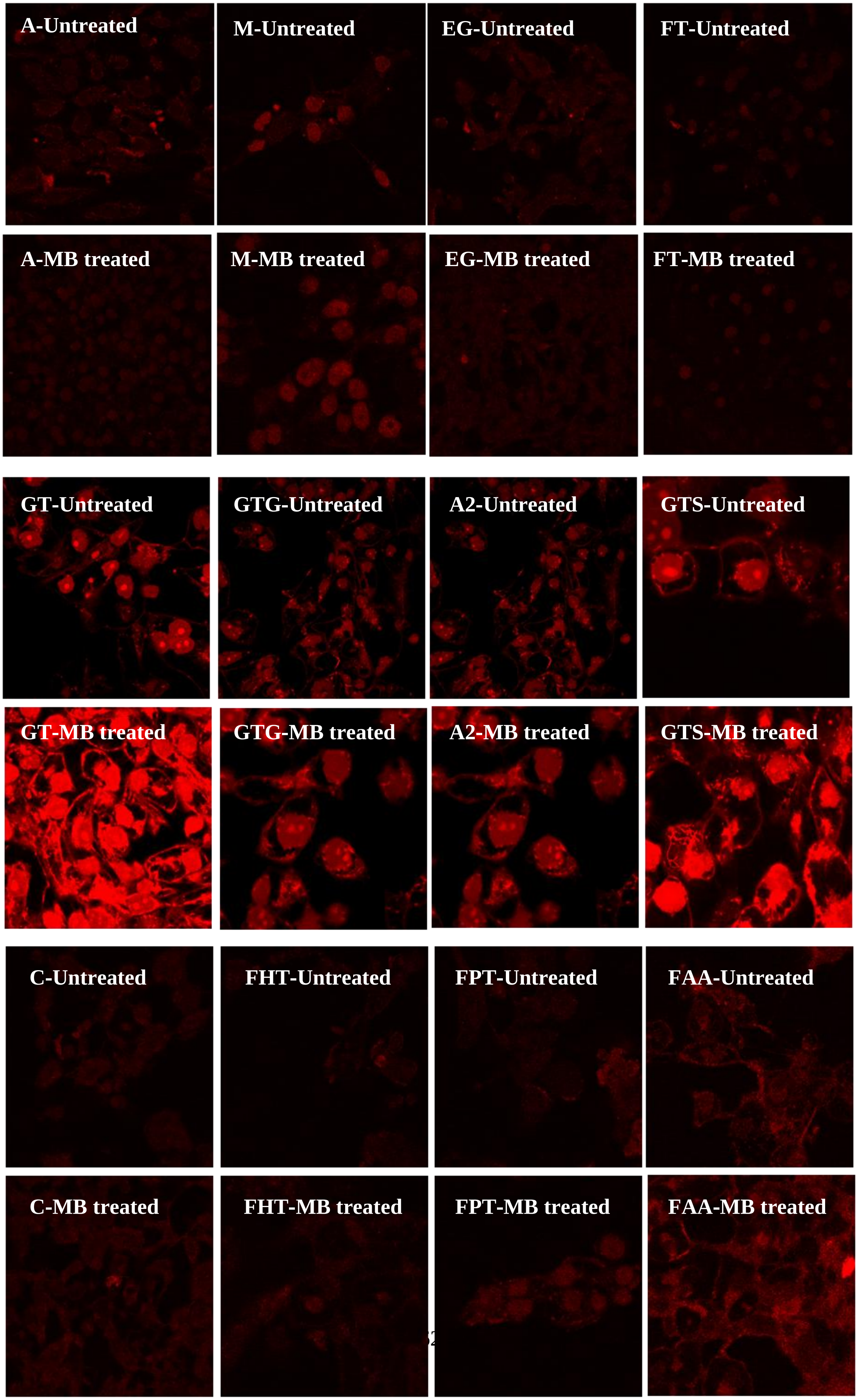
A-Untreated
M-Untreated
EG-Untreated
FT-Untreated
A-MB treated
M-MB treated
EG-MB treated
FT-MB treated
GT-Untreated
GTG-Untreated
A2-Untreated
GTS-Untreated
GT-MB treated
GTG-MB treated
A2-MB treated
GTS-MB treated
C-Untreated
FHT-Untreated
FPT-Untreated
FAA-Untreated
C-MB treated
FHT-MB treated
FPT-MB treated
FAA-MB treated

Figure 85. Images of FISH fix/perm optimization protocols. For each set of fix/perm conditions, both the untreated and molecular beacon treated samples were infected with RSV as described above. Samples were imaged 3 days post infection. Fluorescent signal seen in the untreated samples is the result of autofluorescence whereas fluorescence seen in the molecular beacon treated samples is the result of both autofluorescence and fluorescence as the result of molecular beacon hybridization. Conditions which have increased fluorescence in the molecular beacon treated samples have not had the nucleic acid target compromised by the fix/perm process.

Kristin Halfpenny

Present Address:

1217 15th Ave S.
Nashville, Tn 37212
Kristin.c.halfpenny@vanderbilt.edu
(615) 887 3920

Permanent Address:

9903 Hyacinth Court
Louisville, Ky 40241
(502) 412 4811

Education

- **Vanderbilt University,** Nashville, Tn
  PhD Candidate, GPA 3.305
  GAANN Fellowship
- **Wake Forest University**, Winston Salem, NC May 2004
  Bachelor of Science in Chemistry, Minor in Communications
  Dean's List, 5 Semesters
  Test Scores: GRE- 720 Quantitative, 520 Verbal, 5.5 Analytical Writing

Experience

- **Graduate Research Assistant**, David Wright, Vanderbilt University Chemistry Department, Nashville Tn. March 2005- present.
  - β-hematin degradation by products of macrophage oxidative burst *in vitro*. Fluorescent imaging and quantification of β-hematin inside RAW macrophage-like cells using confocal microscopy and flow cytometry.
  - Fluorescent labeling of Protein Kinase C trafficking in RAW macrophage-like cells under oxidative stress. *In vitro* studies to on the stability of protein kinase C zinc finger under oxidative stress.
  - Development of gold nanoparticle viral probes for live cell imaging using confocal microscopy and viral detection using flow cytometry.
- **Teaching Assistant**, Vanderbilt University Chemistry Department, Nashville Tn. August 2004-December 2007.
  - Oversaw two undergraduate labs of approximately 24 students each.
  - Explained the concepts behind weekly labs, demonstrated necessary laboratory techniques and guided students in the completion of the lab.
  - Evaluated student performance based on written lab reports and in lab behavior. Held office hours twice a week to assist struggling students.
  - Served as liaison between students and professors. Reported student grades to professor and attended weekly TA meetings.
- **Undergraduate Research Assistant**, Richard Manderville, Wake Forest University Chemistry Department, Winston Salem NC. August 2003-May 2004.
  - Research on 2,2'-chlorophenylhydroquinone including reaction with hydrogen peroxide and horseradish peroxidase to result in quinone form, and the subsequent reaction of the quinine form with deoxyguanosine (dG) to form adduct.
  - Attempt to determine the structure of dG adduct through various spectroscopic techniques.
- **Resident Advisor**, Wake Forest University, Winston Salem, NC. August 2002-May 2004.
  - Work with staff of five other advisors to manage a group of buildings with approximately 150 residents. Plan community building programs.
  - Serve as liaison between administration and the residents. Counsel residents on issues or refer them to the proper place. Mediate discussion of problems between residents.

  - Monitor the general state of the building including working with a facilities staff to maintain a safe and clean environment. Also serve as a policy enforcer and document any incidents for university record.

Laboratory and Computer Skills

- **Laboratory Applications:** Flow Cytometry, Confocal Microscopy, Cell Culture, Gel Electrophoresis, Fluorescent labeling and imaging, UV-Vis, IR, western blotting, viral infection and titer, Biological Safety Level 2 and 3 training, Radioactive Materials Training, experience with HPLC/mass spec, experience with NMR, experience with XRD.
- **Software Applications:** LSM Image Browser, FlowJo, Volocity, EndNote, Origin, Microsoft Word, Excel, PowerPoint, and Outlook, Origin, Adobe Acrobat, Adobe Photoshop, Chemdraw, Chemstation, Netscape Communicator, MS Internet Explorer.

Activities

- **Treasurer**, VIBE, Vanderbilt. Hip Hop Dance Co., August 2006 – May 2007
  - Manage an annual budget of approximately $7000 for a group of approximately 25 people including purchase of costumes, payment of outside contractors, organization and execution of fundraising efforts and out of town trips.
  - Serve as liaison between executive board and university including managing reimbursements, organizing university purchases, and proposing and submitting budget renewal applications.
- **President,** Wake Forest Club Fencing, August 2002-May 2004.
  - Manage all club activities of coed club of approximately 20 members. Organize and lead practices, including scheduling practice times and teaching new fencers basic skills
  - Plan the year's budget (of approximately $1000) including purchase of equipment, payment of coaches and dues, and event fees
  - Correspond with approximately 5 other fencing organizations to arrange trips to competitions. Serve as intermediate between club and the university.
- **Ritual Committee Chair**, Phi Mu Sorority, December 2001- December 2002.
  - Plan and implement a number of annual events such as Initiation ceremonies, pledging ceremonies and dinners for members and their parents for a group of 100+ people.
  - Delegate various responsibilities to a committee of approximately five people that include booking event locations, informing the participants of times and locations, and orchestrating the successful completion of events.

Publications and Presentations

- Halfpenny, K.C.; Perez, J.W.; Wright, D.W. "Nanoblossoms: cultivating a novel live cell probe to study RNA trafficking in both space and time." *Abstracts, 60th Southeast/64st Southwest Joint Regional Meeting of the American Chemical Society.* **2008.**
- Halfpenny, K.C.; Perez, J.W.; Wright, D.W. "Nanoblossoms." *In preperation.*
- Carney, C.K.; Halfpenny, K.C.; Wright, D.W. "Protein Kinase C adduction by 2-Hydroxynonenal." *In preparation.*
- Carney, C.K.; Schrimpe, A. C.; Halfpenny, K. C.; Harry, R. S.; Miller, C. M.; Broncel, M.; Sewell, S. L.; Schaff, J. E.; Deol, R.; Carter, M. D.; Wright, D. W. "The basis of immunomodulatory activity of malaria pigment (hemozoin)." *Journal of Biological Inorganic Chemistry.* **2006**. *11.* 917-929.
- Halfpenny, K.C.; Schrimpe, A.C.; Wright, D.W. "Hemozoin: Malaria's Trojan Horse" *Abstract of Papers, 231st ACS National Meeting.* **2006**
- Halfpenny, K.C.; Wright, D.W.; "β-hematin Degradation by Products of Oxidative Burst." *Abstracts, 57th Southeast/61st Southwest Joint Regional Meeting of the American Chemical Society.* **2005.**

BIBLIOGRAPHY

1. Ramadan MA. Sequestration of parasitic excretory products in Schistosoma mansoni infection. *Zeitschrift fur Tropenedizin und parasitologie* 1971;22(4):397-405.

2. Schwarzer E, G. Bellomo GG, D. Ulliers, and P. Arese. Phagocytosis of malarial pigment haemozoin by human monocytes: a confocal microscopy study. *Parasitology* 2001;123:125-131.

3. Pagola S, Peter W. Stephens DSB, Andrew D. Kosar, SK. Madsen. The Structure of Malaria Pigment β-hematin. *Nature* 2000;404:307-310.

4. B Herman JJL, *Optical Microscopy Emerging Methods and Applications*. San Diego: Academic Press, Inc, 1993.

5. Encyclopedia WO. *http://en.wikipedia.org/wiki/fluorescent_microscopy*.

6. Carney CK, Schrimpe AC, Halfpenny KC, Harry SR, Miller CM, Broncel M, Sewell SL, Schaff JE, Deol RS, Carter MD, DW Wright. The basis of the immunomodulatory activity of malaria pigment (hemozoin). *Journal of Biological Inorganic Chemistry* 2006;11(7):917-929.

7. Bohle DS, Helms JB. Synthesis of β-hematin by dehydrohalogenation of hemin. *Biochemical and Biophysical Research Communications* 1993;193(2):504-508.

8. Chen MM, Lirong S, DJ Sullivan. *Haemoproteus* and *Schistosoma* synthesize heme polymers similar to *Plasmodium* hemozoin and β-hematin. *Molecular and Biochemical Parasitology* 2001;113:1-8.

9. Lakowicz JR. *Principles of Fluorescence Spectroscopy*, 3rd edn. New York: Springer Publishing, 2006.

10. Lacey AJ, *Light Microscopy in Biology A Practical Approach*. Oxford: Oxford University Press, 1999.

11. Rubbi CP, *Light Microscopy Essential Data*. Oxford: John Wiley & Sons Ltd, 1994.

12. Pawley JB, *Handbook of Biological Confocal Microscopy*, 3rd ed edn. New York: Springer Science, 2006.

13. Rochow TG, PA Tucker. *Introduction to Microscopy by Means of Light, Electrons, X Rays or Acoustics*, 2nd ed. edn. New York: Plenum Press, 1994.

14. Larry S. Roberts JJ. *Gerald D. Schmidt & Larry S. Roberts' Foundations of Parasitology*, 6th edn: The McGraw-Hill Companies, Inc, 2000.

15. Goldberg DE. Hemoglobin degradation in Plasmodium-infected red blood cells. *Seminars in Cell Biology* 1993;4(5):355-361.

16. Goldberg DE, Slater AF, Cerami A, GB Henderson. Hemoglobin degradation in the malaria parasite *Plasmodium faciparum*: An ordered process in a unique organelle. *Proc. Natl. Acad. Sci. USA* 1990;87(April 15 1990):2931-2935.

17. Slater AF, Swiggard WJ, Orton BR, Flitter WD, Goldberg DE, Cerami A, GB Henderson. An iron-carboxylate bond links the heme units of malaria pigment. *Proc. Natl. Acad. Sci. USA* 1991;88(January 1991):325-329.

18. Francis SE, Sullivan DJ Jr, DE Goldberg. Hemoglobin metabolism in the malaria parasite *Plasmodium falciparum*. *Annual Review of Microbiology* 1997;51:97-123.

19. Schwarzer E, Turrini F, Giribaldi G, Ginsburg H and P Arese. Impairment of Macrophage Functions after Ingestion of *Plasmodium falciparum*-infected Erythrocytes or Isolated Malarial Pigment. *J. Exp. Med.* 1992;176(October 1992):1033-1041.

20. Arese P, E Schwarzr. Malarial pigment (hemozoin): a very active 'inert' substance. *Annals of Tropical Medicine and Parasitology* 1997;91(5):501-516.

21. Poli G, RJ Schaur. 4-Hydroxynonenal in the pathomechanisms of oxidative stress. *Life* 2000;50:315-321.

22. Dekker LV, Leitges M, Altschuler G, Minstry N, McDermott A, Roes J, AW Segal. Protein kinase C-beta contributes to NADPH oxidase activation in neutrophils. *Biochem. J.* 2000;347(1):285-289.

23. Carney CK, Halfpenny KC, DW Wright. *in preperation*.

24. Nishizuka Y. Intracellular signaling by hydrolysis of phospholipids and activation of protein kinase C. *Science* 1992;258(5082):607-614.

25. Nixon JB, McPhail LC. Protein Kinase C (PKC) Isoforms Translocate to Triton-Insoluble Fractions in Stimulated Human Neutrophils: Correlation of Conventional PKC with Activation of NADPH Oxidase. *J Immunol* 1999;163(8):4574-4582.

26. Hu A, Corella M, Tam JS, Rappaport R, SM Cheng. Simultaneous Detection, Subgrouping, and Quantitation of respiratory syncytial virus a and b by real-time PCR. *Journal of clinical microbiology* 2003;41(1):149-154.

27. Freymuth F, Eugene G, Vabret A, Petitjean J, Gennetay E, Brouard J, Duhamel JF, B. Guillois. Detection of respiratory syncytial virus by reverse transcription-PCR and hybridization with a DNA enzyme immunoassay. *Journal of clinical microbiology* 1995;33(12):3352-3355.

28. Gueudin M, Vabret A, Petitjean J, Gouarin S, Brouard J, F Freymuth. Quantitation of respiratory syncytial virus RNA in nasal aspirates of children by real-time RT-PCR assay. *Journal of Virological Methods* 2003;109:39-45.

29. Levsky JM, RH Singer. Fluorescence in situ hybridization: past, present and future. *journal of cell science* 2003;116:2833-2838.

30. Nitin N, Santangelo PJ, Kim G, Nie S, G Bao. Peptide-linked molecular beacons for efficient delivery and rapid mRNA detection in living cells. *Nucleic Acids Research* 2004;32(6):e58.

31. Santangelo PJ, Nie B, Tsourkas A, G Bao. Dual FRET molecular beacons for mRNA detection in living cells. *Nucleic Acids Research* 2004;32(6):e57.

32. Santangelo PJ, Nitin N, LaConte L, Woolums A, G Bao. Live-Cell characterization and analysis of a clinical isolate of bovine respiratory syncytial virus, using molecular beacons. *journal of virology* 2006;80(2):682-688.

33. Chan P, Yeun T, Ruf F, Gonzalex-Maeso J, SC Sealfon. Method for multiplex cellular detection of mRNAs using quantum dot fluorescent *in situ* hybridization. *Nucleic Acids Research* 2005;33(18):e161.

34. Seferos DS, Giljohann DA, Hill HD, Prigodich AE, CA Mirkin. Nano-flares: probes for transfection and mRNA detection in living cells. *Journal of the American Chemical Society* 2007;129(50):15477-15479.

35. Rosi NL, Giljohann DA, Thaxton CS, Lytton-Jean AK, Han MS, CA Mirkin. Oligonucleotide-Modified Gold Nanoparticles for Intracellular Gene Regulation. *Science* 2006;312:1027-1030.

36. WHO. *World Health Organization, Roll Back Malaria* http://who.int/rbm/.

37. MFI. *Malaria Foundation International* http://www.malaria.org/factpack.html; http://www.malaria.org/factpack.html.

38. Roberts LS, J Janovy Jr. *Foundations of Parasitology*, 6 edn: McGraw - Hill Science/Engineering/Math, 2000.

39. Atamna H, Ginsburg H. Origin of reactive oxygen species in erythrocytes infected with Plasmodium falciparum. *Molecular and Biochemical Parasitology* 1993;61(2):231-241.

40. Orjih AU, Banyal HS, Chevli R, CD Fitch. Hemin lyses malaria parasites. *Science* 1981;214:667-669.

41. Green MD, Xiao L, Lal AA. Formation of hydroxyeicosatetraenoic acids from hemozoin-catalyzed oxidation of arachidonic acid. *Molecular and Biochemical Parasitology* 1996;83(2):183-188.

42. Oliveira MF, Timm BL, Machado EA, Miranda K, Attias M, Silva JR, Dansa-Petretski M, de Oliveira MA, de Souza W, Pinhal NM, Sousa JJ, Vugman NV, PL Oliveira. On the pro-oxidant effects of haemozoin. *FEBS Letters* 2002;512(1-3):139-144.

43. Eckman JR, Modler S, Eaton JW, Berger E, RR Engel. Host Heme Catabolism in Drug-sensitive and Drug-resistant Malaria. *Journal of laboratory and clinical medicine* 1977;90:767-770.

44. Beron W, Alvarez-Dominguez C, Mayorga L, PD Stahl. Membrane Trafficking Along the Phagocytic Pathway. *Trends in Cell Biology* 1995;5:100-104.

45. Desjardins M, Huber LA, Parton RG, G Griffiths. Biogensis of Phagolysosomes Proceeds through a Sequential Series of Interactions with the Endocytic Apparatus. *The Journal of Cell Biology* 1994;124(5):677-688.

46. JA Ross, MJ Auger. The Biology of the Macrophage. In: Lewis CE, B Burke, ed. *The Macrophage*. New York: Oxford University Press, 2002:1-72.

47. Geisow MJ, Hart PDa, MR Young. Temporal Changes of Lyosome and Phagosome pH during Phagolysosome Formation in Macrophages: Studies by Fluorescence Spectroscopy. *The Journal of Cell Biology* 1981;89(June):645-652.

48. Rabinowitz S, Horstmann H, Gordon S and G Griffiths. Immunocytochemical Characterization of the Endocytic and Phagolysosome Compartments in Peritoneal Macrophages. *The Journal of Cell Biology* 1992;116(1):95-112.

49. Abbas AK, Lichtman AH, JS Pober. *Cellular and Molecular Immunology*, 4th edn. Philadelphia: W.B. Saunders Company, 2000.

50. Rosen GM, Pou S, Ramos CL, Cohen MS, BE Britigan. Free radicals and phagocytic cells. *FASEB J.* 1995;9:200-209.

51. NE Reiner. Altered signaling and mononuclear phagocyte deactivation during intracellular infection. *Immunology Today* 1994;15(8):374-381.

52. Fiori PL, Rappelli P, Mikarimi SN, Ginsburg H, Cappuccinelli PA, FM Turrini. Reduced microbicidal and anti-tumour activities of human monocytes after ingestion of Plasmodium falciparum-infected red blood cells. *Parasite Immunology* 1993;15(12):647-655.

53. Schwarzer E, Muller O, Arese P, Siems WG, and T Grune. Increased levels of 4-hydroxynonenal in human monocytes fed with malarial pigment hemozoin. *FEBS Letters* 1996;388:99-122.

54. Schwarzer E, Ludwig P, Valente E, and P Arese. 15(S)-hydroxyeicosatetraenoic acid (15-HETE), a product of acrachidonic acid peroxidation, is an active component of hemozoin toxicity to monocytes. *Parassitologia* 1999;41:199-202.

55. Schwarzer E, Kuhn H, Valente E, P Arese. Malaria-parasitized erythrocytes and hemozoin nonenzymaticaly generate large amounts of hydroxyl fatty acids that inhibit monocyte function. *Blood* 2003;101:722-728.

56. Sherry BA, Alava G, Tracey KJ, Martiney J, Cerami A, AFG Slater. Malaria-specific metabolite hemozoin mediates the release of several potent endogenous pyrogens (TNF, MIP-1α, MIP-1β) in vitro, and altered thermoregulation in vivo. *J Inflamm* 1995;45:85-96.

57. Prada J, Malinowski J, Mueller S, Bienzle U, PG Kremsner. Hemozoin differentially modulates the production of interleukin 6 and tumor necrosis factor in murine macrophage. *European Cytokine Network* 1995;6(2):109-112.

58. Pichyangkul S, Saengkrai P, HK Webster. Plasmodium falciparum pigment induces monocytes to release high levels of human necrosis factor-alpha and interleukin-1 beta. *The American Journal of tropical medicine and hygiene* 1994;51(4):430-435.

59. Taramelli D, Basilico N, De Palma AM, Saresella M, Ferrante P, Mussoni L, P Olliaro. The effect of synthetic malaria pigment ([beta]-haematin) on adhesion molecule expression and interleukin-6 production by human endothelial cells. *Transactions of the Royal Society of Tropical Medicine and Hygiene* 1998;92(1):57-62.

60. Taramelli D, Basilico N, Pagani E, Grande E, Monti D, Ghione M, P Olliaro. The Heme Moiety of Malaria Pigment ([beta]-Hematin) Mediates the Inhibition of Nitric Oxide and Tumor Necrosis Factor-[alpha] Production by Lipopolysaccharide-Stimulated Macrophages. *Experimental Parasitology* 1995;81(4):501-511.

61. Taramelli D, Recalcati S, Basilico N, Olliaro P, G Cairo. Macrophage Preconditioning with Synthetic Malaria Pigment Reduces Cytokine Production via Heme Iron-Dependent Oxidative Stress. *Lab Invest*;80(12):1781-1788.

62. Jaramillo M, Gowda DC, Radzioch D, Olivier M. Hemozoin Increases IFN-{gamma}-Inducible Macrophage Nitric Oxide Generation Through Extracellular Signal-Regulated Kinase- and NF-{kappa}B-Dependent Pathways. *J Immunol* 2003;171(8):4243-4253.

63. Biswas S, Karmarkar MG, YD Sharma. Antibodies detected against <i>Plasmodium falciparum</i> haemozoin with inhibitory properties to cytokine production. *FEMS Microbiology Letters* 2001;194(2):175-179.

64. Noland GS, Briones N, Sullivan DJ. The shape and size of hemozoin crystals distinguishes diverse Plasmodium species. *Molecular and Biochemical Parasitology* 2003;130(2):91-99.

65. Derham Bk, Ellory CJ, Bron AJ, JJ Harding. The molecular chaperone α-crystallin incorporated into red cell ghosts protects membrane Na/K-ATPase against glycation and oxidative stress. *European Journal of Biochemistry* 2003;270(12):2605-2611.

66. Steck TL, Kant JA, Sidney F, P Lester. [16] Preparation of impermeable ghosts and inside-out vesicles from human erythrocyte membranes. In. *Methods in Enzymology*. Vol. Volume 31: Academic Press, 1974:172-180.

67. Huckaba CE, FG Keyes. The accuracy of estimation of hydrogen peroxide by potassium permanganate titration. *Journal of American Chemical Society* 1948;70:1640-1644.

68. Ditz H. Chlorometric, bromometric and iodometric determination of available chlorine in hypochlorites and in bleaching powder. *zeitschrift fuer Analytische Chemie* 1930;79:33-345.

69. Nagano T. Practical Methods for detection of nitric oxide. *Luminescence* 1999;14(6):283-290.

70. Babior B. NADPH oxidase: an update. *Blood* 1999;93:1464-1476.

71. DeLeo FR, MT Quinn. Assembly of the phagocyte NADPH oxidase: molecular interaction of oxidase proteins. *Journal of Leukocyte Biology* 1996;60:677-691.

72. Vignais P. The superoxidase-generating NADPH oxidase: structural aspects and activation mechanism. *Cell and Molecular Life Science* 2002;59:1428-1459.

73. Jaramillo M, Godbout M, Olivier M. Hemozoin Induces Macrophage Chemokine Expression through Oxidative Stress-Dependent and -Independent Mechanisms. *J Immunol* 2005;174(1):475-484.

74. Keller CC, Kremsner PG, Hittner JB, Misukonis MA, Weinberg JB, DJ Perkins. Elevated Nitric Oxide Production in Children with Malarial Anemia: Hemozoin-Induced Nitric Oxide Synthase Type 2 Transcripts and Nitric Oxide in Blood Mononuclear Cells. *Infect. Immun.* 2004;72(8):4868-4873.

75. Prada J, Malinowsky J, Muller S, Bienzle U, PG Kremsener. Effects of plasmodium vinckei hemozoin on the production of oxygen radicals and nitrogen oxides in murine macrophages. . *American Journal of Tropical Medicine and Hygiene* 1996;54:620-624.

76. Tenhunen R, Marver HS, R Schimid. Microsomal Heme Oxygenase. Characterization of the enzyme. *Journal of Biological Chemistry* 1969;244(December 1969):6388-6394.

77. Schaefer WH, Harris TM, FP Guengerich. Characterization of the enzymatic and non-enzymatic peroxidative degradation of iron porphyrins and cytochrome p-450 heme. *Biochemistry* 1985;24:3254-3263.

78. Groves JT, Haushalter RC, Nakamura M, TE Nemo, BJ Evans. High-valent Iron-porphyrin complexes related to peroxidase and cytochrome p-450. *Journal of American Chemical Society* 1981;103:2884-2886.

79. Nagababu E, JM Rifkind. Heme degradatoin by reactive oxygen species. *Antioxidants and redox signaling* 2004;6:967-978.

80. K Nakamoto. Infrared and Raman spectra of inorganic and coordination compounds part B: applications in coordination, organometallic and bioinorganic chemistry. In. New York: John Wiley & Sons, Inc, 1997:319-377.

81. Decatur SM, Franzen S, DePillis GD, Dyer RB, Woodruff WH, SG Boxer. Trans Effects in Nitric Oxide Binding to Myoglobin Cavity Mutant H93Gâ€ *Biochemistry* 1996;35(15):4939-4944.

82. Bohle DS, Kosar AD, PW Stephens. Reversible Hydration of the malaria pigment βhematin. *Canadian Journal of Chemistry* 2003;81:1285-1291.

83. Albrich JM, McCarthy CA, JK Hurst. Biological reactivity of hypochorous acid: implications for microbicidal mechanisms of leukocyte myeloperoxidase. *Proc. Natl. Acad. Sci. USA* 1981;78:210-214.

84. Hurst JK, SV Lymar. Cellularly Generated Inorganic Oxidants as Natural Microbicidal Agents. *Accounts of Chemical Research* 1999;32(6):520-528.

85. Miller CM, Carney CK, Schrimpe AC, DW Wright. β-hematin (Hemozoin) Mediated Deomposition of Polyunsaturated Fatty Acids to 4-Hydroxy-2-nonenal. *Inorganic Chemistry* 2005;44:2134-2136.

86. Nakashima I, Liu W, Akhand AA, Takeda K, Kawamoto Y, Kato M, H Suzuki. 4-hydroxynonenal triggers multistep signal transduction cascades for suppression of cellular functions. *Molecular Aspects of Medicine* 2003;24:231-238.

87. Esterbauer H, Schaur RJ, H Zollner. Chemistry and biochemistry of 4-hydroxynonenal, malonaldehyde and related aldehydes. *Free Radical Biological Medicine* 1991;11:81-128.

88. Neely MD, Amarnath V, Weitlauf C, Montine TJ. Synthesis and Cellular Effects of an Intracellularly Activated Analogue of 4-Hydroxynonenal. *Chemical Research in Toxicology* 2001;15(1):40-47.

89. Dianzani C, Parrini M, Ferrara C, R Fantozzi. Effect of 4-hydroxynonenal on superoxide anion production from primed human neutrophils. *Cell Biochemistry and Function* 1996;14(3):193-200.

90. Schwarzer E, Turrini F, Giribaldi G, Ulliers D, P Arese. Phagocytosis of P. falciparum malarial pigment hemozoin by human monocytes inactivates monocyte protein kinase C. *Biochimica et Biophysica Acta (BBA) - Molecular Basis of Disease* 1993;1181(1):51-54.

91. Goldie P, Roth Jr EF, Oppenheim J, JP Vanderberg. Biochemical characterization of plasmodium falciparum hemozoin. *American Journal of Tropical Medicine and Hygiene* 1990;43:584-596.

92. Schwarzer E, De Matteis F, Giribaldi G, Ulliers D. Valente E, P Arese. Hemozoin stability and dormant induction of heme oxygenase in hemozoin-fed human monocytes. *Molecular and Biochemical Parasitology* 1999;100(1):61-72.

93. Coban C, Ishii KJ, Kawai T, Hemmi H, Sato S. Uematsu S, Yamamoto M, Takeuchi O, Itagaki S, Kumar N, Horii T, S Akira. Toll-like receptor 9 mediates innate immune activation by the malaria pigment hemozoin. *J. Exp. Med.* 2005;201(1):19-25.

94. Millington OR, Di Lorenzo C, Phillips RS, Garside P, JM Brewer. Suppression of adaptive immunity to heterologous antigens during plasmodium infection through hemozoin-induced failure of dendritic cell function. *Journal of Biology* 2006;5:5.

95. Tan S-L, Parker PJ. Emerging and diverse roles of protein kinase C in immune cell signalling. *Biochem. J.* 2003;376(3):545-552.

96. Korichneva I, Hoyos B, Chua R, Levi E, U Hammerling. Zinc release from protein kinase C as a common event during activaion by lipid second messenger or reactive oxygen. *Journal of biological chemistry* 2002;277(46):44327-44331.

97. Bruns R, Miller D, Merriman R, Howbert J, Heath W, Kobayashi E, Takahashi I, Tamaoki T, H Nakano. Inhibition of protein kinase c by calphostin c is light-dependent. *Biochemical and Biophysical research communications* 1991;176(1):288-293.

98. Rao A, Luo C, Hogan PG. Transcription Factors of the Nfat Family:Regulation and Function. *Annual Review of Immunology* 1997;15(1):707.
99. Way K, Chou E, G King. Identification of PKC-isoform specific biological actions using pharmacological aproaches. *TiPs* 2000;21:181-187.

100. Quest A, Bloomenthal J, Bardes E, R Bell. The regulatory domain of protein kinase C coordinates four atoms of zinc. *Journal of biological chemistry* 1992;267(14):10193-10197.

101. Stabel S, P Parker. Protein Kinase C. *Pharmacutical Therapy* 1991;51:71-95.

102. Chu F, Koomen J, Kobayashi J, C O'Brian. Identification of an inactivation cystein switch in protein kinase cε, a rational target for the design of protein kinase cε-inhibitory cancer therapeutics. C*ancer Research* 2005;65:10478.

103. Chu F, Chen LH, C O'Brian. Cellular protein kinase C iszyme regulation by exogenously delivered physiological disulfides--implications of oxidative protein kinase C regulation to cancer prevention. *Carcinogenesis* 2004;25(4):585-596.

104. Gopalakrishna R, Gundimeda U. Antioxidant Regulation of Protein Kinase C in Cancer Prevention. *J. Nutr.* 2002;132(12):3819S-3823.

105. Kobayashi E, Nakano H, Morimoto M, T Tamaoki. Calphostin C, a novel microbial compound, is a highly potent and specific inhibitor of protein kinase C. *Biochemical and Biophysical research communications* 1989;159(2):548-553.

106. Schwarzer E, Müller O, Arese P, Siems WG, T Grune. Increased levels of 4-hydroxynonenal in human monocytes fed with malarial pigment hemozoin A possible clue for hemozoin toxicity. *FEBS Letters* 1996;388(2-3):119-122.

107. Nakashima I, Liu W, Akhand AA, Takeda K, Kawamoto Y, Kato M, H Suzuki. 4-Hydroxynonenal triggers multistep signal transduction cascades for suppression of cellular functions. *Molecular Aspects of Medicine*2003;24(4-5):231-238.

108. Tamagno E, Parola M, Bardini P, Piccini A, Borghi R, Guglielmotto M, Santoro G, Davit A, Danni O, Smith MA, Perry G, M Tabaton. β-site APP cleaving enzyme up-regulation induced by 4-hydroxynonenal is mediated by stress-activated protein kinases pathways. *journal of neurochemistry* 2005;92(628-636).

109. Arese P, E Schwarzer. Malarial pigment (haemozoin): a very active 'inert' substance. *Annals of Tropical Medicine and Parasitology* 1997;91:501-516.

110. Shi Q, Vaillancourt F, Cote V, Fahmi H, Lavigne P, Afif H, De Battista J, Fernandes J, M Benderdour. Alterations of metabolic activity in human osteoarthritic osteoblasts by lipid peroxidation end product 4-hydroxynonenal. *Arthritis Research & Therapy* 2006;8(6):R159.

111. Leonarduzzi G, Robbesyn F, Poli G. Signaling kinases modulated by 4-hydroxynonenal. *Free Radical Biology and Medicine* 2004;37(11):1694-1702.

112. JRI Yates. Mass spectrometry and the age of the proteome. *Journal of Mass Spectrometry* 1998;33:1-19.

113. Hanson BT, Davey SW, Ham AL, Liebler DC. P-Mod: An algorithm and software to map modifications to peptide sequences using tandem MS data. *Journal of the Proteome* 2005;4:358-368.

114. Dianzani C, Parrini M, Ferrara C, Fantozzi R. Effect of 4-hydroxynonenal on superoxide anion production from primed human neutrophils. *Cell Biochemistry and Function* 1996;14(3):193-200.

115. Schwarzer E, Muller O, Arese P, Siems WG, Grune T. Increased levels of 4-hydroxynonenal in human monocytes fed with malarial pigment hemozoin: a possible clue for hemozoin toxicity. *FEBS Letters* 1996;388:119-122.

116. Alderton AL, Faustman C, Liebler DC, DW Hill. Induction of redox instability of bovine myoglobin by adduction with 4-hydroxy-2-nonenal. *BIochemistry* 2003;42:4398-4405.

117. Newton AC. Protein Kinase C: Structural and Spatial Regulation by Phosphorylation, Cofactors, and Macromolecular Interactions. *Chemical Reviews* 2001;101(8):2353-2364.

118. Ward N, Gravitt K, C O'Brian. Covalent MOdification of Protein Kinase C isozymes by the Inactivating peptide substrate analog n-biotinyl-arg-arg-arg-cys-leu-arg-arg-leu. *Journal of Biological Chemistry* 1996;271(39):24193-24200.

119. Gopalakrishna R, Chen Z-H, Gundimeda U. Selenocompounds Induce a Redox Modulation of Protein Kinase C in the Cell, Compartmentally Independent from Cytosolic Glutathione: Its Role in Inhibition of Tumor Promotion. *Archives of Biochemistry and Biophysics* 1997;348(1):37-48.

120. Gopalakrishna R, Gundimeda U, Chen Z-H. Cancer-Preventive Selenocompounds Induce a Specific Redox Modification of Cysteine-Rich Regions in Ca2+- Dependent Isoenzymes of Protein Kinase C. *Archives of Biochemistry and Biophysics* 1997;348(1):25-36.

121. Gundimeda U, Chen Z-H, R Gopalakrishna. Tamoxifen modulates proein kinase C via oxidative stress in estrogen receptor-negative breast cancer cells. *Journal of biological chemistry* 1996;271(23):13504.

122. Shiying L, Yuyang J, Jian C, Feng L, Li M, Z Yufen. Inhibitors of Protein kinase C. *Chinese Science Builletin* 2005;50(13):1293-1304.

123. Poli G, RJ Schaur. 4-hydroxynonenal in the pathomechanisms of oxidative stress. *Life* 2000;50:315-321.

124. Dianzani MU. 4-hydroxynonenal and cell signalling. *Free Radical Research* 1998;28:553-560.

125. Isom AL, Barnes S, Wilson L, Kirk M, Coward L, V Darley-Usmar. Modification of *Cytochrome c* by 4-hydroxy-2-nonenal: evidence for histidine, lysine, and arginine-

aldehyde adducts. *Journal of the American Society for Mass Spectrometry* 2004;15:1136-1147.

126. Lee S, Phillips AL, Liebler DC, C Faustman. Porcine oxymyoglobin and lipid oxidation in vitro. *Meat Science* 2003;63:241-247.

127. Singer RH. RNA: traffic report. *Trends in Cell Biology* 1996;6:486-489.

128. Kindler S, Wang H, Richter D, H Tiedge. RNA transport and local control of translation. *Annu. Rev. Cell Dev. Biol.* 2005;21:223-245.

129. Wang J. Nanomaterial-based electrochemical biosensors. *The Analyst* 2005;130:421-426.

130. Hu X, S Dung. Metal nanomaterials and carbon nanotubes--synthesis, functionalization, and potential applications towards electrochemistry. *Journal of Materials Chemistry* 2008;18:1279-1295.

131. Zhang Q, Li Y, RW Tsien. The Dynamic Control of Kiss-And-run and Vesicular Reuse Probed with Single Nanoparticles. *Science* 2009;323:1448-1453.

132. Frias JC, Lipinski MJ, Ibanez MT, Soriano C, Garcia-Espana E, Jimenez-Borreguero LJ, JJ Badimon. Nanoparticles as Constrast Agnts for MRI of Atherosclerotic Lesions. *Clinical Medicine: Cardiology* 2008;2:173-179.

133. Lippard SJ, JM Berg. *Principles of Bioinorganic Chemistry*. Mill Valley, CA: University Science Books, 1994.

134. Daniel M-C, D Astruc. Gold Nanoparticles: Assembly, Supramolecular Chemistry, Quantum-Size-Related Properties, and Applications toward Biology, Catalysis, and Nanotechnology. *Chemical Reviews* 2004;104(1):293-346.

135. Dubertret B, Calame M, AJ Libchaber. Single-mismatch detection using gold-quenched fluorescent oligonucleotides. *Nature Biotechnology* 2001;19(April):365-370.

136. Dulkeith E, Ringler M, Klar TA, J Feldmann. Gold Nanoparticles Quench Fluorescence by Phase Induced Radiative Rate Suppression. *Nano Letters* 2005;5(4):585-589.

137. Collins PL, JE Crowe Jr. Respiratory Syncytial VIrus and Metapneumovirus. In: PH David M. Knipe, ed. *Fields Virology*. Vol. II. Philadelphia: Lippincott Williams & Wilkins, 2007:1601-1646.

138. Fearns R, Peeples ME, PL Collins. Mapping the Transcription and Replication Promoters of Respiratory Syncytial Virus. *J. Virol.* 2002;76(4):1663-1672.

139. Jairath S, Vargas PB, Hamlin HA, Field AK, RE Kilkuskie. Inhibition of respiratory syncytial virus replication by antisense oligodeoxyribonucleotides. *Antiviral Research* 1997;33:201-213.

140. Xu Z, Kuang M, Okicki JR, Cramer H, N Chaudhary. Potent inhibition of respiratory syncytial virus by combination treatment with 2-5A antisense and ribavirin. *Antiviral Research* 2004;61(3):195-206.

141. Player MR, Barnard DL, PF Torrence. Potent inhibition of respiratory syncytial virus replication using a 2-5A-antisense chimera targeted to signals within the virus genomic RNA. *Proceedings of the National Academy of Sciences of the United States of America* 1998;95(15):8874-8879.

142. Singh RD, Puri V, Valiyaveettil JT, Marks DL, Bittman R, RE Pagano. Selective caveolin-1-dependent endocytosis of glycosphingolipids. *Mol Biol Cell* 2003;14(8):3254-3265.

143. Macia E, Ehrlich M, Massol R, Boucrot E, Brunner C, T Kichhausen. Dynasore, a cell-permeable inhibitor of dynamin. *Dev Cell* 2006;10(6):839-850.

144. Zaro JL, Rajapaksa TE, Okamoto CT, WC Shen. Membrane transduction of oligoarginine in HeLa cells is not mediated by macropinocytosis. *Mol Pharm* 2006;3(2):181-186.

145. Khine AA, Tam P, Nutikka A, CA Lingwood. Brefeldin A and filipin distinguish two globotriaosyl ceramide/verotoxin-1 intracellular trafficking pathways involved in Vero cell cytotoxicity. *Glycobiology* 2004;14(8):701-712.

146. Fittipaldi A, Ferrari A, Zoppe M, Arcangeli C, Pellegrini V, Beltram F, M Giacca. Cell membrane lipid rafts mediate caveolar endocytosis of HIV-1 Tat fusion proteins. *J Biol Chem* 2003;278(36):34141-34149.

147. Foerg C, Ziegler U, Fernandez-Carneado J, Giralt E, Rennert R, Beck-Sinkinger AG, HP Merkle. Decoding the entry of two novel cell-penetrating peptides in HeLa cells: Lipid raft-mediated endocytosis and endosomal escape. *Biochemistry* 2005;44(1):72-81.

148. Bentzen EL, House F, Utley TJ, Crowe Jr JE, DW Wright. Progression of Respiratory Syncytial Virus Infection monitored by fluorescent quantum dot probes. *Nano Letters* 2005;5(4):591-595.

149. Silva L, Coutinho A, Fedorov A, M Prieto. Nystatin-induced lipid vesicles permeabilization is strongly dependent on sterol structure. *Biochim Biophys Acta* 2006;1758(4):452-459.

150. Audouy S, Molema G, de Leij L, D Hoekstra. Serum as a modulator of lipoplex-mediated gene transfection: dependence of amphiphile, cell type and complex stability. *J Gene Med* 2000;2(6):465-476.

151. http://www.luc.edu/biology/images/lifecyl.gif